

The dynamics of hairpin vortices in a laminar boundary layer

Citation for published version (APA):

Zondag, H. A. (1997). *The dynamics of hairpin vortices in a laminar boundary layer*. [Phd Thesis 1 (Research TU/e / Graduation TU/e), Applied Physics and Science Education]. Technische Universiteit Eindhoven. <https://doi.org/10.6100/IR492454>

DOI:

[10.6100/IR492454](https://doi.org/10.6100/IR492454)

Document status and date:

Published: 01/01/1997

Document Version:

Publisher's PDF, also known as Version of Record (includes final page, issue and volume numbers)

Please check the document version of this publication:

- A submitted manuscript is the version of the article upon submission and before peer-review. There can be important differences between the submitted version and the official published version of record. People interested in the research are advised to contact the author for the final version of the publication, or visit the DOI to the publisher's website.
- The final author version and the galley proof are versions of the publication after peer review.
- The final published version features the final layout of the paper including the volume, issue and page numbers.

[Link to publication](#)

General rights

Copyright and moral rights for the publications made accessible in the public portal are retained by the authors and/or other copyright owners and it is a condition of accessing publications that users recognise and abide by the legal requirements associated with these rights.

- Users may download and print one copy of any publication from the public portal for the purpose of private study or research.
- You may not further distribute the material or use it for any profit-making activity or commercial gain
- You may freely distribute the URL identifying the publication in the public portal.

If the publication is distributed under the terms of Article 25fa of the Dutch Copyright Act, indicated by the "Taverne" license above, please follow below link for the End User Agreement:

www.tue.nl/taverne

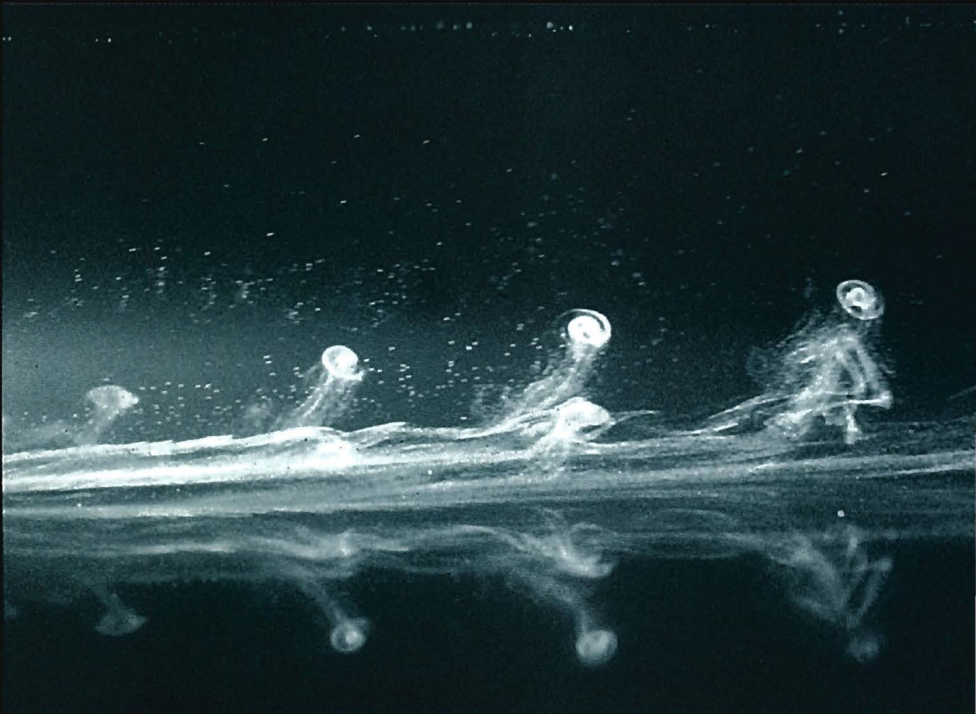
Take down policy

If you believe that this document breaches copyright please contact us at:

openaccess@tue.nl

providing details and we will investigate your claim.

The Dynamics of Hairpin Vortices in a Laminar Boundary Layer



H. A. Zondag

The Dynamics of Hairpin Vortices in a Laminar Boundary Layer

Herman Albert Zondag

CIP-DATA LIBRARY TECHNISCHE UNIVERSITEIT EINDHOVEN

Zondag, H.A.

The Dynamics of Hairpin Vortices in a Laminar Boundary Layer / by H.A. Zondag. - Eindhoven : Technische Universiteit Eindhoven, 1997

Proefschrift. - ISBN 90-386-0517-X

NUGI 812

Trefw.: wervels

Subject Heading: vortices

The Dynamics of Hairpin Vortices in a Laminar Boundary Layer

PROEFSCHRIFT

ter verkrijging van de graad van doctor aan de
Technische Universiteit Eindhoven, op gezag
van de Rector Magnificus, prof.dr. M. Rem,
voor een commissie aangewezen door het College
van Dekanen in het openbaar te verdedigen op

woensdag 9 april 1997 om 16.00 uur

door

Herman Albert Zondag

geboren te Rotterdam

Dit proefschrift is goedgekeurd door de promotoren:

prof.dr.ir. G.J.F. van Heijst

en

prof.dr.ir. A.A. van Steenhoven

Contents

1	Introduction	5
1.1	Background of the research	5
1.1.1	Coherent structures in the turbulent boundary layer	5
1.1.2	The measurement of turbulence	6
1.1.3	Artificially generated coherent structures	7
1.2	Objectives of the study	8
1.3	Strategy	9
1.3.1	Choice of experimental techniques	9
1.3.2	Method of analysis	9
1.3.3	Simulations	10
1.4	Overview of this thesis	11
2	The hairpin vortex: a conceptual model	13
2.1	Introduction	13
2.2	Hairpin vortices in turbulent flow	13
2.3	A conceptual model of the hairpin vortex and its dynamics	17
2.3.1	Introduction and definitions	17
2.3.2	Dynamics of the hairpin vortex	18
3	Visualization	25
3.1	Introduction	25
3.1.1	Overview of the chapter	25
3.1.2	Technical specifications	25
3.1.3	The three configurations	29
3.2	The standing vortex	31
3.3	The wake area	32
3.4	The initial stages of the hairpin vortex	36
3.5	The secondary deformation of the vortex legs and the quasi-spanwise vortex	40
3.6	Discussion	52

4	The wind tunnel data-acquisition facilities	57
4.1	The wind tunnel	57
4.2	The vortex generating obstruction	58
4.3	The hot-wires	59
4.4	The data-acquisition	65
4.5	The method of hot-wire data representation	67
5	Hot-wire measurements	71
5.1	Introduction	71
5.1.1	Overview and interpretation of the measurements	71
5.1.2	Scaling	72
5.1.3	The different types of measurements	72
5.2	The shedding period	73
5.3	The standing vortex	77
5.4	The vortex-induced velocity field	79
5.4.1	Introduction	79
5.4.2	Cross-sections in the Yt -plane	79
5.4.3	Cross-sections in the Zt -plane	82
5.5	The downstream evolution of the hairpin vortices	87
5.5.1	Cross-sections in the Yt -plane	87
5.5.2	Cross-sections in the YZ -plane	90
5.6	The effect of the Reynolds number	96
5.6.1	The modal vortex	96
5.6.2	The average u -velocity profiles	97
5.7	The secondary deformation of the legs	103
5.8	Discussion	105
6	Biot-Savart approximation	109
6.1	Introduction	109
6.2	The model	110
6.3	Results	111
6.3.1	Introduction: obtaining a vortex	111
6.3.2	The effect of the neck	113
6.3.3	The circulation	113
6.3.4	The v -velocity	115
6.4	Conclusions	116
7	Numerical simulations	119
7.1	Introduction	119
7.2	Dimensionless numbers	120
7.3	Special case I - the spanwise vortex	121
7.3.1	Introduction	121
7.3.2	Theory: the equations	122
7.3.3	Theory: a spanwise vortex in a shear flow	124

7.3.4	The circulation	125
7.3.5	The Reynolds number	127
7.3.6	The boundary layer thickness	128
7.3.7	Implications for hairpin vortices	131
7.4	Special case II - the streamwise vortex	132
7.4.1	Introduction	132
7.4.2	The motion of streamwise vortices	134
7.4.3	The streamwise velocity profile	137
7.4.4	Implications for hairpin vortices	138
8	Concluding remarks	143
8.1	Conclusions and Discussion	143
8.1.1	The experimental results	143
8.1.2	The results of the simulations	147
8.2	Suggestions for further research	148
A	The numerical code	151
A.1	Annotation	151
A.2	Description of the numerical program	151
A.2.1	The equations	151
A.2.2	The discretization	156
A.3	The boundary conditions	159
A.4	Testing the program	161
A.4.1	Moving Lamb dipole	161
A.4.2	Lamb vortex impact on the wall	161
A.5	Viscous growth	161
A.6	Tracking a vortex	163
B	The pressure gradient	167
	Bibliography	169
	Summary	173
	Samenvatting	175
	Nawoord	177
	Curriculum Vitae	178

Chapter 1

Introduction

1.1 Background of the research

1.1.1 Coherent structures in the turbulent boundary layer

Turbulent flow is characterised by the existence of eddies of various scales. These eddies are dissipated by viscous effects. Therefore, new eddies have to be created to maintain the turbulent character of the flow: turbulence cannot maintain itself. The creation of new eddies is generally associated with regions of shear. For a wall flow such a region is provided by the boundary layer. If no gradient region is present, no new eddies are generated and the turbulence gradually disappears, as in the case of grid turbulence. The size of the largest eddies is typically of the order of the thickness of the shear layer. Larger eddies transfer their energy to smaller eddies in a process that is called the energy cascade. The smaller the size of an eddy, the larger the proportion of its energy that is lost due to viscous dissipation. The smallest scale is given by the Kolmogorov scale.

New eddies are generated in the turbulent boundary layer. Since many boundary layer flows are turbulent (the flow in the earth's atmosphere, oceanic currents, flow over airfoils), a lot of research has been done to gain insight into this type of flow. This research has been stimulated not only by scientific interest but it also got an important impulse from the importance of the understanding of turbulent flow in industrial applications. In this research, interest in coherent structures has played a role of increasing importance.

Among the many proposed types of coherent structures, it seems that in turbulent boundary layers hairpin-like vortices are the most dominant ones (e.g. Robinson, 1991 and Smith & Walker, 1995). This hypothesis is supported by the observation that this rather complicated flow structure is generated very easily: casual observations in our water channel showed that hairpin vortices even emerge in a laminar flow over a flat plate around obstacles like a hemi-

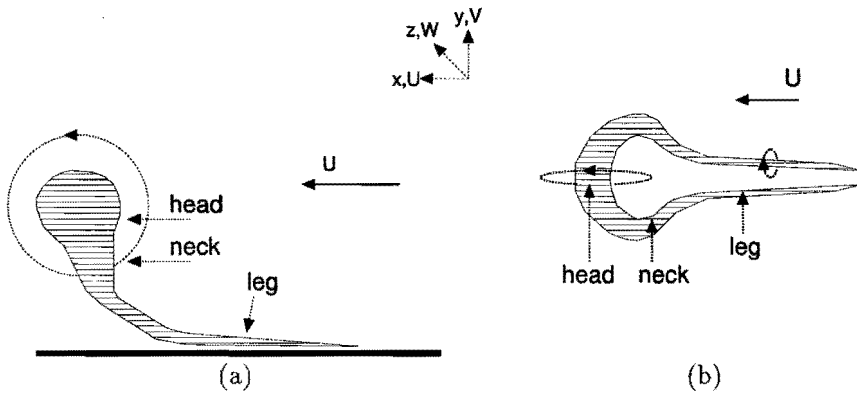


Figure 1.1: A schematic representation of a hairpin vortex (a) side view (b) top view

sphere or a teardrop-shaped obstacle. A hairpin vortex is characterised by its head, neck and legs, as shown in figure 1.1.

However, in a turbulent boundary layer the behaviour of vortices is also strongly determined by the surrounding flow. The boundary-layer flow contains other small scale vortices in the inner layer and incidental large scale vortices in the outer layer. The literature indicates that in turbulent boundary layers complete symmetric hairpins are hardly ever found. More often, distorted structures are observed like one-legged-hairpins, single legs etc. This makes the analysis of the role of hairpins in real turbulence in the presence of other types of flow structures a rather complicated affair.

1.1.2 The measurement of turbulence

The research on turbulence during the first half of this century was fully pre-occupied with the idea of turbulent flow as being a stochastic phenomenon, consisting of a well defined mean flow over which random fluctuations were superimposed. With statistical methods (like Fourier decomposition) the most dominant features were reconstructed. The presently very popular and advocated method of proper orthogonal decomposition is perhaps the most pronounced modern exponent of this strategy.

However, these statistical approaches give information on e.g. the distribution of eddy scales at a certain location. They do not provide direct information with respect to the dynamics: the mechanisms involved in the creation of new eddies or the energy transfer from the larger to the smaller scales. Nor does such an approach specify anything about the shape of the individual eddies involved. Since the character of the micro-structures determines to a large extent

the overall flow behaviour, it is important to gain a better insight into these mechanisms.

From the early 1960s onwards, attention has increasingly been drawn towards the transport ability of non-random large scale vortices appearing in turbulent flow. One step into the direction of the dynamics of individual eddies is the increased interest in 'coherent structures' in turbulent flow. These coherent structures can be understood from the observation that the eddies in the turbulent flow appear in the velocity measurements as regions in which the velocity is spatially correlated. However, this identification is not unique nor does an exact definition of a coherent structure exist. Kline (1992) gives a summary of those points that are more or less accepted about coherent structures and he also reviews the points valuable for future research. His extensive list makes clear that a large number of questions is still open. The mechanisms playing a role in the creation of a turbulent boundary layer are so complex and the experimental requirements to measure the phenomena accurately are so high that at this moment a complete picture of all relevant mechanisms is still a long way off.

1.1.3 Artificially generated coherent structures

Much importance is attributed to the hairpin vortex for the maintenance of turbulence in a turbulent boundary layer flow. Therefore, it is a sensible approach to concentrate our studies on a single type of coherent structure: the hairpin vortex in its purest form. However, to track single hairpin vortices in a turbulent environment is a task that is beyond the possibilities of the present experimental techniques. Therefore, researchers have turned to the artificial generation of hairpin vortices in a laminar environment in order to investigate aspects of the development of a hairpin vortex like the effect of the shear or the interaction with the wall. As stated above, hairpin vortices are created in a laminar environment behind structures such as a hemisphere. This method for the creation of hairpin vortices was also used by Acarlar & Smith (1987a). Other researchers have created artificial hairpins by means of fluid injection (Haidari, 1991; Acarlar & Smith, 1987b). The state-of-the-art is illustrated by a recent paper by Haidari et al. (1994). The main method of analysis in these investigations is flow visualisation. Although some quantitative data can be gained from the approach, a quantitative characterization of the velocity field remains out of scope. In addition, the governing processes and the importance of external parameters are still largely unknown. The importance of the latter is indicated by the observation that in the experiments of different researchers, it seems that the vortex structures tend to have a somewhat different shape. This seems to indicate that the exact shape depends on the generation technique. It thus seems that one cannot even speak of *the* hairpin vortex, but that the shape of a hairpin vortices depends on unknown variables.

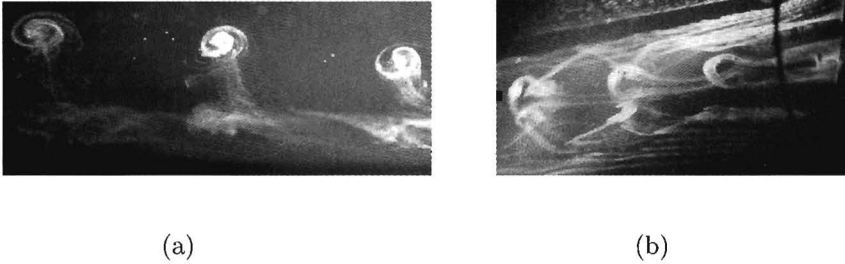


Figure 1.2: Photographs of hairpin vortices in a laminar boundary layer downstream of a hemisphere **(a)** Side view, **(b)** Top view.

In this research project a street of hairpin vortices is created artificially by means of an obstacle placed in a laminar wall flow. The reason to study a street of hairpin vortices and not a single vortex is partly pragmatical, partly intentional. The pragmatic reason is that the hemisphere provides a simple means to generate a stable street of hairpins. The intentional reason is that in real turbulence 'bursts' are observed that consist of a series of ejections. This phenomenon is of a cyclic nature and is probably the most typical phenomenon observed in turbulence. A burst can better be described as a street of hairpins than as a single hairpin. The interaction of hairpins may be as important as the effects of a single hairpin. The photograph in figure 1.2 shows a hairpin that is created in our own experiments in the flow past a hemisphere on a flat plate.

1.2 Objectives of the study

The main justification of this research project lies in the need for quantitative data about hairpin vortices. Measurements should provide us with more data about the three-dimensional spatial character of the structure. A careful analysis of these data then should lead to more insight into the causative mechanics in the process of creation, development and decay of a hairpin. Rather than investigating one specific question related to hairpins into all its smallest details, we will pay attention to a number of effects that are probably the most dominant for the overall behaviour of hairpin vortices. What processes are characteristic for the evolution of a hairpin vortex, what is the influence of the shear profile and what is the influence of the Reynolds number? Such questions lead us to the dynamics of the phenomenon. In the present research, the dynamics of the hairpin vortex will be considered whenever this is possible.

In addition to the fluid dynamics itself, our research has two additional objectives. One is the development of a good method for the analysis of the measurement data provided by hot-wire signals. The other is to improve the

hot-wire instrumentation as used in our laboratory. Attention should be paid to developing a hot-wire probe with a sufficient spatial resolution and the absence of a blockage effect caused by the probe.

1.3 Strategy

1.3.1 Choice of experimental techniques

In order to investigate the dynamics of a hairpin vortex, it is necessary to measure a single structure as it moves downstream. This requires a multi-point measurement technique for the characterisation of the structure at one location, as well as the provisions to track it as it moves downstream. The most natural choice seems to be Particle Image Velocimetry. However, this technique is still in its infant stage and is limited to mainly 2D-flows, so this was not tried. Fortunately, because the hairpin vortices shed behind an obstacle reproduce very well, it is not very important to track one single vortex because the shape of the vortices is to a large extent only a function of the downstream distance. This simplifies the experimental requirements enormously.

However, it is still desirable to be able to characterise a vortex at one location by one measurement, which requires multi-point measurements. However, multi-point Laser Doppler analysis is out of the question. Consequently the natural alternative is hot-wire anemometry. In the Fluid Dynamics Laboratory much experience has been obtained with single-wire constant-temperature anemometers (CTA). On the basis of this experience during the last years an instrumentation system was constructed with a rake of 9 hot-wires (Van Galen, 1994) in order to be able to perform spatially distributed measurements. The array of wires can be rotated around an axis in the streamwise (x) direction. The chosen configuration is such that the blockage effect is minimized. A disadvantage of the set-up is that no data can be obtained about the spatial correlations in the x -direction. In addition, we have to characterize the behaviour of the vortices from the fluctuations in the streamwise velocity component. The interpretation of these fluctuations is not always easy. In order to support the interpretation of the measurements, visualization experiments are conducted in a low-speed water channel in which the hairpins can be visualised rather easily by means of H_2 -bubble techniques.

1.3.2 Method of analysis

In this project we start with the a-priori knowledge that only one type of structure is present in the flow and that the stochastic effects due to other structures are absent. The only stochastic effects that are still present are produced by:

- variations in the shedding frequency of the hairpins

- variations in the strength of the hairpins
- variations in the shape of the vortices (especially in the height of the heads of the hairpin vortices).

These variations seem to be generated by the small background-turbulence ($\sim 0.6\%$) as well as by the influence of the vortex that was shed previously. Owing to the stochastical variations in the shape of the vortices it is necessary to pay special attention to the analysis of the signals. A disadvantage of the use of conditional averages is that the most characteristic features may be averaged out. A situation often encountered in our experiments is one in which one vortex passes above the point of measurement and a second vortex passes a little below it. The temporal average of the two measured signals is almost zero, but zero is not the best description of the effect of the vortex. It is beside the truth to state that the average of male and female is a neuter gender. Attention should be paid to methods that take into account the stochastical aspects of the events, but in such a way that no typical phenomena get lost.

From the visualizations and the interpretation of the measured velocity field it is possible to show the development of an individual hairpin vortex. In addition, it is possible to model the shape of a hairpin by a line vortex with a Rankine-type vorticity distribution that is bent in the shape of a hairpin. It is then possible to calculate the velocity field around such a structure by a Biot-Savart calculation as shown in chapter 6. Comparing the result with the measured velocity field gives an estimate for some vortex parameters that are difficult to measure directly, like the circulation (Γ) of the vortex.

1.3.3 Simulations

The numerical flow simulation is a subject on its own. Close to the wall viscous effects play an important role and we cannot approximate the flows as inviscid. A choice had to be made about a numerical technique. A 2D and a parabolic 3D code have been developed that give promising results for the simulation of vortices in viscous fluids near a wall. The numerical method is based on an ADI-method and is computationally efficient. This code was extended and revised for the type of problems studied here, where we have to account for inflow, outflow and a shear. A related project concerns a complete 3D simulation of flows around bluff bodies using a spectral method (Vissers, 1996). This work is still in progress and, unfortunately, it will take some more time before the first results can be expected from it.

It is not possible to compute the evolution of a hairpin vortex with a 2D or a parabolic 3D code, since a hairpin vortex is a complicated unsteady 3D flow structure. However, in order to understand the dynamics of the development of such a vortex, it is also important to investigate the mechanisms that determine the evolution of the hairpin vortex in isolation. For example, the 2D and parabolic 3D simulations enable us to examine the effect of isolated spanwise

(head) or streamwise (leg) vortices on the viscous wall fluid in the presence of a shear. In this way we can investigate aspects like the creation of low-speed streaks by the legs or the creation of secondary vortices.

1.4 Overview of this thesis

In chapter 2 some general ideas about the evolution of hairpin vortices are presented. Also some earlier results on the evolution of hairpin vortices are discussed. In chapter 3 the visualizations are presented. In chapter 4 the hot-wire equipment and the method of analysis is explained and chapter 5 presents the corresponding hot-wire measurements. Chapter 6 shows the results of some Biot-Savart calculations. The velocity field is calculated in the plane of symmetry between the vortex legs. The calculations are based on the vortex shape that was found in the visualizations. Chapter 7 shows the numerical simulations. The evolution of spanwise vortices (heads) and streamwise vortices (legs) are calculated. Finally, chapter 8 presents the conclusions and gives some suggestions for further research.

Chapter 2

The hairpin vortex: a conceptual model

2.1 Introduction

In the first part of the chapter, a brief description is presented of the historical route leading to the present study and the aims of this study are summarized. The second part of the chapter is devoted to the presentation of some general ideas about hairpin vortex dynamics, in which some comments will be included on the interpretation of previous results by others.

The lengthscales x^+ , y^+ and z^+ , that are used in this chapter, are defined in the conventional way as $y^+ = y\sqrt{\tau/\rho/\nu}$. In this equation τ represents the wall friction, ν the viscosity and ρ the density of the medium.

2.2 Hairpin vortices in turbulent flow

In the first chapter we have indicated that studying coherent structures is necessary to be able to understand the dynamics of turbulent flow. Although the concept of the energy cascade is very useful for statistical purposes, it leaves two questions open:

1. Which mechanism is responsible for the actual transport of energy from larger to smaller scales?
2. Which mechanism is responsible for the generation of new eddies?

With respect to the generation of turbulent eddies, the wall is the only source of new vorticity and its importance is indicated by the fact that $\sim 75\%$ of the turbulence production takes place in the region $y^+ < 50$, as found by Klebanoff (1954). The first attempt to explain *how* turbulent energy is generated near

the wall was made by Theodorson (1952), who proposed a hypothetical three-dimensional Gaussian-shaped eddy that was inclined to the wall under an angle of 45° .

Further research of the turbulent boundary layer led to the establishment of the low-speed streaks as an important feature of the boundary layer in the inner part of the wall layer, that seemed to be related to the near-wall production of turbulence (Kline & Runstadler 1959). This was another indication for the conclusion that the viscous sublayer could by no means be regarded as laminar, as was assumed previously. In subsequent research (e.g. Kline et al. 1967) a number of characteristics of these streaky structures were established. The streaks exist in the wall region for $0 < y^+ < 40$, have a spanwise periodicity of $z^+ \approx 100$ (Kim et al. 1971), a typical velocity of half the local mean (Kline et al. 1967), a typical width Δz^+ of about 20 to 60, a length of $1000x^+$ or more (Hirata & Kasagi 1979) and meandering over $z^+ = 30$ to 50. It was initially concluded that the low-speed streaks ended with a violent 'ejection' of near-wall fluid into the outer region, which was followed by a 'sweep' of high-speed fluid towards the wall. Later, it was found by Smith & Metzler (1983) that the low-speed streaks are not terminated by such a burst, but continue to grow although the ejection takes a large part of the low-speed fluid away. In addition, it has been suggested that the conditional sampling results which produced the evidence for the initially proposed mechanism did not so much represent the termination of a low-speed streak, as well as the passage of a meandering low-speed streak in the z -direction over the detector (Kunen 1984, Blokland & Prasad 1986).

These observations gave rise to a new series of phenomena to be explained. New questions arose that have haunted the research on the turbulent boundary layer ever since:

1. What processes are involved in the creation of low-speed streaks?
2. What processes are involved in the violent break-up of low-speed streaks?
3. How can the spanwise periodicity be explained?

The origin of the low-speed streaks has often been ascribed to long, quasi-streamwise vortices. These vortices seemed to appear in counter-rotating vortex pairs, as indicated by e.g. Blackwelder & Eckelman (1979). Such vortex-pairs were also visualized by Smith & Schwartz (1983). After numerical simulation had entered the field, Ersoy & Walker verified that long quasi-streamwise counter-rotating vortices were indeed able to create low-speed streaks. The origin of these counter-rotating vortex pairs remained obscure. As a possible candidate for their creation, a Görtler instability was proposed by various researchers (see Blackwelder 1982). It was suggested that the random background turbulence produced sufficient curvilinear motion to reach the critical Görtler number instantaneously. On the other hand, the deformation of an initial spanwise vortex in a region with a strong shear also leads to the creation of a pair

of streamwise counter-rotating vortices, as indicated in e.g. Hinze (1975). A kernel study to this effect was performed by Acarlar & Smith (1987) and this view was also adopted by Ersoy & Walker (1985).

The bursting phenomenon is most important in the production of turbulence. The origin of this effect was even more obscure than the origin of the counter-rotating vortices. In a visualization study, Nychas et al. (1973) associated the ejections with large spanwise vortices on a scale of approximately $200 y^+$ units and whose centre of rotation was in the range of $200 y^+$ to $400 y^+$ from the wall. They suggest that the ejections might be due to the near-wall pressure induced by the spanwise vortex. The creation of the spanwise vortices was associated with a region of low-speed fluid that was followed by a region of high-speed fluid and was not associated directly with the ejections, which were on a smaller scale (up to a height of $80 - 100 y^+$). The sweep effect was also a consequence of the high-speed fluid. In Hinze (1975) it is also suggested that the ejection of the near-wall fluid is due to the effect of the spanwise head of a hairpin-vortex-like structure, that is created near the wall as a consequence of some large outer-layer disturbance. Hinze claims that underneath this hairpin vortex structure a low-speed streak is created and he attributes the sweep to the subsequent breakdown of this low-speed streak, due to the instability of the inflectional profile that exists on top of the streak. This point of view, in which a spanwise vortex was due to the ejection of the near-wall fluid, was also adopted in a numerical study of Doligalski and Walker (1984). The idea that the ejections were provoked by large scale eddies in the outer region of the turbulent boundary layer was supported by the earlier work of Rao et al. (1971), who concluded that the bursting frequency scaled with the variables of the outer layer, rather than with inner variables. On the other hand, Ersoy and Walker (1985) claimed that the streamwise counter-rotating vortex pairs were in itself enough to create an ejection of the boundary layer fluid. However, the review of Doligalski, Smith & Walker (1994) seems to indicate that they consider the effect of the spanwise vortex as dominant.

The importance of both spanwise and streamwise vortices is indicated above. A model that provides both is given by the hairpin vortex shape, that was already proposed by Theodorson. It supports the general idea that while streamwise vortices are most common close to the wall, in the outer region spanwise vortices are dominant (see e.g. Robinson 1991). More support for this hairpin-hypothesis came when Head and Bandhyopadhyay (1981) were able to visualize hairpin vortices in the turbulent boundary layer directly, using smoke visualization. These structures were inclined to the wall at about 45° - as predicted by Theodorson. Their size and shape turned out to be strongly dependent on the Reynolds number, but essentially resembling Theodorson's Gaussian vortices. The importance of the hairpin-shaped vortices was again affirmed in an article by Perry and Chong (1982), who were able to prove that a hierarchy of

A-shaped vortices can indeed reproduce the turbulent flow velocity profile and the turbulent intensity.

All this support for the hairpin-vortex hypothesis seemed to require further research into the nature of the interaction between the hairpin-vortex and the flow. A visualization study of artificially created hairpin vortices behind an obstruction in a laminar flow was performed by Acarlar & Smith (1987a). This study revealed that hairpin vortices cause a substantial thickening of the viscous flow near the wall. In addition, secondary vortices were found to grow just upstream of the vortex head. These secondary vortices were observed to interact with the primary vortices to produce a burst-like event as the combined structure was suddenly ejected into the main flow. Additionally, Acarlar & Smith found vortical structures generated alongside the hairpin which they ascribed to the influence of the standing vortex that flanked the hairpin vortices for the case of a blunt obstruction. Further research on the dynamics of hairpin vortices was performed by the numerical study of Hon & Walker (1987), who computed the evolution of the hairpin vortex as a function of the shear layer thickness. They found the growth of subsidiary vortices alongside the primary hairpin vortex, that were caused by an inviscid interaction of the hairpin with the infinitely long spanwise vortex with which their calculations were initiated. Although this does not have an obvious implication for fully developed turbulence, it might correspond to the deformation of the Tollmien-Schlichting waves in the region of transition. The importance of the hairpin-vortex hypothesis in the transition region was further stressed by Sankaran (1988) with respect to the substructures in turbulent spots. Haji-Haidari (1990) introduced a more sophisticated method for the artificial creation of hairpin vortices by using controlled fluid injection, which enabled him to create single vortices. He found that these primary vortices were able to generate large amounts of secondary and tertiary structures that started to interact with each other and finally degenerated into a turbulent spot.

In summary, hairpin-vortices seem to be able to give explanations for many special features of the turbulent boundary layer. They are proposed as the causative mechanism behind the creation of the low-speed streaks as well as the eruption of the near-wall flow. In addition, experiments and simulations have verified that hairpin vortices can produce new vortices in a viscous-inviscid interaction with low-speed fluid near the wall.

The present study concerns the creation of hairpin vortices behind a solid obstruction in a laminar boundary layer, similar to the visualization study of Acarlar & Smith (1987a). However, an extensive set of hot-wire measurements is provided in addition to the visualizations and several effects have been investigated numerically. Much attention is paid to the effect of the standing vortex,

that exists upstream of a blunt obstruction. Its effect on the near wall velocity is shown and its interaction with the hairpin vortex will be examined. It will be shown that the effect of the standing vortex strongly affects the ability of the hairpin vortex to generate secondary vortices. In addition, in the present study the generation of secondary hairpin vortices seems to be related to a deformation of the vortex legs. This deformation seems to be related to the creation of a quasi-spanwise vortex in a mechanism that resembles the observations of Nychas (1973). This effect indicates that the change that a hairpin vortex brings about in its environment seems to play an active role in the subsequent deformation of the hairpin vortex itself: hairpin vortices not only generate secondary hairpin vortices but also quasi-spanwise vortices.

Finally, the effect of riblets is investigated. Although it is well established that streamwise riblets with a width of $6 < z^+ < 20$ cause a reduction in surface drag (Walsh & Lindemann 1984, Nitschke 1984), it is still not clear why they do so (Coustols 1995). In this study, the effect of riblets on the artificially generated hairpin vortices and the surrounding flow is measured. It will be shown that the riblets cause an important reduction of the standing vortex, with corresponding consequences for the subsequent evolution of the hairpin vortex.

2.3 A conceptual model of the hairpin vortex and its dynamics

2.3.1 Introduction and definitions

The hairpin vortex is characterised by its three-dimensional structure, which consists of a head, two necks and two legs, as depicted in figure 2.1. In addition, the direction of rotation is indicated.

It seems that the development of hairpin-like structures is a general phenomenon related to shear flows. Not only have hairpin vortices been found in the turbulent boundary layer, but also e.g. in free shear flows (see e.g. Cantwell, 1981). The generation of hairpin vortices can be understood as follows. If a spanwise vortex that is moving in a shear flow contains a local perturbation in the direction of the velocity gradient, the perturbed part of the initially spanwise vortex arrives in a location with a higher velocity and is drawn along with this higher velocity. Consequently, two streamwise ‘legs’ develop, which connect the spanwise ‘head’ with the original spanwise vortex.

It is also possible to create a hairpin vortex by inserting an obstruction in the flow or by injecting low-speed fluid. In the present study, the first method was applied. However, it will be shown later that the type of obstruction used influences the shape and the evolution of the hairpin vortex.

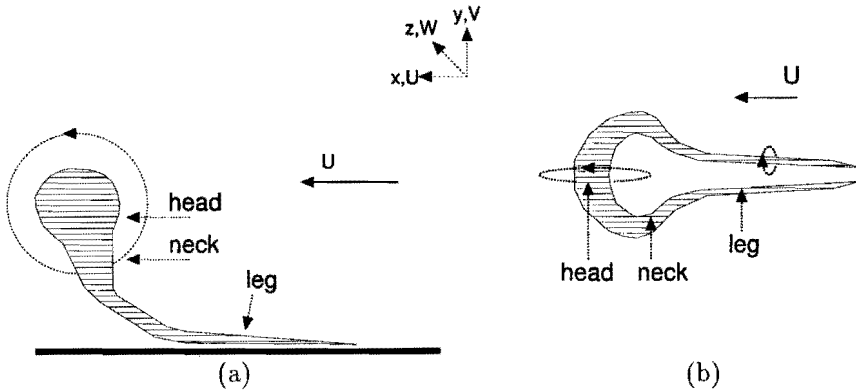


Figure 2.1: The hairpin vortex consists of a head, two necks and two legs. (a) side view, (b) top view.

2.3.2 Dynamics of the hairpin vortex

The hairpin vortex is a complex structure that is convected along with the flow. During its evolution, several effects play a role:

1. The effect of the local velocity profile.
2. The mutually induced velocities of the legs and the head (its internal dynamics).
3. The effect of the wall.

The analysis of this complicated combination of effects is complicated even further by the fact that also second-order effects are of importance: e.g. the local velocity profile is also deformed by the hairpin vortex.

In the remainder of this section, these three effects will be analysed separately. Since the effect of the hairpin vortex on the velocity profile depends, among other things, on the vorticity distribution of the vortex, this effect will be treated in a separate paragraph. Finally, as this study is concerned with the artificial creation of vortices in a laminar flow downstream of an obstruction, the effect of the type of obstruction will be indicated.

The effects of the velocity profile The evolution of a distorted spanwise vortex with a core radius of 0.02 in a flow with a constant shear has been calculated by Hon & Walker (1987). Their results are illustrated by figure 2.2. It is clearly shown that the spanwise vortex grows into a hairpin shape by the effect of the shear. In the evaluation of their results, it should be remembered that two effects are not taken into account: (1) the effect of the wall and (2) the

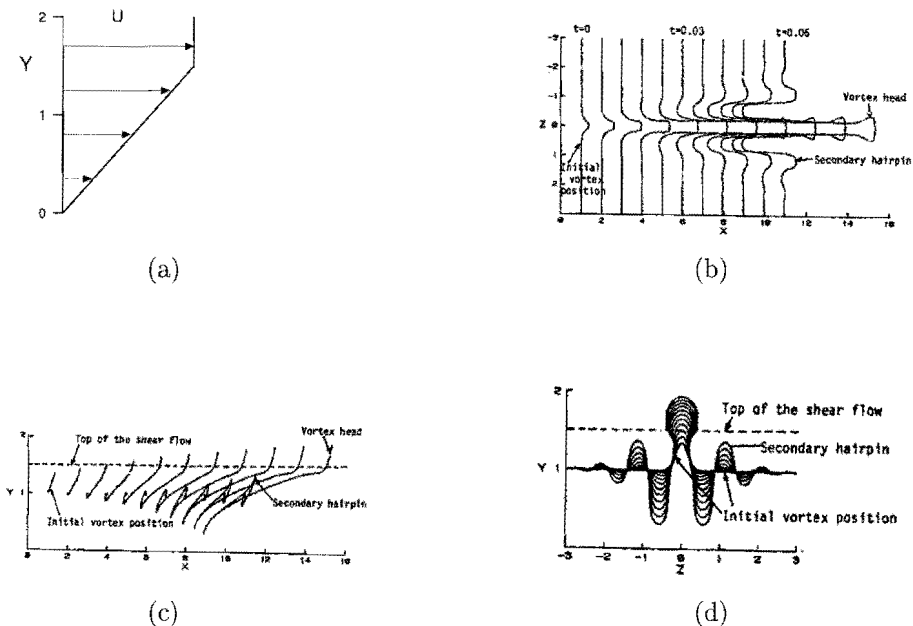


Figure 2.2: The evolution of a distorted spanwise vortex in a linear shear flow as computed by Hon & Walker (1987) (a) the imposed velocity profile, (b) top view, (c) side view, (d) front view.

second-order effect of the distortion of the velocity profile by the hairpin, since the velocity profile was fixed in their calculations.

A general observation is that a hairpin vortex can be considered in first order as passively convected along with the flow. The mutual induction effects are relatively small here: they are of importance mainly when they cause a small distortion of the vortex in the y -direction, because in that case this distortion is subsequently amplified by the velocity gradient.

Finally, the 'shear effect' should be mentioned that was introduced by Head & Bandopadhyay. The idea is illustrated by figure 2.3, which shows that the vortex seems to be tilted towards the direction of the main flow. Obviously, although the vortex is rotated towards the main flow direction, no fluid is displaced in the directions perpendicular to the flow.

The effect of mutual induction The effects of mutual induction can also be discussed with the help of figure 2.2. Four effects deserve special attention:

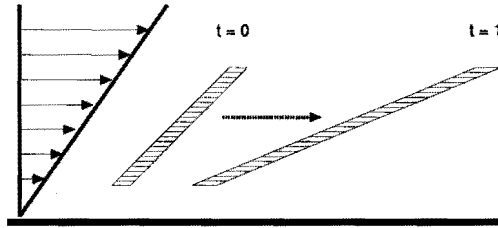


Figure 2.3: The "shear effect".

1. the rise of the head
2. the widening of the head
3. the wallward growth of the legs
4. the creation of secondary (subsidiary) vortices adjacent to the primary hairpin vortex.

The rise of the head is well-known from the literature (e.g. Head & Bandhyopadhyay, 1981). It seems that the head is pushed upwards by the effect of the legs, even though it is not located directly above these legs.

The widening of the head is a less well-known effect. It should be attributed to the fact that once the head has arrived above the legs (in which 'above' is not meant with respect to the y -direction but with respect to the mathematical plane that contains both legs), the legs push the vortices in the neck apart. This effect should be expected to play a role whenever $\partial^2 u / \partial y^2 < 0$, which is the case in any boundary layer flow.

The other two effects mentioned above seem to be a consequence of the interaction of the hairpin vortex with the accompanying infinitely long spanwise vortex that was imposed on the flow in the initial conditions of the calculations. This interaction is highly relevant when related to a Tollmien-Schlichting wave in a transitional flow, but, to the opinion of the present author, these calculations do not apply to the present case of vortex shedding as a consequence of a local distortion of the flow, although Walker, Smith and others seem to claim a more general validity of these results. In particular, the secondary vortices which grow alongside the primary hairpin vortex¹ seem to result from this interaction. With the experimental set-up used in the present study, these secondary

¹Walker renamed these secondary vortices into 'subsidiary vortices' in his later papers to distinguish them from the secondary vortices that were observed upstream of the vortex head (Acarlar & Smith 1987).

vortices did not appear. Similarly, it seems that the wallward growth of the hairpin legs in the model of Hon & Walker is also due to this interaction: this phenomenon just seems to show the part of the spanwise vortex that is pushed towards the wall by the legs. The observed spanwise spreading of the vortex that is indicated in figure 2.2d is only applicable if such a long spanwise vortex exists.

The method of calculation applied by Hon & Walker is limited to this type of vorticity-distributions because of the fixed velocity profile. Since the conservation of circulation requires that vortex lines do not end in the flow, the vortex tube has to end at infinity. However, in a real flow where the instantaneous velocity profile is not constant in the spanwise and streamwise directions, it is more realistic to represent an eddy in a turbulent flow as a temporal and spatial merging of some of the vortex lines that are present in the flow. In the latter case the situation is not adequately described by a vortex superimposed on a background velocity field that is constant in the spatial directions.

In addition to these problems, the fixed velocity profile gives unphysical results with respect to secondary effects in which the hairpin affects the shear flow. In our experimental set-up, these second-order effects become important when the hairpin legs create patches of high-speed fluid adjacent to the hairpin vortex. These patches have a destabilizing effect on the near-wall flow (see chapter 3). Finally, the legs tend to push each other upwards into the flow, although this effect is not very obvious from Hon & Walker's calculations. This phenomenon depends strongly on the circulation of the original vortex tube, as well as on the width of the original distortion. Note that the spanwise width of the distortion is more or less preserved during the entire evolution of the hairpin vortex (see figure 2.2b)! This indicates the importance of the initial conditions for these simulations.

The effect of the wall The effect of the wall can be represented by mirror vortices. Although strictly speaking, the mirror-vortex analogy is only valid in inviscid flow, it can be applied to viscous flow too, as long as the diffusion of the vorticity from the vortex or the wall can be considered to be small.

In this approximation, the wall has two effects: pushing the legs together and retarding the head. The effect of the wall on the legs amplifies the rise in the legs due to their mutual induction. In our experimental set-up it was not possible to estimate the development of the height of the legs with sufficient accuracy to measure this effect. The observation of the movement of the legs due to this effect was obscured by the effect of the subsequent hairpin vortex that ran over them. But, just as in the calculations of Hon & Walker, it did not seem very prominent: the legs remained close to the wall. Since the legs are very close together, this has to be explained by assuming a low value for Γ in the legs. This was indeed found by Acarlar & Smith who estimated the circulation of the legs at $\frac{1}{7}$ of the circulation of the head. This variation in the circulation along the

vortex can be explained by taking into account that the legs originate from the shear layers at the sides of the wake. These regions are closer to the wall than the shear layer at the tip of the obstruction that rolls up into the vortex head. Therefore, the velocity difference over these shear layers is smaller and since this velocity difference determines the circulation of the newly created vortex, the circulation of the legs can be expected to be smaller than the circulation of the head². In addition, since the hairpin vortex legs contain vorticity of opposite sign, mutual cancellation of vorticity can be expected to play a role.

The vortex head is pushed upstream by the mirror-image effect of the wall. Although the head is retarded by its mirror-image effect, the vortex neck is not. Acarlar & Smith (1987a) observed that the head of the vortex was driven back to such an extent that finally it was located upstream of the legs, which they explained by means of this mechanism. However, the image of the vortex head does not only affect the vortex head itself, but the entire flow in the area between the location of the vortex head and the wall, including the vortex neck that is located in this region and that therefore is driven back just like the head. Therefore their explanation cannot be correct. The phenomenon in which the head arrives upstream of the neck was observed in our experiments too, but in our case it seemed to be related to a mechanism that accelerated the lower part of the neck, rather than one that retarded the head.

The vorticity distribution The 'shear-effect' mentioned previously is related to a stretching of the vortex tube, which leads to an increase of the vorticity in the legs of the hairpin. For inviscid flow, the effects of vortex stretching and vortex tilting follow directly from Kelvin's circulation theorem, which states that Γ is constant along a streamtube. This effect can be described as a concentration of the vorticity in the vortex core. The redistribution of vorticity affects only the velocity in the centre of the vortex.

In a shear flow, the ω_x in the legs increases linearly in time, in contrast to the exponential increase that is found in the case where the stretching is in the same direction as the velocity gradient (as is the case in a contraction).

The effect of the viscosity is to diffuse the vorticity in the directions perpendicular to the streamtube (which can be represented by a 'leaking' streamtube). For a vortex tube in a shear flow, as a consequence of the tilting of the vortex, the core decreases in size and the vorticity in the core displays a corresponding increase until the core has become sufficiently small so that viscous effects become important, which stops further reduction of the vortex core.

It will be shown in chapter 3 that the radius of the legs and the head is generally not the same, as might be expected from the observation that, while the shear causes the elongation of the legs, the head is not subject to this effect.

²There is no need to assume a constant value of Γ along the hairpin vortex, since the flow field is non-homogeneous in all spatial directions. All over the surface of the hairpin vortex, vorticity lines are fanning out into the flow field.

The analysis above is only concerned with hairpin vortex legs under the effect of a constant shear flow. For vortex shedding from an obstruction, more effects come into play. In particular, the wake of the obstruction imposes a pressure distribution downstream of the obstruction and a corresponding positive $\partial u/\partial x$. It will be shown in chapter 3 that this effect is quite substantial. Immediately downstream of the obstruction, therefore, a strong vortex stretching effect should be expected. In addition, the corresponding w and v velocities around the obstruction affect the development of the hairpin vortex.

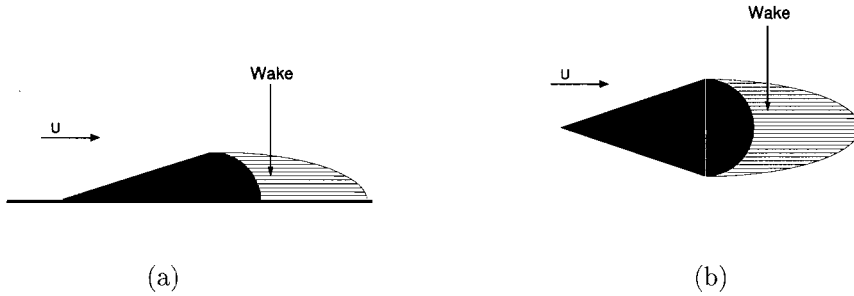


Figure 2.4: The structure of the flow field around a droplet. (a) Side view (b) Top view.

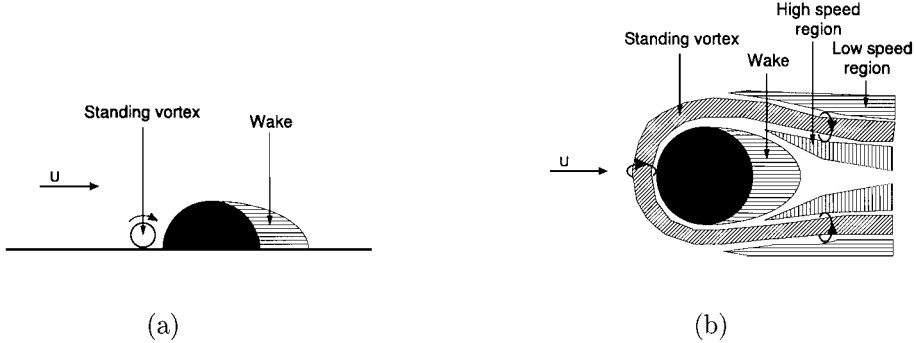


Figure 2.5: The structure of the flow field around a hemisphere. (a) Side view (b) Top view.

The effect of the obstruction In the case of vortex shedding behind an obstruction, the obstruction affects the velocity field that in its turn determines the initial evolution of the hairpin vortex. In the present work two obstructions are used: a hemisphere (a blunt obstruction) and a droplet (a streamlined obstruction). These same obstructions are used in the experiments of Acarlar &

Smith (1987a).

The structure of the flow fields for the droplet and the hemisphere are indicated in figures 2.4 and 2.5. Two effects are important in the modification of the velocity profile: the wake of the obstruction and the standing vortex. The appearance of a standing vortex is a particular feature of the flow around a blunt obstruction. It is a steady spanwise vortex upstream of the obstruction, as indicated in figure 2.5. For the range of Reynolds numbers examined in the experiments, it remains fixed in its place upstream of the hemisphere. This vortex has two streamwise 'legs' that trail downstream adjacent to the wake of the obstruction. The standing vortex creates regions of high-speed fluid and low-speed fluid near the wall, as indicated in figure 2.5b. This significantly increases the near-wall velocity along the trajectory of the hairpin vortices, with corresponding consequences for the development of these hairpin vortices.

For vortex shedding behind an obstruction, the ratio of the height of the obstruction H over the boundary layer thickness δ deserves some attention. In general, it should be expected that the behaviour of the hairpin vortices scales with the Reynolds number with respect to the height of the obstruction and the velocity at the tip of the obstruction, $Re_{(H,U_{tip})}$. However, this does not take into account the effect of the velocity profile, that also determines the evolution of a hairpin vortex. For instance, if the obstruction is entirely embedded in the linear part of the laminar boundary layer, the neck of the hairpin vortex is convected with a lower velocity than if the obstruction would have been large with respect to the size of the boundary layer, although the tip velocity might be the same in both cases. In general, a larger value of δ/H can be expected to result in a smaller angle of the neck of the vortex with respect to the wall, except when the obstruction is entirely embedded in the linear part of the laminar boundary layer. In the present measurements, only one height is used for the obstruction and the ratio δ/D was kept approximately equal to 1.

The concepts introduced in this chapter will be used frequently in the next chapters. Although the considerations presented here are only some basic ideas and simplified models, they are useful as a point of departure in the analysis to come.

Chapter 3

Visualization

3.1 Introduction

3.1.1 Overview of the chapter

In this chapter, first the water channel and the method of visualization are introduced. Next, various aspects of the shedding and the subsequent evolution of hairpin vortices will be explained and illustrated by photographs. Three configurations will be examined: vortex shedding behind a droplet on a smooth wall, vortex shedding behind a hemisphere on a smooth wall and vortex shedding behind a hemisphere on a wall with longitudinal grooves. First, the standing vortex is examined that originates upstream of a blunt obstacle like the hemisphere, as explained in chapter 2. Then the wake area and the initial phases of the evolution of the hairpin vortex are examined. Special attention is devoted to the creation of what will be called 'the quasi-spanwise vortex'. Finally, the later stages of the evolution of the hairpin vortex are examined, in which the occurrence of a secondary instability is of major interest. The chapter is concluded with a short discussion.

3.1.2 Technical specifications

The water channel The visualization experiments have been performed in a low-speed water channel with a test section of 7 m long, 0.30 m wide and 0.16 m high. For a flow over a flat plate, $Re_x = 3.2 \times 10^5$ is the critical Reynolds number for the laminar-turbulent transition¹. The velocities were typically in the range 80 - 140 mm/s and therefore the flow is expected to remain laminar up to at least $x = 2.5$ m. Inside this section a plate of 0.60 m long, 0.30 m wide and 0.01 m high with a sharpened leading edge was placed 0.09 m above the bottom,

¹This is the lower limit, which is valid for flows with a sizable level of free stream turbulence (Schlichting, 1955).

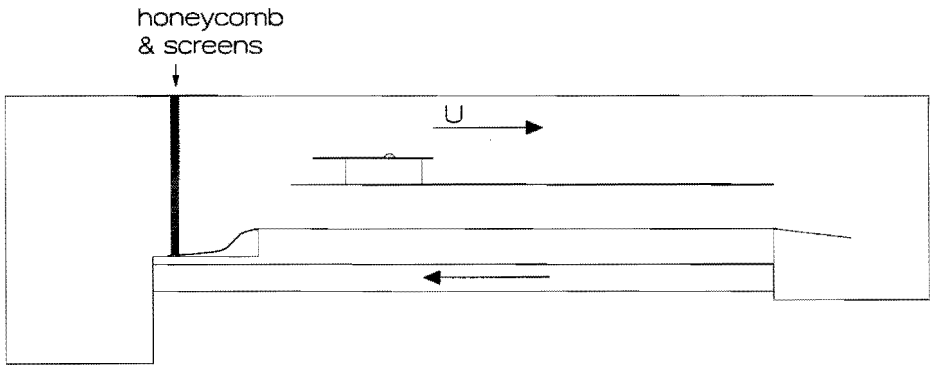


Figure 3.1: Schematic representation of the water channel.

supported by 3 thin metal stands. Visualizations showed that the flow was indeed laminar and did not contain disturbances (as might have been generated at the upstream edge of the plate). The experimental set-up is depicted in figure 3.1. The temperature of the room was fixed at 17.5 ± 0.3 °C and the heat of the pump raised the temperature of the water to 18.5 ± 0.5 °C, corresponding to a kinematic viscosity $\nu = 1.02 \times 10^{-6} \pm 0.01 \times 10^{-6}$ m²/s. A more detailed description of the water channel is given in the thesis of Schwartz-Van Manen (1992).

The visualization The visualization is performed by means of a platinum bubble wire with a diameter d of 40 μm , which is framed in an isolated metal fork and is aligned along the z -direction. For the range of velocities that is applied, this corresponds to $Re_d = Ud/\nu < 5.6$. This Reynolds number turns out to be sufficiently small, as no vortex shedding from the wire is observed. By means of electrolysis, hydrogen bubbles are generated along the wire. The bubbles are shed and move along with the flow, providing a bubble sheet that is transformed by the vortices. Both a continuous and a pulsed voltage are applied for the electrolysis: with a pulsed voltage it is possible to show the high- and low-velocity areas more clearly because of the deformation of the originally straight bubble lines, as shown by figure 3.2. The disadvantage of a pulsed voltage is a decrease in the overall bubble concentration.

The bubbles are made visible by illumination with a 100 W mercury lamp. Its beam is focussed upon the vortex trajectory by means of a cylindrical lense in such a way as to have a large width and a small height.

The vortices are recorded on VHS video-tape by means of a CCD-camera with a resolution of 756×581 pixels. This film is played at low speed and analysed: single pictures of the film are selected, digitally stored and converted into the figures presented here (like figure 3.2), in which the contrast is artificially enhanced by a suitable digital filter. The digitization is accomplished by means

of the DigImage system in the Fluid Dynamics Laboratory. This procedure is preferred over taking photographs directly, because of the low intensity of the scattered light and the greatly increased control over the sharpness and the contrast of the pictures that can now be optimized on line with the recording. The disadvantage of the digitization is a loss in resolution in the presented images. In addition, for elucidating purposes some photographs are shown. In these cases, the Reynolds number is not as accurately known as for the video-frames and the estimated values have to be used with some caution. The flow is made visible by the light that is scattered from the bubbles. These bubbles concentrate in three types of regions:

- **low-speed regions**

Since the time to create a bubble is more or less constant, low-speed areas that pass along the bubble wire end up with a higher concentration of bubbles than high speed areas.

- **wake area**

Bubbles that are shed in the wake area are confined to this region and can only escape by diffusion or by the interaction of the wake and a hairpin vortex.

- **vortices**

The centre of a vortex has a low pressure (e.g. Robinson, 1991) and, because the hydrogen bubbles are lighter than water, they assemble in these regions (Lian, 1990).

These three different regions are easily observed in figure 3.2. However, there are a few effects that should be kept in mind when analysing the photographs:

1. The middle of the bubble wire tends to be slightly closer to the wall than the supports. Therefore, when the wire is positioned close to the wall, for pulsed injection the hydrogen bubble lines are slightly curved, indicating a lower velocity in the centre of the fork as compared to the velocity at the supports.
2. One should be careful with the interpretation of bubble-wire visualization because the pictures are influenced strongly by the history of the flow, and particularly so by the flow conditions at the location of bubble generation.

An example of the first item is provided by figure 3.2b. Clearly, the bubbles in the centre are lagging behind compared to those close to the supports. An example of the second item is also given by figure 3.2, in which can be seen that only the legs show up: the middle part of the head does not contain any bubbles, although vorticity is surely present here. Because of the location of the bubble wire, only the neck and the legs contain bubbles.

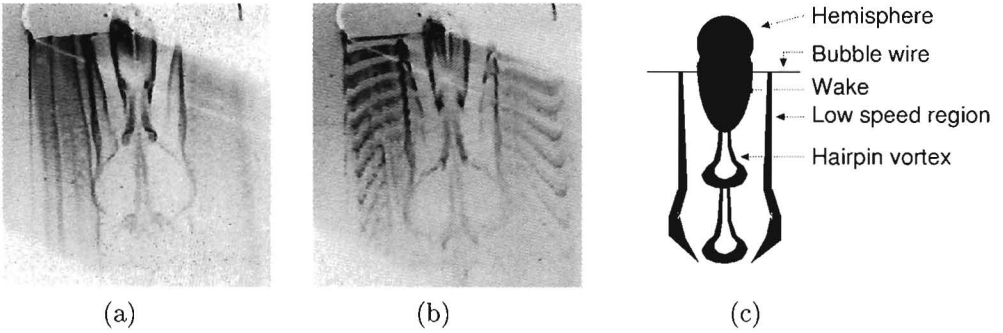


Figure 3.2: Bubble-wire visualization of the vortex shedding behind a hemisphere (top view, flow direction downwards), wire at $x/D = 0.5, y/D = 0.06, Re_D = 1570$. (a) continuous voltage, (b) pulsed voltage, (c) definition sketch.

The pressure gradient For a flow over a flat plate, the growing boundary layer causes the main stream velocity to increase. This means that $\partial p/\partial x < 0$. This pressure gradient enhances the stability of the boundary layer. In the work of Taylor (1990) it was determined that, when hairpin vortices were created in the flow by injection of a small amount of low speed fluid, an adverse pressure gradient supports the growth rate and the amount of secondary instabilities. However, for a positive, as well as for a negative pressure gradient, he finds the same general shape for the pattern of primary, secondary and subsidiary vortices.

Our water channel did not have the possibility of adjusting the pressure gradient and therefore a small negative $\partial p/\partial x$ was always present. Nevertheless, from Taylors observations it should be expected that although the growth rate might be less, the same general pattern would evolve as for a zero-pressure-gradient boundary layer. In addition, one should be aware that in the wake of the obstacles that we used, pressure gradients can be found that are considerably larger than those imposed by the growing boundary layer (see appendix B). In chapter 5, it will be shown that the flow close to the wall is accelerated over a considerable downstream distance. This was also reported by Acarlar & Smith (1987), who claimed that as far as $x/D = 40$, the near-wall velocity was developing towards the turbulent boundary layer profile. In order to test the effect of the boundary-layer induced pressure gradient, the obstacle was placed further downstream. It was verified that the hairpin vortices developed in a similar way and no change was observed with respect to secondary instabilities.

Notation Throughout this chapter, x is directed downstream, while y is directed perpendicular to the wall. The location $x = 0$ corresponds to the centre

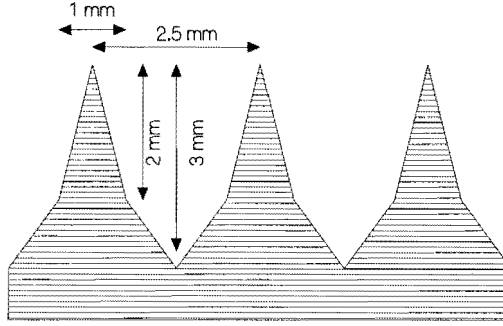


Figure 3.3: The shape of the riblets.

of the hemisphere. D denotes the hemisphere diameter and Sr_D and Re_D are the Strouhal number and the Reynolds number with respect to D . The boundary layer thickness δ is defined as the height at which the local flow velocity is 99% of the mean flow velocity.

3.1.3 The three configurations

The two obstacles examined here are a hemisphere and a droplet with a diameter of 16 mm. The length of the droplet is 50 mm. In all cases, the obstacle is placed at 0.31 m downstream of the leading edge of the plate. This leads to the following ratio of the boundary layer thickness δ of the diameter D of the obstacle:

Re_D	δ/D
1360	0.59
1570	0.56
1830	0.52
2090	0.48

The boundary layer thickness is therefore always of the same order of magnitude as the height of the obstacle (which equals $\frac{1}{2}D$). Shifting the obstacle somewhat upstream or downstream does not change the general features of the hairpin vortex shedding to a noticeable extent: the boundary layer thickness does not seem to have a critical effect within the range applied here.

Comparing the present research with the results of Head & Bandhyopadhyay (1981, hairpin vortices in a turbulent boundary layer) or Haidari (1990, artificial creation of hairpin vortices by fluid injection in a laminar boundary layer), it should always be kept in mind that the development of a hairpin vortex is strongly dependent on the velocity profile, which deforms the shape of the vortex

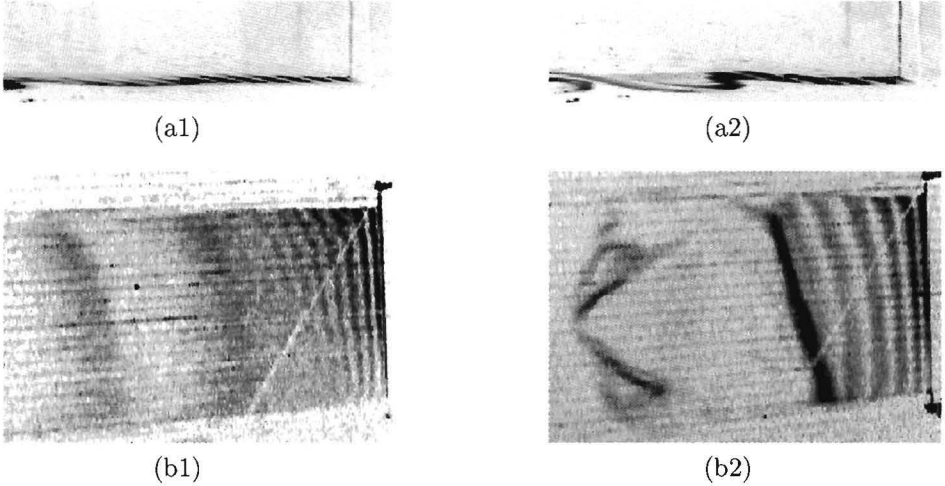


Figure 3.4: The secondary instability caused by our riblets (flow from right to left). (1) $Re_D = 1790$, (2) $Re_D = 2180$. (a) side view, (b) top view.

and changes its interaction with the main flow. This velocity profile is partly determined by the applied method of generation.

Next, the hemisphere was placed on a grooved surface in order to find out whether a change in the near-wall velocity underneath the hairpin vortices could be found that could be associated to the well-known drag reducing ability of riblets in turbulent flow. The width of the riblets was related to the radius of the hemisphere in the same way as in turbulent flow the riblet width is related to the height of the low-speed streaks. In turbulent flow the riblets exhibit maximum drag reduction for a riblet spacing of approximately $s^+ = 12$. The low-speed streaks that are associated with the creation of new vortices (Hinze, 1959) can be found up to $y^+ = 40$ (Kline, 1992). In our case, the hemisphere radius R is 8 mm. The riblet width was therefore chosen to be $8 \text{ mm} \times 12/40 \approx 2.5 \text{ mm}$. The shape of the riblets is indicated in figure 3.3 and was largely determined by convenience². This choice of the riblet shape turned out to be somewhat unfortunate: for $Re_D > 1750$ it turned out that, in contrast to triangular riblets, our riblets create an instability in the flow near the wall. The phenomenon can be seen in figure 3.4: the near-wall flow rolls up into spanwise vortices that resemble Tollmien-Schlichting waves. The instability is not due to the upstream edge of the plate. Probably, it is caused by the shape of the velocity profile that is induced by the riblets and that creates a kind

²As it was assumed that the particular shape of the riblets would not lead to notable differences, we just took a grooved plate that was already there.

of Tollmien-Schlichting instability. The presence of the instability inhibits a neat comparison between a smooth and a grooved wall for the vortex shedding behind a hemisphere for higher Re_D : for the grooved plate, for $Re_D > 1750$ the vortex shedding downstream of the hemisphere becomes very irregular, as could be expected. However, for $Re_D < 1750$ a comparison is still possible.

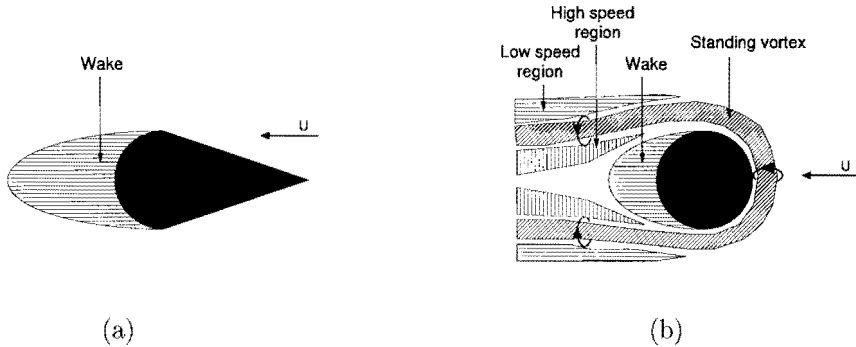


Figure 3.5: The effect of the obstacle on the u -velocity (top view). (a) droplet (b) hemisphere (with standing vortex)

3.2 The standing vortex

Before an analysis of the evolution of the hairpin vortex is made, it is essential to understand the behaviour of the standing vortex, that is created upstream of a blunt obstacle. An indication of the effect of the standing vortex is given by figure 3.5. The importance of the standing vortex lies largely in its effect on the near-wall velocity. Of particular importance is its effect on the region immediately downstream of the hemisphere, where the standing vortex draws high-speed fluid towards the wall.

Figure 3.6 indicates that the standing vortex is present for the case of a hemisphere on both a grooved and a smooth wall and that it is absent for the case of the droplet. Although the photographs indicate that the standing vortex is present for a hemisphere in both configurations, it will be shown by the hot-wire measurements presented in chapter 5 that the presence of the riblets causes a substantial weakening of this vortex. This can also be seen from a comparison of the amount of retardation of the bubble lines at the location of the low-speed regions that are created along the standing vortex: the amount of low-speed fluid drawn up by the standing vortex is less in the case of riblets (see e.g. figure 3.10) than in the case of a smooth wall (see e.g. figure 3.2). In chapter 5, which presents the hot-wire measurements, the reduction of the effect of the

standing vortex by the riblets is determined quantitatively. The effect of the standing vortex on the u -profile has important consequences for the evolution of the hairpin vortex, as will be seen later in section 3.4 of this chapter.

The visualizations seem to indicate that the standing vortex is weakened strongly with downstream distance: although it is clearly visible close to the hemisphere, it is almost impossible to visualize it further downstream. Cine recordings show a decrease in the rotation of the bubbles around the downstream trailing legs of the standing vortex that might be due to viscous diffusion of the vorticity³. Figures 3.6b1 and 3.6b2 indicate that the standing vortex is strongly distorted by the necks of the hairpin vortices, that draw it sideways into the path of the hairpin vortex at $x/D \approx 3$.

In addition to the spanwise distortion, the standing vortex is lifted away from the wall. Figure 3.6 indicates that the deformation is very reproducible and almost independent of Reynolds number for the smooth wall. For the hemisphere on the grooved wall, at $Re_D > 1750$ the instability of the flow over the grooved surface distorts the regular vortex shedding.

Figure 3.6 shows a large decrease in the concentration of the bubbles contained in the standing vortex once it starts interacting with the hairpin vortex. It is suggested here that, although the standing vortex is already substantially weakened at this location by the effect of viscous diffusion, the dispersion of the bubbles is less than the diffusion of the vorticity and the bubbles are still present in the vortex core. The distortion of the standing vortex by the hairpin is now enough to disperse these bubbles over a larger area. After this interaction, it is not possible to track the standing vortex any further.

Although the standing vortex is too weak to be visualized any further, the low speed regions that were created by the standing vortex (see figure 3.5b) continue to exist. Although these regions are sped up by the surrounding flow and deformed by the influence of the hairpin vortices passing along it, streaks of low-speed fluid can be observed over a long downstream distance.

3.3 The wake area

The flow immediately downstream of the obstacle contains an area in which reversed flow is found. Further downstream, an area of retarded fluid exists. This area is unstable (the velocity profile in the plane of symmetry contains a

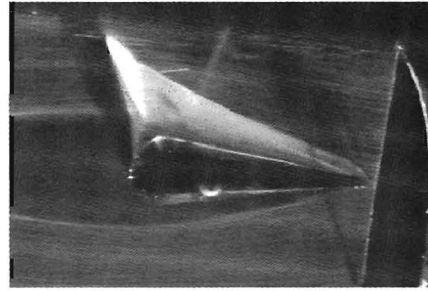
³The strong weakening of the standing vortex is to be expected from the fact that a Gaussian vorticity distribution is diffused according to

$$R(t) = \sqrt{4\nu t + R_0^2}$$

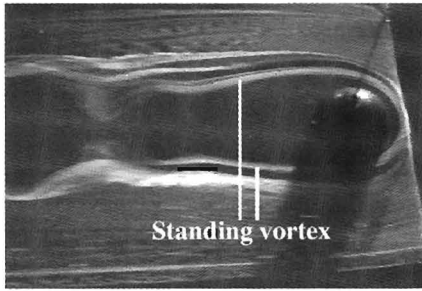
which means that for water, $\Delta R \approx 2 \times 10^{-3} \sqrt{t}$. For $t = 1$ s (approximately the time a fluid particle needs to reach $x/D = 1$) the increase in the vortex radius is already of the order of the initial diameter of the standing vortex, which implies a quadrupling of the vortex core area and a corresponding pressure loss.



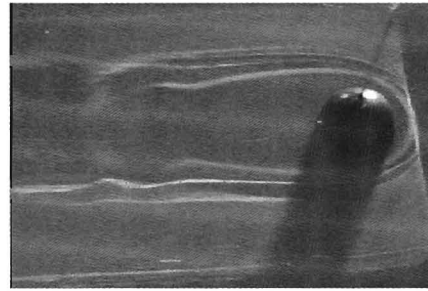
(a1)



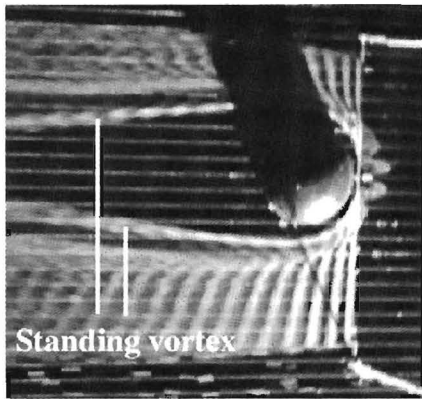
(a2)



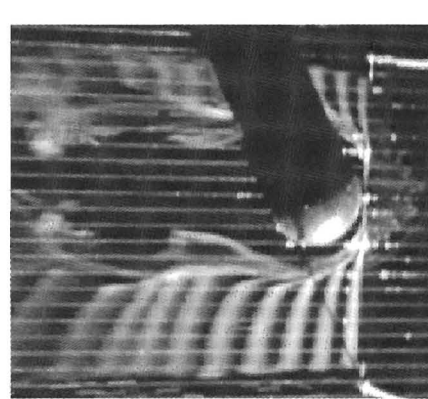
(b1)



(b2)



(c1)



(c2)

Figure 3.6: The standing vortex for the case of an obstacle on a smooth wall (top views, flow direction to the left) (1) $Re = 1360$, (2) $Re = 2090$. (a) droplet (b) hemisphere. In addition, the standing vortex is shown for a (c) hemisphere on a grooved wall.

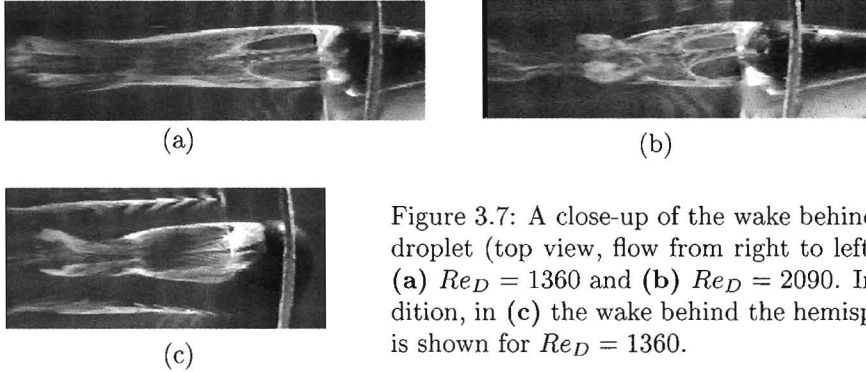


Figure 3.7: A close-up of the wake behind the droplet (top view, flow from right to left) for (a) $Re_D = 1360$ and (b) $Re_D = 2090$. In addition, in (c) the wake behind the hemisphere is shown for $Re_D = 1360$.

point of inflection as will be shown by the hot-wire measurements in chapter 5). It rolls up into vortices with a well defined frequency in a way that closely resembles a Von Karman vortex street. The area downstream of the obstacle, but upstream of the location where the hairpin vortices appear, is defined here as the wake area.

In figure 3.7 the wake is shown for the droplet at $Re_D = 1360$ and $Re_D = 2090$ and the wake of the hemisphere is shown at $Re_D = 1360$. The figure indicates that the wake does not simply consist of stagnant fluid. It contains a lot of vorticity: the visualization shows mainly ω_y and also some ω_x . Side views of the wake area are presented in figures 3.8 and 3.9.

From a comparison of figures 3.8 and 3.9a it follows that above a smooth wall, at lower Reynolds numbers the wake area downstream of a droplet is substantially larger than the wake downstream of a hemisphere. In figure 3.8a the wake extends downstream up to $x/D \approx 4.5$. In addition, for the droplet, the downstream extent of the wake area decreases with increasing Reynolds number. For the hemisphere, the Reynolds number has hardly any effect on the size of the wake. It extends downstream up to $x/D \approx 1.5$. This is only as short as the wake behind the droplet for $Re > 2000$. The difference between the hemisphere and the droplet is ascribed to a destabilizing effect of the standing vortex on the wake of the obstacle. In particular, the standing vortex pushes high speed fluid downwards and sideways into the wake area.

Figure 3.9b shows the wake-area for a hemisphere on a grooved wall. Clearly, for low Re_D , the wake is strongly elongated as compared to the case of a hemisphere on a smooth wall. For increasing Re_D the length of the wake becomes less, just as in the case of the droplet on a smooth wall. However, the vortex shedding becomes very irregular for $Re_D > 1750$, as explained before in section 3.1. A top view of the wake of the hemisphere on the grooved plate is shown in figure 3.10.

Returning to the top views of the wake in figure 3.7, it should be noted that although the wake area downstream of the droplet is shortened by an increase

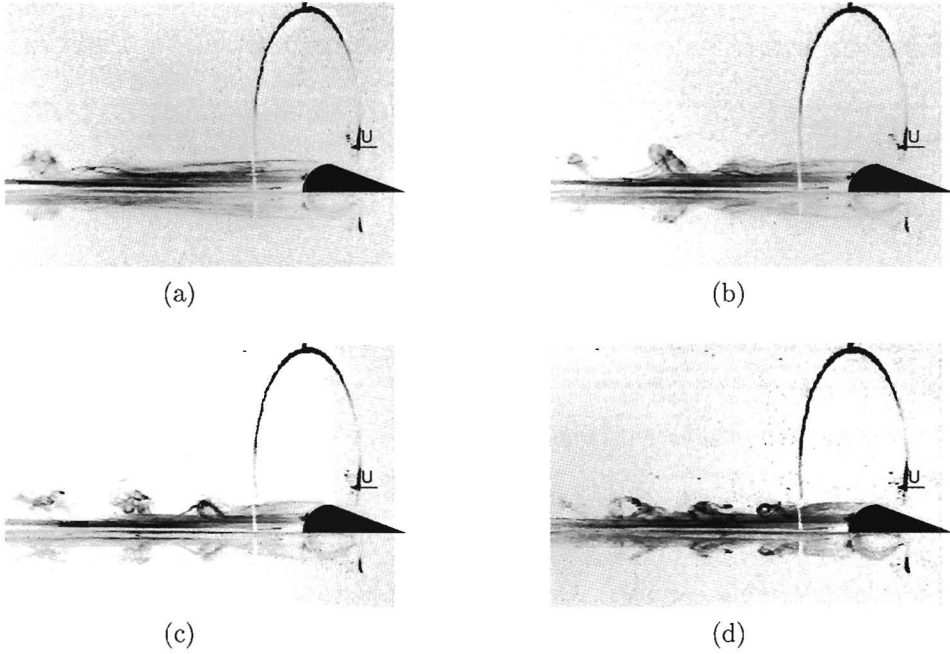


Figure 3.8: The wake downstream of a droplet on a smooth wall (side views, flow direction to the left). (a) $Re_D = 1360$, (b) $Re_D = 1570$, (c) $Re_D = 1830$, (d) $Re_D = 2090$.

of Re_D , the recirculation region retains approximately the same size. In addition, the recirculation region seems to have the same size for both the droplet and the hemisphere. It seems that only the region of retarded flow downstream of the recirculation area is destabilized and rolls up into new hairpin vortices. However, for the hemisphere, the effect of the standing vortex is so large that the retarded flow is destabilized immediately downstream of the recirculation area.

In figure 3.11 the bubble wire is set close to the wall at the downstream edge of the recirculation area ($x/D \approx 1.5$). At this location, $u \approx 0$. The photograph indicates a nearly vertical movement of bubbles from the wall at the location of the wire. This layer is localized in a very thin layer in the plane of symmetry between the vortex legs. The observation that this layer is very thin can be explained from the proximity of the legs. The effect can be observed over the entire range of Reynolds numbers⁴. Further downstream, the effect is less spec-

⁴In the case of a droplet for low Reynolds numbers, if the bubble wire is located at this position the long wake is destabilized by the movement of the bubbles, which, at these low speeds, do not follow the flow properly anymore. This results in a shorter wake area and a somewhat larger shedding frequency.

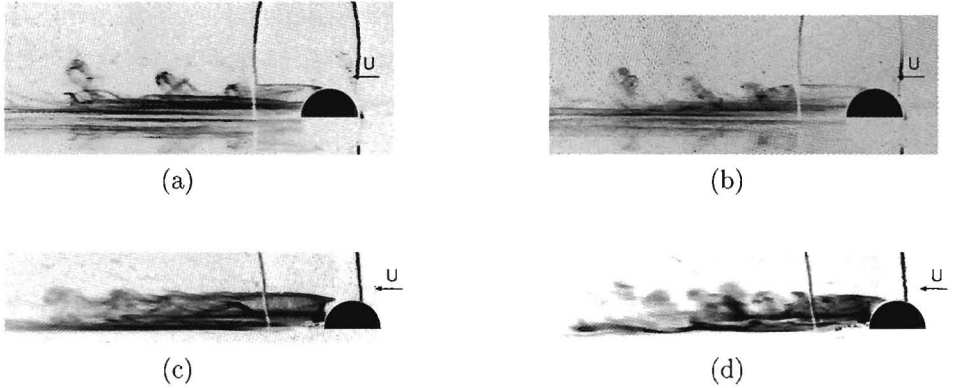


Figure 3.9: The wake downstream of a hemisphere (side views, flow direction to the left) (a) smooth wall, (b) grooved wall (1) $Re_D = 1360$, (2) $Re_D = 2090$

tacular because u assumes substantial values again and the trajectory of the bubbles makes a smaller angle with the wall. Further upstream, the bubbles are convected backwards and remain confined in the wake area.

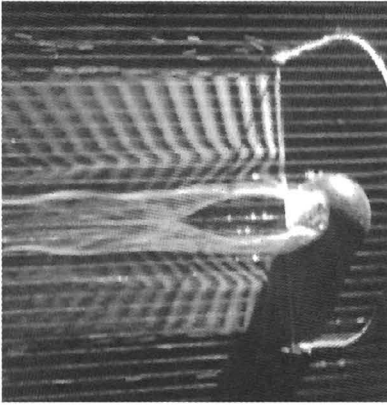
3.4 The initial stages of the hairpin vortex

At the downstream end of the wake, hairpin vortices are shed. In figure 3.12 the flow is shown for a hemisphere on a smooth wall⁵.

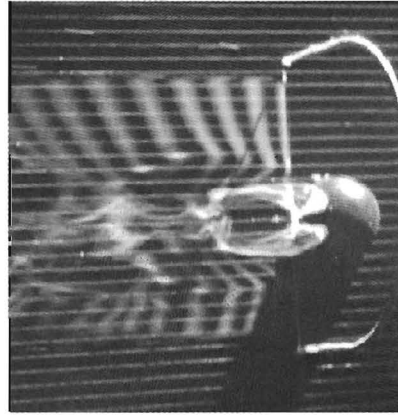
As soon as the vortex exists, its shape starts to be modified by the local velocity profile. This profile is not equal to the flat plate laminar boundary layer profile, as it is strongly deformed by the presence of the obstacle. One consequence of this is the substantial vortex stretching that occurs in the region immediately downstream of the wake. Figure 3.12 shows that the diameter of the head is much larger than the diameter of the legs. The small diameter of the vortex legs is attributed to vortex stretching. The vortex head does not undergo significant stretching and its radius continues to grow by viscous diffusion.

Because of continuity, a large $\partial u/\partial x$ implies either a substantial $\partial w/\partial z$ or $\partial v/\partial y$. From the spanwise movement of the low-speed area into the wake zone, it should be concluded that $\partial w/\partial z$ is quite large immediately downstream of the obstacle. This w -velocity pushes the legs together. Figure 3.12 shows clearly that for the vortex that is about to be shed, the distance between the legs is of the size of the width of the wake area, while for the vortex that was

⁵Figure 3.12 is similar to figure 3.2 but in figure 3.12 the bubble wire was positioned slightly higher. Consequently, a larger part of the head is visible and the density of bubbles in the undisturbed flow area is less.



(a)



(b)

Figure 3.10: A close-up of the wake behind the hemisphere on a grooved wall (top view, flow direction to the left) for (a) $Re_D = 1360$ and (b) $Re_D = 2090$.

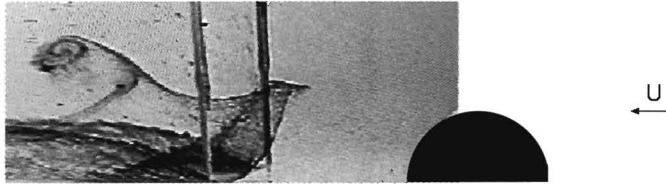


Figure 3.11: The upwelling of near-wall fluid at the edge of the wake area ($x/D \approx 1.5$) downstream of the hemisphere (side view, flow direction to the left).

shed previously, the distance between the legs is already very small. Further downstream, this distance remains approximately constant at $\Delta z/D \approx 0.2$. A different explanation for the decreasing distance between the vortex legs could be that the legs approach each other due to mirror-image effects at the wall. In that case, the legs should contain a substantial amount of circulation and the decrease in the distance between the legs should be expected to lead to a rapid rise of the legs into the flow. Since this is not observed, it is concluded that the effect of the spanwise velocity is more important⁶. It should be expected that the u -velocity profile downstream of the obstacle has a large influence on the shape of the vortex. As the velocity profile downstream of

⁶This conclusion is supported by the simulations of chapter 7, that indicate that the effect of the wall on the motion of the hairpin legs seems to be negligible.

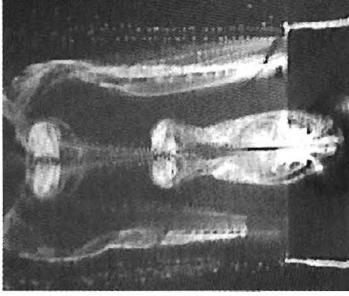


Figure 3.12: Vortex shedding behind a hemisphere on a smooth wall, wire at $x/D = 0.5, y/D = 0.06, Re_D \approx 1700$ (top view, flow direction to the left).

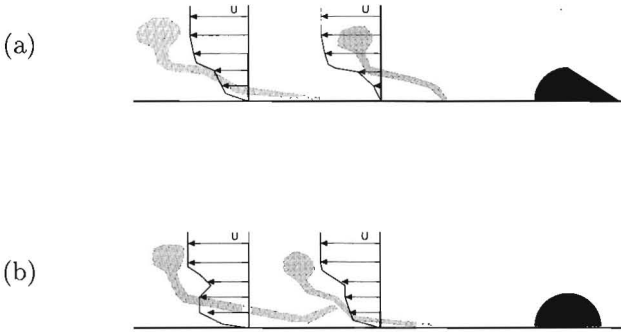


Figure 3.13: A schematic representation of the influence of the u -velocity profile on the initial shape of the hairpin vortex. (a) droplet, (b) hemisphere.

a droplet is different from that downstream of a hemisphere, the hairpin vortex assumes a somewhat different shape. This effect is schematically represented in figure 3.13. The velocity profiles in this figure have been obtained from the hot-wire measurements presented in chapter 5. In particular, the difference between the velocity profiles for the droplet and the hemisphere leads for the droplet to the presence of a streamwise part of the hairpin neck at approximately the height of the obstacle⁷. The difference between the hairpin shapes for the hemisphere

⁷In evaluating the influence of the velocity profile on the vortex shape, as is done in figure 3.13, it should be recalled that the shape of the hairpin vortices is strongly determined by the history of the flow. For instance: although the creation of legs is determined by the near-wall shear, the continued presence of the legs does not require the continued presence of this shear.

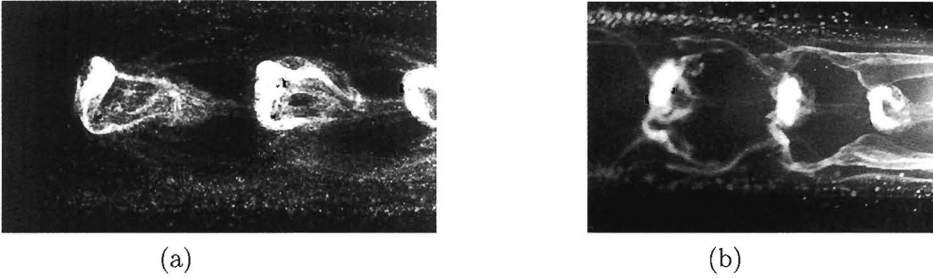


Figure 3.14: The differences in the vortex shape between a vortex shed from a droplet and from a hemisphere for $Re \approx 1700$ (top view, flow direction to the left). (a) droplet (b) hemisphere

and the droplet is illustrated in top view by figure 3.14⁸.

Figure 3.15 shows the shape of the hairpin vortex for a hemisphere at increasing Re_D . The figure shows that for $Re_D = 1350$ the lower part of the vortex is retarded by the effect of the wake of the hemisphere and assumes a shape that resembles the case of the droplet. This corresponds to the effect of Re_D on the velocity profile: the hot-wire measurements in chapter 5 indicate that for decreasing Re_D the velocity in the wake of the obstacle decreases with respect to the main velocity. It is suggested that this is due to the increase in the boundary layer thickness⁹.

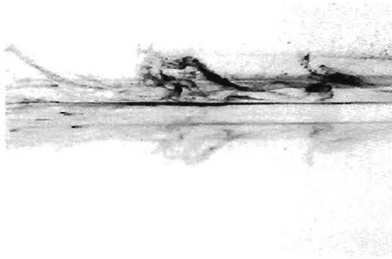
In the resulting vortex street, some interaction exists between the subsequent vortices. Since the part of the vortex that is close to the wall is transported slower than the part higher up, the lower parts of the legs lag behind and are overrun by the head and necks of the subsequent hairpin vortex. This subsequent vortex then lifts the legs away from the wall and disperses them, as indicated in figure 3.17. In this way, the part of the legs that is closest to the wall is removed by the next vortex. Therefore, it should be expected that at

⁸Obviously, this shape can not be explained by the mutual effect of the vortex legs. Although these tend to push each other upwards into the flow, in the risen area, the legs are actually quite far apart, whereas the legs are much closer together further upstream, where they remain close to the wall. This is exactly the opposite of what might have been expected from the the mutual effect of the legs.

⁹To illustrate the assumed influence of the boundary layer thickness, in figures 3.16a and 3.16b two sketches are made of different δ/D . In both figures, the Reynolds number with respect to the velocity at the tip of the hemisphere (Re^*) is equal, while the main-stream Reynolds number (Re) is larger in figure 3.16b. Although Re is larger in the second case, the velocity close to the wall is lower and it is therefore very likely that

- the standing vortex is weaker
- the effect of the standing vortex on the u -profile is smaller, since the fluid that is pushed towards the wall by the standing vortex has a smaller u -velocity

If the boundary-layer increases, therefore, the effect of the standing vortex becomes less and the evolution of the hairpin vortices that are shed from it will become more droplet-like.



(a)



(b)



(c)

Figure 3.15: The vortex shape downstream of a hemisphere at $2 < x/D < 7$ (side view, flow direction to the left). (a) $Re_D = 1350$ (b) $Re_D = 1575$ (c) $Re_D = 1825$

a sufficient distance downstream, all parts of the vortex in the near-wall shear will have been removed by subsequent vortices and the resulting hairpin vortices actually move over the near-wall shear¹⁰

3.5 The secondary deformation of the vortex legs and the quasi-spanwise vortex

The evolution of the hairpin vortex A topic of special interest is the generation of a secondary deformation in the hairpin vortex shape. This phenomenon has been observed by e.g. Acarlar & Smith (1987) and by Taylor (1990)¹¹. Figure 3.18 shows a sketch from Taylor indicating this secondary de-

¹⁰In will be shown in section 3.5 that this is not entirely true. There is an effect (the quasi-spanwise vortex, to be treated in section 3.5) that pushes the upstream part of the legs back to the wall again.

¹¹Comparing our results with the results of Taylor (1990) and Haidari (1990), it should be kept in mind that they created single vortices instead of vortex streets. Haidari observed that the legs of the primary vortex created large amounts of secondary vortices in such a way that the resulting cluster of vortices resembled a turbulent spot. In our case, the oncoming subsequent primary vortex inhibits continued contact between the wall and the legs of the primary vortex, and clusters of vortices such as Haidari's are not observed. However, a

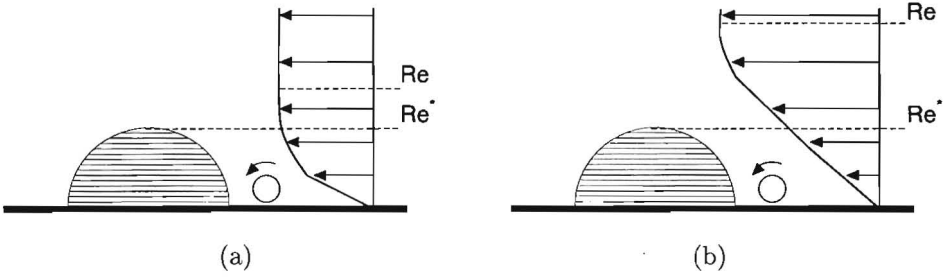


Figure 3.16: The effect of the boundary layer thickness with respect to the height of the hemisphere. (a) experimental configuration, (b) large δ/D

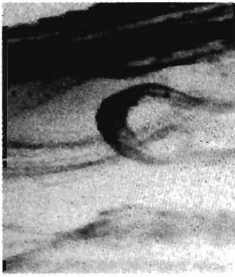


Figure 3.17: The interaction between two subsequent vortices close to the hemisphere at $x/D = 3$ (top view, flow direction to the left). The legs of a hairpin vortex are lifted from the wall by the subsequent vortex.

formation. The important observation here is that the lower part of the neck actually starts to move towards the wall.

The evolution of the hairpin vortices for the droplet and the hemisphere is shown in figure 3.19. The figure shows that for the case of the droplet, a rise in the legs midway between two subsequent vortices occurs, while the lower part of the neck moves towards the wall. This is similar to the phenomenon described by Taylor. The downstream location at which this secondary deformation occurs depends on the Reynolds number. Below $Re_D \approx 1500$ only a minor rise in the legs occurs. Above this value, with increasing values of the Reynolds number the deformation of the legs seems to become stronger and to move somewhat further upstream, although this effect is not very clear. For $Re_D > 2200$ the evolution of the vortices becomes increasingly irregular and the rise in the legs decreases. The reduction in the rise of the legs for $Re_D < 1500$ seems to be related to the increasing length of the wake area¹².

secondary vortex is formed, as will also be indicated by the hot-wire measurements in chapter 5.

¹²It was argued in section 3.3 that for the droplet, for low values of Re_D a large wake area exists where no hairpin vortices are present. On the other hand, it will be shown in

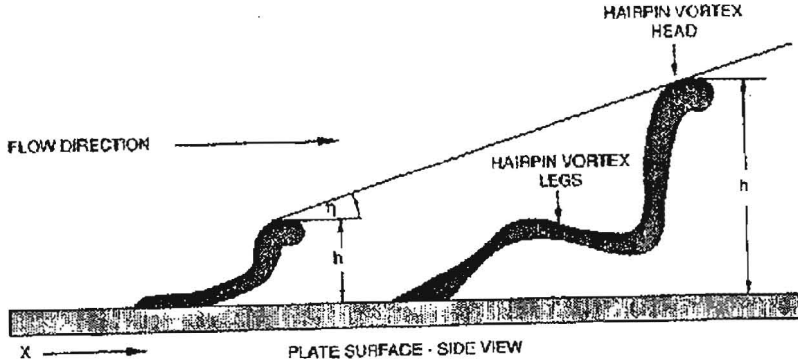


Figure 3.18: The secondary deformation of the hairpin vortex shape (side view, flow direction to the right). (sketch from Taylor, 1990).

The importance of the velocity profile on the secondary deformation of the legs is also illustrated by the differences between the droplet and the hemisphere. Figure 3.19 demonstrates that the rise halfway the legs does not occur for the hemisphere. In figure 3.20 the hairpin vortices are visualized in the region $2 < x/D < 7$. The bubble wire was positioned at $x/D \approx 1.5, y/D \approx 0.3$ and $Re_D = 1825$. These photographs show a more detailed view of the differences in the evolution of the hairpin vortex for the cases of a hemisphere and a droplet, as indicated before in figure 3.19. The photographs show that for the droplet, the legs are bent and the downstream part of the hairpin neck is moving towards the wall¹³. For the hemisphere, the legs show up as almost straight lines at an angle with the wall.

The secondary deformation of the hairpin legs for the droplet is caused by a secondary vortex that is induced underneath the primary hairpin vortex. It is visualized in figure 3.21. This secondary vortex will be called 'the quasi-spanwise vortex' throughout the remainder of this thesis. These photographs indicate that initially, this vortex is located approximately underneath the hairpin head. The quasi-spanwise vortex is convected along with the near-wall velocity, that is

chapter 5 that for a droplet, irrespective of the presence of hairpin vortices, the velocity profile downstream of the obstacle at $x/D = 2.5$ is largely independent of the main stream velocity. For high values of Re_D a vortex is already present at this location, for low values it is generated further downstream. Therefore, for low values of Re_D , the hairpin vortex interacts with a different velocity profile in its initial stages, which seems to affect the mechanism that leads to this secondary deformation of the vortex legs.

¹³While this movement cannot really be seen in a photograph, cine recordings of the flow show it clearly. An indication of this effect can be drawn from the fact that in the figure, with increasing downstream distance (from right to left) the part of the legs closest to the head approaches the wall.

(a)



(b)

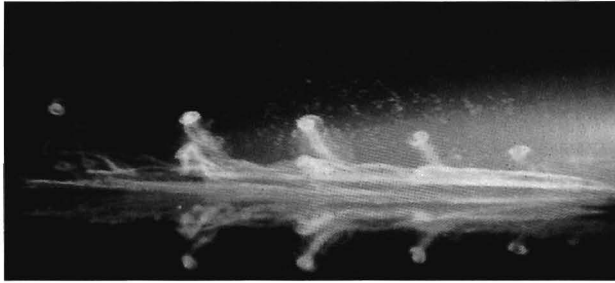


Figure 3.19: The secondary deformation of the hairpin vortex at $Re \approx 1700$ (side view, flow direction to the left). (a) droplet (b) hemisphere

smaller than the velocity of the head of the primary hairpin vortex. Therefore, the quasi-spanwise vortex lags behind with respect to the head and starts to deform the vortex legs. A comparison of the two subsequent vortices in figure 3.21 illustrates this effect.

For the hemisphere, this rise in the legs is not observed. However, here another secondary phenomenon is observed: a secondary vortex is seen to rise up underneath the hairpin head, as shown in figure 3.19b. A close-up of this effect is presented in figure 3.22. Although this phenomenon is not exactly similar to the case of the droplet, it results in a similar 'quasi-spanwise vortex'. The near-wall velocity is much higher for the hemisphere than for the droplet, due to the effect of the standing vortex. Therefore, for the hemisphere, the secondary vortex remains located approximately underneath the vortex head instead of lagging behind like in the case of the droplet. The effect is schematically indicated in figure 3.23. Figure 3.20b shows that for the hemisphere, the hairpin vortex has straight legs at $x/D \approx 5$, where the legs of the droplet are already strongly deformed. Figure 3.19b indicates that for the hemisphere, the legs are deformed later and the deformation is much weaker: the figure shows a quasi-spanwise vortex underneath the leftmost primary vortex that deforms the



Figure 3.20: The vortex shape for $Re_D = 1825$ in the region $2 < x/D < 7$ (side view, flow direction to the left). (a) droplet, (b) hemisphere.

downstream part of the legs of the primary vortex. Immediately upstream of the quasi-spanwise vortex the legs are lifted upwards, while immediately downstream they are drawn downstream and towards the wall again, similar to the case of the droplet. However, the phenomenon occurs further downstream and almost underneath the vortex head, while for the droplet the effect starts almost immediately downstream of the obstacle and affects the region midway between two primary vortex heads.

The effect of the quasi-spanwise vortex is to push the region immediately upstream of it upwards into the flow. In the case of the droplet this means that the legs are lifted and also that the head is dragged down. In chapter 5 it will be shown that in the case of the hemisphere on a smooth wall, the head of the hairpin vortex rises faster than for the other two configurations, which is attributed to this effect.

It was shown in figure 3.15 that for the hemisphere, when Re_D is decreased below 1500, the wake of the obstacle increasingly affects the shape of the vortex, since the lower part of the vortex is retarded more. However, this does not lead to the creation of a quasi-spanwise vortex similar to that of a droplet. In figure 3.24 the vortex shape is shown for a hemisphere at $Re_D = 1350$. The wallward movement of the downstream part of the neck does not occur and the kink that is induced by the retarding effect of the wake largely disappears while the vortex is advected along.

The origin of the quasi-spanwise vortex The creation of the quasi-spanwise vortex can be attributed to several mechanisms:

1. The effect of the lifted legs of the previous vortex.
2. The effect of the vortex head that induces a pressure gradient near the wall, leading to an upwelling of low speed fluid (e.g. Doligalski et al, 1994).

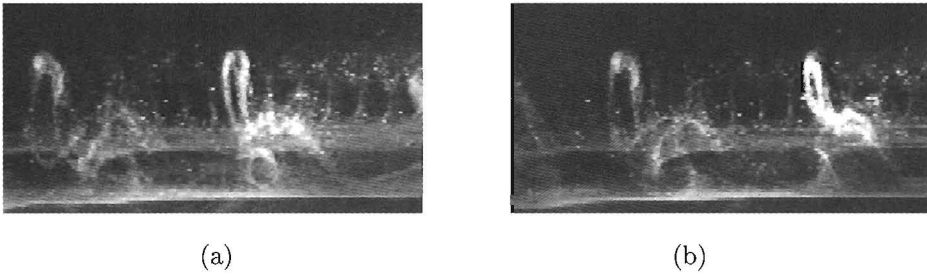


Figure 3.21: The creation of the quasi-spanwise vortex underneath the primary hairpin vortex for a droplet at $Re_D = 1825$ (side view, flow direction to the left). (a) the quasi-spanwise vortex is just created underneath the hairpin head (b) the flow at $t = 0.1$ s before the situation presented in photograph (a).



Figure 3.22: A close-up of the secondary vortex that is created underneath the primary vortex head for the case of a hemisphere on a smooth wall (side view, flow direction to the left).

3. The effect of the vortex necks on the near-wall flow.
4. The effect of the legs on the near-wall flow.

The first possibility should be excluded since the secondary deformation has not only been observed for vortices in a street but also for single vortices (Taylor, 1990). The second possibility seems to be contradicted by the observation that the head does not seem to have much effect on the near-wall velocity, as will be shown in chapter 5. This will be confirmed by the simulations presented in chapter 7. A different mechanism will now be proposed that includes the last two items.

The observation at the basis of the proposed mechanism is given by the fact that the hairpin vortex distorts the velocity profile near the wall. Of special importance is the observation that adjacent to the legs, patches of high-speed fluid exist near the wall in the region outside of the vortex legs. This will be shown in chapter 5. The effect is indicated in figure 3.25a¹⁴. This implies that a series of

¹⁴It is illustrative to compare this figure to 3.14a.



Figure 3.23: A schematic representation of the difference between the deformation of the legs for (a) a droplet (b) a hemisphere.

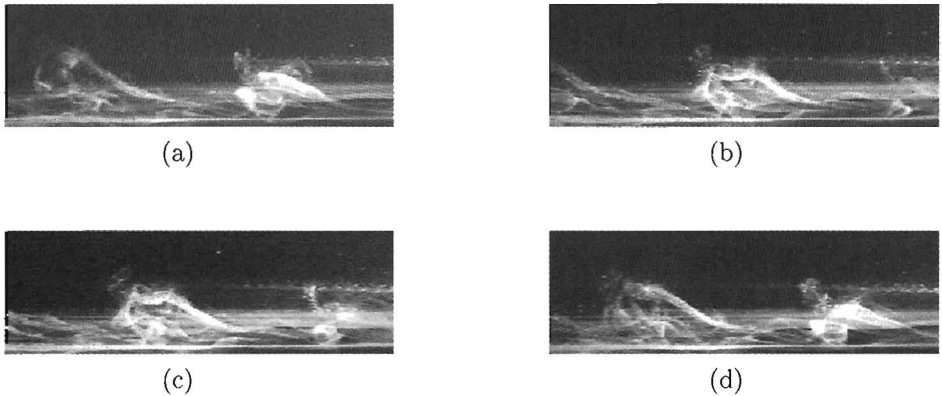


Figure 3.24: The vortex shape for the case of a hemisphere at $Re_D = 1350$. The temporal evolution of a single vortex is shown in the region $2.5 < x/D < 6$ (side view, flow direction to the left). (a) $tU/D = 0.0$ (b) $tU/D = 1.0$ (c) $tU/D = 1.5$ (d) $tU/D = 2$

alternating patches of high-speed fluid and low-speed fluid exists in the streamwise direction, as indicated in figure 3.25a. This series of alternating high-speed and low-speed patches is highly unstable, and the interfaces between the areas of different speed start to roll over, as indicated in figure 3.25b. This instability is proposed to produce the quasi-spanwise vortex. It is called 'quasi-spanwise' because it contains streamwise as well as spanwise vorticity and largely is located around the patches of high-speed fluid adjacent to the legs. For the droplet, it can be weakly seen in figure 3.14a, for the hemisphere it appears very clear in figure 3.14b.

The mechanism described above is mainly concerned with the effect of the necks and the legs on the near-wall flow. This corresponds to the case of the droplet. In the case of the hemisphere, the velocity gradient in the fluid at the height

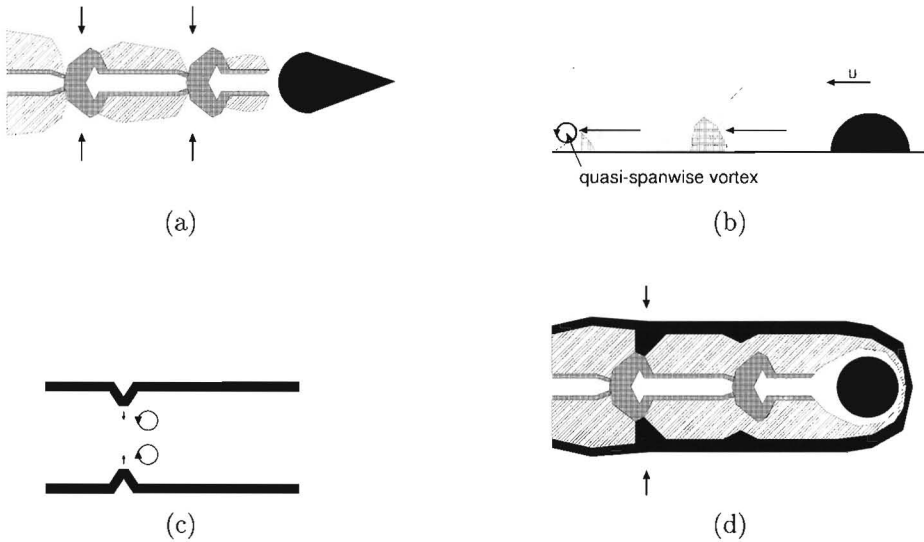
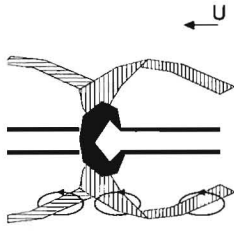


Figure 3.25: Schematic diagrams illustrating the proposed mechanism that leads to the generation of the quasi-spanwise vortex. **(a)** The legs create patches of high-speed fluid near the wall (shaded). **(b)** The low-speed fluid rolls over into quasi-spanwise vortices. **(c)** The neck draws in low-speed fluid sideways. **(d)** A top view of the velocity field for a hemisphere, in which the high-speed areas (shaded) and the low-speed fluid drawn in by the neck (arrows) are indicated.

of the vortex legs is much smaller, due to the effect of the standing vortex, that increases the velocity downstream of the obstruction. Therefore, the effect indicated in figure 3.25a is reduced. Nevertheless, a quasi-spanwise vortex is created, but this is due to a different mechanism that will be explained now. The neck of the hairpin vortex draws in fluid sideways into the vortex trajectory as indicated in figure 3.25c. Since the standing vortex has amassed large amounts of low-speed fluid at both sides of the hairpin vortex, this effect is here much more important than for the case of the droplet. The low-speed fluid is drawn towards the neck of the passing vortex, as can be seen in figure 3.25d. The low-speed regions are drawn inwards until they reach the hairpin neck. This occurs when the hairpin vortex arrives at $x/D \approx 4$ and the next hairpin vortex has just been created (see e.g. figure 3.12). In this way, the neck of a hairpin vortex creates a similar variation in the streamwise velocity, as was found in the case of the droplet. For the case of the hemisphere, the quasi-spanwise vortices appear



(a)



(c)



(b)

Figure 3.26: The effect of the quasi-spanwise vortex on the primary vortex in the case of the hemisphere. **(a)** Top view of the quasi-spanwise vortex (schematic). **(b)** The interaction between the two quasi-spanwise vortices and the hairpin head (schematic). **(c)** Top view of the evolution of the quasi-spanwise vortex.

very clearly¹⁵ around the high-speed patches adjacent to the legs as indicated in figures 3.2 and 3.14b.

It seems reasonable to assume that the circulation of the quasi-spanwise vortex depends on the gradient in the background velocity profile, that is deformed by the primary hairpin vortex. For the droplet, the vortex experiences a substantial velocity gradient over its entire height (see figure 3.13) and a weak quasi-spanwise vortex starts to grow immediately after the creation of the primary vortex. For the hemisphere, only the velocity gradient very close to the wall is high. Therefore, the effect of the necks and the legs on the near-wall velocity is reduced and the formation of the quasi-spanwise vortex is delayed. But as soon as the necks succeed in destabilizing the low-speed regions, a quasi-spanwise vortex is created quite suddenly (compare figures 3.25a and 3.25d). Figure 3.19b shows how the low-speed region adjacent to the hairpin vortex trajectory is increasingly destabilized, leading to the quasi-spanwise vortex that appears in this figure underneath the hairpin vortex furthest downstream.

¹⁵Since the low-speed regions created by the standing vortex contain large amounts of bubbles, it is easier to visualize the spanwise vortex for the hemisphere than for the droplet, as can be seen from figure 3.14.

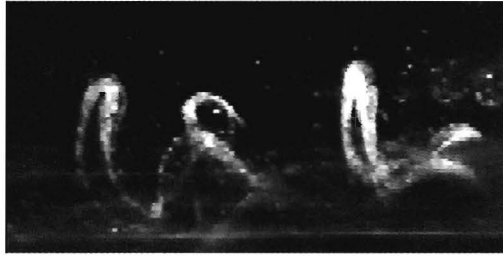


Figure 3.27: For a droplet, a new vortex head develops above the location of the rise in the legs (side view, flow direction to the left).
 $Re_D = 1900$

Figure 3.19b and 3.22 indicate that several hemisphere diameters downstream of the obstacle, the quasi-spanwise vortex suddenly rises upwards underneath the primary vortex head. This rise is explained in figure 3.26. In 3.26a a schematic representation of the hairpin vortex and the quasi-spanwise vortices is drawn, as shown previously in figure 3.14b, in which the direction of rotation is indicated. Close to the head of the vortex, the quasi-spanwise vortex related to the previous hairpin vortex (horizontally shaded) and the quasi-spanwise vortex related to the present hairpin vortex (vertically shaded) move over each other. This leads to a sudden interaction, in which the upstream vortex is pushed away from the wall by the downstream one, as indicated in figure 3.26b. A visualization of the effect is shown in figure 3.26c.

The creation of a new spanwise vortex A particularly interesting effect is the observation that in the case of a droplet a new vortex head seems to develop above the location of the rise in the legs. Figure 3.27 shows a circular concentration of bubbles above the legs of the vortex furthest downstream. Cine recordings clearly indicate that these bubbles are rotating around the centre of this patch. In addition, the hot-wire measurements in chapter 5 indicate that upstream of the vortex head a new low-speed patch appears in the flow, that can be related to this new vortex. The new vortex head does not have a very concentrated vorticity, but its total circulation is sufficient to push the primary vortex head towards the wall again. This slows down the primary vortex head, which enables the newly created vortex to catch up with it and envelop it. However, the subsequent interaction of the primary hairpin vortex and the newly created vortex causes a large diffusion of the bubbles, so that it is difficult to visualize the final stages of the process properly. Figure 3.28 shows this process from the onset of the secondary deformation (at the right) to the final stages (at the left).



Figure 3.28: The final stages in the evolution of the hairpin vortex as formed behind the droplet-shaped obstacle for $Re_D \approx 1850$ (side view, flow direction to the left).

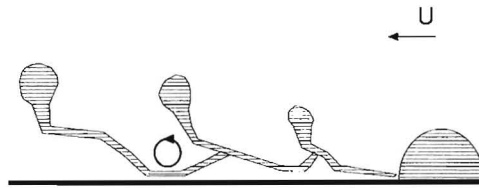


Figure 3.29: A schematic indication of the movement of the legs downstream of a hemisphere. Below the second vortex, the quasi-spanwise vortex is indicated.

The movement of the vortex legs The movement of the vortex legs is affected by (1) the effect of the velocity profile that stretches and bends them, (2) the effect of the quasi-spanwise vortex underneath (explained above), (3) their mutually induced velocity, which lifts them away from the wall, (4) the effect of the quasi-spanwise vortex underneath the subsequent vortex, which presses them against the wall when it is moving over them and (5) the effect of the neck of the subsequent hairpin vortex which lifts them out of the near-wall region. All these effects play a role in the resulting vortex shape, as depicted in figure 3.20. A schematic representation of the vortex shape downstream of a hemisphere is presented in figure 3.29. This figure shows the deformation of the legs by the combination of the background u -velocity profile, the effect of the subsequent hairpin vortex and the effect of the quasi-spanwise vortex preceding this subsequent hairpin vortex.

Many effects play a role in the movement of the legs, and the smaller effects, such as the internal dynamics of the hairpin vortices (item 3), are obscured by the larger ones. It seems that the effect of the mutually induced velocity on the legs is not very large: a rise in the legs is hardly observed although the distance between them is small (see figure 3.12).

It should be expected that, the effect of the legs on the near-wall fluid is enhanced when they are pressed towards the wall by the quasi-spanwise vortex.

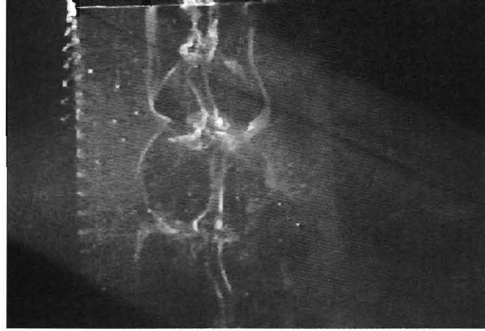


Figure 3.30: Top view: intermittently irregular behaviour of the vortex street behind a hemisphere for $Re_D = 1825$ (flow direction downwards). Note that the legs develop large spanwise distortions.

Indeed, the hot-wire measurements of chapter 5 show that a low-speed patch of fluid can be found at the location where this happens.

Irregularity of the vortex street When Re_D is increased over approximately 1800, the vortex street intermittently exhibits irregular behaviour: the regular vortex street is intersected by intervals during which the vortex street behaves irregularly. An example of such irregularity is shown for the hemisphere in figure 3.30. This photograph shows the vortices in the region $1.5 < x/D < 6.5$. It can be seen that the location of the legs shows a spanwise distortion. This observation confirms the conclusion made in chapter 5 that over a certain Reynolds number no regular vortex street can be measured anymore.

The near-wall flow The influence of the hairpin vortex on the near-wall area remains substantial over a long streamwise distance. In figure 3.31 the near-wall flow is visualized. The bubble wire is located at $x/D = 7.5$, $y/D \approx 0.06$. For both the droplet and the hemisphere, the hairpin vortex still has a marked effect at this location. The main effect of the vortex is to increase the u -velocity near the wall. In addition, the near-wall flow shows long streaky low-speed regions, which are indicated by markers in the photograph. Figure 3.31a shows that, in the case of the droplet, in the middle of the vortex street a low-speed streak appears from the effect of the legs (that draw up low-speed fluid from the wall in the region between them). However, even in this low-speed region the u -velocity is higher than the undisturbed velocity adjacent to the vortex street! For the hemisphere, no such low-speed region is created by the legs.

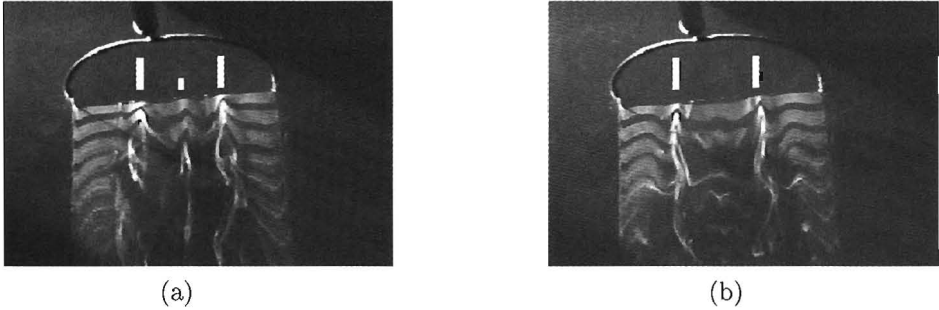


Figure 3.31: Top view of the near-wall fluid below the hairpin vortices at $x/D = 7.5$, $y/D \approx 0.06$ for $Re_D = 1570$. (a) droplet, (b) hemisphere (flow direction downwards). The low-speed streaks are indicated by white markers.

This may be due to the fact that for a hemisphere, $\partial u/\partial y$ is large only very close to the wall. The vortex legs move over this region when they are as far downstream as $x/D = 7.5$. This means that in this case, the legs hardly affect the near-wall fluid, in contrast to the case of the droplet. This corresponds to the measurements presented in chapter 5.

The near-wall flow also shows the effect of the quasi-spanwise vortices. To see this, it is illustrative to compare figure 3.31 to figure 3.14. Figure 3.31 shows that the area of high-speed fluid in the center (the area below the hairpin vortex trajectory), is flanked at both sides by a small low-speed region. This low-speed region is associated with the streamwise part of the quasi-spanwise vortex. The effect looks much the same as the effect of the standing vortex in the initial stages of the development of a vortex behind a hemisphere, but now it also appears in the case of the droplet, where no standing vortex is present! In addition, for the hemisphere, the figure shows an additional high-speed streak at the outside of the indicated low-speed streaks, that would not have appeared when the low-speed streak was caused by the standing vortex¹⁶. Note that the fact that the effect of the quasi-spanwise vortex can be found all around these high-speed patches corresponds to figure 3.14.

3.6 Discussion

The wake The differences in the streamwise extent of the wake for the hemisphere and for the droplet might seem somewhat surprising, as the shear layer that is separated from the top of the obstacle can be expected to be largely the

¹⁶The streamwise part of the quasi-spanwise vortex has a rotation whose direction is opposite to the rotation of the standing vortex.

same in both cases. The differences seem to be due to the fact that this shear layer gets destabilized not so much by 'infinitesimal disturbances' but by quite large disturbances in the flow that are caused by:

- the v -velocity that is imposed by the legs of the previous hairpin vortex
- the v - and w -velocities that are caused by the standing vortex.
- the v - and w -velocities of the flow around the obstacle, that are a consequence of the low-pressure area immediately downstream of the obstacle.

The first effect is essential for the formation of a regular vortex street in general as it leads to a regular spacing between the vortices, but the location where the hairpin vortices are shed from the wake depends also on the other two effects. For the hemisphere, the standing vortex destabilizes the wake immediately downstream of the recirculation area, which results in a small size of the wake. For the case of the droplet, where no standing vortex is present, the v - and w -velocities around the obstacle destabilize the shear layer¹⁷. By increasing Re_D these velocities become larger and, correspondingly, the wake becomes shorter.

The growth of the hairpin vortex According to Head & Bandyopadhyay (1981) and Acarlar & Smith (1987), the hairpin vortex grows over the extent of the boundary layer, although the computations of Hon & Walker (1987) indicate that the hairpin vortex may grow out of this layer. In our case, where the hemisphere is of the size of the boundary layer thickness, a substantial rise of the vortex head is still observed, in accordance with the results of Hon & Walker. Acarlar & Smith (1987) reported a backward movement of the vortex head, that can be observed as soon as the vortex head moves out of the laminar boundary layer. This movement brings the head upstream of the vortex neck. Although a similar phenomenon could be observed in our case (see figure 3.19b, this occurred when the height of the vortex head was already substantially larger than the laminar boundary layer thickness in which the obstacle was embedded. The interpretation of this phenomenon given by Acarlar & Smith has some theoretical shortcomings (see chapter 2) and in the present study the phenomenon is attributed to the effect of the quasi-spanwise vortex, as explained in section 3.5.

¹⁷In order to get some impression of the effect of the downstream side of the obstacle, a modified 'droplet'-structure was tried: a double cone (one point pointing upflow and one downflow). It was found that the shear layer that was separated from the double cone did not roll up into hairpin vortices at all, in contrast to the behaviour of the flow behind a droplet structure. It seems that when neither the low-pressure area nor the standing vortex are present, it takes a substantially larger time for the separated shear layer to roll over into a new vortex.

The effect of the hairpin vortex on the near-wall flow It was indicated in figure 3.31 that the main effect of the hairpin vortex was to speed up the near-wall flow. In the region between the legs an area of low-speed fluid is present, but even here the u -velocity is higher than in the surrounding undisturbed flow. This corresponds to the observation of Acarlar & Smith (1987) who also indicated an increase of the near-wall velocity due to the effect of the hairpin vortex.

On the other hand, several recent publications model the hairpin vortex head with a spanwise vortex and try to prove that such a vortex is able to push low-speed fluid at the wall upwards into a spiky eruption. They suggest that new vortices are generated by the instability that is created in this way (e.g. Doligalski, Smith and Walker, 1994). The present observations show that, with respect to the near-wall flow and the wall shear stress, the upflow of low-speed fluid is not the most dominant effect of the hairpin vortices. In addition, it will be shown in chapter 7 that such 2D-calculations cannot reproduce the large increase in the near-wall velocity that is the most prominent effect in the present visualizations. This throws some doubts on the validity of their claim that the spiky upflow of low-speed fluid that emerged from their 2D-calculations is similar to the effect of a hairpin vortex head.

The deformation of the vortex legs It is argued that the deformation of the vortex legs, that is found in the case of a droplet, is caused by the quasi-spanwise vortex. For a droplet, the creation of the quasi-spanwise vortex is due to the effect of the vortex necks and legs which create patches of high-speed fluid adjacent to the hairpin vortex. Although a quasi-spanwise vortex was found for a hemisphere as well, it is caused by a different mechanism in this case. Here, the quasi-spanwise vortex is created by the destabilization of the low-speed regions that flank the hairpin vortex trajectory. These regions are caused by the standing vortex: they are not present in the case of a droplet. For the droplet, as compared to the hemisphere, the quasi-spanwise vortex is created further upstream.

It is suggested that this quasi-spanwise vortex causes the secondary deformation of the vortex legs. Taylor (1990) found a similar deformation of the legs in his experiments. However, he gave a different explanation for this phenomenon: he attributed the wallward motion of the lower part of the neck to the near-wall shear instead of to the quasi-spanwise vortex, as is argued here. Taylor claimed this to be in accordance with the results of Hon & Walker (1987), who calculated the effect of a shear flow on an infinite spanwise line vortex with a small wall-normal distortion (see chapter 2). However, the effect calculated by these authors takes place at the upstream ends of the legs that move downwards under the influence of the infinitely long spanwise vortex. This effect cannot be related to the presently observed phenomenon.

For the droplet, the secondary deformation of the vortex legs appears midway

between two primary vortex heads. This effect might be related to a similar observation of Savaş & Coles (1985), who created vortices by periodically inserting a set of needles through the wall. They found that some distance downstream of the needles, new vortices appeared midway between the primary vortex heads, while these primary heads themselves disappeared.

The quasi-spanwise vortex is a secondary vortex that is generated near the wall with a vorticity that is of the same sign as the vorticity in the head of the primary vortex. An interesting observation is that the presence of such a secondary vortex is also argued by Doligalski, Smith & Walker (1994) from their 2D-calculations on a spanwise vortex. However, they claim that the creation of such a secondary vortex should be attributed to the effect of the pressure gradient imposed by the spanwise head of the hairpin vortex on the near-wall fluid. In the present study, it is argued that this secondary vortex is rather a secondary effect of the deformation of the background velocity profile caused by both the neck and the legs of the hairpin vortex.

The growth of irregularity in the vortex street It is difficult to indicate the effect that is responsible for the onset of irregularity in the vortex street for increasing Reynolds numbers. It seems that this irregularity is largely due to the effect of the quasi-spanwise vortex. For the droplet, the quasi-spanwise vortex distorts the vortex legs in a slightly irregular way, but this does not have much effect on the vortex heads, which still appear in a fairly regular vortex street. For a hemisphere, however, the quasi-spanwise vortex affects the region close to the vortex head, and in this case, the entire hairpin vortex is deformed. In particular, the quasi-spanwise vortex distorts the interaction between the vortex head and the legs of the previous vortex. In chapter 5 it will be shown that, if the Reynolds number is increased, the vortex street behind a hemisphere starts to display irregular behaviour sooner than the vortex street behind a droplet.

Chapter 4

The wind tunnel data-acquisition facilities

4.1 The wind tunnel

Dimensions of the wind tunnel The hot-wire measurements were performed within a low-speed wind tunnel. The speeds used were typically in the range of 1.5 - 2.0 m/s. The test section of the wind tunnel was 2.3 m long, 0.40 m wide and 0.50 m high. At a height of 0.24 m an additional floor was inserted with a rounded upstream edge. Above this floor the actual measurements took place, as shown in figure 4.1. For a flow over a flat plate the critical Reynolds number for the laminar-turbulent transition¹ is $Re_x = 3.2 \times 10^5$. Therefore, the flow is expected to remain laminar up to at least $x = 2.4$ m which is the size of the entire test section. The turbulent intensity of the wind tunnel was about 0.5%. The wind tunnel is depicted in figure 4.1. More information about the wind tunnel is provided by the thesis of Blom (1970).

Pressure vane During the measurements it was found that turbulence was generated at the upstream tip of the inserted floor. We attributed this to the fact that the supports below the floor caused an extra obstruction for the flow underneath the floor. This turned the section above the floor in the preferred flow channel, causing a small positive v -velocity component just upstream of the inserted floor, which we assume to be responsible for the additional turbulence. The effect is schematically represented in figure 4.2

To compensate for this effect a pressure vane was inserted in the measurement section as indicated in figure 4.1: downstream of the hot-wires, but still above the floor. This created an artificial additional obstruction above the floor that

¹This is the lower limit, which is valid for flows with a sizeable level of free stream turbulence (Schlichting, 1955).

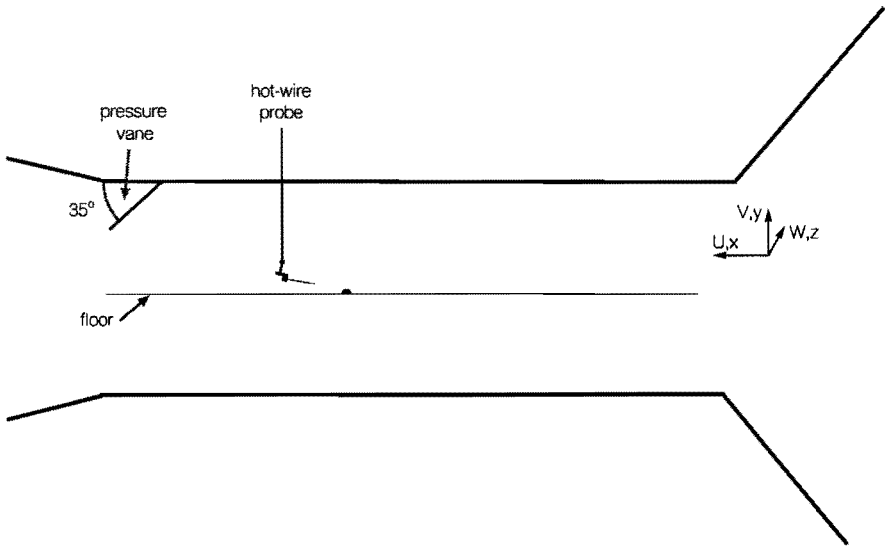


Figure 4.1: Schematic representation of the wind tunnel.

compensated for the obstruction by the supports below the floor. Although this created a higher pressure in the measurement channel, it did not create a pressure **gradient** at the location of measurement: a large pressure gradient is created only beneath the vane itself. As long as the vane is sufficiently far upstream of the hot-wires, it can be assumed that the behaviour of the measured hairpin vortices was not influenced by the vane. The presence of the vane probably generated turbulence underneath the floor, since that was now turned into the preferred channel. This did not affect the flow above the floor, as can be seen from figure 4.3, showing that the vane enabled us to get a neat laminar flow. The effect of the pressure vane on the near wall turbulence is indicated in figure 4.4: it causes a considerable reduction in the turbulent intensity near the wall.

4.2 The vortex generating obstruction

For the artificial vortex generation several obstructions were used. Hemispheres were applied with diameters of 50 mm down to 10 mm. Good results were obtained for a hemisphere of 16 mm for Reynolds numbers of about $Re_D = 1500 - 2000$. In addition, a droplet shape has been used with the sharp tip pointing upstream, in order to suppress the standing vortex generated upstream of a blunt obstruction, as discussed in chapter 2. The diameter of the head of the droplet corresponds to the diameter of the hemisphere, while the length of the tail of the structure is chosen to be about 2.5 times this diameter. The absence

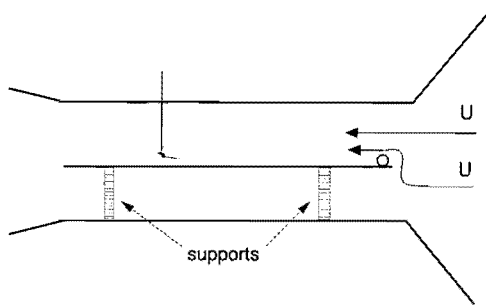


Figure 4.2: Schematic representation of the creation of an eddy (indicated as a circle) at the upstream edge of the inserted floor in the wind tunnel. The eddies are generated by the v -velocity that is induced by the fact that the lower channel is partially obstructed by the supports.

of a standing vortex upstream of the obstruction was verified by visualization in the water channel (see chapter 3).

4.3 The hot-wires

Hot-wire configuration and characteristics The measurements are performed with a rake containing an array of 9 parallel single-wire hot-wires in one row, as depicted in figure 4.6. The probe can be positioned parallel to the flow in two modes: either perpendicular or parallel to the wall. In the case of the parallel positioning of the rake, accurate vortex detection requires an additional detection probe, because the height of the probe with respect to the hemisphere influences the amount of detections, as is shown in figure 4.5. This is caused by the fact that the applied detection criterion does not function with the same accuracy at all heights. Figure 4.5 can be understood by comparing it to the velocity contour plot for a passing vortex, figure 4.8. It can be seen that in this case the best location to position a detection wire is just underneath the head. During a measurement, the detection probe is fixed at a height where the detection criterion functions properly while the measurements are performed at a different height.

Each hot-wire is adjusted to the tips of 2 needles with a length of 13 mm, extending before a ceramic (Al_2O_3) pole with a length of 85 mm and a diameter of 2.2 mm. The 9 poles are placed in a metal holder of $\Delta x \times \Delta y \times \Delta z = 7.5 \text{ mm} \times 7.5 \text{ mm} \times 28 \text{ mm}$. The dimensions were chosen after careful testing in order to find a configuration that would not measurably disturb our flow. The

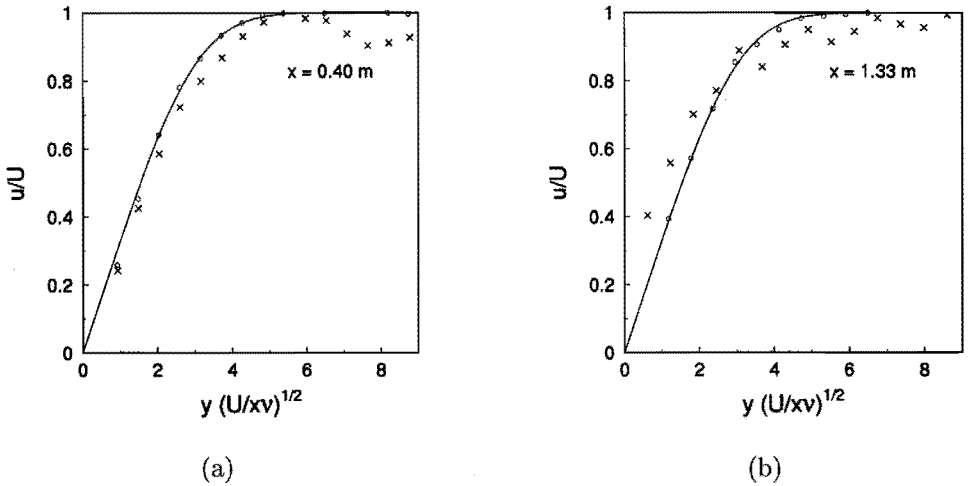


Figure 4.3: The measured u -velocity profile at two different downstream locations. (a) $x = 0.40$ m, (b) $x = 1.33$ m. (o) with pressure vane, (x) without pressure vane. In addition, the theoretical curve for the laminar boundary layer velocity is shown as a solid line.

resolution in the spatial direction between the hot-wires was determined by the distance between the hot-wires: 2.7 mm. For the standard hemisphere in our experiments ($D = 16$ mm), this implies a resolution of 0.17 times the diameter of the hemisphere. In reality, the distance between the different hot-wires was only approximately constant and for the drawing of the contour plots the real distance was measured between the hot-wires by means of a measuring telescope (that was also used for the calibration of the height of the hot-wires). The time resolution was determined by the frequency response of a hot-wire: about 60 kHz.

The position of this probe could be varied within the y -direction by a traversing mechanism driven by a stepper-motor. The x -direction was varied by moving the probe and the traversing mechanism affixed to it by hand over the rails on top of the wind tunnel.

The hot-wires have a length l of 1.0 mm and a diameter d of $2.5 \mu\text{m}$. This implies an l/d -ratio of 400; this is clearly larger than the minimum value of 200 below which the heat-losses to the supports start to affect the dynamic behaviour of the hot-wire (Bradshaw, 1971). The hot-wires consist of tungsten with a platinum cover, in order to combine the strength of tungsten and the low corrosivity of platinum. Free convection becomes important when $\sqrt[3]{Gr} > Re$

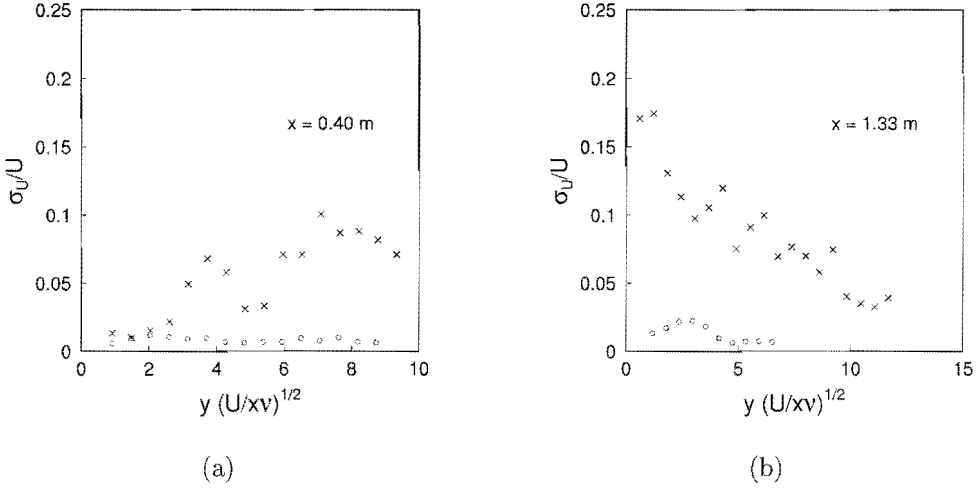


Figure 4.4: The measured near-wall turbulent intensity σ_u/U of the velocity at two downstream locations. **(a)** $x = 0.40$ m, **(b)** $x = 1.33$ m. (\circ) with pressure vane, (\times) without pressure vane.

(Goldstein, 1983). Gr represents the Grashof number, which equals:

$$Gr = \frac{gd^3 \Delta T}{\rho \nu^2 T}$$

This implies in our case that for $u > 0.04$ m/s free convection can be ignored.

Calibration of the hot-wires Each wire is inserted in a branch of a Wheatstone bridge, that keeps the wire at a constant temperature. The wires are then calibrated by measuring the voltage over the Wheatstone bridge, while varying the flow velocity from a valve-controlled nozzle. The pressure drop over the nozzle is measured by a capacitance pressure sensor (type 590, Datametrics). From the pressure drop over the nozzle (Δp) the nozzle velocity is calculated by application of Bernoulli's theorem: $u = \sqrt{2\Delta p/\rho}$. For air, a linear approximation around a reference value $\rho_*(T = T_*, P = P_*)$ can be used that includes ambient temperature T (in K) and ambient air pressure P and vapor pressure P_d (both in Pa):

$$\begin{aligned} \rho &\approx \rho_* \frac{T_* P}{T P_*} \\ &= 1.2929 \frac{273.13 (P - 0.3783P_d)}{T \cdot 1.013 \times 10^5} \end{aligned}$$

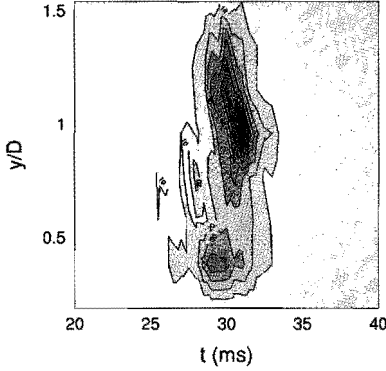


Figure 4.5: **Hemisphere:** The time distribution of shedding times as detected by our detection criterion as a function of height for a hemisphere on a smooth plate at $x/D = 5$, $z/D = 0$, $Re_D = 1920$ ($U = 1.8$ m/s). The shading becomes darker for an increasing amount of detected vortices.

$$\approx 0.349 \times 10^{-2} \frac{P - 442.6}{T}$$

This approximation for P_d is valid within 0.5 % for air moisture within the range 20% - 80% (Van Galen, 1994). This leads to the calibration formula:

$$u = 23.94 \sqrt{\frac{T}{P - 442.6}} \sqrt{\Delta p} \quad (4.1)$$

The actual calibration curve is obtained by fitting a fourth order polynomial to the data. In this way a better fit can be obtained than from the application of King's Law (Herweijer, 1995).

During an actual measurement, the power required to heat the hot-wire is a function not only of the flow velocity but also of the temperature difference ΔT between the hot-wire and its surroundings. The power equals the convective heat transfer Φ , which is given by (Goldstein, 1983)

$$\Phi = N_u \pi 2l k_f \Delta T \quad (4.2)$$

in which k_f is the thermal conductivity of the fluid, l is the effective length of the wire and N_u is the Nusselt number. For the latter, the theoretical expression for air is:

$$N_u = (A + B Re^n) \left(1 + \frac{\Delta T}{2T}\right)^{0.17} \quad (4.3)$$

where A , B and n are constants and T is the ambient temperature. During the calibration, the voltage over the Wheatstone bridge is measured as a function of the velocity. In order for this calibration to remain valid, the wire should have the same resistance (and therefore the same temperature) during the measurements as it had during the calibration: only then the dissipation over the hot wire is a constant fraction β of the total dissipation over the Wheatstone bridge. This means that the wire should have the same temperature at all measurements, irrespective of the ambient temperature. This implies that when the ambient temperature increases, the temperature difference between the wire

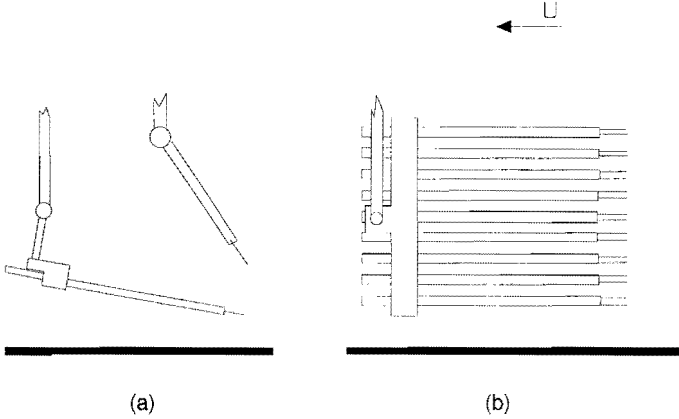


Figure 4.6: Schematic representation of the hot-wire probe (side views).
(a) probe positioned parallel to the wall, including the detection probe above the rake. The lower pole is the nearest of a parallel array of 9 similar poles **(b)** probe positioned perpendicular to the wall. When used in this mode the detection probe was absent.

and the ambient temperature has to decrease, which decreases the heatflow away from the wire. In order for the calibration to remain valid, a temperature correction is required to compensate for this. Use is made of the fact that the resistance r of the wire is linearly proportional to the temperature.

$$\Delta r = (r_*/T_*)\Delta T \quad (4.4)$$

The correction follows from the equations (4.3) and (4.2) and fact that the convective heat transfer Φ has to be equal to the dissipation over the wire, $\beta^2 V^2/r$, in which V is the voltage over the Wheatstone bridge and r the resistance of the hot-wire. In this way one finally arrives at

$$\frac{V^2}{r_t(r_t - r_0)} = \frac{T_*}{\beta^2 r_*} \pi 2 l k_f (A + B R e^n) \left(1 + \frac{\Delta T}{2T}\right)^{0.17} \quad (4.5)$$

where r_0 is the resistance of the wire without heating and r_t is the resistance of the heated wire.

The right hand side of equation 4.5 can be considered as more or less constant for the small temperature changes involved (typically up to 4°C).

r_t/r_0	$r_t - r_0$	$(1 + \Delta T/2T)^{0.17}$
1.55	5.5 Ω	1.0422
1.53	5.3 Ω	1.0408

From this table it can be seen that when Δr changes by 4%, the change in the right hand side of the equation is only 0.13%, which is sufficiently small to be ignored.

To account for changes in the ambient temperature, the measured voltage should therefore be multiplied with the correction

$$\sqrt{\frac{r_t^c(r_t^c - r_0^c)}{r_t(r_t - r_0)}} \quad (4.6)$$

in which r is the resistance of the wire during the experiment and r^c is the resistance during the calibration.

In our experimental set-up, the cold resistance of the hot-wires is measured automatically when the apparatus is switched on. The measured voltage is multiplied by this correction factor, before it is inserted into the calibration polynomial.

Using this procedure it was found that the wires could be calibrated with a mutual deviation up to 4 cm/s. Although the calibration is now valid for a large temperature range, recalibration is required periodically (monthly) because of degradation of the wire and pollution of the wire surface. For further information about the calibration equipment and the hardware and software used during the measurements, the reader is referred to the report of Van Galen (1994) and the thesis of Herweijer (1995).

Cautions with respect to the calibration

1. The calibration is very accurate within the proper range of velocities. Since our valve-controlled nozzle was only accurate down to 0.40 m/s we are not able to measure very low velocities with the same accuracy. Since we are using a fourth order polynomial instead of King's law, the *extrapolation* from the calibration curve to low velocities is not very reliable.
2. The hot-wires are calibrated in a parallel flow, whereas in the measurements also v - and w -components were present. These other flow components influence the measurements only to a negligible extent for most practical purposes, since a hot-wire measures the absolute perpendicular velocity. This implies that the hot-wire is far more sensitive to fluctuations in the velocity component parallel to the main flow than to the perpendicular components. Considering only the flow components perpendicular to the hot-wire:

$$\begin{aligned} |U| &= \sqrt{(U + u)^2 + v^2} \approx \sqrt{U^2 + 2uU} \\ &\approx U + u \end{aligned} \quad (4.7)$$

The approximation (4.7) is only valid when the main velocity is large enough with respect to the fluctuations. Very close to the wall, this assumption is not accurate anymore. Therefore, we could not accurately

measure the very low velocities in the near-wall region. To give some impression with respect to the size of the inaccuracy due to the v -component for large fluctuations, assuming that all fluctuations have the same magnitude ($u = v$) and have negative value (u is opposite to U):

u/U	error
10 %	0.6 %
25 %	5.4 %
50 %	41.4 %

However, this is the most disastrous scheme. In our case, close to the wall the v - and w -fluctuations are expected to be smaller than the u -fluctuations (especially the w -component is assumed zero in the plane of symmetry between the vortex legs). Nevertheless, these components might have some influence on the measured velocities. In these cases, the values found for u are somewhat higher than in reality. For the presented measurements, the error is at most in the order of 5%. This low value is confirmed by chapter 6, where the error is calculated from the circulation of the hairpin vortex: it is found to be at most 3%.

4.4 The data-acquisition

The PHYDAS-system is the computer system that is used for all our measurements. It is developed by the group Measurement and Computer Science and the support group Laboratory Automation at the Physics Department of the Eindhoven University of Technology. It is controlled by a VME-Motorola M68030 microprocessor that has a fast VME-bus for the assessment of the RAM and the hard disk and a slower dedicated bus structure (PhyBUS) for the connection of external measurement hardware. It is to be programmed in EPEP², a language that is especially designed for the system and that contains special commands for the flexible assessment of the external hardware in such a way as to enable interactive controlling of the measurements.

The external hardware connected to the PhyBUS is depicted in figure 4.7. The **CTA** is a Constant Temperature Anemometer. Each hot-wire is kept at a constant temperature by a Wheatstone bridge, that is built into the CTA. The overheat ratio was set to be 1.5 (corresponding to a hot-wire temperature of approximately 200 °C).

The anemometer voltage is read by a 12-bits **PARSAM** (PARAllel SAMpling unit), that has also been developed by the group Laboratory Automation. This device has 16 input channels and is able to store the voltages applied to these channels simultaneously in digital form (with negligible time delay as compared

²Eindhoven Program Editor and Processor

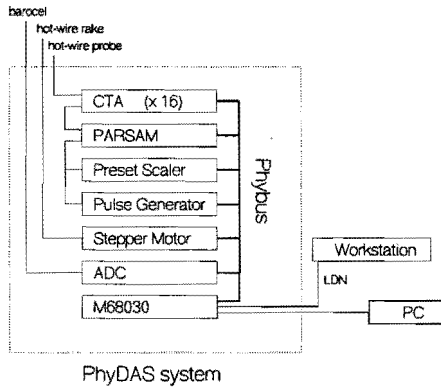


Figure 4.7: Schematic overview of the PhyDAS system.

to the time scale relevant in the experiment). The range of the input-voltage for the PARSAM can be controlled by setting the (analogous) offset-voltage and the amplification factor. The amplification can have 8 fixed values and is given by 2^n , in which $1 < n < 8$. The maximum storage frequency is about 22 kHz for all channels. For the experiment, the usual storage frequency (1000 Hz) is adjusted by external triggering, which was done by means of a **pulse generator** and a (computer controlled) **preset-scaler**.

The data are read in an internal memory of 512 kB. The PARSAM contains two such memories: when one is filled, the data storage automatically switches to the other memory without missing a sample. The filled memory can then be read by the computer system and cleared thereafter in the time required to fill the other memory.

The data that are read out of the PARSAM-memory are transferred to an EPEP-array that is subsequently analyzed by the software. First, it is checked whether the array contains numbers equal to the minimum and maximum output values of the PARSAM (0 and 4095). If these values are found, the input voltage of the PARSAM was out of range. In that case, the array is cleared, the amplification and the offset-voltage for the PARSAM are determined anew and a new measurement is made (continuity of the measurement is not important). If the array does not contain these values, it is stored on the system hard-disk as a temporal file. Next, a lookup table is consulted that provides the velocity corresponding to the digital output of the PARSAM. This table is created anew each time a new amplification factor or a new offset is established for the PARSAM. In order to save memory, the value of the measured velocity is truncated to round mm/s in order to be able to use 16-bit integers instead of 32-bit reals. In this way an array of speeds is generated that is ready for further treatment by the software, like (conditional) averaging. These further routines

produce an output file on the hard disk of the workstation that can be read by the graphical software. The resulting contour plots are the final result of a measurement. Optionally, it is possible after one treatment of the data, to apply another treatment to the temporal file and generate another set of contour plots from the same data.

4.5 The method of hot-wire data representation

For the investigation of a street of hairpin vortices, it seems a logical step to use conditional averaging, in order to find some average vortex structure. However, a conditional average tends to smooth features that do not exactly reproduce. The main goal of this research is to gain insight in the dynamics of hairpin vortices and especially in secondary structures that might appear. This aim requires that secondary structures or strong localized upflow of low-speed fluid from the wall are not smoothed away. Therefore, a method was to be found that would combine (some of) the statistical value of a conditional average with continued sensitivity for such features.

The method that is used, emphasizes the **modal** form of a hairpin vortex, in which these characteristic features are retained. This modal vortex can be interpreted as a photograph of a representative part of the signal. For a very regular signal, it is equal to the conditional average, for a very irregular signal it does not give any useful results. However, for a signal that contains intervals in which the signal behaves regular, it is a useful method. During a measurement a time-series is measured of typically 10 seconds. As the shedding frequency behind a hemisphere having a diameter of 16 mm at $U = 1.8$ m/s is about 30 Hz, a measurement contains typically around 300 vortices. The sampling frequency was chosen to be 1000 Hz, so about 30 samples are taken during the passage of one hairpin vortex by each hot-wire. The signal is stored and subsequently analyzed in a number of stages:

1. From the collected array of speeds, the average velocity and the standard deviation is calculated.
2. The data are normalized by subtracting the average and dividing by the standard deviation.
3. The signal from a selected hot-wire was used for detecting the location of the maxima in the signal, which are associated with the passage of a vortex. The location of the maxima was determined as the location halfway between a positive and a negative zero-crossing. This method turned out to be a lot more reliable than using the location of the maximum value itself, as this was rather sensitive to noise in the signal.
4. A histogram was made of the time interval between two maxima, within a resolution of 2 ms. From this histogram, the most frequently occurring

time interval between two peaks was determined.

5. In addition, whenever a maximum was detected by the selected hot-wire, the normalized velocity fluctuation was recorded for a specified number of other hot-wires (usually two). The recorded values were assembled into histograms, within a resolution of $0.2 \times \sigma$. From these, the most frequently occurring values for the normalized velocity deviation were determined at the locations of the specified hot-wires.
6. The parts of the signal are selected that contain a vortex having the most frequently occurring time distance to both its neighbours upstream and downstream, as well as having the most frequently occurring value for the normalized velocity fluctuations at the location of the other specified hot-wires. In other words: a vortex was selected having a normal velocity distribution as well as a normal time interval to its neighbours. There might typically be zero to ten of these vortices in the recorded time series. The (non-normalized) velocity in the specified direction during the specified time interval is recorded.

Apart from this modal vortex, often the conditionally averaged vortex is calculated too. The two pictures for the modal and the average vortex can be compared in order to have an additional check of whether the modal vortex as determined by the limited set of tests mentioned above is really representative for the structures that are shed. In addition to the conditionally averaged values for the velocity, also the standard deviation for the conditional average can be calculated. This result can be interpreted as the error with respect to the conditionally averaged velocity profile. Since the velocity contour plot of a modal vortex is like a photograph, it is not possible to indicate the error in the registered speeds. The difference between the average hairpin and the modal structure can be seen from figure 4.8. While they are calculated from the same datafile, figure 4.8a gives the average u -contour plot from the passage of a hairpin and figure 4.8b gives the modal hairpin. In this case, the main differences are the less extremal values for the velocity and the somewhat different shape of the area below the vortex heads. Both effects are caused by the conditional averaging of shapes that are not exactly aligned in such a way that the areas with the most extremal values do not exactly overlap. Conditional averaging tends to smooth the most extremal effects.

Cautions with respect to the contour plots

1. By the fact that in the figures the t -scale is depicted as shorter than the y -scale, one should not be misled into thinking that the distance between the vortices is small as compared to their height. As the typical main stream velocity is about 2.0 m/s, the distance between two vortices is about 60 mm, while the height of a vortex is about the diameter of the obstruction,

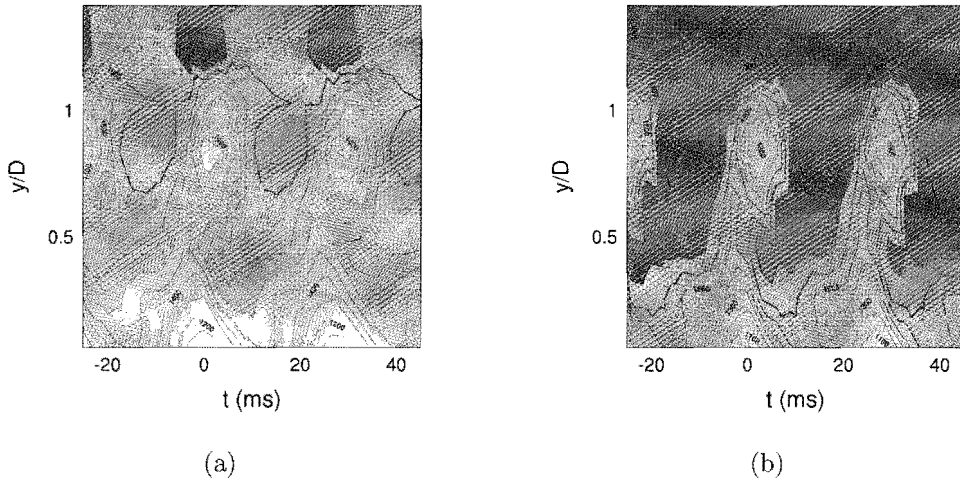


Figure 4.8: The u -velocity contour plot measured at $x/D = 5$ downstream of a hemisphere for $Re_D = 1920$ ($U = 1.80$ m/s). (a) The average hairpin vortex as found from the averaging of 221 vortices, (b) the modal hairpin vortex. Both contour plots are calculated from the same datafile. Since the signal is very regular the resulting contour plots are largely the same.

that is, 16 mm. For practical purposes, however, in the figures the distance between the vortices is depicted as shorter than their height.

2. The contour plots are presented as a function of time instead of downstream distance, since the hot-wires did measure a time-series. The result differs from a spatial representation because of the spatial evolution of the vortex.
3. It was not possible to measure the velocity in the region nearest to the wall, because of our calibration which was only valid for velocities larger than 0.4 m/s and because of the finite size of the hot-wires and the size of the rake. In most contour plots the lowest measuring station was at 1.5 mm ($y/D = 0.09$) above the wall. A linear interpolation between this value and the zero value at the wall might be too much of a simplification in the rather complicated near-wall area. In the presented contour plots therefore, the lowest value for y is still somewhat above the wall and the velocity does not go to zero value. As can be seen, the velocities are still quite large at this lowest distance from the wall, implying large values of $\partial u/\partial y$ close to the wall.

4. The exact location of the contours in a contour plot of a region with small gradients in the plane of measurement is very sensitive to small changes in velocity. This may lead to unexpected asymmetries in the contour plots.
5. The nine hot wires that are present in the rake do not exactly lie in one line. For the contour plots in the Zt -plane, the small variation in height among the different wires (at most 0.5 mm) is particularly important, since it introduces an error for measurements in locations with a large vertical velocity gradient ($\partial u/\partial y$) that is found in the near wall boundary layer.
6. It should be kept in mind that the resolution of the measurements is limited and the contour plots contain a lot of interpolation from the contour plotting routine. The routine uses a simple linear extrapolation scheme for this, which does not always give the best physical results. However, no large errors were observed either and there is no obvious way to do better than this.

Chapter 5

Hot-wire measurements

5.1 Introduction

5.1.1 Overview and interpretation of the measurements

With the measurement equipment described in chapter 4 a large series of hot-wire measurements has been made. This chapter is concerned with the analysis of these measurements. Several topics are addressed. First, the vortex shedding period is examined for several types of obstructions (a droplet, a hemisphere and several types of cones). Then, the three flow configurations are examined that were used previously in chapter 3:

1. a hemisphere on a smooth surface
2. a hemisphere on a grooved surface (longitudinal riblets)
3. a teardrop-shaped obstacle on a smooth surface

The diameters of the hemisphere and the droplet are both 16 mm, the distance between the riblets is 2.5 mm. The main difference between the hemisphere and the droplet is the standing vortex that is created in the former case. The effect of the standing vortex on the velocity profile is indicated in chapter 2.

First, the shedding period is measured for these obstructions as a function of Reynolds number. Then the vortex dynamics are once again examined. The effect of the standing vortex is shown. Next, the hairpin vortex itself is examined. The flow field around individual vortices is shown and the effects of downstream distance and Reynolds number are indicated. Special attention will be paid to the secondary deformation of the vortex legs, that was indicated before in chapter 3. Finally, a short discussion is presented.

5.1.2 Scaling

The variables along the axes of the contour plots are dimensionless. The height is scaled with the diameter D of the hemisphere or droplet that was used, the time is scaled with the time that is required for the main flow to move across the chosen unity lengthscale. In this way one arrives at the dimensionless quantities:

$$\begin{aligned} t^* &= tU/D & Re_D &= UD/\nu \\ y^* &= y/D & Sr_D &= D/Ut \\ z^* &= z/D \end{aligned}$$

For practical reasons, in some cases the height H of the obstruction is used instead of D . For a hemisphere, $Re_H = \frac{1}{2}Re_D$.

The measurements have been performed for different main stream velocities U . The increase of U implies a decrease of the boundary layer thickness, whereas the obstacle is fixed at its downstream location¹ and is thus embedded in a somewhat different flow profile. However, for the range of Reynolds numbers examined, the boundary layer thickness was always of approximately the same magnitude as the height of the obstruction, as can be seen below. Therefore the effect of the variation in the flow profile is assumed to be small in the measurements presented here.

It is to be expected that the circulation of the vortex head scales with the velocity in the undisturbed laminar boundary layer at the height of the tip of the obstruction, u_{tip} . Since the obstruction is entirely embedded in the laminar boundary layer, u_{tip} is somewhat smaller than the main stream velocity U that is used for the scaling. Since for the applied range of Reynolds numbers the velocity difference between the main stream velocity and u_{tip} is small, it was decided to use the main stream velocity for the determination of the Reynolds number.

Re_D	δ/D	u_{tip}/U
1600	0.66	0.94
2400	0.54	0.98

5.1.3 The different types of measurements

In this chapter, three different techniques are used to represent the hot-wire measurements.

- Velocity contour plots are shown of the modal vortex (explained in chapter 4) in order to show the evolution of individual vortices. The choice to investigate modal vortices was made in order to avoid the smoothing that is inherent in averaging. This method gives cross-sections in the Zt -plane and the Yt -plane of the u -velocity field around the vortices. The results

¹Because of the limited extent of the measurement section over which the hot-wire rake could be moved, it was decided to keep the location of the obstruction fixed.

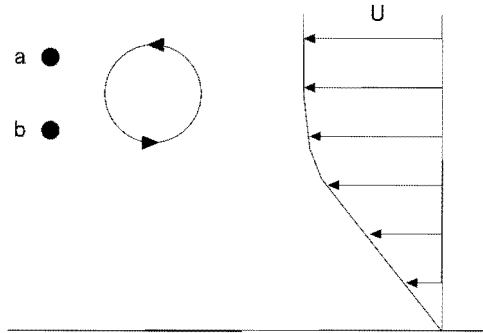


Figure 5.1: The velocity profile and the u -velocity induced by a spanwise vortex. A hot-wire at location **a** will measure a velocity peak when the vortex passes, a hot-wire at location **b** will measure a dip.

have some resemblance with photographs of a vortex street (a top view for the Zt -plane or a side view for the Yt -plane) of a vortex street, but do not show the spatial evolution of the velocity profile in the streamwise direction. In these figures, $t = 0$ corresponds to the passage of the head of the modal vortex at the location of measurement.

- Conditional averages were calculated to be able to show a cross-section of the vortex street in the YZ -plane.
- The average velocity is measured to show the velocity profile downstream of the obstruction.

A large part of the figures in this section will consist of contour plots of the streamwise (u -) velocity, that is presented as a fraction of the main stream velocity U . The contour plots have been shaded in such a way that the darker shading marks higher speeds. In addition, the value u/U has been indicated at the contour lines.

5.2 The shedding period

The results of the visualizations presented in chapter 3 show that hairpin vortices are shed from the two obstructions used with a well-defined period. This can also be concluded from the hot-wire measurements. As indicated in figure 5.1, a hot-wire registers a dip in the u -velocity when a vortex head passes over the wire. These dips were measured and the period between two subsequent dips

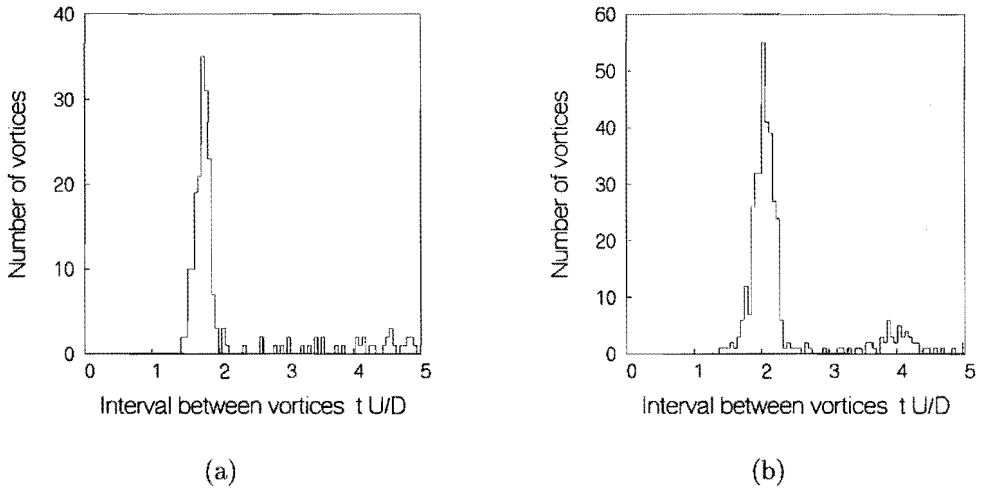


Figure 5.2: **Hemisphere:** The time interval between the subsequent vortices shed behind a hemisphere at $x/D = 5$ for $Re_D = 1730$ ($U = 1.62$ m/s) on (a) a flat plate or (b) a grooved plate.

was calculated in the way described in chapter 4. It is then possible to make histograms of the vortex shedding period. The regularity of the vortex shedding period is shown by figure 5.2, in which histograms of the vortex shedding at $Re_D = 1730$ are shown for a hemisphere on either a smooth or a grooved surface. The shedding period was measured in this way for several types of obstructions at $Re_H = 970$. These obstructions are shown in figure 5.3 and all have the same height H (8 mm):



Figure 5.3: The four obstructions for which the shedding frequency was measured. (a) hemisphere, (b) droplet, (c) cone, (d) double cone.

type of obstruction	tU/D
hemisphere	1.91 ± 0.1
cone, tail = $2.6H$, width = $2H$	2.36 ± 0.1
droplet, tail = $1.5H$, width = $2H$	2.42 ± 0.05
droplet, tail = $2.6H$, width = $2H$	2.59 ± 0.05
droplet, tail = $2.6H$, width = $4H$	2.89 ± 0.1
double cone	no shedding

It seems that the smoother the obstruction becomes, the more the shedding period increases. This is true for the upstream, as well as the downstream part of the obstruction. This indicates that the shear layer that separates from the obstruction is destabilized by the v - and w -velocities induced in the flow around the obstruction. Of particular importance is the effect of the standing vortex, as can be concluded from the difference between the shedding frequency for the hemisphere and the different types of droplet-shapes. This can be understood from the fact that the standing vortex pushes high-speed fluid sideways into the wake area, as indicated in chapter 3. But also the downstream side of the obstruction is important. When the downstream side is smoother, the shedding frequency decreases and for the double cone no vortex shedding is found at all, and only a very long wake area can be observed downstream of the obstruction! In order to indicate the effect of the main stream velocity on the vortex shedding frequency for the three chosen configurations (droplet and hemisphere on smooth surface, hemisphere on riblets), histograms of the shedding period were measured for the range $1200 < Re_D < 2600$ at $x/D = 4.7$. These histograms were combined to form figure 5.4.

In figures 5.4a-c contour plots are shown representing the time-distribution of the trigger events. Although the normalized shedding interval remained more or less constant with increasing Re , the absolute shedding interval decreased and therefore the number of detections increased during the fixed measurement time. To correct for this effect, the number of detections was multiplied by D/U .

It can be seen that only a limited range of Reynolds numbers exists for which a regular vortex street is found. For small Re_D no shedding is found anymore, while for high Re_D the shedding becomes too irregular for the detection criterion to function properly. In the visualizations presented in chapter 3 an example of such irregular behaviour is shown on page 51 for the case of the hemisphere (for $Re_D = 1830$). The decreasing amount of detections should be attributed to

1. the irregular shedding period
2. variations in the height of the vortices, which makes it impossible to optimize the detection criterion to the same extent as for lower Reynolds numbers
3. low-frequency variations in the background velocity, with a period of several times the hairpin vortex shedding period. These variations cannot be

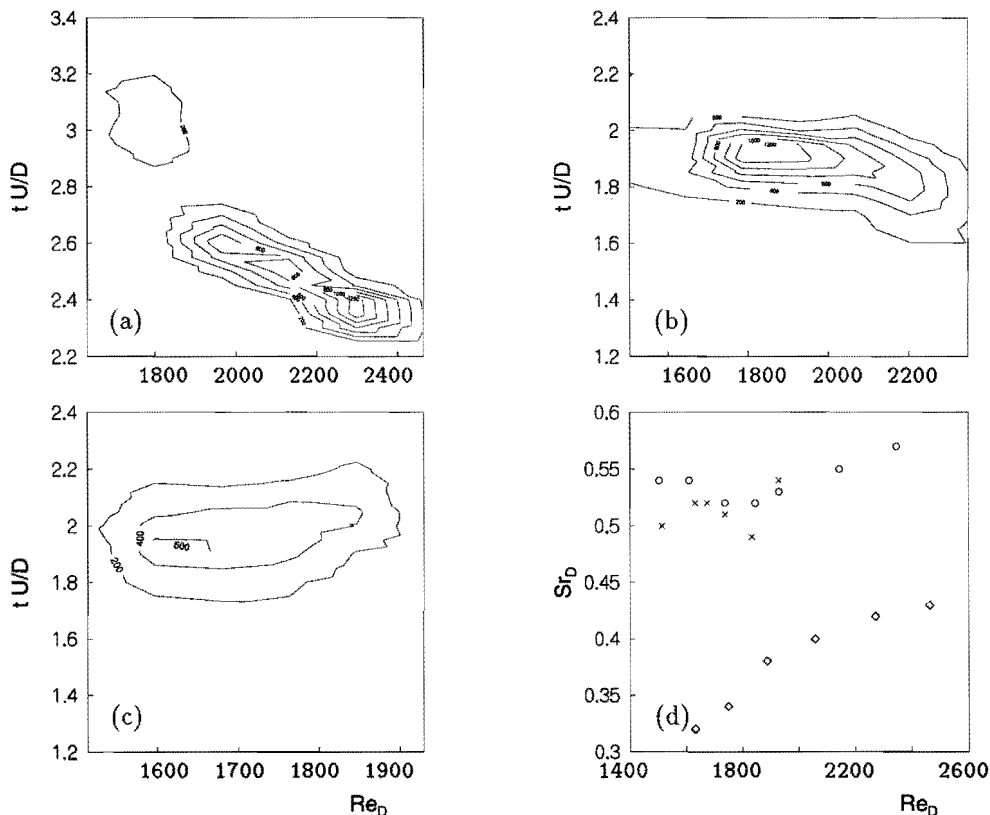


Figure 5.4: In the first three figures the distribution of shedding periods is shown as a function of Reynolds number for (a) droplet, (b) hemisphere on a smooth surface and (c) hemisphere on a grooved surface. (d) Strouhal number (obtained from the maxima in the former three period distributions) versus Reynolds number for (o) hemisphere (smooth wall) (x) hemisphere (riblets) and (◊) droplet.

handled by our detection criterion.

In figure 5.4d, the Strouhal number with respect to the diameter of the obstruction, St_D , is plotted as a function of Reynolds number. The values of St_D have been calculated from the peak values of the interval distributions in figure 5.4a-c. The shedding period of the droplet decreases with Reynolds number, whereas the shedding period downstream of the hemisphere remains relatively constant over this range of Reynolds numbers². The shedding time for a hemisphere is

²This result does not agree with the results of Acarlar and Smith (1987) who find a strong Reynolds dependency for both the droplet and the hemisphere. However, they calculate Re_D from the velocity at the height of the tip of the obstruction in the undisturbed flow, instead of the main stream velocity U . In addition, they used a large range of obstruction heights in

hardly changed by the presence of riblets.

A comparison of figure 5.4b and 5.4c shows that if the hemisphere is placed on riblets the range of Reynolds numbers over which can be measured effectively is reduced. This effect should be attributed to an instability that is created by the shape of our riblets: even in the absence of the hemisphere, above the surface of the grooved plate near-wall vortices started to appear at $Re_D \approx 1750$. Visualizations of this effect have been shown in chapter 3. By impinging on the hemisphere, these vortices affect the regularity of the vortex shedding. This invalidates a comparison between the vortex streets shed behind a hemisphere with and without riblets for $Re_D > 1750$. However, for lower values of Re_D it is still possible to compare the cases with and without riblets.

The droplet has a much lower shedding frequency than the hemisphere. For $Re_D = 1720$ the value of the Strouhal number St_D for a droplet is about 60% of that for a hemisphere. In addition, in contrast to the case of a hemisphere, the Strouhal number for a droplet increases with increasing Reynolds number. Over the range $1600 < Re_D < 2600$ the Strouhal number increases about 40%. The effect of the Reynolds number on the length of the wake of the obstruction was discussed in chapter 3. It was shown that, for the droplet, the wake area is relatively long, but is reduced by an increase in the Reynolds number. For the hemisphere, the wake area was short irrespective of the Reynolds number. It seems that a more violent disruption of the wake area, as provided both by the presence of the standing vortex and by an increase in the Reynolds number, not only reduces the length of the wake, but also increases the shedding frequency.

5.3 The standing vortex

In chapter 3, it was indicated that a standing vortex is present in the case of the hemisphere and absent in the case of the droplet. The standing vortex was visualized for the case of the hemisphere on the smooth surface as well as for the hemisphere on the grooved surface. The effect of the standing vortex is to draw high-speed fluid into the wake of the obstruction, as well as to create low-speed regions adjacent to the vortex street (see chapter 3).

In figure 5.5 velocity contour plots are shown of a cross-section of the velocity field in the YZ -plane (perpendicular to the direction of the flow). The location $z/D = 0$ corresponds to the plane of symmetry between the hairpin vortex legs. The figure shows the u -velocity field for two different time delays: the first cross-section shows the velocity just before the passage of a new hairpin vortex and the second cross-section shows the u -velocity at the time of passage.

order to get a large range of Reynolds numbers. Although this seems a reasonable approach, it does not take into account the effect of the shape of the velocity profile over the obstruction (as indicated in chapter 2). In our case this is more or less kept at a constant value. It seems that our method of scaling corresponds closer to the physical processes involved in the vortex shedding.

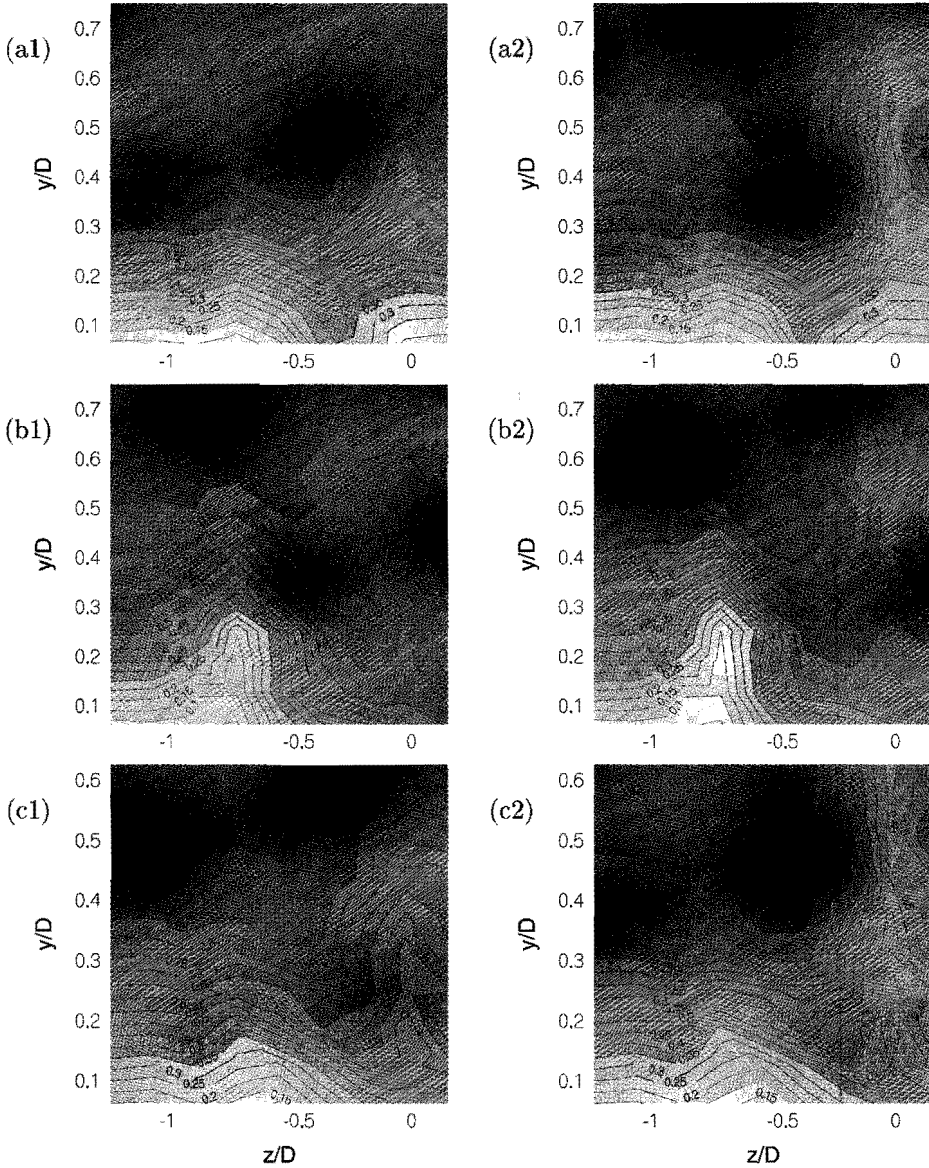
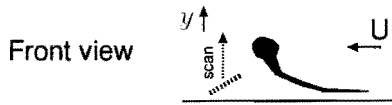


Figure 5.5: The conditionally averaged u -velocity contour plots in the YZ -plane relative to the passage of a vortex head at $x/D = 3.125$, $Re_D = 1754$. Note that in the last figure the y/D -range is smaller. (a) droplet, (b) hemisphere (smooth wall), (c) hemisphere (riblets). (1) $tU/D = -0.61$, (2) $tU/D = 0.0$.

For the hemisphere on the smooth surface, the low-speed region that is created by the standing vortex appears very clearly at $z/D \approx -0.75$. Obviously, while this upwelling is very clear for the hemisphere on the smooth surface, for *both* other configurations the effect is far less. This means that although the riblets do not inhibit the formation of the standing vortex (as could be seen from the visualizations), the standing vortex is strongly weakened. Throughout this chapter, this will be shown to have important consequences for the evolution of the hairpin vortices. From a comparison of 5.5b1 and 5.5b2 it is clear that the standing vortex is hardly affected by the passage of the hairpin vortex. This is also observed at $x/D = 3.125$ in the visualizations (see chapter 3). For larger values of x/D the standing vortex is deformed strongly by the hairpin vortices, as indicated before in the visualizations. The evolution of the low-speed region further downstream will be discussed in section 5.5.

5.4 The vortex-induced velocity field

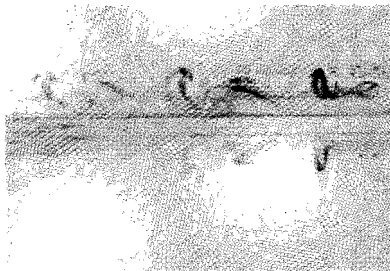
5.4.1 Introduction

In chapter 3 visualizations were shown indicating the shape of the hairpin vortices. Since there is a close correspondence between the shape of the hairpin vortex and the induced velocity field, more or less the same features show up in the hot-wire measurements as in the visualizations. However, while the visualizations show the evolution of the entire vortex in a Lagrangian view, the hot-wire measurements show the evolution of the velocity field at one fixed location in space, an Eulerian view. Since the interpretation of the latter is much more difficult, it is necessary to compare the results of the measurements in close relation to the results of the visualizations.

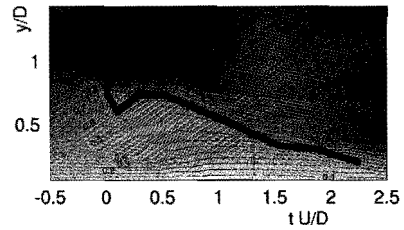
An additional complication is given by the fact that there is no one-to-one relation between the vortices and the velocity field. A patch of low velocity appearing in a contour plot might be due to the induced velocity of a hairpin vortex, to an upwelling of low-speed fluid from the wall or to a secondary vortex that is generated in the interaction of the hairpin vortex with the near-wall fluid. This is especially problematic for the case of a hairpin leg, since it is largely oriented parallel with the flow. In that case the vortex itself only induces a very small u -velocity and only the upwelling of low-speed fluid can be detected. This upwelling takes place only if the velocity field around the vortex contains a substantial velocity gradient.

5.4.2 Cross-sections in the Yt -plane

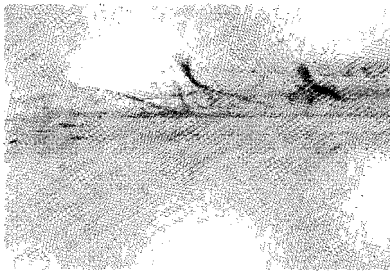
A side-view of the hairpin vortex for the cases of the droplet and the hemisphere on a smooth wall are shown in figure 5.6. In figure 5.7 the corresponding modal velocity contour plots are shown. In addition, figure 5.7c shows the velocity



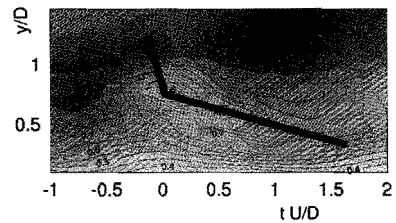
(a1)



(a2)



(b1)



(b2)

Figure 5.6: Side view for $Re_D \approx 1800$ at $x/D \approx 5$ (a) droplet, (b) hemisphere. (1) photograph, (2) the velocity field in the Yt -plane in which a tentative sketch of the vortex shape is drawn.

contour plots for a hemisphere on a grooved surface.

In the velocity contour plots, the heads show up clearly as a patch of high-speed fluid above a patch of low-speed fluid, as indicated in figure 5.1. The centre of the vortex head is then indicated by the middle of the gradient area ($\partial u/\partial y$) between these two patches. Note that the low-speed patch is substantially larger and deviates more from the local flow velocity than the high-speed patch. This effect should be attributed to the fact that the low-speed patch is not only created by the head, but also by the neck (see chapter 6). The heads are located at $y/D \approx 1$, which means that at $x/D = 5$ they have already risen over $0.5D$ in the flow.

Since it is not very straightforward to make the translation from the velocity contour plots to the visualizations shown in chapter 3, the hairpin vortex shapes for a droplet and a hemisphere have been indicated schematically in the velocity contour plots shown in figures 5.6a2 and 5.6b2. In these figures, in contrast to all

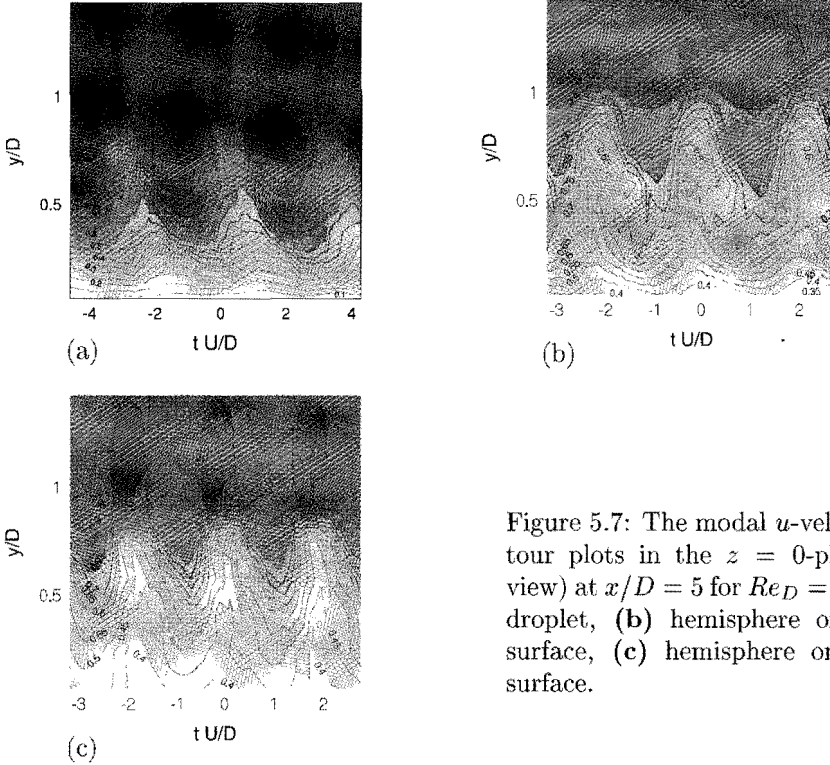


Figure 5.7: The modal u -velocity contour plots in the $z = 0$ -plane (side view) at $x/D = 5$ for $Re_D = 1730$. (a) droplet, (b) hemisphere on smooth surface, (c) hemisphere on grooved surface.

the other velocity contour plots presented in this chapter, the unity scale along the x -axis have been taken equal to the unity scale along the y -axis, instead of the usual compressed x -axis, to facilitate the comparison with the photographs. The shape of the vortex drawn in the figures is not exactly known, but just represents an 'educated guess', partly based on the results of chapter 6.

The background velocity strongly depends on the type of obstruction. Figure 5.7 indicates clearly that for the hemisphere on a smooth surface, the average velocity at $y/D \approx 0.3$ is substantially higher than for the other two configurations. On the other hand, the hemisphere on the grooved surface shows a near-wall velocity that is far larger than the near-wall velocity for the droplet and about as large as for the hemisphere. It is suggested that these effects should be attributed to the effect of the standing vortex. While the standing vortex is strongly weakened by the riblets, it is still present and its effect seems to be enough to increase the near wall velocity. This effect is even clearer for smaller downstream distance as will be shown in section 5.5.

A puzzling feature is the upwelling of low-speed fluid close to the wall, that appears in figure 5.7. For the hemisphere on the smooth surface, a region of low-speed fluid is present underneath the vortex head. For the droplet a similar region can be found somewhat further upstream. In both cases it is located

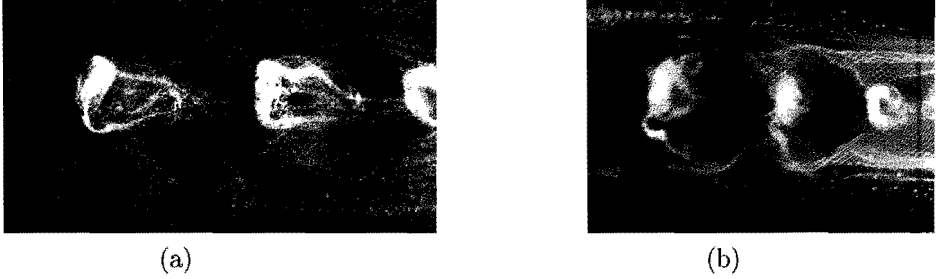


Figure 5.8: The differences in the vortex shape between a vortex shed from a droplet and from a hemisphere for $Re \approx 1700$ (top view, flow direction to the left). (a) droplet (b) hemisphere

immediately downstream of the location where the vortex necks approach the wall. It was shown in chapter 3 that for the hemisphere, the neck of the vortex draws the low-speed regions that were created by the standing vortex into the trajectory of the hairpin vortices (see figure 5.8b). These low-speed regions reach the head at $x/D \approx 4$, where the quasi-spanwise vortex is created. Furthermore, the quasi-spanwise vortex moves over the legs of the previous hairpin vortex and pushes these legs towards the wall, where they draw up low-speed near-wall fluid. It is suggested here that the observed low-speed area underneath the hairpin vortex head is caused by a combination of these effects.

5.4.3 Cross-sections in the Zt -plane

A top-view of the hairpin vortex for the case of the hemisphere is shown in figure 5.8b. In figure 5.9 the corresponding modal velocity contour plots are shown.

- Close to the wall (figures 5.9e and 5.9f) two regions with large gradients can be seen for $|z/D| > 0.4$. They are associated with the low-speed regions that are caused by the standing vortex.
- Close to the wall (figures 5.9d, 5.9e and 5.9f) two patches of high-speed fluid are present that have their centre at $|z/D| \approx 0.2$. These patches are caused by the combined effect of the necks and the legs of the hairpin vortex and the effect of the standing vortex. Due to these effects, high-speed fluid is drawn towards the wall in the region between the hairpin vortex and the standing vortex. Note the correspondence between the indicated high-speed patches and the regions adjacent to the legs in figure 5.8b.
- Somewhat higher in the flow (figures 5.9c and 5.9d) the low-speed region at $|z/D| > 0.4$ is not as static as it was close to the wall (figures 5.9e and 5.9f), but seems to meander. This effect is due to the interaction of the

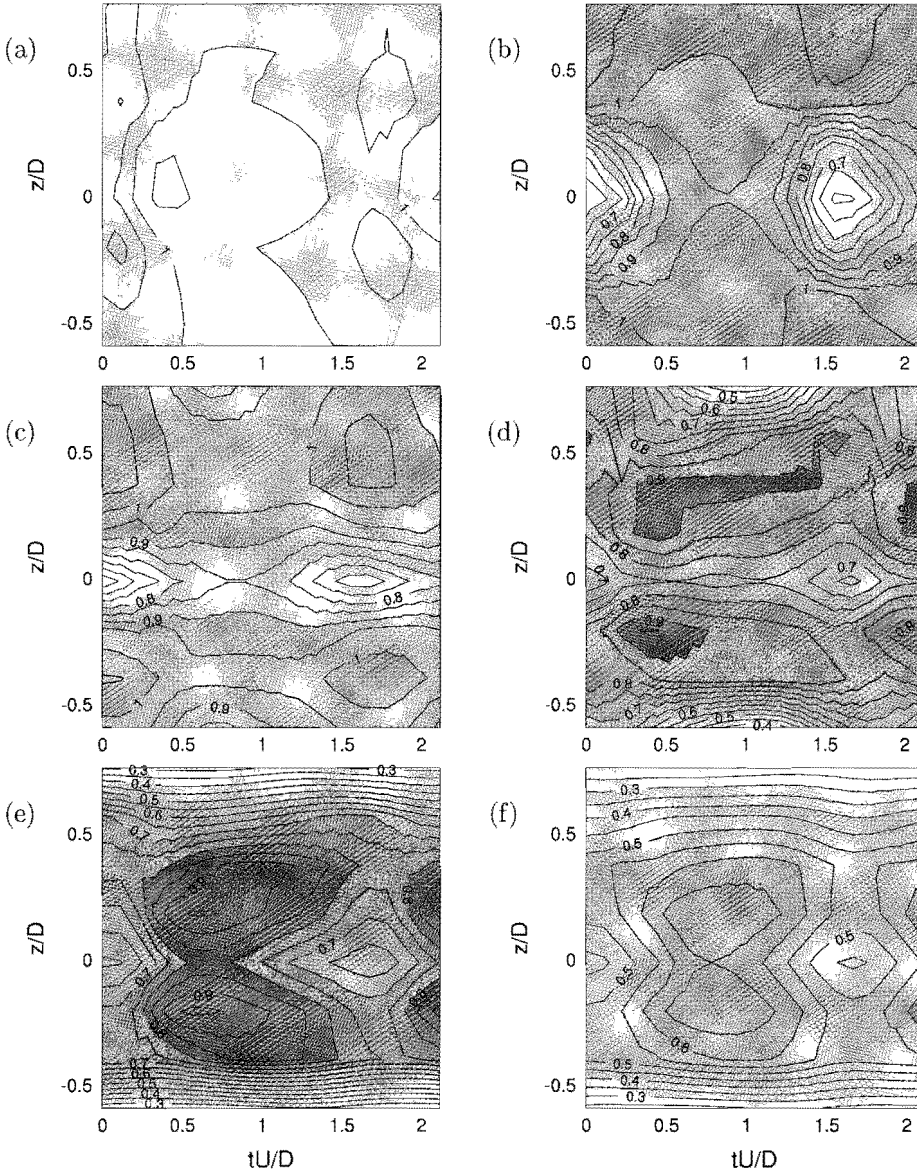
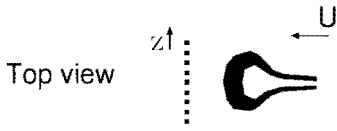


Figure 5.9: **Hemisphere (smooth wall)**: The conditionally averaged u -velocity in the Zt -plane for decreasing height at $x/D = 5$ for $Re_D = 1920$ ($U = 1.80$ m/s). (a) $y/D = 1.03$, (b) $y/D = 0.81$, (c) $y/D = 0.50$, (d) $y/D = 0.38$, (e) $y/D = 0.25$, (f) $y/D = 0.13$

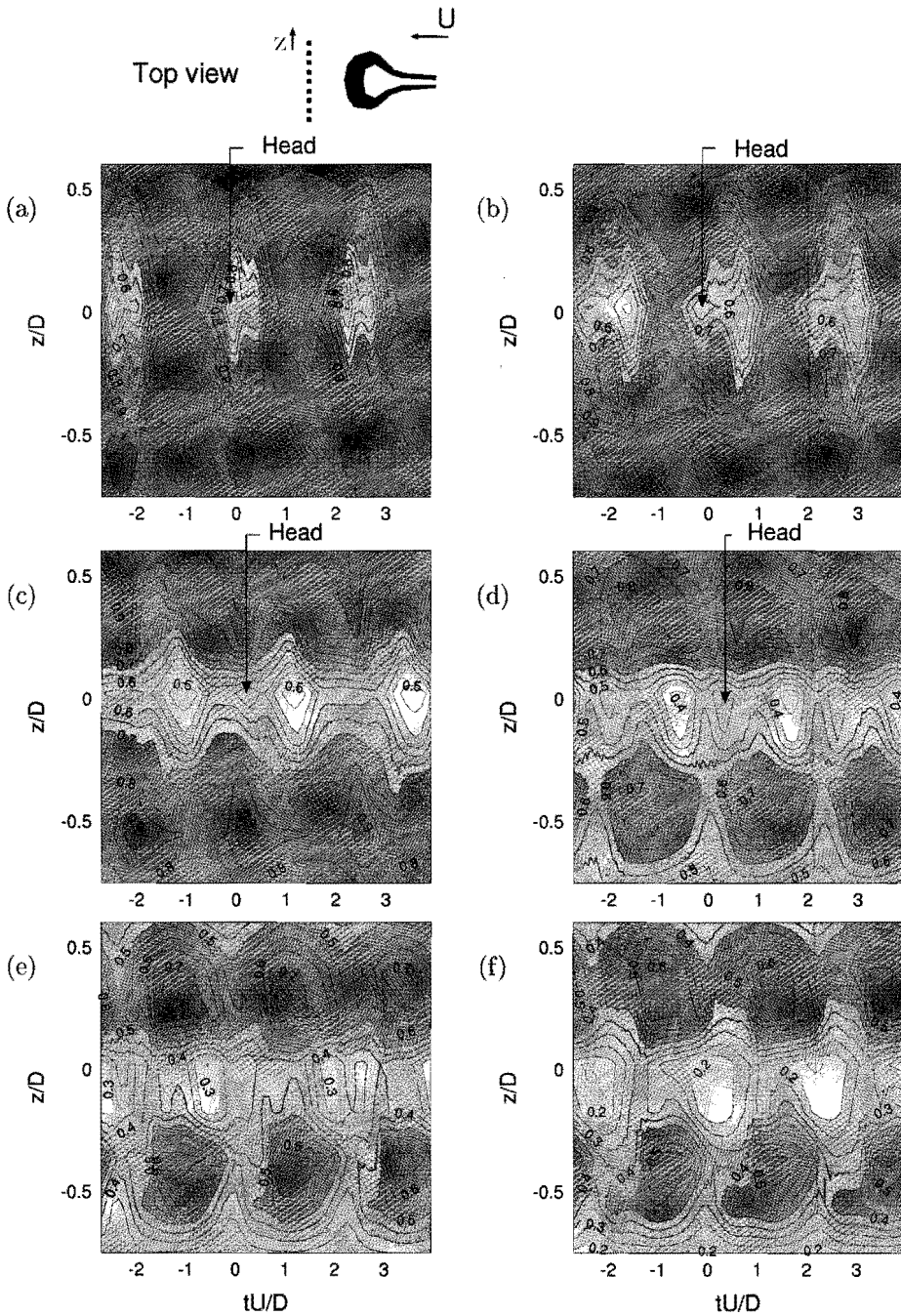


Figure 5.10: **Droplet:** The modal u -velocity in the Zt -plane for decreasing height at $x/D = 5$ for $Re_D = 1920$ ($U = 1.80$ m/s). (a) $y/D = 0.63$, (b) $y/D = 0.50$, (c) $y/D = 0.38$, (d) $y/D = 0.25$, (e) $y/D = 0.18$, (f) $y/D = 0.13$

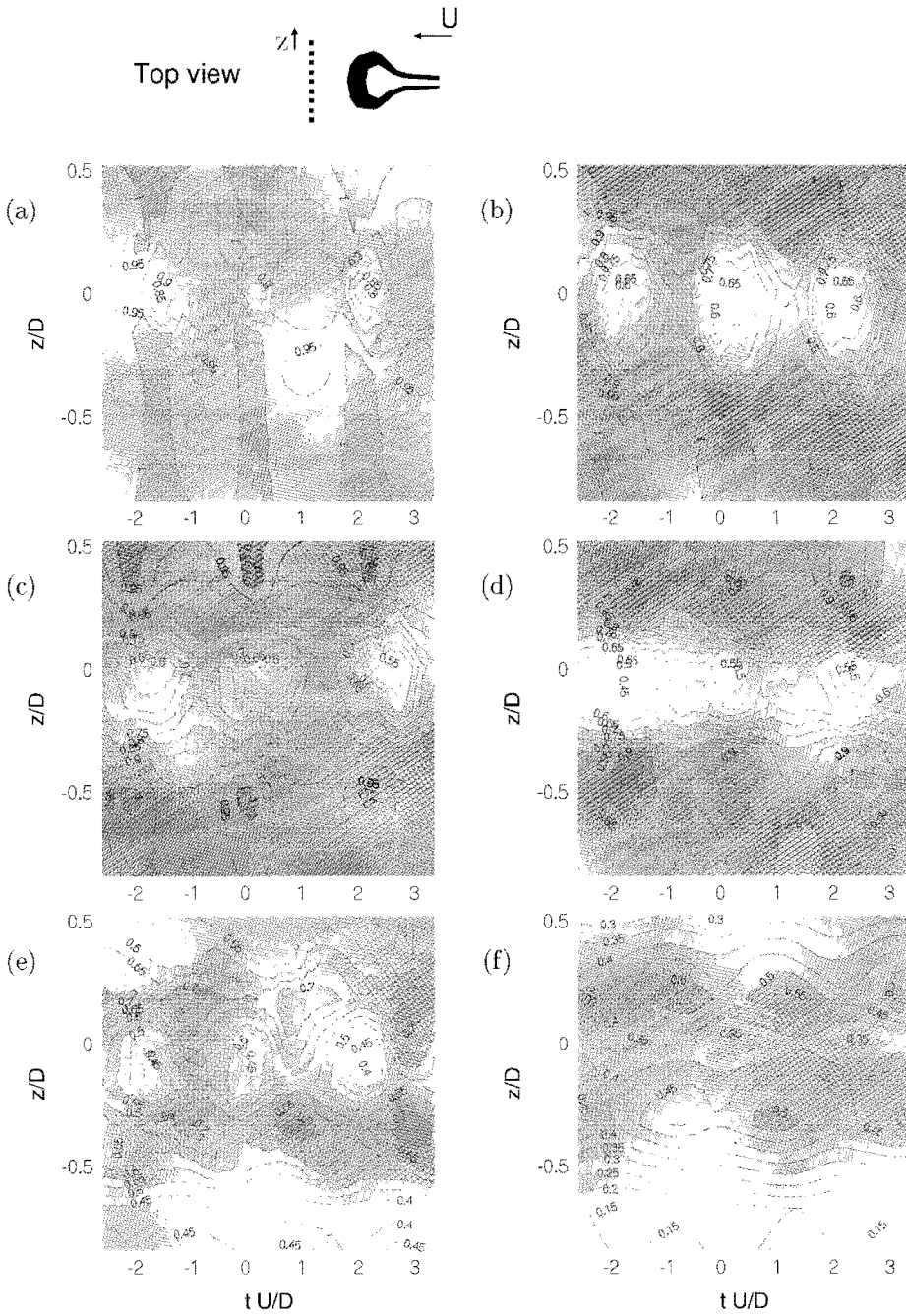


Figure 5.11: **Hemisphere (riblets)**: The modal u -velocity in the Zt -plane for decreasing height at $x/D = 5$ for $Re_D = 1730$. (a) $y/D = 0.81$, (b) $y/D = 0.63$, (c) $y/D = 0.50$, (d) $y/D = 0.38$, (e) $y/D = 0.25$, (f) $y/D = 0.13$.

low-speed region with the neck of the hairpin vortex. The neck draws the higher part of the low-speed region towards the vortex trajectory, as was shown before by the visualizations in chapter 3 (see also figure 5.8b).

- Close to the wall, a low-speed patch of fluid appears at $z = 0$. Figure 5.7 indicates that this low-speed area should not be associated directly with the head! In section 5.4.2 it was suggested that this patch is caused by several effects, among which is the effect of the quasi-spanwise vortex. This vortex pushes the legs of the previous hairpin vortex towards the wall at this location, which results in an additional upflow of low-speed fluid.

In the case of a droplet-shaped obstacle (figure 5.10), similar features can be seen as in the case of a hemisphere. However, there are also some notable differences:

- The low-speed regions that in the case of a hemisphere were present at $|z/D| > 0.4$ are now formed at about $|z/D| > 0.6$ and they are already meandering at $y/D = 0.13$, while in the case of a hemisphere significant meandering was only found for $y/D > 0.25$. The standing vortex is not present here and the 'low-speed region' in this case is just the undisturbed flow, while the high-speed patches are fully caused by the effect of the necks and the legs. Note the correspondence of the high-speed patches in these figures with figure 5.8a, where adjacent to the vortex legs regions appear that are almost entirely devoid of bubbles.
- Close to the wall, the velocities in the case of a droplet are lower than in the case of a hemisphere due to the absence of the standing vortex.
- The velocity fluctuations that are caused by the passage of the legs are larger than the corresponding fluctuations in the case of a hemisphere. This effect can be attributed to the fact that for a droplet, the legs are located in a region with a larger $\partial u/\partial y$ (see figure 5.7).
- In figures 5.10b-d, two low-speed patches appear, due to the secondary deformation of the vortex legs. This corresponds to the side view that is shown in figure 5.7.

Figure 5.11 shows the velocity contour plots for a hemisphere on a grooved wall.

- The area beneath the head has a lower velocity for the hemisphere on the grooved wall than for a hemisphere on a smooth wall, but a larger velocity than for the case of the droplet. This can be explained by a residual effect of the standing vortex as argued in section 5.3.
- Close to the wall, the distance between the legs is larger than for the case of a smooth wall and comparable to the distance found for the droplet.

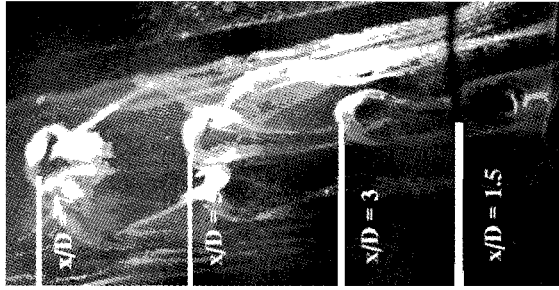


Figure 5.12: The vortex street downstream of the hemisphere (bubble wire visualization). The downstream distance is indicated.

- The patches of low-speed fluid created by the legs are less pronounced for this configuration than for the other two. At least a partial explanation is found in the assumption that, just as in the case of a hemisphere on a smooth wall, due to the effect of the standing vortex the area surrounding the vortex legs does not contain a large velocity gradient (see also figure 5.7c). The small size of the patches might be related to an effect of the riblets on the spanwise movement of the high-speed fluid that is pushed towards the wall by the necks and the legs.

5.5 The downstream evolution of the hairpin vortices

Some feeling for the downstream evolution of the hairpin vortex can be gained by the photograph presented in figure 5.12. The downstream distance is indicated to facilitate a comparison with the hot-wire measurements.

5.5.1 Cross-sections in the Yt -plane

Figure 5.13, shows the downstream evolution of the vortex induced velocity.

- Very close to the obstruction, the velocity profile is largely determined by the wake of the obstruction, as follows from the large amount of low-speed fluid present here for $y/D < 0.3$. The wake is most prominent in the absence of the standing vortex, as can be seen from figures 5.13a1 and 5.13c1.
- With increasing downstream distance, the direct effect of the vortex on the velocity field decreases and the head rises in the fluid.

Apart from these general observations, several differences are observed between the three flow configurations. The location of the head is higher for a hemisphere

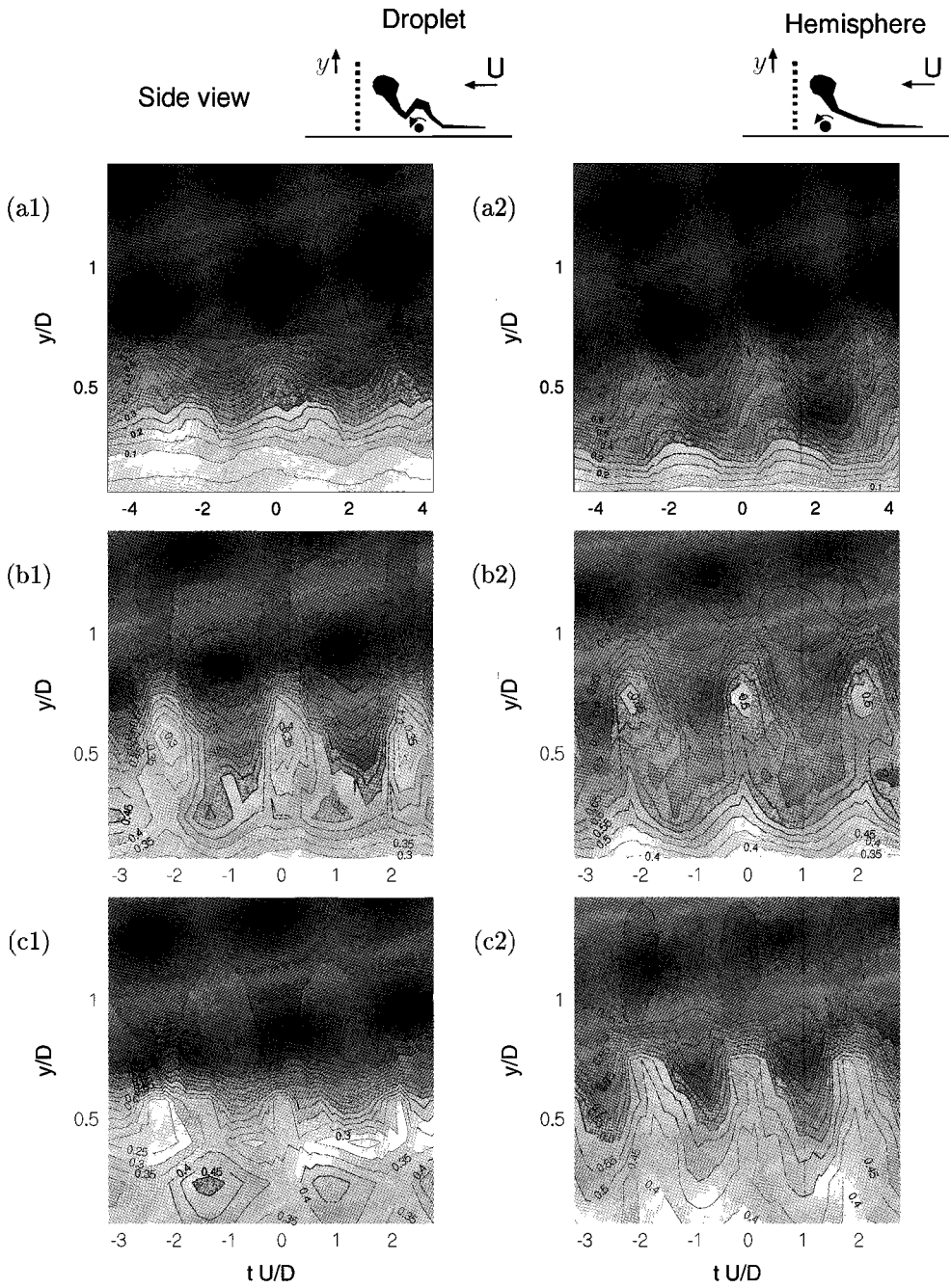


Figure 5.13: The modal u -velocity contour plots in the $z = 0$ -plane for increasing downstream distance at $Re_D = 1730$. **(a)** droplet, **(b)** hemisphere (smooth wall), **(c)** hemisphere (riblets). **(1)** $x/D = 3.75$, **(2)** $x/D = 5$, **(3)** $x/D = 6.25$, **(4)** $x/D = 7.5$.

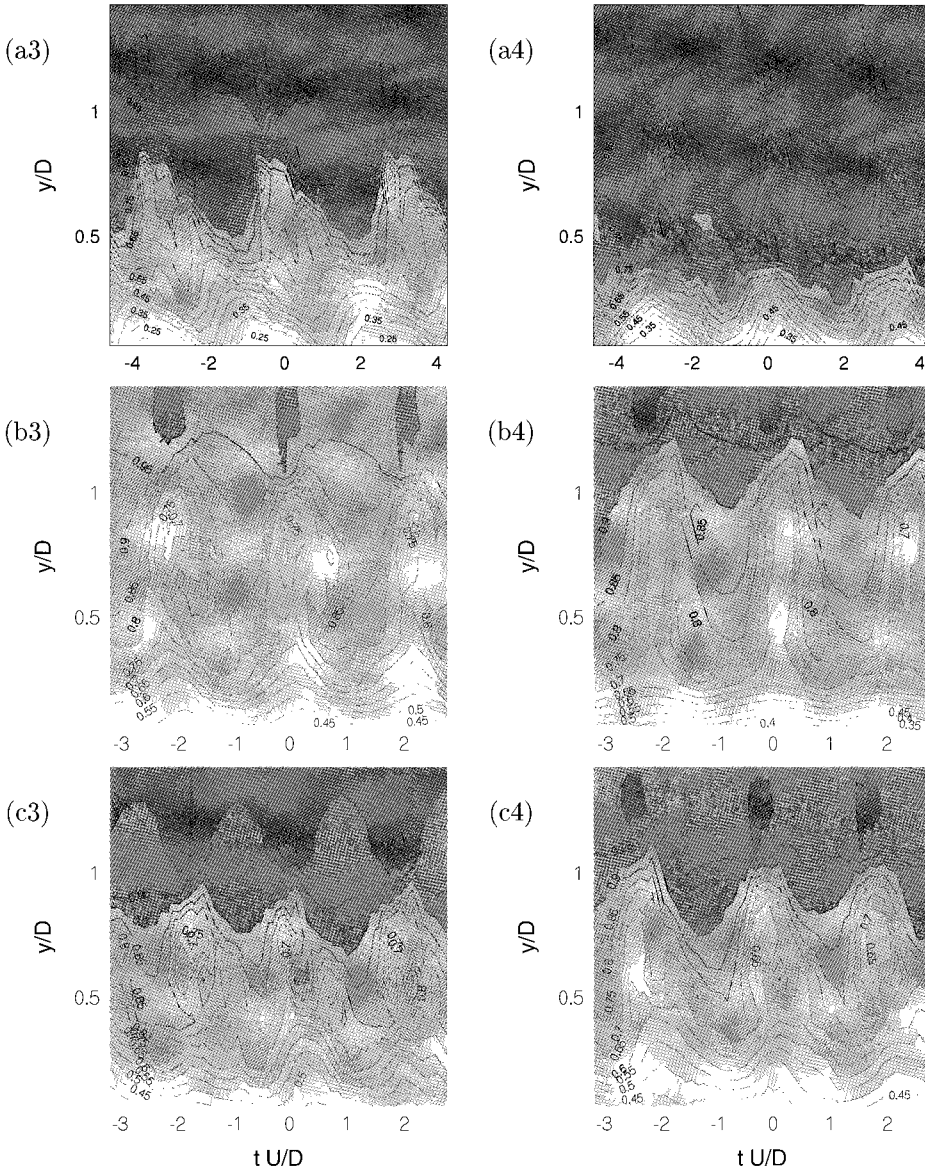
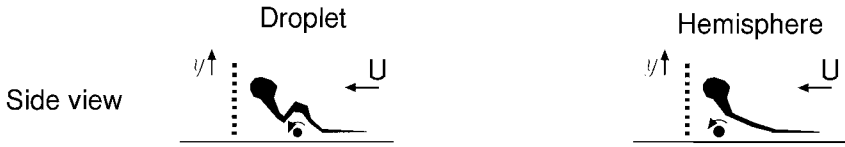


Figure 5.13: For caption see previous page

on a smooth wall, than for the other two configurations. In addition, for the droplet, the effect of the secondary deformation of the vortex legs on the u -velocity is easily recognized at $x/D = 6.25$. The same mechanism seems to distort the legs of the hairpin vortex for the case of the hemisphere on the grooved wall, where a similar patch of low-speed fluid is observed upstream of the primary hairpin head at the same distance from the obstruction. The secondary deformation is even observed at the same downstream location as for the droplet. This indicates that the mechanism that is responsible for the secondary deformation does not depend on the details of the velocity field. The secondary deformation seems to be a general mechanism, that is absent only when the fluid in the wake of the obstruction is strongly accelerated by the effect of the standing vortex.

In addition, some notable differences appear in the near-wall region. In the case of a hemisphere on a smooth wall, with increasing distance, the effect of the passing vortices on the near-wall fluid seems to decrease. At $x/D = 7.5$ the near wall region is hardly affected by the vortices passing overhead. For the other configurations significant fluctuations are still present near the wall at $x/D = 7.5$. This is especially true for the droplet. At $x/D = 7.5$ near-wall fluctuations are found that are larger than the fluctuations created by the hairpin vortex itself.

5.5.2 Cross-sections in the YZ -plane

In order to show the effect of the downstream distance not just in the $z = 0$ -plane, but also in the region adjacent to the vortex, velocity contour plots of the YZ -plane are indicated in figure 5.14. Since these measurements require a scan with the hot-wire rake, it was not possible to show the instantaneous velocity: conditionally averaged u -velocity contour plots are shown for the different configurations. In figure 5.14 the u -velocity field is shown for increasing x/D for $Re_D = 1740$ at the moment the head of a hairpin vortex passes through the plane of measurement.

The location of the head is given by the large velocity gradient³ that is found at approximately $y/D = 0.9$. From the data presented in figure 5.14 the location of this region as a function of x/D is shown separately in figure 5.15a. For the cases of the droplet and the hemisphere on a grooved surface, the location of the head is very similar, whereas for the case of a hemisphere on a smooth surface, the head is located higher.

In addition, in figure 5.14 the vortex heads show substantial weakening over the range $3.75 \leq x/D \leq 7.5$, as indicated by their decreasing ability to retard the flow. In figure 5.15b the dimensionless velocity just underneath the large gradient area is shown for the three configurations as a function of downstream

³It is caused by the fact that above the vortex centre the induced velocity is in the stream-wise direction, while beneath it the induced velocity is in the opposite direction.

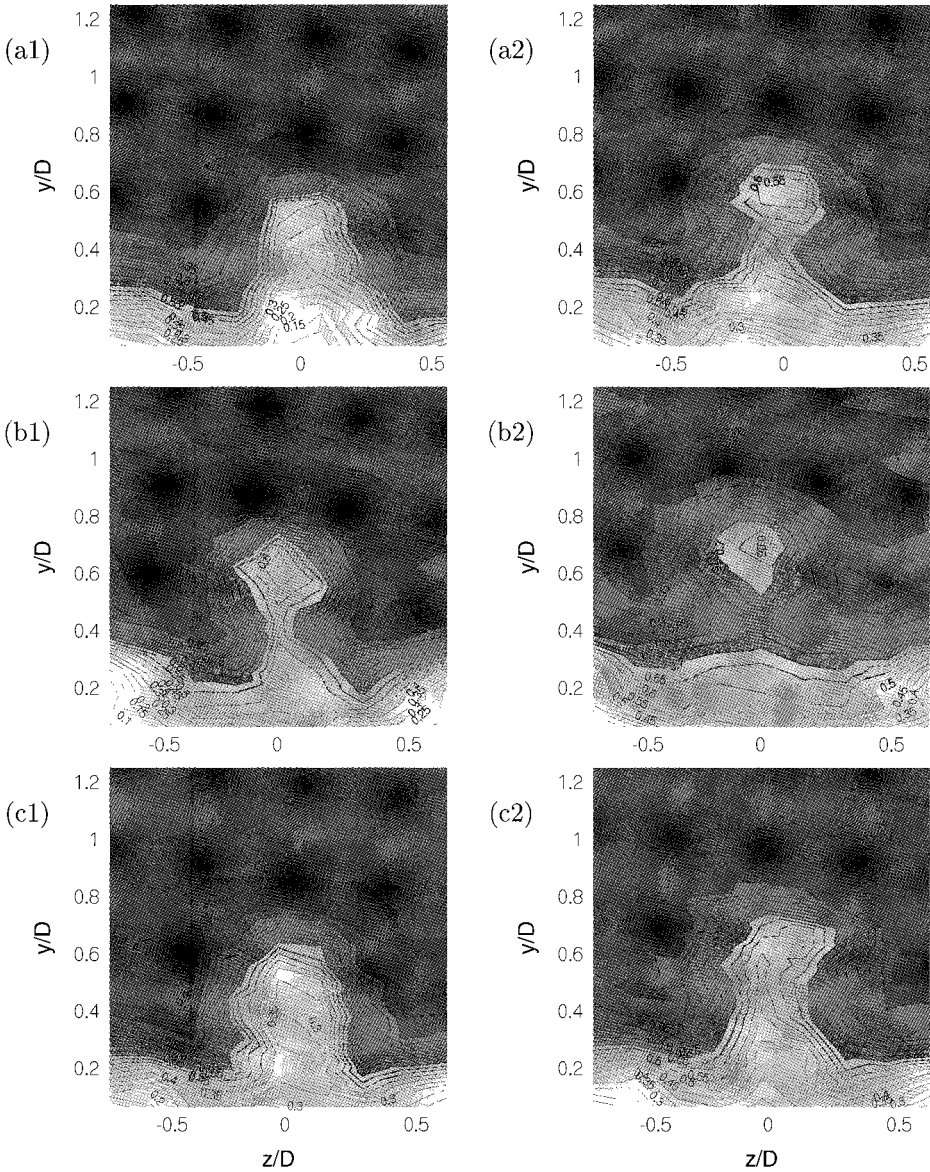
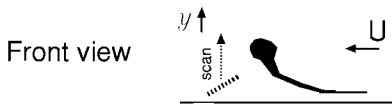


Figure 5.14: The conditionally averaged u -velocity contour plots in the YZ -plane relative to the passage of a head for increasing x/D at $tU/D = 0$, $Re_D = 1740$. **(a)** droplet, **(b)** hemisphere (smooth wall), **(c)** hemisphere (riblets). **(1)** $x/D = 3.75$, **(2)** $x/D = 5$, **(3)** $x/D = 6.25$, **(4)** $x/D = 7.5$.

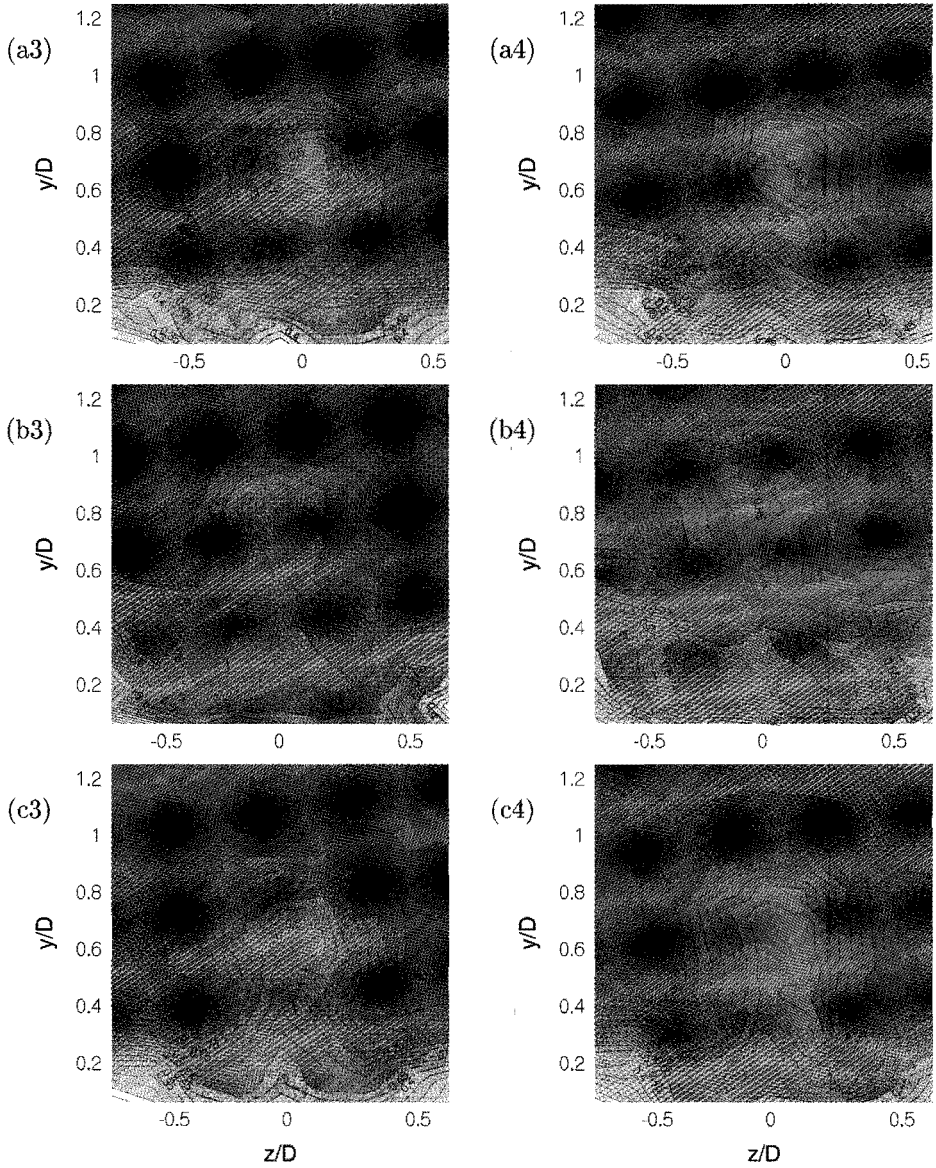
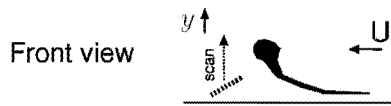


Figure 5.14: For caption see previous page

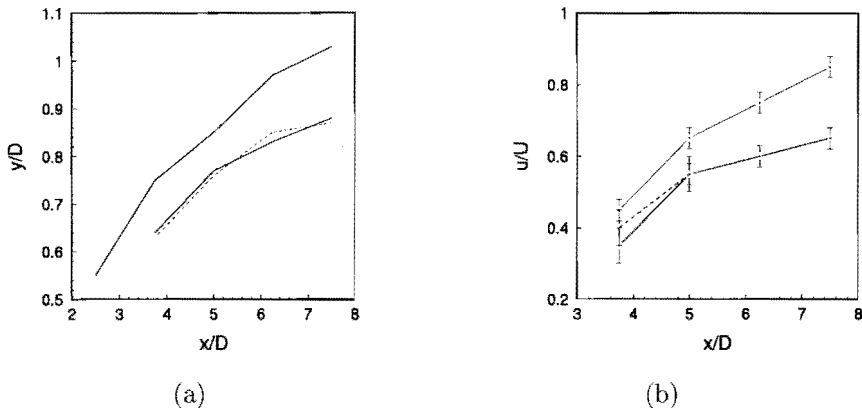


Figure 5.15: (a) The height of the head as a function of downstream distance from the obstruction. (b) The value of u/U just below the vortex head as a function of downstream distance from the obstruction. Upper line: hemisphere on smooth surface, lower line: hemisphere on grooved surface, broken line: droplet. $Re_D = 1740$

distance. This quantity is associated with the circulation of the vortex. The decay is fastest for the case of a hemisphere on a smooth plate. For the other two obstructions the decay is slower and the decay curves show similar values for both obstructions

In figure 5.16 the conditionally averaged velocity profiles are shown for a time-delay $tU/D = -0.6$, a short time (about 25% of the dimensionless shedding time) *before* the head appears. These profiles give information with respect to the effect of the vortex legs. The differences with figure 5.14 are very clear, as was to be expected since the effect of the head should not appear in these figures. The necks and the legs cause an upwelling of low-speed fluid at $z/D = 0$ (in the plane of symmetry) and a downwash of high-speed fluid at $z/D \approx 0.3$. The figures show that with increasing downstream distance, the upwelling becomes less pronounced. Notable differences show up between the different obstructions. For the case of a hemisphere on a smooth plate, only a very weak upwelling is detected, while for the two other cases the upwelling is much larger and appears over a longer streamwise distance. For all x/D , the near-wall velocity is the lowest for the droplet, but the upwelling of low-speed fluid is most pronounced for the case of the hemisphere on the grooved surface, as shown in figures 5.16a and 5.16c. The observation that for a smooth surface, the legs of the hairpin have larger effect for the droplet than for the hemisphere, corresponds to the observations in the visualizations of chapter 3. There, it was shown that for the

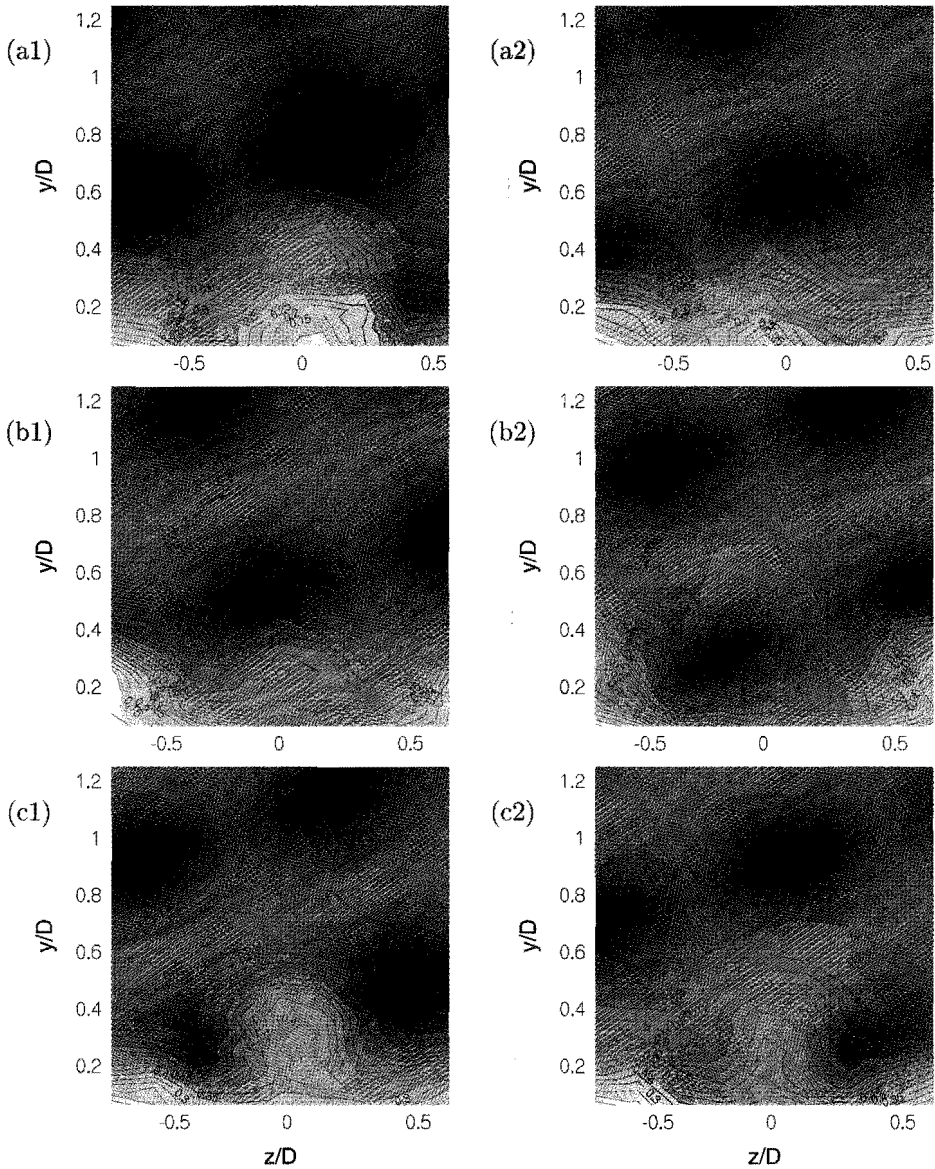
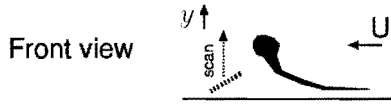


Figure 5.16: The conditionally averaged u -velocity contour plots in the YZ -plane relative to the passage of a head for increasing x/D at $tU/D = -0.6$, $Re_D = 1740$. (a) droplet, (b) hemisphere (smooth wall), (c) hemisphere (riblets). (1) $x/D = 3.75$, (2) $x/D = 5$, (3) $x/D = 6.25$, (4) $x/D = 7.5$.

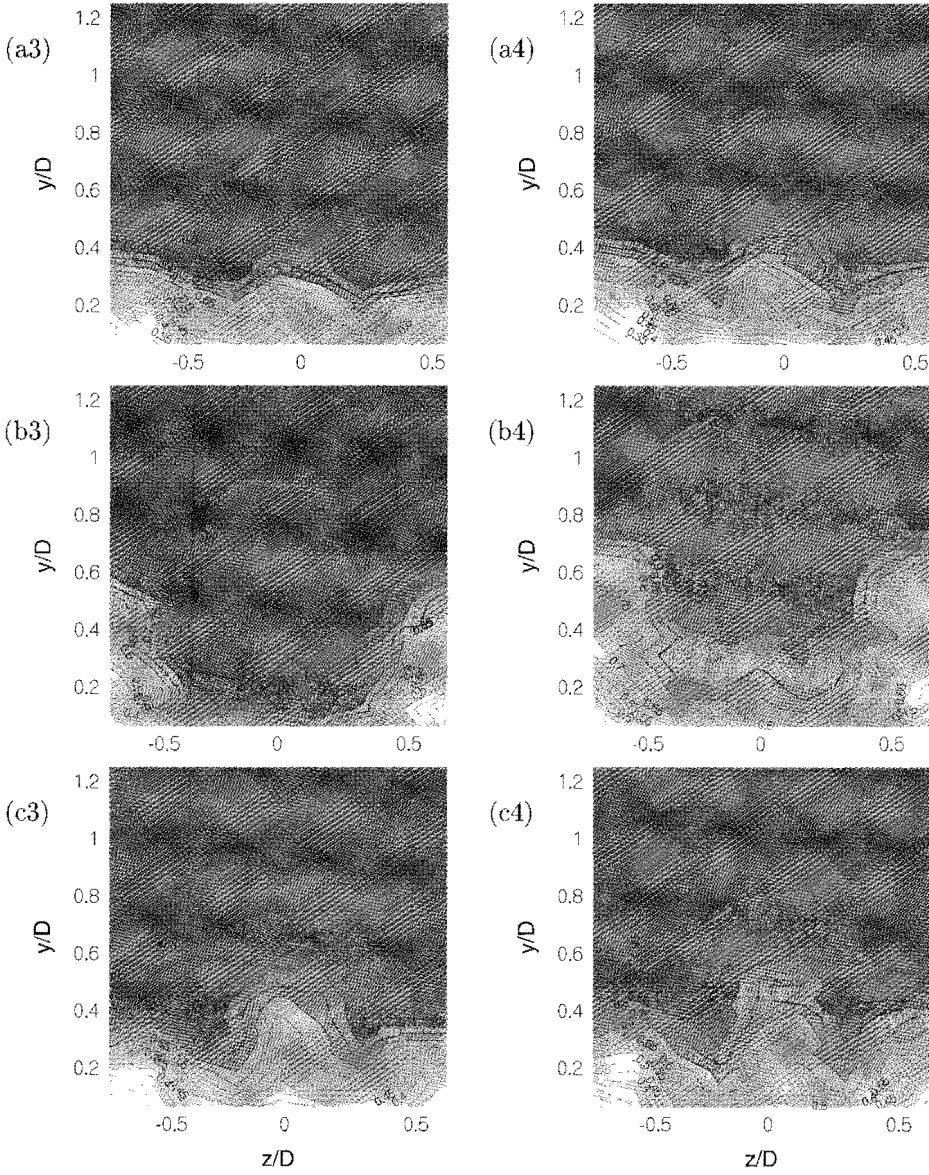
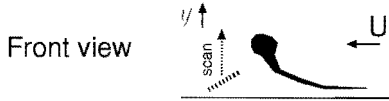


Figure 5.16: For caption see previous page

hemisphere, the near-wall fluid was hardly affected by the legs of the hairpin vortex, in contrast to the case of the droplet.

The magnitude of this upwelling cannot be related directly to the circulation of the legs, since it depends strongly on the velocity gradient in the surrounding flow. From the shape of the velocity profile at $x/D = 7.5$ it is obvious that the effect of the legs on the velocity profile in the case of a hemisphere on a smooth surface is less than for the other two cases. Probably, this is because the legs move *over* the region where a velocity gradient is found. Remember that the near-wall region over which a substantial velocity gradient exists, is located closer to the wall for the hemisphere on a smooth surface than for the other two cases.

A comparison of figure 5.14 and 5.16 shows that the passage of the head does not affect the low-speed region at $|z/D| > 0.5$ for small values of x/D , but that for $x/D \geq 5$ the top of the low-speed region shows fluctuations in the y -direction and reaches its lowest height at $tU/D = 0$ when the head passes (compare figure 5.14b2 and figure 5.16b2). This phenomenon was shown previously in figure 5.9c-d and is associated with the effect of the neck of the hairpin vortex drawing the higher part of the low-speed region towards the vortex trajectory.

5.6 The effect of the Reynolds number

5.6.1 The modal vortex

Figure 5.17 and 5.18 show the effect of increasing Reynolds number on the velocity field for the droplet and the hemisphere on the smooth surface at $x/D = 3.125$ and $x/D = 7.5$ respectively.

- For both configurations, the height of the head does not seem to depend on the Reynolds number.
- The circulation of the vortex head is approximately proportional to Re_D , which is concluded from the fact that the low-speed area just below the head has a velocity that for all Reynolds numbers is approximately the same fraction of the main flow velocity (this is not very clear in the figures presented here, but it can also be concluded from e.g. figures 5.21a2 and 5.21c2).
- Velocity fluctuations appear in the near-wall region. They grow in time initially and then decrease in amplitude again when the vortex legs do not disturb the near-wall fluid anymore (see figure 5.13). The figure shows that at $x/D = 3.125$, these fluctuations become larger for increasing Reynolds number. For the hemisphere, irrespective of the Reynolds number, at $x/D = 7.5$ the near-wall flow is hardly affected anymore. In addition, the patch of low-speed fluid underneath the head seems to disappear for increasing Reynolds numbers. For the droplet, the secondary deformation

of the legs leads to the creation of a new vortex on top of the rise in the legs. In figure 5.18a1 and 5.18b1 vortex has just been created. It seems that the Reynolds number influences both the downstream location at which this effect occurs (as will be shown in figure 5.21) and its effect on the near-wall flow.

- For $Re_D > 2200$ the hairpin vortex street becomes increasingly irregular, as indicated before in figure 5.4. Since this introduces variable interactions between the different hairpin vortices and the background velocity field, it is not possible anymore to analyse the results in terms of the dynamics of single hairpin vortices.

5.6.2 The average u -velocity profiles

To understand better the effect of the Reynolds number on the evolution of the hairpin vortex, it is illustrative to examine the effect of the Reynolds number on the average u -velocity profiles downstream of the obstructions. The result of the averaging of the flow downstream of a hemisphere on a smooth wall at $x/D = 5$ and $Re_D = 1920$ is shown in figure 5.19a. The figure shows the familiar features of the velocity field around an obstruction, such as the (average) effect of the passing vortex head, the average effect of the patches of high-speed fluid adjacent to the hairpin and the low-speed regions between $|z/D| = 0.5$ and $|z/D| = 1$ that are created by the standing vortex. These effects are schematically indicated in figure 5.19b.

Downstream of the obstruction, the average u -velocity profile has been measured in the plane $z/D = 0$ for several values of the main stream velocity U as a function of downstream distance x/D . The results are plotted in figure 5.20. In addition, for $x/D = 7.5$ the measured velocity profile without obstruction (a Blasius profile) is indicated. Since each velocity contour line consists of only 9 measurement points, the sharp angles that appear in the drawn lines are due to the limited resolution.

The average velocity profiles show the combined effects of (1) the wake of the obstruction (which might be affected by the standing vortex), (2) the average effect of the passing vortex head and neck and (3) the standing vortex that increases the near-wall velocity (together with the vortex legs). The effect of the vortex head is particularly clear for the hemisphere, where a velocity deficit can be observed at $x/D = 3.75$ and $x/D = 5$ at $y/D \approx 0.7$. For $x/D = 7.5$ the velocity induced by the vortex head is too small to be noticed on the total average. For the other two configurations, the effect of the head is obscured initially by the velocity gradient in the wake of the obstruction and gets pronounced only at larger downstream distance: it appears weakly at $x/D = 5$ and $x/D = 7.5$.

From figure 5.20 it appears that not all mechanisms involved in the evolution

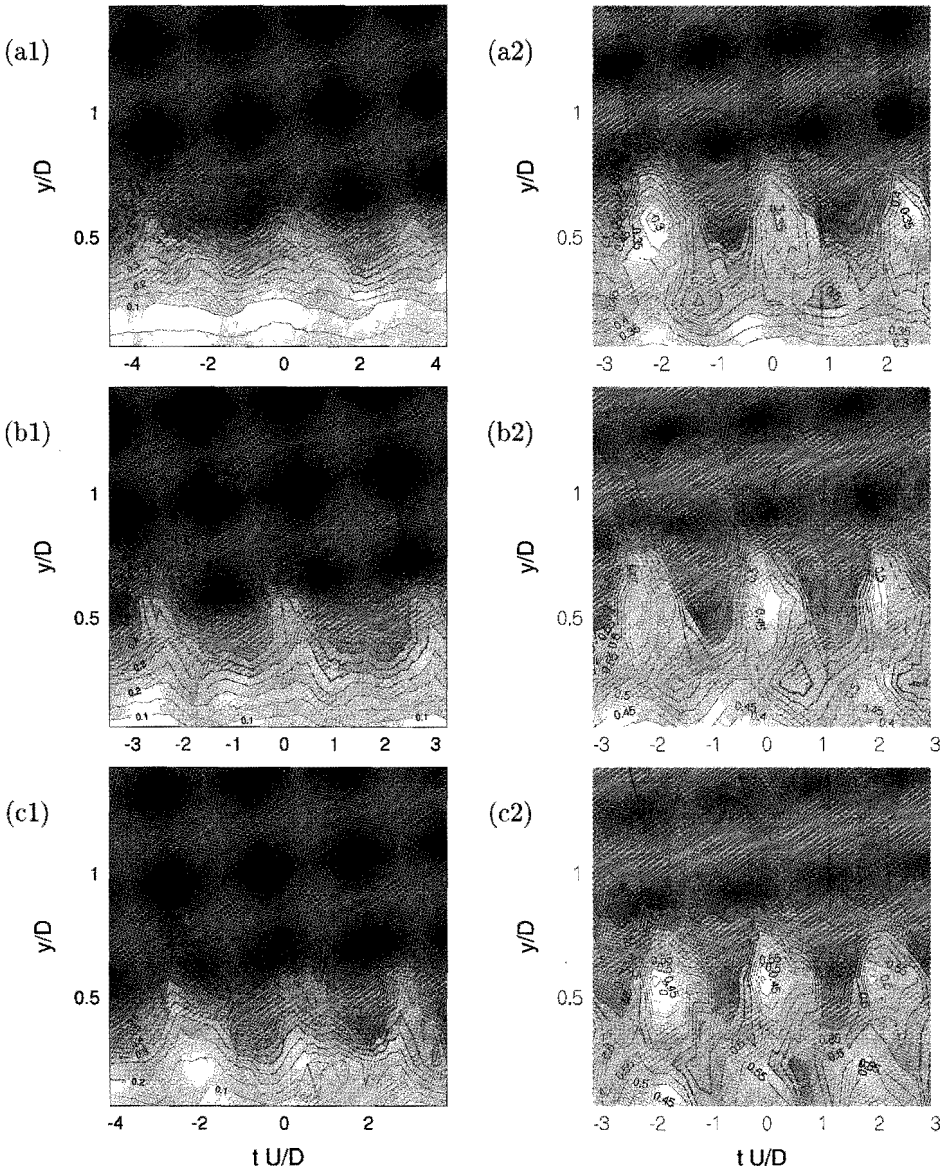
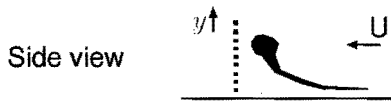


Figure 5.17: The modal u -velocity contour plots in the $z = 0$ -plane for increasing main stream velocity at $x/D = 3.125$ (smooth wall). (a) $Re_D = 1730$, (b) $Re_D = 1940$, (c) $Re_D = 2350$. (1) droplet, (2) hemisphere.

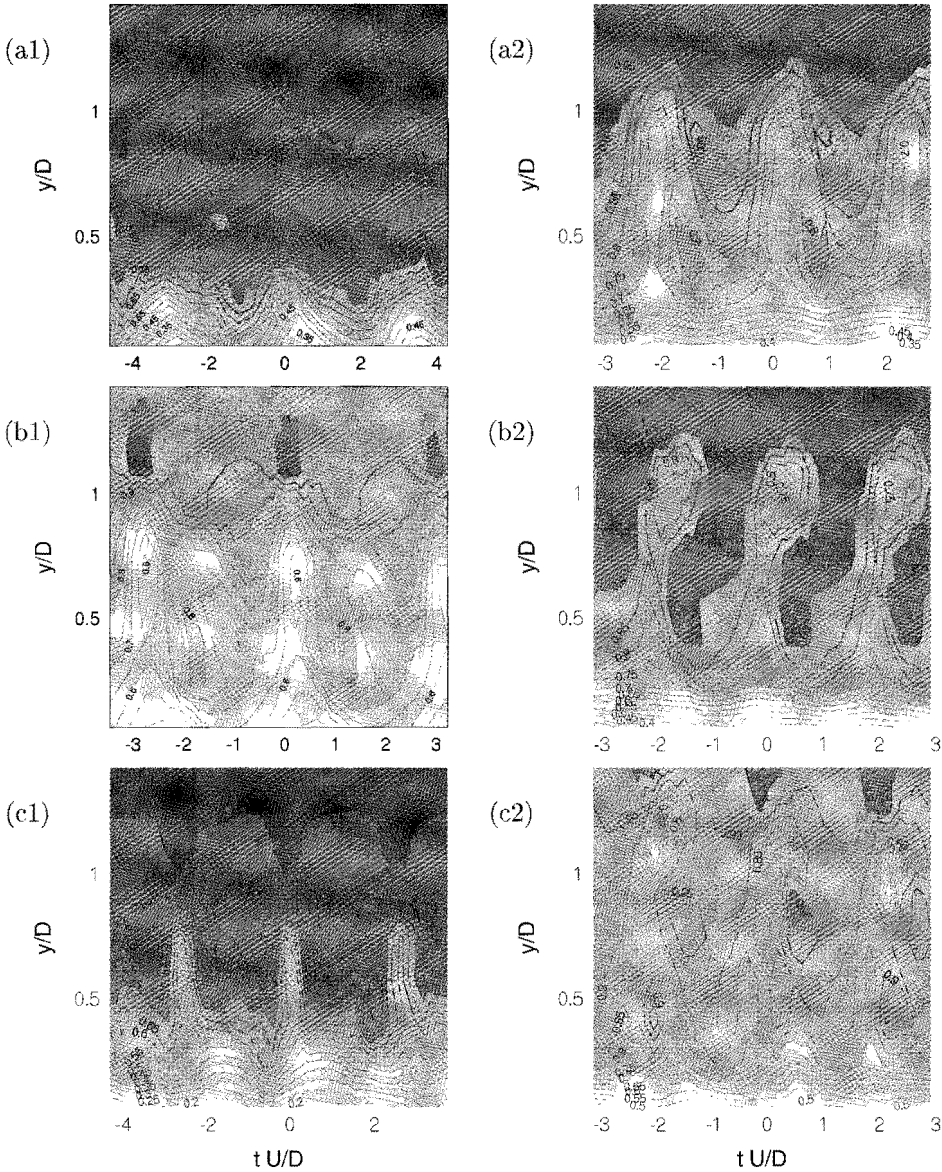
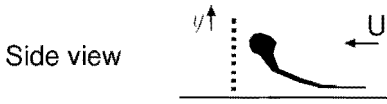


Figure 5.18: The modal u -velocity contour plots in the $z = 0$ -plane for increasing main stream velocity at $x/D = 7.5$ (smooth wall). (a) $Re_D = 1730$, (b) $Re_D = 1940$, (c) $Re_D = 2350$. (1) droplet, (2) hemisphere.

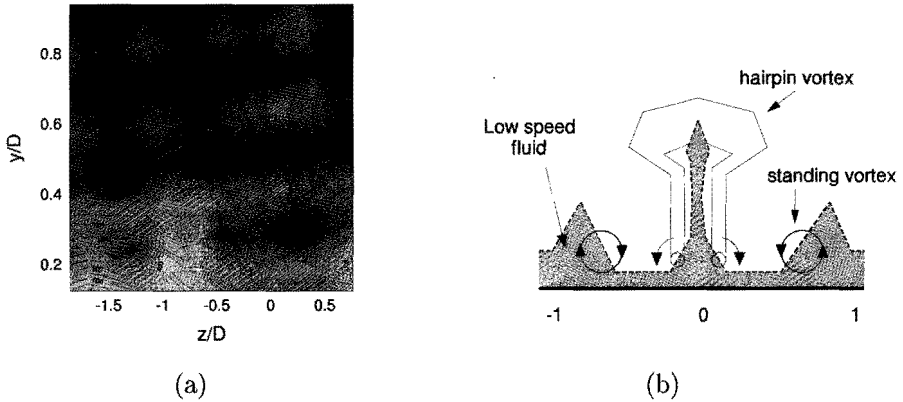


Figure 5.19: **Hemisphere (smooth wall):** (a) The averaged u -velocity contour plots in the YZ -plane at $x/D = 5$ for $Re_D = 1920$ (b) Schematic representation of the standing vortex and the hairpin vortex, indicating their effect on the low-speed near-wall fluid (the shaded area in the figure).

of a hairpin vortex scale linearly with the main stream velocity. Several effects can be observed:

- In the region $2.5 \leq x/D \leq 7.5$, the near-wall velocity increases with increasing x/D for all obstructions. Although initially the effect of the wake is dominant, at $x/D = 7.5$ for all obstructions the near-wall velocity is larger than the velocity at the same height would have been if no obstructions were present. To illustrate this observation, in figures 5.20 at $x/D = 7.5$ the Blasius profile is indicated that is measured when the obstruction is removed.
- The near-wall velocity differs for the three obstructions, and for all x/D the hemisphere on a flat surface shows the largest near-wall velocity.
- At $x/D = 2.5$ for all three configurations, the effect of the wake of the obstruction is clear. Nevertheless, the flow profile is remarkably different for the three obstructions. The droplet shows the lowest velocity for $y/D < 0.5$ (the height of the obstruction) and the hemisphere on the smooth surface shows the largest velocity. For all obstructions, the (scaled) near-wall velocity increases with increasing U . This might be due to the reduction in the size of the boundary layer thickness and possibly an increased effect of the standing vortex. For the droplet, this is also related to the increase in the shedding frequency. For the hemisphere on the grooved surface, with increasing Reynolds number the increase in the near-wall velocity is the most prominent for the three configurations but

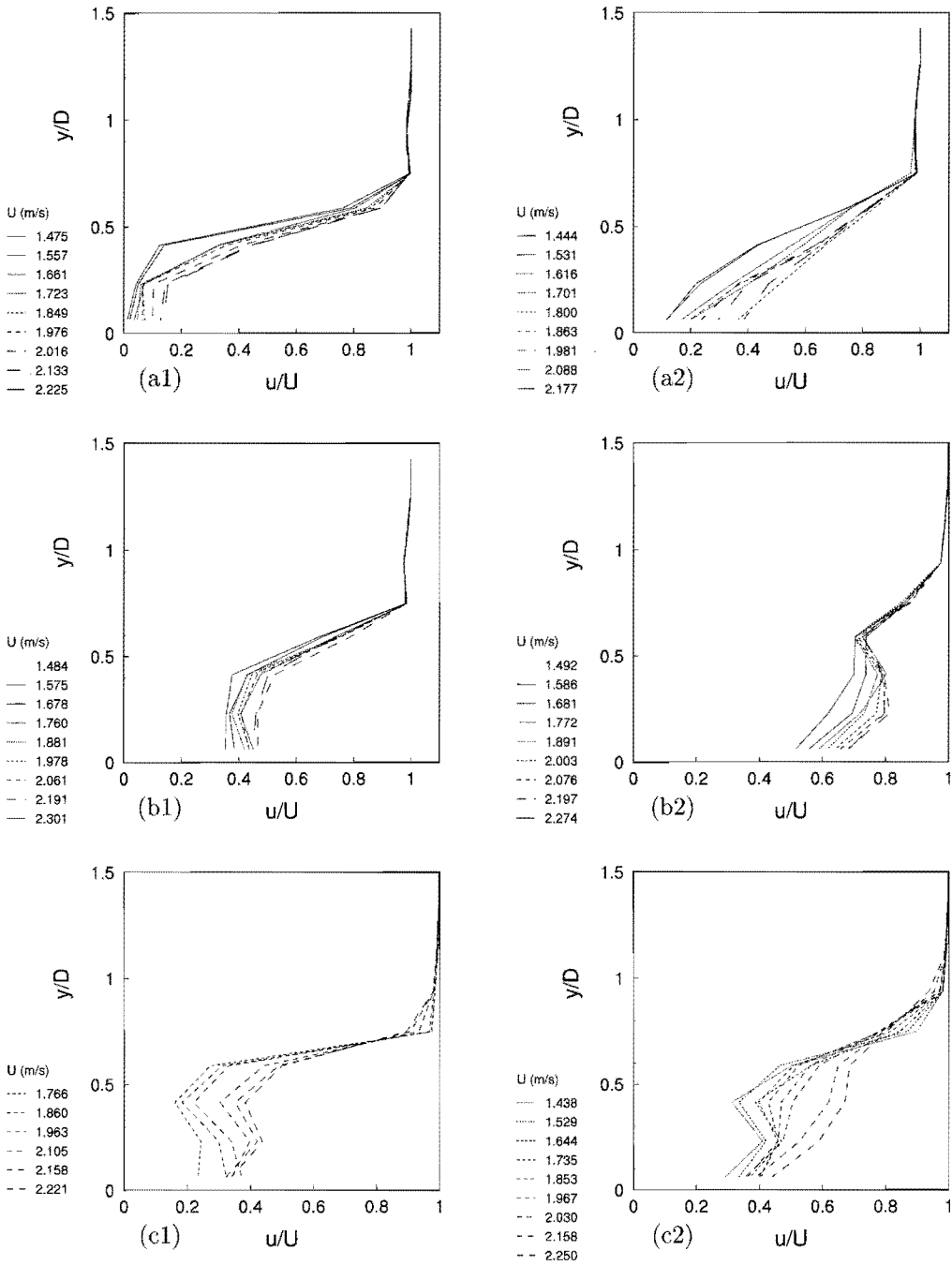


Figure 5.20: The average u -velocity profile for different U for different obstructions at increasing x/D . (a) droplet, (b) hemisphere (smooth), (c) hemisphere (riblets). (1) $x/D = 2.5$, (2) $x/D = 3.75$, (3) $x/D = 5$, (4) $x/D = 7.5$. Also the profiles without obstruction are shown (indicated by 'Blasius') at $x/D = 7.5$.

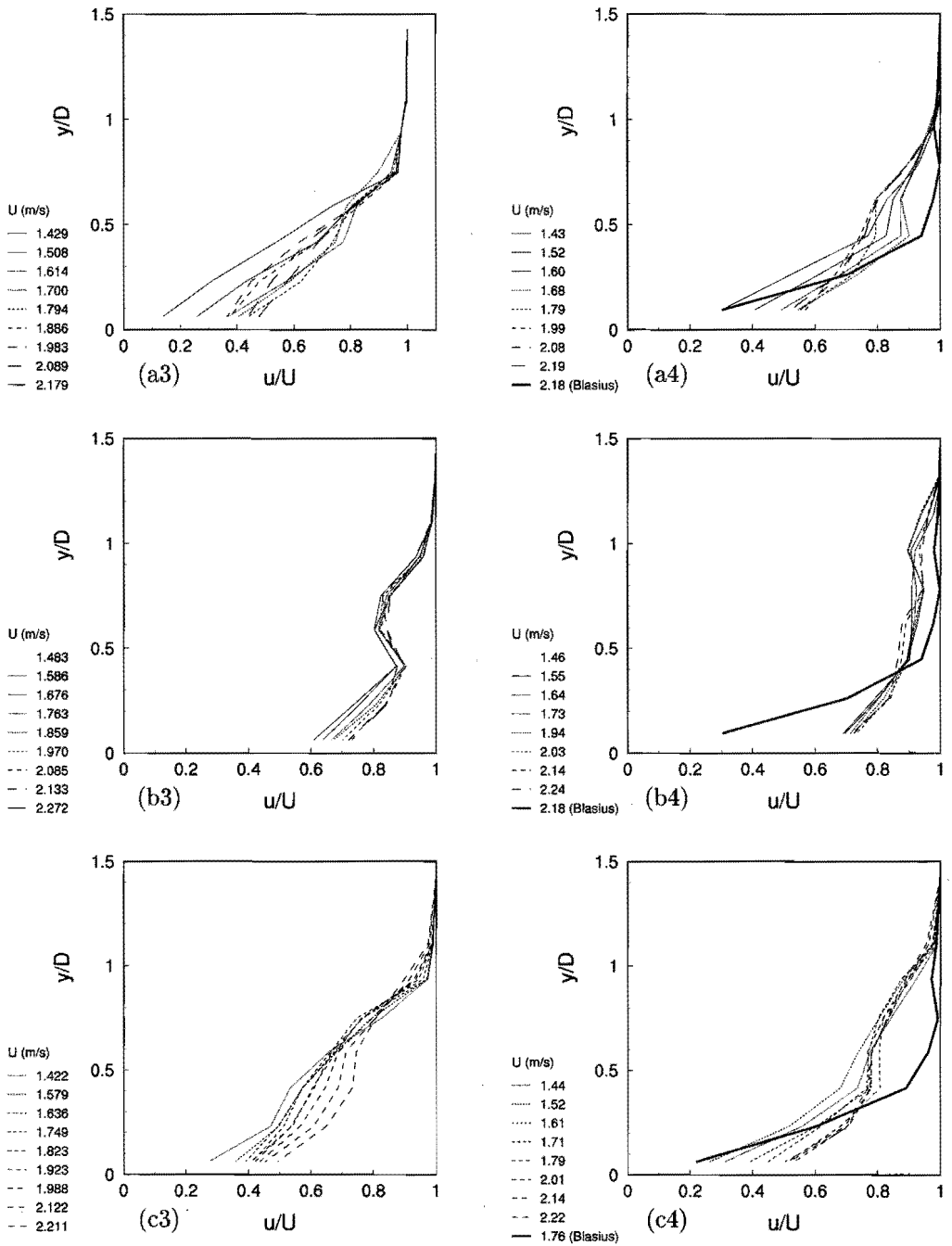


Figure 5.20: For caption see previous page

this increase should be related to the mixing effect of the additional eddies generated by the riblets, as indicated in chapter 3 (page 30).

5.7 The secondary deformation of the legs

In chapter 3, much attention is paid to the phenomenon of the secondary deformation of the hairpin vortex legs in the case of the droplet. In that chapter it is shown that such a secondary deformation does not occur for the hemisphere, as indicated in this chapter in figure 5.6. Figure 5.21.1 gives the velocity contour plots for the downstream distance at which the effect of the secondary deformation of the legs on the velocity field shows up most clearly. Three different Reynolds numbers have been used. In addition, in figure 5.21.2 the corresponding velocity contour plots for the hemisphere on a smooth surface are shown. It is clear that for the hemisphere the secondary deformation of the legs is not present, as follows from the absence of a low-speed upwelling upstream of the primary vortex head.

In the presented figures, the upwelling shows most clearly for $Re_D = 1940$. It seems that a higher Reynolds number tends to shift the location of the secondary deformation further upstream, but the increasing irregularity of the vortex shedding obscures this effect for $Re_D > 2200$.

It was argued in chapter 3 that a secondary vortex 'head' is created on top of the vortex legs when these are pushed upwards in what is called the secondary deformation of the vortex legs. Strictly spoken, the velocity contour plots show only the u -velocity and therefore one cannot distinguish a patch of low-speed fluid from a secondary vortex. Nevertheless, an indication that a secondary vortex is indeed created is given by the fact that figure 5.21b1 shows that, for $Re_D = 1940$, in the centre of the effect of the secondary deformation, a patch of fluid appears that has a velocity that is even lower than the velocity of the surrounding fluid. It should be concluded that, by this mechanism, a primary vortex is indeed able to produce a secondary vortex!

Note that the conditions of figure 5.21b1 correspond with those of figure 5.10. A comparison between these figures shows that the low-speed patch that appears in figure 5.10f at $z/D = 0$ is caused by the combined effect of the neck of the hairpin vortex and the effect of the (deformed) vortex legs of the previous vortex. At larger height these areas do not overlap anymore and two distinct patches of low-speed fluid appear in figure 5.10a-d. Particularly interesting is the fact that the upstream low-speed patch in figures 5.10b and 5.10c (that should be associated with the upwelling and not with the primary vortex) is the largest of the two.

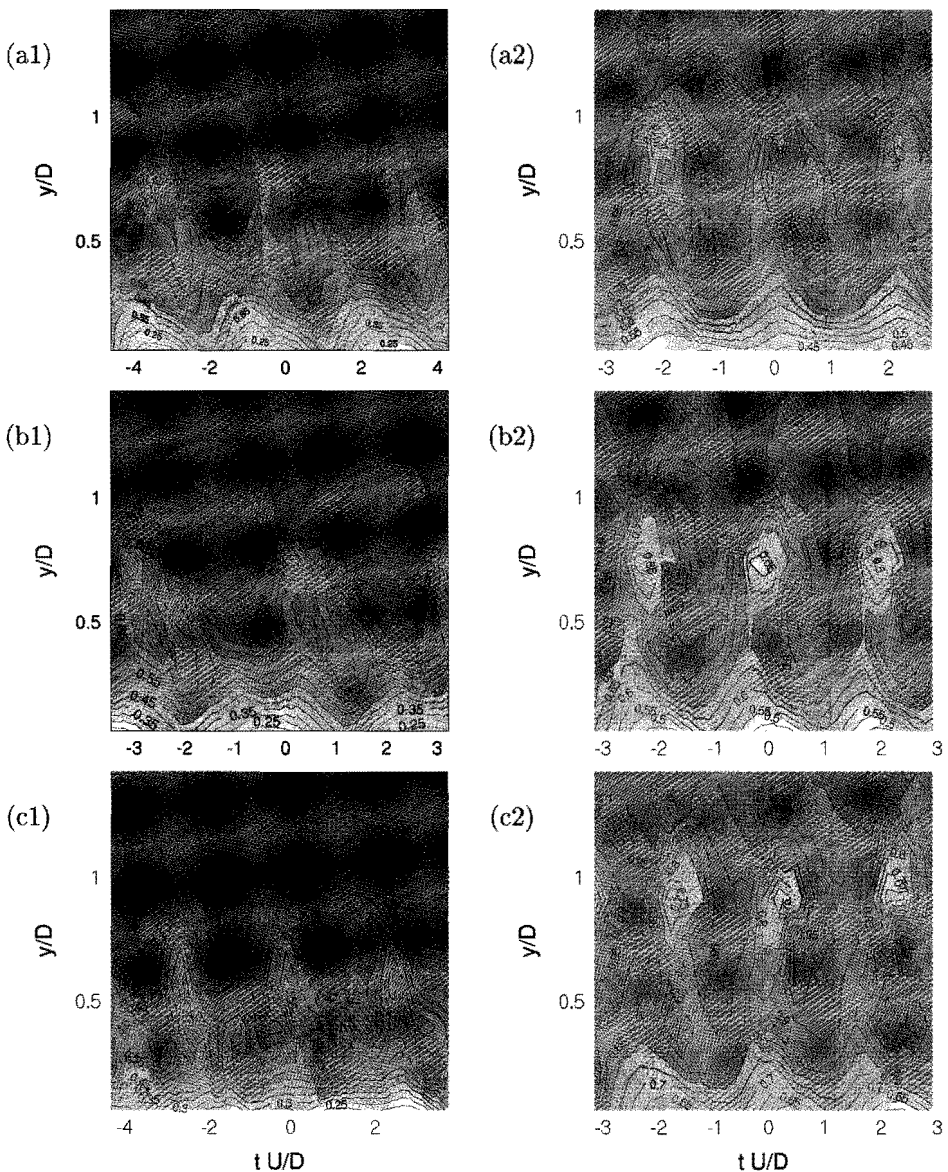
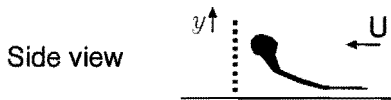


Figure 5.21: The modal u -velocity contour plots in the $z = 0$ -plane for increasing Reynolds number at the location at which the upwelling in the case of the droplet shows most clearly. (1) droplet, (2) hemisphere. (a) $Re_D = 1730$, $x/D = 6.25$, (b) $Re_D = 1940$, $x/D = 5$, (c) $Re_D = 2350$, $x/D = 6.25$.

5.8 Discussion

The effect of the standing vortex The measurements show that many similarities exist for the cases of a droplet and a hemisphere on a grooved surface, in contrast to the hemisphere on a smooth surface. In particular, the first two configurations tend to have a lower near-wall velocity, as demonstrated by the shape of the velocity profiles (figure 5.20).

Figure 5.5 shows that the presence of the riblets weakens the standing vortex considerably. It is suggested here that the differences in the u -velocity contour plots between the hemisphere on a smooth surface and the other two configurations are mainly caused by the effect of the standing vortex. Although the standing vortex is seriously weakened by the riblets, it is not extinguished entirely, as shown in the photographs in chapter 3 (page 33). This is confirmed by the fact that the vortex shedding frequency is hardly affected by the presence of the riblets: obviously the standing vortex is still able to destabilize the wake of the hemisphere even in the presence of the riblets. In addition, figure 5.14 shows that the near-wall velocity is larger for the hemisphere on the grooved surface than for the droplet.

The presence of the standing vortex delays the mechanism that is responsible for the creation of the secondary deformation of the vortex legs. This secondary deformation appears for the droplet on a smooth surface and for the hemisphere on a grooved surface, but not for the hemisphere on a smooth surface, where the effect of the standing vortex is strongest.

The effect of the obstruction The type of obstruction seems to have two kinds of influence on the evolution of the hairpin vortex: (a) it produces a wake area that affects the shape of the vortex that has to move through this wake area (see chapter 3, page 38) and (b) a standing vortex might be created at the upstream side of the obstruction and, if this is the case, the wake of the obstruction might be strongly affected by it, which affects the further evolution of the vortex. However, the exact shape of the obstruction is not very important: for both the droplet on a smooth wall and the hemisphere on a grooved wall, a similar secondary deformation of the vortex legs is found at approximately the same distance downstream of the obstruction. In addition, the rise of the hairpin vortex head and the decay of the hairpin vortex are similar for these two obstructions, while they are different for the hemisphere on a smooth wall. This means that as long as the effect of the standing vortex is not very strong, a similar evolution of the hairpin vortices (at least with respect to the effects mentioned above) should be expected for the different obstructions.

Nevertheless, the strong effect of the standing vortex on the evolution of the hairpin vortex indicates that one should be careful with generalizing the results of vortex shedding behind a solid obstruction to the evolution of hairpin vortices in a turbulent boundary layer flow. In the measurements presented here, always some effect of the wake of the obstruction is present that affects the initial

development of the hairpin vortex. It is not clear to what extent the presence of the wake affects the further evolution of the hairpin vortices.

The velocity profile For $x/D < 2.5$ for all obstructions the velocity profile is strongly determined by the effect of the wake of the obstruction. For the hemisphere, the effect of the wake is counteracted by the effect of the standing vortex, that enlarges the near-wall velocity. However, even if the standing vortex is not present, it is still obvious (figure 5.20a4) that at large x/D the velocity near the wall ($y/D < 0.2$) is larger than for the undisturbed u -profile. This effect is caused by the necks and the legs, that draw up low-speed fluid from the wall and replace it by high-speed fluid. It is to be expected that the legs have a strong effect because they operate directly in a region that has a large $\partial u/\partial y$ and therefore their mixing effect is strong.

The effects of the legs and the standing vortex result in a streamwise increase in the u -velocity. Figure 5.16 indicates that the increase of the u -velocity decreases strongly with downstream distance. Initially, for the case of a hemisphere on a smooth wall, $\partial u/\partial x$ is larger than for the other two cases, but the region over which this gradient is substantial is also shorter than for the other two cases.

Vortex stretching It was stated above that downstream of the obstruction a region exists in which $\partial u/\partial x > 0$. This stretches the legs in the region close behind the obstruction. In addition, to a lesser extent, the vorticity of the legs is increased by tilting. The vortex head is simply convected along and does not undergo the same stretching and tilting processes as the lower parts. Therefore, it should not be expected that a hairpin vortex has a constant vorticity distribution all along its length: rather, it should be expected that the vortex legs have a much smaller radius than the vortex head and that their vorticity is correspondingly more concentrated.

The rise of the vortex head Figure 5.15a shows that, for a hemisphere on a smooth wall, the head of a hairpin is located higher in the flow than for the other two configurations. The vortex head does not rise on its own account. The simulations of Hon & Walker (see chapter 2) indicate that the rise of the head should be attributed to the effect of the legs. In our case, it can be assumed that the rise of the head is caused by (1) its own legs, (2) the legs of the previous vortex and (3) the quasi-spanwise vortex (see chapter 3). For a hemisphere, the quasi-spanwise vortex is located approximately underneath the hairpin vortex head, whereas for a droplet it is upstream of the head. This means that for the hemisphere the height of the head is hardly affected by the quasi-spanwise vortex, while for the droplet the head is drawn downwards. This might explain the difference in the location of the vortex head for the different configurations.

Streamwise vortices In the literature, hairpin vortices have been called the 'building blocks of turbulence'. However, in this chapter it has been shown that in our case the standing vortex has a considerable influence upon the near-wall velocity. It might well be that the low-speed streaks in turbulent flow do not only create hairpin vortices, but also long streamwise vortices in a similar way as the standing vortex was created here. Although counter-rotating vortex pairs have been observed in turbulent flow (Smith & Schwartz, 1983), the presence of single streamwise vortices is almost universally claimed from experimental work as well as from numerical simulations (e.g. Robinson, 1991). It has been shown here how easy it is to generate a standing vortex. Hence, it is most likely incorrect to see each streamwise vortex simply as belonging to a pair of legs of a hairpin vortex or as an 'individual leg' that was somehow shed from a hairpin vortex. It is more likely that several different mechanisms are responsible for the mixing in turbulent flow, among which are hairpin-like three-dimensional vortices and streamwise vortices. Of course, both 'hairpin vortex' and 'streamwise vortex' are idealizations, because a streamwise vortex is bent and twisted by the surrounding flow, while the hairpin vortex is generated from an asymmetric patch of low-speed fluid on which individual turbulent eddies are impinging in an asymmetric way.

Drag reduction by riblets Much is known about the drag reducing properties of riblets. In our experiments the presence of riblets weakens the standing vortex. In this way, the riblets in our experiment reduce the average near-wall velocity, and therefore the wall shear stress, in the region downstream of the obstruction. It might be that a similar process operates in a turbulent flow. In addition, it is interesting to see that the riblets seem to reduce the spanwise extent of the high-speed patches adjacent to the vortex legs, as indicated by a comparison of figure 5.9f and figure 5.11f. These patches are created by the necks and the legs of the vortex. For both the droplet and the hemisphere on a smooth wall, the spanwise extent of the high-speed patches is of the order of the diameter of the obstacle, while for the hemisphere on a grooved surface it is clearly less.

Although the riblets decrease the extent of the high-speed patches, it is not possible to relate this phenomenon directly to drag reduction, since the presence of the riblets also increases the surface of the wall underneath these high-speed areas. Nevertheless, this mechanism might give an indication as to why in turbulent flow the presence of riblets leads to drag reduction.

Chapter 6

Biot-Savart approximation

6.1 Introduction

The u -velocity fields shown in chapter 5 can be thought of as due to (1) the undisturbed background u -profile on which the vortex is imposed, (2) the u -velocity deviations that are imposed by the vortex itself and its mirror-image and (3) the viscous-inviscid interaction in which the vortex periodically deforms the background velocity profile. If the velocity gradients in the background velocity profile are small, the third effect is also small and the figures just show the sum of the first two velocities. This allows a mathematical reconstruction of the experimentally determined u -contour plots by a Biot-Savart calculation in which the velocity field around a vortex is determined.

In chapter 3 the visualizations showed the shape of the hairpin vortices, in chapter 5 the u -velocity field was shown. Calculating the velocity field around a vortex shape links the results of the visualizations and the hot-wire measurements together, provides an estimate of the circulation of the vortex and separates the vortex-induced velocity field from the indirect effects of the vortex.

An additional reason for this analysis is the general tendency among researchers in numerical simulations to model the effect of a hairpin vortex on the near-wall flow by considering the head and the legs in isolation as simple spanwise or streamwise vortices. For the head such calculations have been performed by Doligalski & Walker (1984); for the legs by Ersoy & Walker (1985). In order to evaluate the significance of these results for experimental observations of the effect of the hairpin vortex on the near-wall fluid, it might be worthwhile to have some idea of the effect of the shape of the vortex on the velocity field. It will be shown that this is quite substantial.

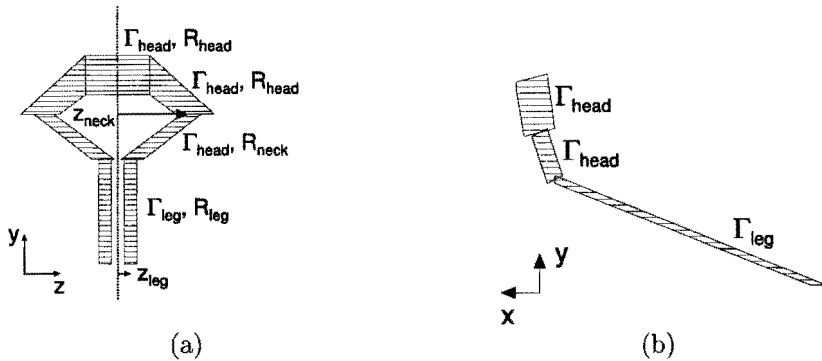


Figure 6.1: The model used for the vortex shape. The broken line in the YZ -plane indicates the plane of symmetry in which the u -velocity is calculated.

6.2 The model

The shape of the vortex is approximated with 4 vortex-tube segments, as indicated in figure 6.1. These segments have a finite core-radius, over which the vorticity is non-zero. To each segment a value for the circulation is attributed, resulting in a distribution of the circulation over the vortex that is piecewise constant. For each segment, the induced velocity can then be found from the Biot-Savart formula for a straight vortex-line segment (extending from a to b):

$$\begin{aligned}
 u_\phi &= -\frac{\Gamma r}{4\pi} \int_a^b \frac{dz}{(r^2 + z^2)^{3/2}} \\
 &= \frac{\Gamma}{4\pi r} \left(\frac{b}{(r^2 + b^2)^{1/2}} - \frac{a}{(r^2 + a^2)^{1/2}} \right)
 \end{aligned} \tag{6.1}$$

where Γ is the circulation integrated over a cross-section of the corresponding vortex tube, z is the distance along the tube and r is the distance to the centre of the tube, in the direction perpendicular to z .

A short program was written in Fortran, determining the u - and v -velocity fields that were calculated in the plane of symmetry of a symmetrical vortical shape. In this program, the angles between the vortex segments can be varied to allow for a flexible determination of the vortex shape. For the vorticity within the tube, a homogeneous distribution is used. This implies that whenever $r < R_{core}$, the value of Γ should be multiplied with r^2/R_{core}^2 . However, since the velocities were determined in the plane of symmetry, this was only relevant in the cross-section of this plane with the head of the vortex.

It was argued before (chapter 2, page 22) that there are no theoretical argu-

ments that require a constant value for the circulation along the vortex¹. There are strong experimental indications that the circulation in the head of the vortex is larger than the circulation in the legs. This might be explained by the distribution of the circulation over the separated shear layer downstream of the obstruction (see chapter 2) or by assuming that mutual cancellation in the legs (who have opposite values of ω_x) annihilates part of the vorticity in the legs (Acarlar & Smith, 1987). In order to model this effect, in our model the vortex line segments constituting the hairpin vortex do not all have the same value for the circulation².

To the velocity field obtained in this way, an experimentally obtained background u -velocity profile is added, to be able to compare the result of the Biot-Savart calculations with the experimental results presented in chapter 5.

6.3 Results

6.3.1 Introduction: obtaining a vortex

The first step in the analysis presented here is to model the shape and the circulation of the vortex. The visualizations provide the instantaneous shape of the vortex, that extends over a certain streamwise distance. It is assumed that this shape remains approximately constant during the time in which the vortex is advected past the location of measurement. The parameters for the computation are chosen in such a way as to approximate this shape and then the u -velocity is calculated in the plane of symmetry, using some value for the circulation. This value is varied until the experimentally obtained u -velocity field at this location is sufficiently well reproduced. In reproducing the velocity field, the emphasis lies on the part of the vortex that is not close to the wall (the vortex head and necks), because in the near-wall region the interaction between the hairpin vortex and the local shear becomes dominant over the Biot-Savart induced velocity of the hairpin vortex.

After some trial and error it was found that the best results were obtained when the circulation in the head and the necks was taken to have approximately the same value $\Gamma/UD = -0.26$, while a much smaller value was used for the circulation of the legs ($\Gamma/UD = -0.024$). For the legs, the core radius R is taken to be smaller than half the distance between the legs ($R_{leg}/D < 0.09$), while the

¹Recall that a hairpin vortex is not a vortex tube: (1) mutual cancellation of vorticity in the legs can lead to a lower circulation in the legs than in the head (2) the circulation can be expected to be lower in the parts of the vortex that are shed close to the wall where u is small.

²This introduces a theoretical weakness into the model, since now vortex lines end at various locations along the hairpin vortex, where in a real flow they fan out from the surface of the hairpin vortex in such a way as to reproduce the flat plate laminar boundary layer velocity profile at sufficient distance from the hairpin vortex. Notwithstanding this theoretical weakness, the present model was the best we could construct with simple means and as the results correspond fairly well to the measured velocity field we decided to adopt this model.

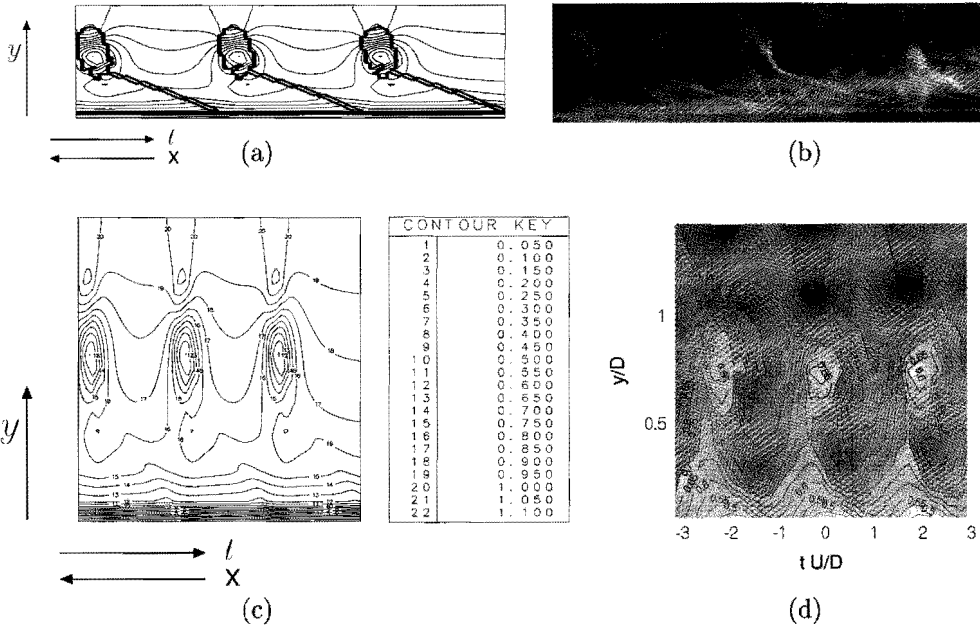


Figure 6.2: **(a)** Side view of the vortex shape used for the calculation (the vortex contour is indicated by the thick line in the figure), imposed on the calculated velocity field. **(b)** Photograph of a hairpin vortex (side view, $2 < x/D < 7$, $Re_D = 1825$), **(c)** The u -velocity field calculated from the vortex shape shown in (a), **(d)** the corresponding experimental u -velocity field at $x/D = 5$, $Re_D = 1920$ (from chapter 5).

radius in the vortex head is taken to be much larger ($R_{head}/D = 0.2$). These values are used in figure 6.2.

The sensitivity of the result to the parameters varies. The width of the vortex neck did not have much influence: for a larger z_{neck} , the increased overall distance from the neck to the plane of symmetry is compensated for by the increased length of the corresponding vortex segments. Due to their weakness, the legs had hardly any effect at all, and a moderate decrease in z_{leg} did not change the picture significantly. A reduction in the core radius of the head increased the number of velocity contours close to the head. When the core radius of the head is decreased while the circulation is decreased too, the patch of low-speed fluid that is located below the head in figure 6.2c retains the same value for u but is shifted towards the head.

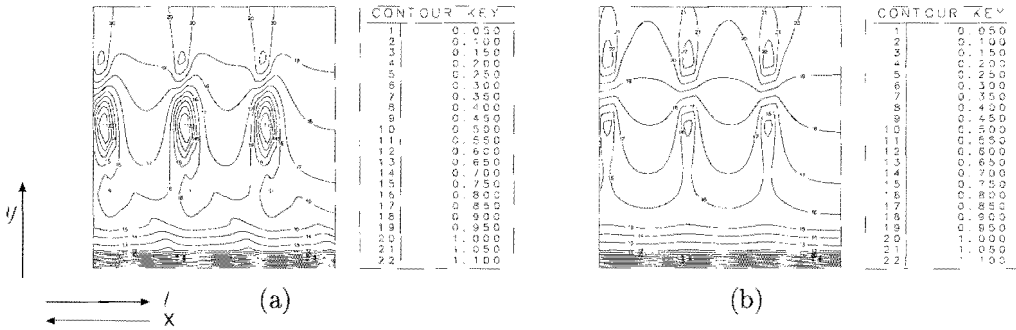


Figure 6.3: The effect of the neck on the experimentally obtained u -velocity field (a) The u -velocity field due to the entire vortex (b) the u -velocity field due to the head only.

6.3.2 The effect of the neck

It was mentioned in chapter 5 that the presence of the neck causes the asymmetry in the vortex-induced velocity above and below the head. The neck has a substantial influence on the velocity field, as can be observed from a comparison of figure 6.3a and 6.3b. Since the neck affects the velocity underneath the vortex head, it should be included in calculations of viscous upwelling due to the vortex-induced near-wall pressure, as performed by Doligalski & Walker (1984). However, it should be recalled that in our experiments, the shape of the vortex is such that the angle of the neck with the wall is quite large and then the effect of the neck is particularly strong. The shape of the vortex depends on the velocity profile. For a different velocity profile (e.g. when the vortex is entirely embedded in a linear shear flow), the vortex will make a smaller angle with the wall and consequently the effect of the neck will be less pronounced.

6.3.3 The circulation

The circulation of the head By comparing the computed velocity field with the measured one, it is possible to estimate the circulation of the head and the neck of the vortex. This value is important since it can also be used as a parameter in the simulations. For the case of the hemisphere at $x/D = 5$ and $Re_D = 1940$ (shown in figure 6.2), a value for the dimensionless circulation was found of $\frac{\Gamma}{UD} = -0.26$. The circulation of the vortex can be expected to be time-independent. It was also concluded before that the dimensionless circulation was largely independent of Re_D (see chapter 5). Therefore, the value calculated above should be a reasonable approximation for the circulation throughout the measurements presented in chapter 5, for the case of the hemisphere. For the droplet, the circulation is not as easy to estimate, because of the kinked neck

that complicates the calculation of the velocity field and the larger effects of the interaction of the hairpin vortex with the background shear flow. As this chapter is only meant to give some general insight, this calculation was not tried.

In inviscid flow, the head of the vortex is pushed upstream by its mirror-image. Although this effect is modified in a viscous flow, the inviscid theory gives a first estimate of the magnitude of the effect of the wall on the vortex head. In our case, this effect is quite small. The effect of the wall is to retard the head with a velocity Δu that can be calculated from

$$\frac{\Delta u}{U} = \frac{\Gamma/DU}{4\pi y_{head}/D} \quad (6.2)$$

where Γ/DU is the dimensionless circulation. For $\Gamma/DU = -0.26$ and $y_{head}/D = 1.00$ this results in $\Delta u/U = 2.1\%$. It is to be expected that this effect is small when compared to the effect of the necks and the legs on the vortex head. In the experiments, the retardation of the head seems to be only a minor effect. In chapter 5 it was shown that the effect of the vortex head and necks on the flow decreases in the downstream direction. This might have been expected since the vortex radius grows through viscous diffusion. However, the increase in the vortex radius can be approximated by

$$R \approx \sqrt{R_0^2 + 4\nu t} \quad (6.3)$$

For $Re = 1940$, this means that from $x/D = 5.0$ to $x/D = 7.5$ the radius of the head can be expected to grow from $R = 0.20D$ to $R = 0.21D$. Since the increase of the radius of the head is then only 5%, it should be concluded that the observed weakening of the effect of the head is due to other effects, like a change in the orientation of the head and the necks.

The circulation in the legs In chapter 2 we stated that the circulation in the head and the legs of the hairpin vortex do not need to be equal. The circulation of the legs can be expected to be smaller than the circulation of the head. In the experiment, the circulation in the vortex legs turns out to be so much less than the circulation in the head of the vortex, that the effect of the legs can hardly be observed (see figure 6.2). An indication for the weakness of the legs comes from figure 6.4a, where the u -velocity field is shown in which the necks and the legs have the same circulation as the head. Clearly, figure 6.4a does not correspond to the experimental velocity field and the small value for the circulation used in figure 6.2 gives more realistic results. In figure 6.4b, the same values are used for the circulation in the legs as in figure 6.4a, but now the core radius of the legs has also been set equal to the core radius of the head. The result looks more like the experimental velocity field, but the core radius is such that the legs overlap substantially. Since the legs contain vorticity of opposite

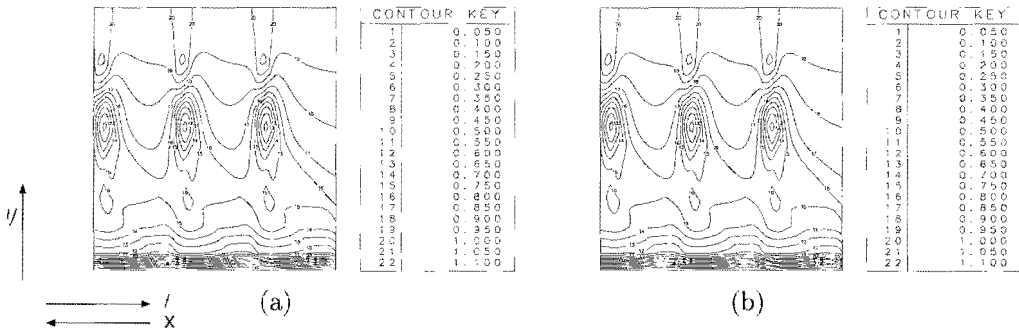


Figure 6.4: The u -velocity field for strong vortex legs with a circulation equal to the circulation of the vortex head ($\Gamma_{leg} = -0.26UD$). (a) $R_{leg}/D = 0.09$, (b) $R_{leg}/D = R_{head}/D = 0.2$

sign, this implies that in a real flow, a substantial cancellation of vorticity would occur ($\sim 80\%$!). However, this core radius is most likely a gross overestimation since, in the experimental situation, the radius of the vortex legs is reduced by the vortex stretching effects downstream of the hemisphere, as indicated in the visualizations (see chapter 3). Consequently, the cancellation of vorticity would be less and the effect of the legs on the velocity field should be expected to be much higher than in figure 6.4b. If, in a real flow, the vortex legs would have a circulation that is similar to the circulation of the vortex head, the velocity induced by such vortex legs should be substantially larger than observed in our experiments.

6.3.4 The v -velocity

Given the circulation and the shape of the vortex, it is also possible to calculate the v -velocity. However, estimating the v -velocity from the u -velocity in this way is due to a large error, specifically where the effect of the legs is calculated. The picture presented in figure 6.5 therefore just serves to obtain an impression of this effect. The figure indicates that the v -velocity is largest near the head and is of the order of up to 20% of the main stream velocity. Since in chapter 5 only the u -velocity was measured, this value cannot be compared to the measurements. In chapter 4 it was argued that in the hot-wire measurements, an error occurred in the determination of the u -velocity: the hot-wire measures the absolute value of the velocity normal to the wire, which has a u - and a v -component. The measured velocity u' is given by:

$$u' = \sqrt{(\bar{u} + \tilde{u})^2 + \tilde{v}^2} \quad (6.4)$$

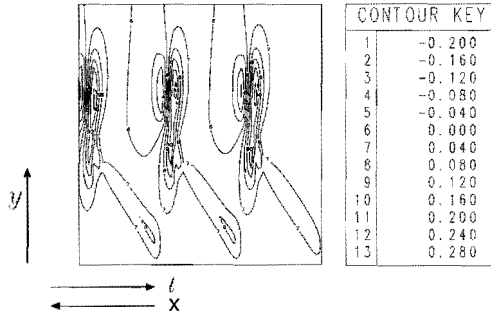


Figure 6.5: The v -velocity field as corresponding to the u -velocity shown in figure 6.2

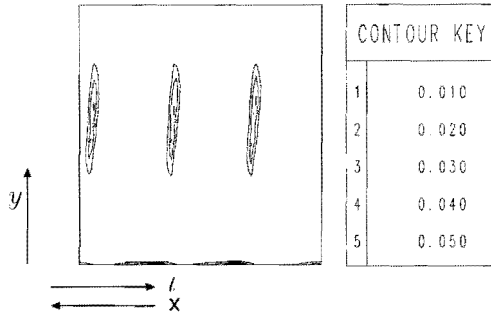


Figure 6.6: The error in the determination of the u -velocity component for the case presented in figure 6.5.

where \bar{u} is the real average velocity at the location of measurement, and \tilde{u} and \tilde{v} are the real velocity fluctuations. Since we can now make an estimate of the v -velocity, it is possible to calculate the error, which is defined as:

$$e \equiv u' - (\bar{u} + \tilde{u}) \tag{6.5}$$

This error is shown in figure 6.6 for the case presented in figure 6.2. At worst, it is about 3%. It is largest near the head and in the region very close to the wall due to the fact that the average velocity \bar{u} is small there.

6.4 Conclusions

- The necks of the vortex seem to have a significant influence on the u -velocity below the vortex head. Most probably, they cause the observed

asymmetry between the velocity deviations above and below the head.

- The dimensionless circulation Γ/UD in the vortex head is approximately -0.26 for $Re_D = 1940$. The accuracy of the method that was used for the determination is not very high: a simultaneous increase in both the circulation and the radius of the vortex core can lead to quite similar results for the velocity field. Nevertheless, the estimate for the circulation seems to be correct within 15%.
- A core radius R/D of 0.20 was used for the head to reproduce the measured velocity field around it. However, the measured u -velocity contour plots can not indicate a radius that is smaller than the spatial resolution of the hot-wire rake: $\Delta/D = 0.17$. Since this is similar to the measured 'core radius', it is very likely that the result is partially determined by the resolution of the rake. However, the visualizations show that the core radius of the vortex head is approximately $0.15D$, while the measurements presented in chapter 5 indicate that at large x/D for decreasing values of Re a larger core radius can indeed be observed. This means that, although the real core radius might be somewhat smaller than the value used in figure 6.2, the magnitude is approximately correct.
- Only the direct effect of the primary hairpin vortex is calculated. The experimental figures show that other effects are observed too: in particular the presence of the patch of low-speed fluid below the head is missing, that is observed in the case of the hemisphere (see figure 6.2d). It is suggested in chapter 5 that this patch is due to the effect of the quasi-spanwise vortex.

Chapter 7

Numerical simulations

7.1 Introduction

In chapter 2 a brief survey has been presented introducing the various effects that are thought to play a role in the evolution of a hairpin vortex. Several of the arguments presented there are qualitative ideas based on the behaviour of vortices in an irrotational and inviscid flow. However, in reality, hairpin vortices are generated in the turbulent boundary layer and to treat this situation as inviscid and irrotational might be too much of a simplification. In order to get a more fundamental understanding of the effects of the different parameters involved in this study of hairpin vortices, the experimental study is complemented by numerical work.

Instead of a full three-dimensional simulation of the problem, the numerical part of the work is limited to two-dimensional and parabolic three-dimensional calculations. The choice for this approach was based on three considerations:

- In a three-dimensional calculation, either the initial conditions or the boundary conditions present a problem. The initial shape and the initial circulation of the hairpin vortex and the surrounding flow field should be specified, for which no straightforward approach exists, or the hairpin vortex shedding downstream of a hemisphere should be calculated, which is from a numerical perspective a very tricky problem to solve. In our group, a start has been made to build a 3D spectral DNS code to solve the problem, but this work is still in progress (Vissers, 1996).
- Many investigators have considered two-dimensional spanwise and streamwise vortices in a shear flow to approximate the effect of a three-dimensional hairpin structure (e.g. Ersoy & Walker (1985), Doligalski et al. (1995)). The same strategy is followed here, which enables us to compare our results with the literature.

- Simple models can provide a better way to understand the basic causal mechanisms behind a complex phenomenon than a full time dependent 3D simulation.

Since this approach addresses mainly the effect of a two-dimensional vortex on the near-wall flow, the intention of this chapter is to study some general phenomena associated with the interaction of a 2D vortex in a rotational viscous shear layer, and to make a comparison with the experimental results when this is possible.

The calculations have been performed with an existing code, that is described in appendix A. The code is able to perform two kinds of simulations:

- **Instationary 2D calculations** These are used for the calculation of the temporal evolution of a spanwise vortex moving over a wall in the XY -plane, given a vorticity distribution at $t = 0$.
- **Stationary (parabolic) 3D calculations** These are used for the calculation of the evolution along the x -direction (spatial!) of an infinitely long streamwise vortex above a wall, given a fixed vorticity distribution at $x = 0$.

The initial vorticity distribution has to be specified by the user. The code then uses the Poisson equation to find the velocity field from the vorticity and then uses the vorticity equation to calculate the vorticity distribution at the next time step. For the 2D calculations, the ω_x - ψ_x -relation is solved in the XY -plane¹. For the parabolic 3D calculations, the ω_x - ψ_x -relation is solved in the YZ -plane and the streamwise velocity u is then calculated from the Navier-Stokes equations for the computation of the vorticity further downstream. By these two approaches the evolution of either the head or the legs can be calculated in isolation. The boundary conditions that have been used for these calculations are presented in appendix A.3.

During a simulation, the vortex trajectory was determined by following the local maximum in the vorticity. The details of the tracking procedure are described in appendix A.

In section 7.2 the relevant dimensionless parameters are introduced. The remaining sections 7.3 and 7.4 are devoted to an analysis of the results for a spanwise and a streamwise vortex in a boundary layer flow.

7.2 Dimensionless numbers

The experimental situation is fully characterised by two Reynolds numbers: the Reynolds number with respect to the boundary layer thickness δ and the

¹For a definition of the spatial coordinates, see chapter 2.

Reynolds number with respect to the diameter of the hemisphere D . In the experimental section, the latter was given in the form of the aspect ratios of these Reynolds numbers, which equals δ/D . In the case of the simulation of a vortex near the wall, an initial distribution for the vorticity has to be imposed. In this case, the magnitude of the circulation of the vortex and the distribution of its vorticity. For all the simulations, a Gaussian distribution is applied for the initial vorticity of the vortex. A full characterisation of the flow then requires two more dimensionless numbers: one for the magnitude of the circulation of the vortex and one for the initial radius R of the vortex core. The vortex radius was kept at $R/H = 0.25$ for all the calculations on the spanwise vortex. For the streamwise vortices, a value of $R/H = 0.035$ was used. For the simulations, all dimensionless numbers are based on the main velocity U and the distance H of the vortex centre to the wall. This results in the subsequent dimensionless numbers:

$$\begin{aligned}
 Re &= UH/\nu & R^* &= R/H \\
 \delta^* &= \delta/H & U^* &= U/U \equiv 1 \\
 \Gamma^* &= \Gamma/UH & H^* &= H/H \equiv 1 \\
 t^* &= tU/H
 \end{aligned}$$

In the simulations, the initial vortex height is therefore always 1, and so is the main stream velocity.

In the simulations, U has been taken to be the experimental mainstream velocity and H to be the diameter of the obstacle in the experiments, so that the Reynolds number based on these unity scales should correspond to the experimental values given in chapter 3 and 5. To set the initial vortex height H equal to the diameter of the obstacle D is justified by the fact that the experiments indicate that the vortex rises quickly in the flow from $0.5D$ to approximately $1D$.

In the remainder of this chapter, only dimensionless numbers will be used. Therefore, the asterisk will be dropped from now on.

7.3 Special case I - the spanwise vortex

7.3.1 Introduction

The effect of the head of a hairpin vortex on the near-wall flow has been investigated by e.g. Doligalski et al. (1995). For reasons of convenience, they approximated the head by a 2D (infinitely long) spanwise vortex, whose effect on the near-wall flow was simulated. The motion of a 2D spanwise Gaussian vortex near the wall has been investigated by several other investigators too (e.g. Luton et al., 1995). Luton observed that, for a vortex with a sign of rotation similar to the hairpin vortex head, the vortex moves towards the wall,

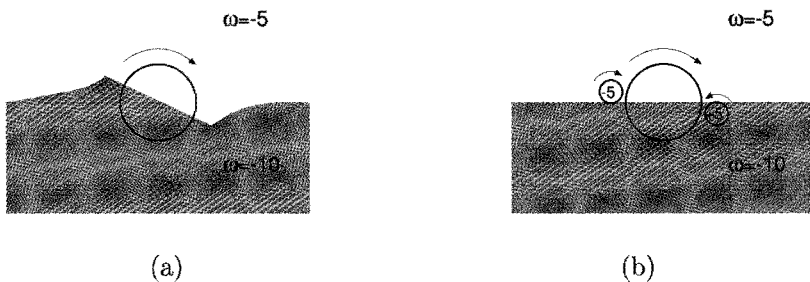


Figure 7.1: The interaction between a negative vortex and a background vorticity field (a) the vortex redistributes the vorticity in the background (b) effect of the situation indicated in (a) can be compared to the effect of an additional vortex pair that is superimposed on the background vorticity profile. This vortex pair pushes the primary vortex downwards.

approaching it up to some critical distance and then moves away from the wall again (a 'rebound'). This rebound is due to the fact that the vortex induces vorticity at the wall and, if the vortex is sufficiently close to the wall, this vorticity is advected upwards. The wall-induced vorticity is of opposite sign compared to the vorticity of the initial vortex and it pushes the primary vortex away from the wall again (Stoffels, 1994; Van den Bosch, 1997).

The motion towards the wall, as well as the subsequent rebound, are well established phenomena. In these processes, several effects play a role. Luton et al. calculated the motion of a spanwise vortex in a laminar boundary layer for three values of the circulation, and presented the results largely without theory. In this section, a more extensive analysis is presented: the effects that play a role in this phenomenon will be disentangled and the effect of various parameters, such as the circulation of the vortex, the Reynolds number and the boundary layer thickness, will be established. In addition, in the last part of the section, conclusions will be drawn regarding the evolution of hairpin vortices.

7.3.2 Theory: the equations

The full two-dimensional vorticity equation is:

$$\frac{\partial \omega}{\partial t} + u \frac{\partial \omega}{\partial x} + v \frac{\partial \omega}{\partial y} - \frac{1}{Re} \left(\frac{\partial^2 \omega}{\partial x^2} + \frac{\partial^2 \omega}{\partial y^2} \right) = 0 \quad (7.1)$$

In order to gain some feeling for the results shown in this chapter, it is useful to decompose this equation into the contribution of the shear (U , V , Ω) and the contribution of the vortex (\tilde{u} , \tilde{v} , $\tilde{\omega}$). Inserting these terms into equation 7.1, it

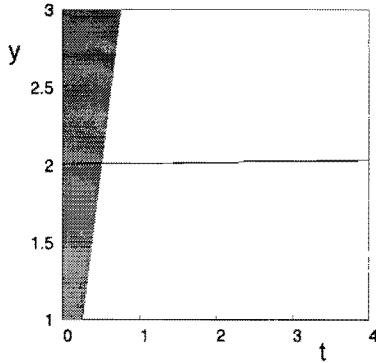


Figure 7.2: The interaction between a negative vortex and a linear shear flow for $\Gamma = -2$. The vortex moves along a straight path.

follows that

$$\begin{aligned} \frac{\partial}{\partial t}(\Omega + \tilde{\omega}) + (U + \tilde{u})\frac{\partial}{\partial x}(\Omega + \tilde{\omega}) + (V + \tilde{v})\frac{\partial}{\partial y}(\Omega + \tilde{\omega}) \\ - \frac{1}{Re}\left(\frac{\partial^2}{\partial x^2}(\Omega + \tilde{\omega}) + \frac{\partial^2}{\partial y^2}(\Omega + \tilde{\omega})\right) = 0 \Rightarrow \end{aligned} \quad (7.2)$$

$$\begin{aligned} \frac{\partial \Omega}{\partial t} + U\frac{\partial \Omega}{\partial x} + V\frac{\partial \Omega}{\partial y} - \frac{1}{Re}\left(\frac{\partial^2 \Omega}{\partial x^2} + \frac{\partial^2 \Omega}{\partial y^2}\right) + \\ \frac{\partial \tilde{\omega}}{\partial t} + \tilde{u}\frac{\partial \tilde{\omega}}{\partial x} + \tilde{v}\frac{\partial \tilde{\omega}}{\partial y} - \frac{1}{Re}\left(\frac{\partial^2 \tilde{\omega}}{\partial x^2} + \frac{\partial^2 \tilde{\omega}}{\partial y^2}\right) + \\ U\frac{\partial \tilde{\omega}}{\partial x} + \tilde{u}\frac{\partial \Omega}{\partial x} + V\frac{\partial \tilde{\omega}}{\partial y} + \tilde{v}\frac{\partial \Omega}{\partial y} = 0 \end{aligned} \quad (7.3)$$

The resulting vorticity equation is the sum of the independent vorticity equation for the shear layer and the vorticity equation for the imposed vortex, plus four interaction terms, which are given in the last line of (7.3). Note that the interaction terms are purely convective.

Initially, two of the four interaction terms are zero, since $\partial\Omega/\partial x = 0$ and $V = 0$. The interaction is given by the two remaining terms, in which the first ($U\partial\tilde{\omega}/\partial x$) resembles the advection of the vortex by the main flow and the last ($\tilde{v}\partial\Omega/\partial y$) resembles the lift up of the vorticity of the boundary layer by the vortex. However, by the influence of this last term the wall vorticity sheet gets distorted and V and $\partial\Omega/\partial x$ now both are no longer equal to zero. The term $\tilde{u}\partial\Omega/\partial x$ indicates the convection of the near wall vorticity by the vortex into the streamwise direction (which is not homogeneous anymore). The term $V\partial\tilde{\omega}/\partial y$ indicates the displacement of the vortex into the y -direction by the displaced boundary layer vorticity. In the next section, it will be shown that this effect is very important for the behaviour of a spanwise vortex in a boundary layer.

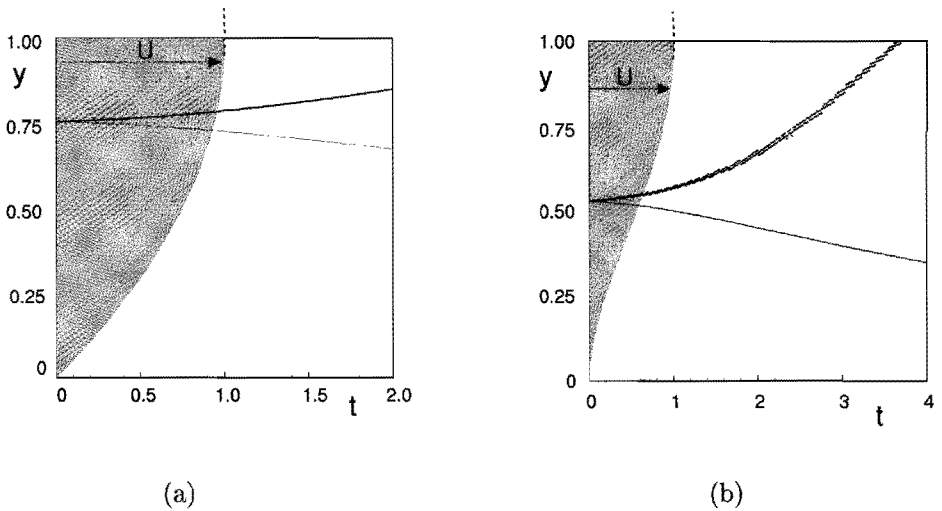


Figure 7.3: The effect of the background velocity profile on the motion of a vortex with circulation $|\Gamma| = 2$. The vortex trajectories are indicated by a thick line for a positive vortex and by a thin line for a negative vortex. The shape of the velocity profile is indicated by the shaded area. (a) parabolic velocity profile (b) inflectional velocity profile

7.3.3 Theory: a spanwise vortex in a shear flow

The analysis of the motion of a vortex in a laminar boundary layer is a special case of the motion of a vortex in a rotational flow. A vortex in such a flow will advect the vorticity in the background flow as indicated in figure 7.1a. The deformation of the background vorticity then starts to affect the motion of the vortex. This is the effect of the term $V\partial\omega/\partial y$ in equation 7.3, as indicated in section 7.3.2. Effectively, the vortex creates a bipolar perturbation on top of the original background vorticity field, as indicated in figure 7.1b. This perturbation pushes the original vortex in the direction perpendicular to the main flow velocity.

The important characteristic of the background velocity profile is its value for $\partial\omega/\partial y$. In a flow with a linear shear, the vorticity field is uniform and the vortex is not affected by the deformation of the background velocity profile, as indicated in figure 7.2. If the vorticity gradient is nonzero, the deformation of the background velocity profile induces a motion of the vortex that can be summarized as follows: a vortex that contains negative circulation moves in the direction in which the background vorticity is decreasing, a vortex that contains positive circulation moves in the direction in which the background vorticity is

increasing. In summary: positive vorticity moves in the direction of increasing vorticity, negative vorticity moves in the direction of decreasing vorticity. The effect indicated above is illustrated in figure 7.3a for a parabolic velocity profile. In this figure, the initial velocity profile² is given by

$$\begin{aligned} u(y) &= y(2 - y) \Rightarrow \\ \frac{\partial\omega}{\partial y} &= -\frac{\partial^2 u}{\partial y^2} = 2 \end{aligned} \tag{7.4}$$

In this case, as the vorticity gradient is positive, a vortex with negative circulation will move downwards and a vortex with positive circulation will move upwards, as indicated in the figure. A somewhat more complicated case is shown in figure 7.3b. In this case, the velocity profile is given by

$$\begin{aligned} u(y) &= (y(2 - y))^2 \Rightarrow \\ \frac{\partial\omega}{\partial y} &= -\frac{\partial^2 u}{\partial y^2} = -8 + 24y - 12y^2 \end{aligned} \tag{7.5}$$

In this case, the velocity profile contains two inflection points and the vorticity is the most negative at $y \approx 0.43$. Figure 7.3b shows that the negative vortex stays in this area, while the positive vortex moves upward towards the region with positive vorticity.

The motion along the vorticity gradient is a fully inviscid phenomenon and as such does not depend on the Reynolds number. All velocities scale with the main stream velocity: if U is doubled, the vorticity is also doubled and consequently the vorticity gradient is doubled too, which implies that the wallward motion of the vortex increases. These effects do not affect the vortex trajectory, although the vortex moves faster. When the circulation of the vortex is increased, the amount of displacement of the background vorticity will be correspondingly larger, leading to a faster wallward motion of the vortex. This mechanism depends both on the background vorticity distribution and on the circulation of the vortex.

7.3.4 The circulation

Now the trajectory of a spanwise vortex is calculated that is immersed in a laminar shear flow. Since the value of $\partial\omega/\partial y$ is positive in a flat-plate laminar boundary-layer velocity profile $u(y)$, a negative vortex can be expected to move down, just as in the case presented in section 7.3.3. In figure 7.4 the path of the vortex core is shown for different values of the circulation. The figure shows that with decreasing Γ the initial motion of the vortex towards the wall is reduced. This can be understood from the fact that its effect on the boundary-layer vorticity is reduced, in accordance with the theory presented above.

²During the calculation this is modified by the effect of the vortex and by viscous diffusion.

In contrast to the simulations for the jet, a wall is now present at $y = 0$. By the effect of the no-slip condition, the vortex induces an amount of vorticity at the wall that is of opposite sign as compared to its own vorticity. This vorticity diffuses away from the wall and is caught by the vortex and advected upwards in such a way that an asymmetric dipole vortex is created that moves away from the wall (a 'rebound'). The induced vorticity is always of opposite sign to the primary vorticity. For a vortex with negative circulation, positive secondary vorticity appears upstream of the primary vortex, for a vortex with positive circulation, negative secondary vorticity appears downstream of the primary vortex. In both cases, the secondary vorticity pushes the primary vortex away from the wall and a rebound occurs (Luton et al. 1995).

The circulation of the vortex affects the processes involved in the rebound mechanism. Luton observed that for large values of Γ the vortex moves away from the wall, whereas for small values of Γ the vortex moves towards the wall. These observations are confirmed by our results. However, the vortex does not move either up *or* down, but rather it moves down initially due to the effect of the background vorticity and after a sufficient amount of time starts to move up due to the effect of the secondary vorticity that is created at the wall and that is located slightly upstream of the primary vortex. A decrease in the circulation of the primary vortex leads to a lower wall-induced vorticity and a corresponding lower diffusion of the vorticity from the wall. In addition, the upward advection of this vorticity is reduced. Therefore, a delay in the rebound of the vortex occurs and a smaller value is found for the distance of the vortex centre to the wall at which the rebound takes place (H_r), as can be seen from figure 7.4a.

In summary, the value for Γ affects the computed flow in several ways:

- it deforms the background shear profile, as indicated in figure 7.1 and thus determines the velocity with which the vortex moves towards the wall.
- it determines the magnitude of the induced circulation at the wall.
- it advects the wall-induced vorticity away from the wall.

In figure 7.4b, the vortex trajectory is shown that corresponds to figure 7.4a. Both figures closely resemble each other. The differences are caused by the fact that the streamwise location of the vortex depends on the distance of the vortex to the wall, due to both the velocity profile and the mirror-image effect. The streamwise location of a vortex at $t = t_0$ is given by

$$x(t_0) \approx \int_0^{t_0} \left(u(y(t)) + \frac{\Gamma}{4\pi y(t)} \right) dt$$

When the vortex approaches the wall, its streamwise velocity decreases, and this increases again as the vortex leaves the wall. This effect only complicates the figures without adding anything to the physics. Therefore, attention will be focussed on the vertical motion of the vortex as a function of time. Because of

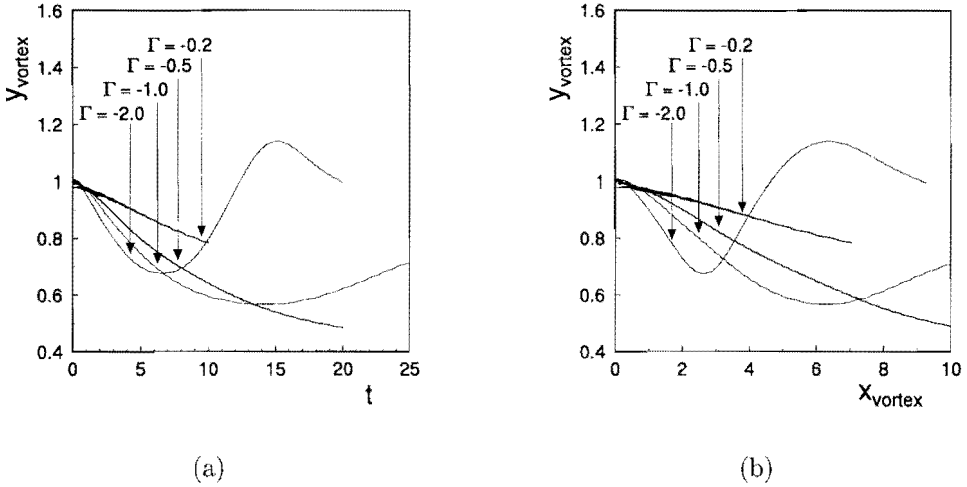


Figure 7.4: The path of a spanwise vortex for different values of the initial circulation at $Re = 1500$ for $\delta/H = 1.75$ (δ is the laminar flat-plate boundary layer thickness). **(a)** the distance of the vortex centre to the wall as a function of time **(b)** the vortex trajectory

their conceptual importance, the vortex trajectories are shown, but only very limited attention will be given to them in the text.

7.3.5 The Reynolds number

The vorticity contour plots for various values of the Reynolds number are shown in figure 7.5. This figure shows the vorticity at $t = 1$ for $Re = 1000, 500$ and 250 , for an initial circulation of the primary vortex of $\Gamma = -2$. The predominant effect of a decrease in the Reynolds number is to speed up the diffusion of the wall-induced vorticity into the flow. Once this vorticity is sufficiently far removed from the wall, the vortex is able to advect this vorticity upwards into the flow, which results in a rebound. The result from the advection by the vortex can already be seen in this early stage from the difference between the distribution of wall-vorticity upstream and downstream of the vortex.

For decreasing Reynolds number, the wall-induced vorticity is diffused faster away from the wall. The secondary vorticity is advected upwards in an earlier stage and the rebound occurs after a shorter time. This effect of the Reynolds number on the path of the vortex is illustrated by figure 7.6a. Figure 7.6b shows the corresponding vortex trajectories.

For large Reynolds numbers, the primary vortex is pushed up higher by the

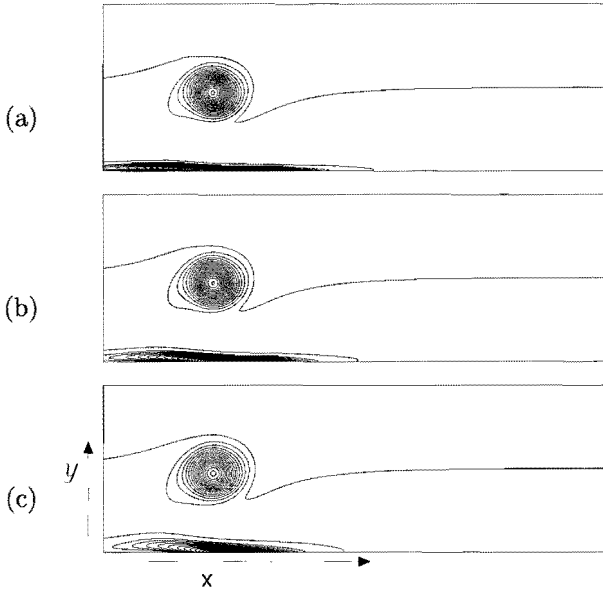


Figure 7.5: The vorticity contour plots at $t = 1$ for a spanwise Gaussian vortex with $\Gamma = -2$ moving over a wall in a laminar boundary-layer ($\delta/H = 1.75$). (a) $Re = 1000$, (b) $Re = 500$, (c) $Re = 250$. Between two contours, $\Delta\omega = 0.5$

secondary vorticity than for lower Reynolds numbers. This may be due to the fact that for low Reynolds numbers, a lower value can be expected for $\partial\Omega/\partial y$ and therefore the effect of the term $v\partial\Omega/\partial y$ is reduced: the rebound occurs more gradually. The vorticity contour plots for $t = 8$ are shown in figure 7.7. For the three Reynolds number shown, the rebound has already occurred. The figure indicates that for $Re = 250$, the wall-induced vorticity remains largely in the region below the primary vortex and the secondary vorticity is weaker. This is also indicated by the decrease in the tertiary vorticity that is induced at the wall by the secondary vorticity, and that is clearly weaker for lower Reynolds numbers³.

7.3.6 The boundary layer thickness

In a boundary layer velocity profile, the same effect plays a role as described above. Figure 7.8 indicates the distribution of the vorticity in the flat-plate

³The figures show the vorticity distribution. Therefore they cannot give more than an indication of the magnitude of certain effects, since the truly important quantities are the secondary and tertiary circulation. Unfortunately, these are not easy to define uniquely for the present case.

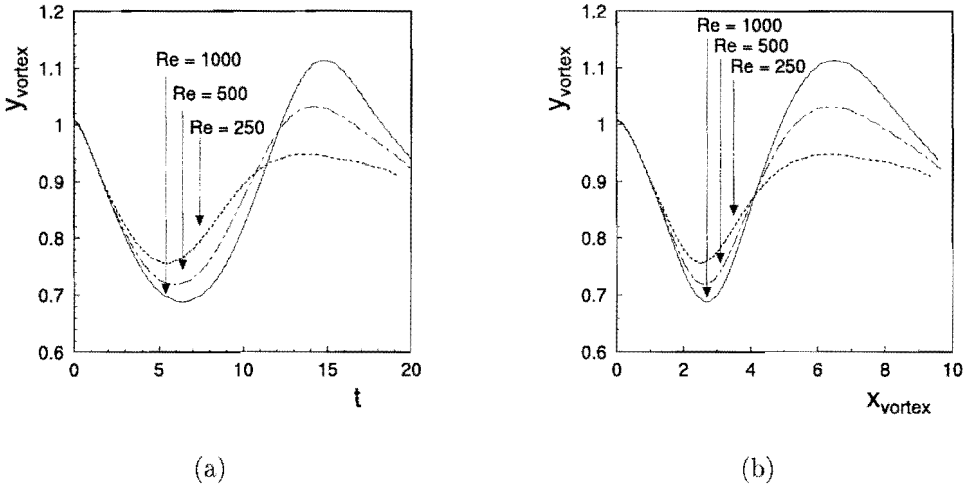


Figure 7.6: The path of a spanwise vortex with $\Gamma = -2.0$ and $\delta/H = 1.75$ for different values of Re . (a) the distance of the vortex centre to the wall as a function of time (b) the vortex trajectory

laminar boundary layer. Throughout the boundary layer, $\partial\omega/\partial y$ is positive. Therefore, a negative vortex will be drawn towards the wall, while a positive vortex will be pushed away from the wall. For the laminar flat-plate boundary layer velocity profile, the value of $\partial\omega/\partial y$ is most positive at $y/\delta \approx 0.58$. In the lower part of the boundary layer, the velocity profile is more or less linear and $\partial\omega/\partial y$ is approximately zero. Therefore, a negative spanwise vortex located halfway in the boundary layer will move towards the wall, while a small vortex close to the wall is hardly affected by the boundary layer vorticity. It is to be expected that if the distance H of the vortex centre to the wall is much larger than the boundary layer thickness δ , the vortex actually moves in irrotational flow and does not approach the wall. This is shown in figure 7.9a. When the ratio δ/H is decreased below 0.5, the motion of the vortex towards the wall decreases. For values of δ/H larger than 2 the motion of the vortex towards the wall is reduced too. Figure 7.9b shows the effect of the boundary layer thickness on the vortex trajectory.

The boundary layer thickness also affects the vortex height H_r at which the vortex rebound occurs. Although the initial height of the vortex is kept constant, for decreasing values of the boundary layer thickness, the rebound occurs closer to the wall. This is also evident from figure 7.10. The figure shows that for $\delta/H = 3.5$ the advection of the wall-induced vorticity by the vortex is already a prominent effect, while for $\delta/H = 0.25$ only the deformation of the boundary

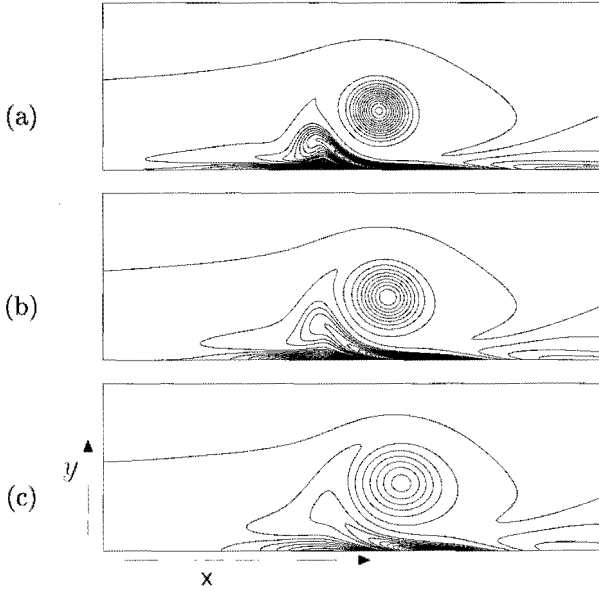


Figure 7.7: The vorticity contour plots at $t = 8$ for a spanwise Gaussian vortex with $\Gamma = -2.0$ moving over a wall in a laminar boundary layer ($\delta/H = 1.75$). **(a)** $Re = 1000$, **(b)** $Re = 500$, **(c)** $Re = 250$. Between two contours, $\Delta\omega = 0.5$

layer vorticity shows up prominently⁴. The figure also shows that for a thinner boundary layer, the vortex moves faster, since the velocity at the height of the vortex is larger. The delay of the rebound can be understood from the observation that for large Reynolds numbers, the initial stage, which is dominated by diffusion, is a bottleneck for the rebound mechanism. When the initial diffusion of the wall-induced vorticity is much slower than the velocity with which the vortex moves over the wall, the vortex has moved too far away during this stage to be able to advect the vorticity upwards. When δ/H is decreased down to 0.5, the vortex is less immersed in the boundary layer and therefore moves faster with respect to the diffusion velocity with which the wall-induced vorticity moves away from the wall. It is to be expected that for very small values of δ/H the height of the rebound becomes independent of the thickness of the boundary layer. Simulations with such small values for the boundary layer thickness have not been performed due to the magnitude of the required computational domain and the fact that the boundary layer growth over the computational domain would be substantial for such thin boundary layers.

⁴Since δ is smaller, the vorticity in the boundary layer increases. In general, the circulation Γ of the boundary layer is constant for a constant main stream velocity and the vorticity can be given in first order by Γ/δ .

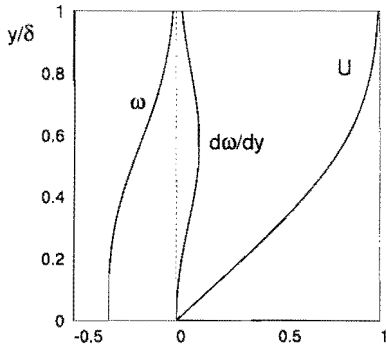


Figure 7.8: The vorticity distribution in a flat-plate laminar boundary layer (from Schlichting (1955)).

7.3.7 Implications for hairpin vortices

In the literature, much interest has been drawn to the ability of the hairpin vortex to generate secondary vortices. In the simulations presented above, secondary vorticity is indeed created by the vortex head⁵. However, its circulation is opposite to the circulation that is found for the secondary vortices that are created upstream of the hairpin vortex in the experiment. In the experiment, the secondary vortices have the same direction of rotation as the primary hairpin head. This is an indication that the mechanism that creates these secondary vortices in the experiment is more complex than the effect of the hairpin vortex head on the near-wall fluid only. To calculate the secondary vortex that is created underneath the primary hairpin vortex head (indicated in chapter 3), it seems to be necessary to take into account 3D-effects. This observation leads to the rather complicated mechanism that is proposed for the generation of the quasi-spanwise vortex underneath the hairpin vortex head in chapter 3. In figure 7.11 the effect of a hairpin vortex head is calculated using the circulation $\Gamma = -0.25$, as obtained in chapter 6 for the experimental case, using a Reynolds number of 1900, which also corresponds to the experiments. The figures indicate that no secondary vortex can be observed and that the boundary layer vorticity is hardly affected by the vortex head. While the simulation indicates that the vortex moves slowly towards the wall, a rebound does not occur within the timescale of the experiment.

⁵A patch of vorticity does not have to correspond to a vortex. To find out whether a secondary vortex is created in our simulations, the pressure contour plots have been calculated. Some tentative calculations have been made with initial values for the circulation of $\Gamma = -10$. It was found that in this case, at the location of the drawn-up secondary vorticity a circular low-pressure region exists if $Re > 100$. This indicates that the secondary vorticity is indeed concentrated in a vortex. For physically more realistic values of the circulation ($\Gamma \approx 0.25$), no low-pressure region can be discerned anymore. Nevertheless, the presence of tertiary vorticity seems to indicate that a real vortex is created.

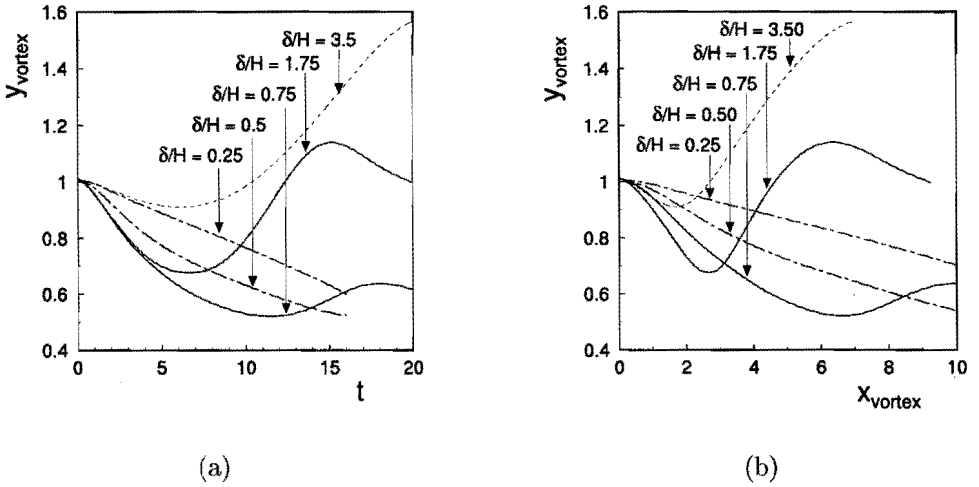


Figure 7.9: The path of a spanwise vortex for different values of the boundary layer thickness δ at $Re = 1500$. **(a)** the distance of the vortex centre to the wall as a function of time **(b)** the vortex trajectory

A different observation is the fact that in the experimental situation, the hairpin vortex head moves away from the wall, while in the present chapter it has been indicated that a spanwise vortex in a boundary layer profile should be expected to move towards the wall. Most probably, the upward motion in the experiments is due to the effect of the vortex legs and necks (recall that the upward motion of the head was reproduced in the simulations of Hon & Walker (1987), as discussed in chapter 2). This indicates that a simulation of an isolated spanwise vortex has only limited significance for the evolution of the flow in the case of a hairpin vortex. The details of the velocity profile can not be expected to be the same in both cases, although previous investigators have tried to link these to the generation of secondary vortices (Doligalski et al., 1995). However, in spite of claims by others, in our case it is found that a negative secondary vortex is not created in a purely 2D simulation.

7.4 Special case II - the streamwise vortex

7.4.1 Introduction

While the spanwise vortex resembles the vortex head, the vortex legs can be considered as two counter-rotating streamwise vortices. The computational code was modified for this new configuration, as described in chapter 7.1. The mech-

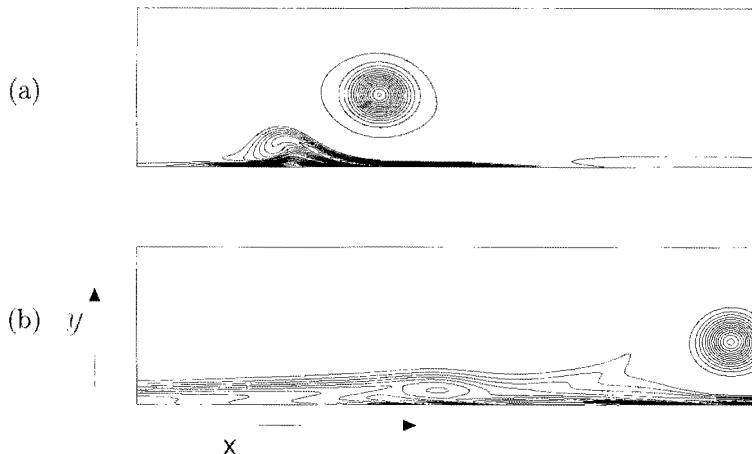


Figure 7.10: The vorticity contour plots at $t = 8$ for a spanwise Gaussian vortex with a circulation $\Gamma = -2$ near the wall with $Re = 1500$. Between two contours, $\Delta\omega = 0.5$. (a) $\delta/H = 3.5$, (b) $\delta/H = 0.25$.

anisms that are involved in the interaction of a streamwise vortex with the wall are similar to the mechanisms that play a role in the evolution of the spanwise vortex, as described in the previous section. Also the magnitude of the interaction is similar: while the legs are weaker than the vortex head (see chapter 6), they are also closer to the wall.

At the other hand, the physical picture of one spanwise head or two streamwise legs is entirely different, which leads to some new results. Since the flat-plate laminar boundary layer profile only contains ω_z and does not contain any ω_x , the effects of the background rotation that played a role for the spanwise vortex do not occur here and the vortex can be expected not to move towards the wall initially. Consequently, the boundary layer thickness does not affect the initial migration of the vortex in the way it did in section 7.3, as will be shown below. Also, two new issues appear in an analysis of the motion of the legs:

- the cancellation of the vorticity of the legs due to diffusive overlap between of legs
- the deformation of the streamwise velocity profile along the vortex

The parameter L is introduced for the initial distance of the centre of the legs to the wall. This value is chosen to be 0.2 according to the results of the visualizations of chapter 3.

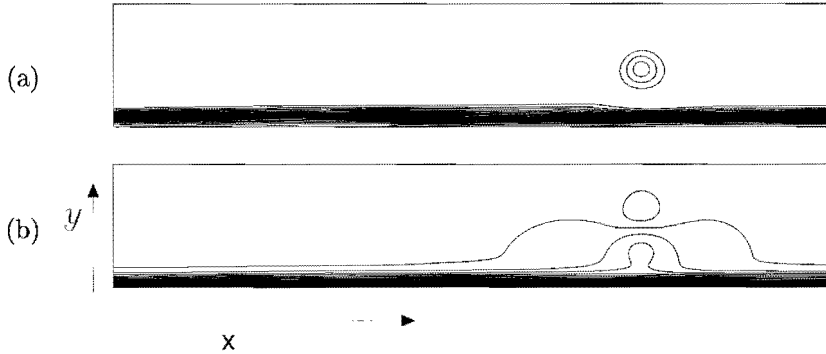


Figure 7.11: A spanwise vortex with a circulation $\Gamma = -0.25$ near the wall with $Re = 1900$ and $\delta/H = 0.25$ at $t = 8$. (a) vorticity contour plot ($\Delta\omega = 0.25$) (b) u -velocity contour plot ($\Delta u = 0.05$)

7.4.2 The motion of streamwise vortices

The motion of a single streamwise vortex above a wall can be expected to depend on the circulation and the Reynolds number in a way that is largely similar to the case of the spanwise vortex that was analyzed before. Figure 7.12a shows the location of a single streamwise vortex in the YZ -plane as a function of the streamwise distance. As indicated above, the vortex does not move down initially as in the case of a spanwise vortex. Due to its mirror-image, it is pushed to the left. Then, again, secondary vorticity is advected from the wall, which pushes the primary vortex upwards. The strength of this effect again depends on the circulation of the primary vortex and the Reynolds number in a way that is similar to the case of the spanwise vortex. Note that the trajectory of the vortex does not depend on the boundary layer thickness.

Although the trajectory does not depend on the boundary layer thickness in this case, the figure shows that for a large boundary layer thickness, the vortex has moved over a somewhat larger distance in the YZ -plane. To explain this, it is important to be aware of the effect of the u -velocity on the development of the vortex. The main effect of the streamwise velocity⁶ is caused by the fact that it is non-uniform. The simulations produce cross-sections of the flow at various downstream distances x . In regions with a low u -velocity, the flow has more time to develop during a step dx than in regions where the u -velocity is high. Therefore, in any YZ -plane, in regions with a low u -velocity the effect of diffusion is more pronounced and similarly the effect of the vortex-induced v - and w - velocities is more important. A smaller boundary layer thickness means

⁶Effects of vortex stretching are negligible in the present computations since no significant acceleration of the flow takes place.

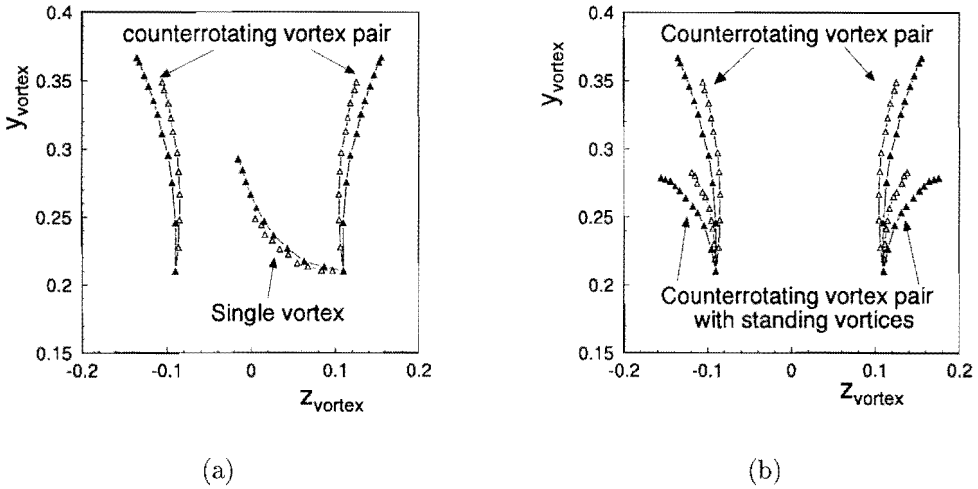


Figure 7.12: **(a)** The vortex trajectory for a single streamwise vortex and a counter-rotating streamwise vortex pair at $Re = 1900$. **(b)** The vortex trajectory for a vortex pair with or without an adjacent standing vortex pair (with opposite circulation) at $Re = 1900$. All vortices have a circulation of $|\Gamma| = 0.03$, except the standing vortices (for which $|\Gamma| = 0.06$). Open triangle: $\delta/L = 1$, Filled triangle: $\delta/L = 3$. Between two successive markers, the downstream step $dx = 1$ and at $x = 0$ the height of the vortices equals $0.2 (= L)$.

that the u -velocity is higher and that any motion in the YZ -plane has less time to develop.

In figure 7.12a the location of two counter-rotating vortices in the YZ -plane is shown as a function of downstream distance for two values of the boundary layer thickness δ/L . The effect of the counter-rotating vortex is far larger than the effect of the wall. This is partially due to the fact that the effect of the wall is reduced, since the circumferential velocity of a dipole decreases with $1/r^2$ while for a monopole this decreases with $1/r$. This is also confirmed by the vorticity contour plots in figure 7.13. These plots show that for the counter-rotating vortices the near-wall vorticity is much smaller than for the case of a single vortex. Figure 7.12a shows that, initially, counter-rotating vortices tend to move somewhat towards the plane of symmetry, due to their image vortices. However, this effect is very small and is quickly overcome by a much larger effect that drives the vortices away from the plane of symmetry.

This motion away from the plane of symmetry can be understood by the observation that for thicker boundary layers, the motion becomes more prominent.

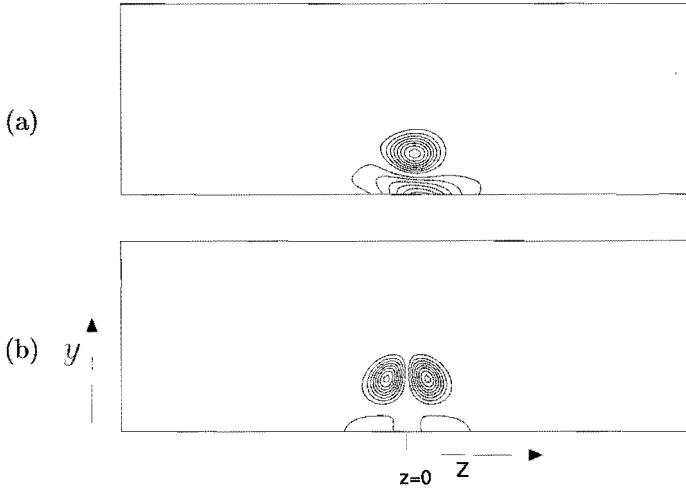


Figure 7.13: The effect of a streamwise vortex with circulation $|\Gamma| = 0.03$ on the near-wall vorticity for $Re = 1900$ at $x = 2.5$ with $\delta/L = 3$. (a) single vortex (b) two counter-rotating vortices

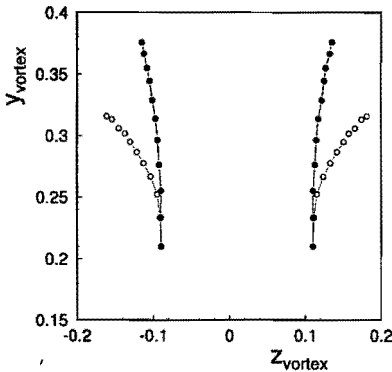


Figure 7.14: The vortex trajectory for a counter-rotating vortex pair with $|\Gamma| = 0.03$ in a uniform flow without walls. $\circ Re = 800$, $\bullet Re = 1900$. Between two successive markers, the downstream step $dx = 1$ and at $x = 0$ the distance of the of the vortices to the wall equals $0.2 (= L)$.

This may seem surprising: it was just argued that the boundary layer thickness does not affect the ratio of the v - and w -velocities, since these velocities are affected equally by a change in u . Therefore, the motion cannot be due to an increase in w with respect to v . It follows that this 'motion' is due to the increased diffusion. For two counter-rotating vortices, the effect of mutual cancellation comes into play. If δ/H is large, the diffusion is large and the legs overlap more. Since all the cancellation occurs in the region between the vortices, the location of the maximum in the vorticity of the vortices, which is tracked by our procedure, should be expected to move away from the plane of symmetry. This effect is also illustrated by figure 7.14. In this figure, the trajectories are shown of two counter-rotating vortices with $|\Gamma| = 0.03$ in a uniform flow. The figure shows that irrespective of the Reynolds number, the vortices

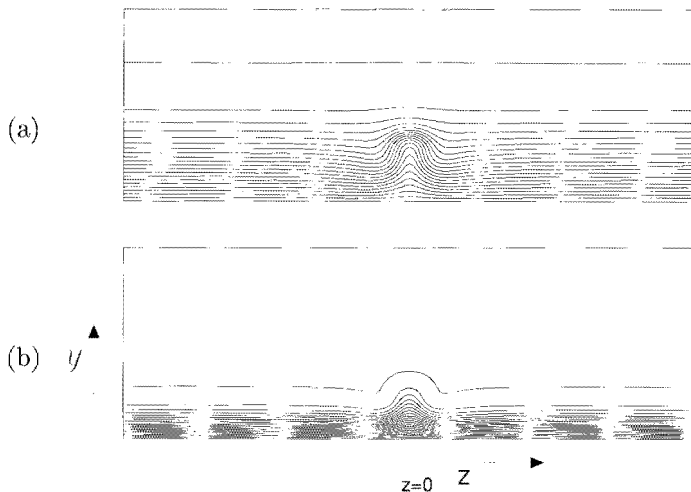


Figure 7.15: The u -velocity contours at $x/D = 2.5$ for a laminar boundary-layer velocity profile that is affected by two counter-rotating streamwise vortices at an initial distance from the wall of $y = L = 0.2$ with circulation $|\Gamma| = 0.03$ for $Re = 1900$. (a) $\delta/L = 3$, (b) $\delta/L = 1$.

move up with a constant speed initially. However, once the vortex radii start to overlap, with decreasing Reynolds number the counter-rotating vortices move away from each other and their upward speed becomes less.

The visualizations in chapter 3 show that in the case of a hemisphere, the trajectory of the vortices is flanked by two standing vortices. It was argued that these draw high speed fluid towards the wall in the region between them. In order to calculate their effect on the vortex legs, figure 7.12b shows the motion of the vortex legs with and without the effect of an adjacent standing vortex pair. At both sides of the streamwise vortex pair, an additional streamwise vortex is located with a circulation that is opposite to that of the nearest leg. The magnitude of these additional vortices is $|\Gamma| = 0.06$ (twice the circulation of the legs, in accordance of the estimate of the circulation of the standing vortex made by Acarlar & Smith (1987)) and they are located at $|z| = 0.6$ (a distance to the nearest leg of 2.5 times the distance between the legs). As expected, the figure illustrates that the standing vortices strongly reduce the upward motion of the counter-rotating legs.

7.4.3 The streamwise velocity profile

In figure 7.15 the u -velocity contours in the YZ -plane are shown at $x = 2.5$ for two counter-rotating vortex legs with a circulation $|\Gamma| = 0.03$. The figure indicates that between the vortex legs a large upwelling of low-speed fluid takes place. Figures 7.15a and 7.15b show the velocity field for $\delta/L = 3$ and

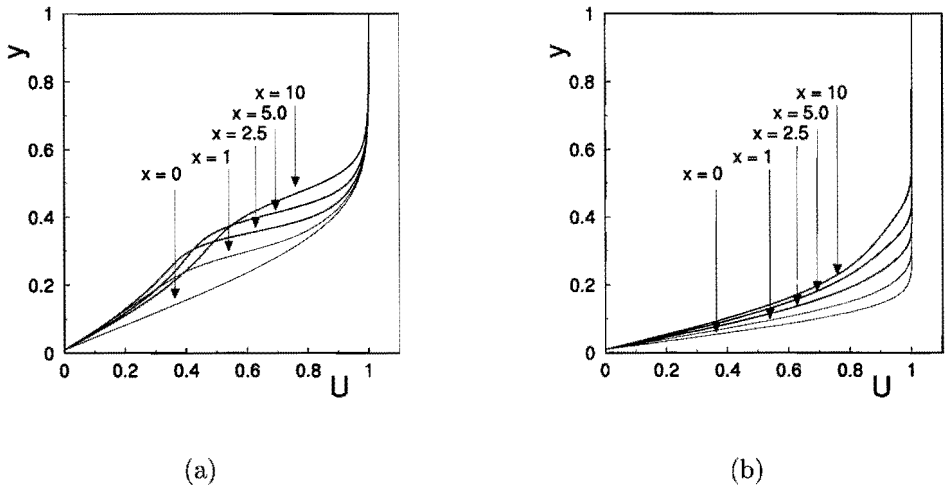


Figure 7.16: The evolution of the u -velocity profile between two counter-rotating streamwise vortices with $|\Gamma| = 0.03$ at $Re = 1900$.
(a) $\delta/L = 3$ **(b)** $\delta/L = 1$

$\delta/L = 1$ respectively. The figures show that the boundary layer thickness has an important effect on the resulting velocity profile. For a small boundary layer thickness, in the region between the legs an inflectional velocity profile is created above the vortex legs. This is shown in more detail in figure 7.16. This figure clearly indicates that an inflectional profile is created only when the boundary layer thickness is significantly larger than the distance of the vortex legs to the wall. If this is not the case, low-speed fluid is drawn up but no inflectional point appears in the velocity profile.

It was argued in the visualizations of chapter 3 that the standing vortex strongly influences the u -velocity profile by pushing high-speed fluid sideways into the wake region. The calculated effect of a standing vortex on the u -velocity is indicated in figure 7.17. The presence of this vortex has an obvious effect on the u -velocity profile. In figure 7.18 the u -velocity profile is shown at $z = 0.25$ (at 30% of the distance between the leg and the standing vortex). The standing vortex clearly increases the near-wall velocity in the region between the standing vortex and the hairpin legs.

7.4.4 Implications for hairpin vortices

The motion of the vortex legs It was shown that two counter-rotating legs push each other upwards in the flow. The effect of the mirror images of the counter-rotating vortices, which tend to press the vortices towards each other,

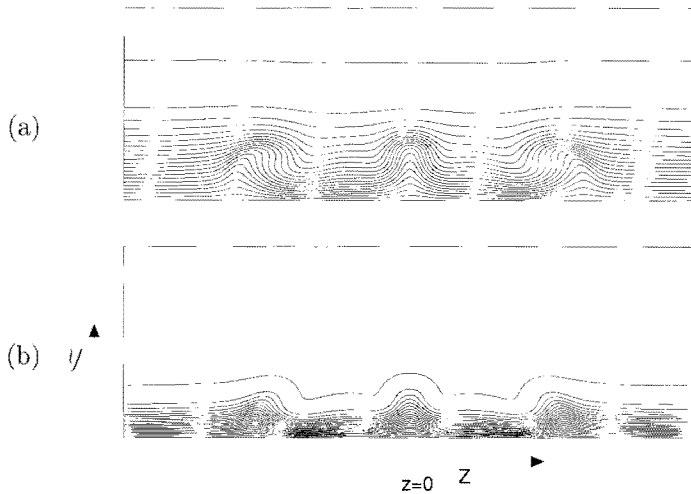


Figure 7.17: The effect of two counter-rotating streamwise vortices with circulation $|\Gamma| = 0.03$ on the streamwise u -velocity profile for $Re = 1900$ at $x = 2.5$ when flanked by two streamwise 'standing vortices' of $|\Gamma| = 0.06$ with opposite rotation as compared to the nearest 'leg'. (a) $\delta/L = 3$, (b) $\delta/L = 1$.

is very small. This was also concluded from the visualizations in chapter 3. The magnitude of the motion of the vortices due to each other is much larger. Nevertheless, during the experimental time scale it is of the same magnitude as the distance between the legs. This distance is small, which is in agreement with the experimental observations, where it was found that the internal dynamics did not seem to play a dominant role in the development of the vortex. In the experiments it was found that the motion of the legs seemed to be dominated by the effect of the background velocity field and the effect of the subsequent vortex in the vortex street, that deformed the upstream part of the vortex legs, as indicated in chapter 3. To estimate the magnitude of the internal dynamics of the hairpin vortex from the experiment is difficult, since the observation of the motion of the legs is complicated by the fact that the legs are not exactly aligned with the flow. Therefore, it is difficult to distinguish between a rise in the legs and a change in the local advection rate of the legs due to the increase of the background velocity.

The simulations also showed that the vortices move away from each other due to viscous diffusion. Although this motion is very small and could not possibly be observed in the experiment, it indicates that substantial cancellation of the vorticity in the vortex legs should be expected. This can explain the large difference in the circulation of the head and the legs indicated in chapter 6, as suggested before by Acarlar & Smith (1987).

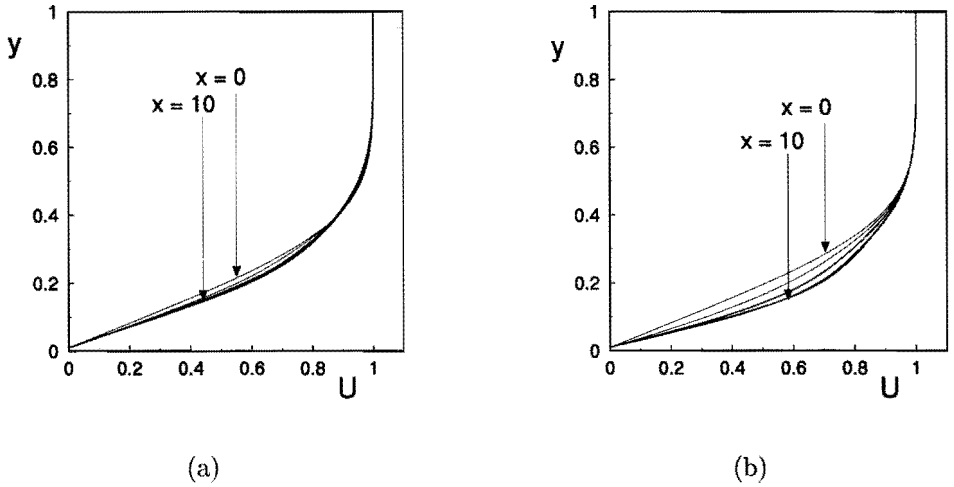


Figure 7.18: The evolution of the u -velocity profile at $z = 0.25$ (adjacent to the streamwise counter-rotating vortices) with $|\Gamma| = 0.03$ at $Re = 1900$ for $\delta/L = 3$. (a) without standing vortex (b) with standing vortex

The streamwise velocity profile The first conclusion should be that vortices with a circulation of the same magnitude as estimated for the hairpin vortex legs, are indeed able to create substantial deformation of the u -velocity profile within the length scale of the experiment. In addition, the standing vortices are indeed able to produce a substantial increase in the near-wall velocity, although the simulations indicate that the increase is less than in the case of the experiments (chapter 5).

It was observed in the experiments that for the case of the droplet, a rise midway in the legs occurs, that was called the secondary deformation of the legs. This deformation leads to the creation of a secondary vortex just above the location of this rise (see chapter 3). In the foregoing section it has been shown that the legs create an inflectional profile in the streamwise velocity, as shown in figure 7.16. It is likely that the creation of this inflectional profile is related to the creation of the secondary vortex that is observed in the experiment. This is supported by the fact that the secondary vortex is only observed in the case of the droplet, where a background velocity gradient exists over the entire region from the wall to the head of the vortex, and not in the case of the hemisphere, where the background velocity gradient is concentrated near the wall. This might also account for the fact that in the case of the droplet, the legs seemed to have more effect on the u -velocity profile than in the case of the hemisphere. If this inflectional profile is indeed created by the legs, it should be recalled that, due

to the effect of the quasi-spanwise vortex, just behind the head, the lower part of the necks is drawn towards the wall again (see chapter 3). It is likely that such an effect rapidly destabilizes an inflectional u -profile.

In figures 7.15 the effect of the streamwise vortices on the u -velocity was shown. The figures demonstrate that the effect of the legs on the near-wall fluid is mainly to draw up low speed fluid from the wall. This is surprising because it means that the high speed patches, which were prominent in the measurements (chapter 5), are hardly observed in the simulations. In addition, both the visualizations and the hot-wire measurements indicated that the near-wall velocity was increased (also reported by Acarlar & Smith (1987)), an effect that cannot be observed in the simulations. Probably, this is due to the fact that, in the experiment, the legs are oriented at an angle with the wall and are not really neat streamwise vortices as in the case of the simulation. A full 3D simulation is required to calculate these effects properly.

The 2D simulations have many limitations for a complete understanding of the dynamics of hairpin vortices. They can only address a limited range of topics in the evolution of a 3D hairpin vortex. Nevertheless, the results support the measurements where this should be expected and they indicate the same order of magnitude of various effects. In addition, they give some new physical insight. A more elaborate approach requires an instationary 3D code, as is presently under development.

Chapter 8

Concluding remarks

8.1 Conclusions and Discussion

8.1.1 The experimental results

The background velocity field The visualizations shown in chapter 3 indicate that downstream of a droplet a long wake exists whose length decreases by increasing Re_D . Downstream of a hemisphere a short wake is observed that does not become shorter by an increase in Re_D . This observation suggests that the presence of the standing vortex affects the size of the wake to such an extent that, for all Reynolds numbers examined here, the wake is destabilized immediately downstream of the recirculation area. An increase in Re_D tends to decrease the length of the wake, but for the hemisphere the wake simply cannot become shorter anymore.

In chapter 5 the velocity profile in the wake of the obstruction is shown for various values of Re_D . From a comparison between the velocity profiles for the droplet and the hemisphere, it is concluded that the standing vortex substantially increases the near-wall velocity downstream of the obstruction. This confirms the suggestion that the standing vortex affects the flow sufficiently to have a large destabilizing effect on the wake area. In addition, the velocity profiles show that the dimensionless velocity u/U also becomes larger in the wake with an increase in Re_D . It is suggested that this is due to a reduction of the boundary layer thickness in which the obstacle is embedded. A decrease of the boundary layer thickness increases the effect of the standing vortex.

The vortex shedding The shedding frequency of the hairpin vortices is found to be larger for the hemisphere than for the droplet. In addition, the shedding frequency does not change when the hemisphere is placed on a grooved wall. For the droplet, the Strouhal number increases by an increase in the Reynolds number, whereas for the hemisphere the Strouhal number remains constant.

This resembles the effect of the Reynolds number on the length of the wake: a droplet has a longer wake that gets shorter when increasing Reynolds number, whereas the hemisphere has a short wake that is not shortened any further by an increase in the Reynolds number. It seems that the perturbing effect of the standing vortex both shortens the wake and increases the shedding frequency. Although hairpin vortices can be observed over a wide range of Reynolds numbers, a regular hairpin vortex street is only found within a narrow range. For the hemisphere, a regular vortex street requires Reynolds numbers within the range $1600 < Re_D < 2000$. For $Re_D > 2000$ the increased interaction between the subsequent vortices increasingly distorts the vortex street. In particular, irregular behaviour seems to originate from the interaction of the legs with the head of the subsequent vortex, as shown in chapter 3. For the droplet, it was observed that the Reynolds number should be in the range $1900 < Re_D < 2400$. The lower limit is probably related to some irregularity induced by the longer wake area, the higher limit is again due to the increasing interaction between the hairpin vortices. Note that the distance between two successive vortices is larger for a droplet than for a hemisphere, due to the lower shedding frequency.

The effect of the background velocity profile on the vortex shape The most prominent effect of the background velocity profile occurs downstream of the wake, where the background velocity field affects the development of the hairpin vortex shape. The legs of the hairpin vortex are stretched by the positive $\partial u/\partial x$ -gradient that is present at the downstream side of the obstruction. This concentrates the vorticity in the centre of the legs and makes the radius of the legs much smaller than the radius of the head. In addition, the spanwise w -velocity of the flow around the obstacle pushes the legs together. In this way the characteristic hairpin-shape is obtained with a large spanwise head and two thin streamwise legs close to each other.

Due to the wake of the obstruction, the lower part of the hairpin vortex (below $y/D = 0.5$) tends to be retarded. This was observed for the droplet, as well as for the hemisphere when Re_D was below 1500. For the hemisphere, for Re_D above 1500, this retarding effect is largely cancelled by the substantial positive value of $\partial u/\partial x$ ¹. This Reynolds-dependency corresponds to the increased effect of the standing vortex on the velocity profile at higher Re_D , as indicated above. Further downstream, a secondary deformation of the hairpin vortex legs occurs for the droplet, which does not occur for the hemisphere. This secondary deformation is ascribed to the effect of the quasi-spanwise vortex on the vortex legs. Both the generation of the quasi-spanwise vortex and the effect of the quasi-spanwise vortex on the legs are influenced by the velocity profile (see chapter 3).

For the droplet, the creation of the quasi-spanwise vortices is related to the

¹This gradient is due to the effect of the standing vortex, that increases the near-wall velocity along the vortex trajectory.

patches of high-speed fluid adjacent to the legs. For the hemisphere, the quasi-spanwise vortex is generated by a different mechanism: the low-speed regions adjacent to the vortex trajectory² are destabilized by the effect of the hairpin vortex neck and roll up into quasi-spanwise vortices, as explained in chapter 3. The secondary deformation of the legs leads to the creation of a new spanwise vortex upstream of the original vortex head. Since the secondary deformation occurs only for the droplet, this new vortex is observed for the droplet but not for the hemisphere. This new vortex has also been observed by Acarlar & Smith (1987) and Doligalski et al. (1995). The latter also claim the generation of new vortices between the legs of the hairpin vortex, due to the upwelling of low-speed fluid by the legs. These vortices have not been observed in the present experiments.

Internal dynamics of the hairpin vortex The Biot-Savart analysis in chapter 6 indicates that the vortex head and necks contain a substantially larger circulation than the vortex legs. In the case of the hemisphere on a smooth wall, the dimensionless circulation in the head was estimated at $\Gamma = -0.26$ whereas the circulation in the legs was found to be of the order $|\Gamma| \approx 0.024$.

Only the configuration of the hemisphere on a smooth wall has been examined in this way. For a hemisphere, the legs are very close together and mutual cancellation of the vorticity might be very important, while for the droplet, the necks and the downstream part of the legs are separated further from their counterparts, which reduces their cancellation and leads to a higher circulation. The numerical simulations indicate that, given the experimental values for the Reynolds number and the circulation of the legs, mutual cancellation of vorticity plays an important role in the vortex legs. This can also be illustrated by an analytical argument. For an isolated Gaussian vortex with a dimensionless radius $R^*(t)$ the radius is a function of the dimensionless time t^* according to:

$$R^*(t) = \sqrt{R^{*2} + 4t^*/Re}$$

This means that with $Re = 1900$, at $t^* = tU/D = 10$ (a timescale approximately corresponding to the experiment), the radius has already grown from an initial value $R^* = R/D = 0.035$ (as used in the simulations) to a value of 0.15. In reality, the growth is even stronger since the legs are advected with a velocity that is lower than the mean flow velocity U . Recall that the half distance between the legs is approximately $R^* \approx 0.1$ (as indicated by the visualizations), so a substantial overlap of the legs should be expected. It seems likely that, initially, the hairpin vortex has the strongest legs in the case of the hemisphere (since the standing vortex creates a large near-wall velocity and therefore the circulation in the vortex wake is higher). However, due to mutual cancellation (by cross-diffusion), its legs quickly lose their circulation and only a strong head

²These low-speed regions are created at the far side of the standing vortex as indicated in chapter 2.

and two strong necks remain. In the case of the droplet, the downstream parts of the legs are separated further. Therefore, their mutual cancellation is reduced and the legs remain stronger. This effect might account for the observation that for the droplet the direct effect of the vortex legs on the u -velocity field is stronger than for the hemisphere, as shown by the hot-wire measurements. However, this is not the only explanation: the larger effect of the legs is also partially due to the legs being located in a region with a larger $\partial u/\partial y$. An indication for this is given in chapter 7 where the effect of the vortex legs on the u -velocity profile is simulated.

Theoretically, the vortex legs push each other upwards in the flow. The vortex head is pushed backwards by the effect of its mirror image and the necks and upwards by the effect of the necks and the legs. In the present experiments, the retarding effect of the necks and the wall on the head could not be observed. According to the estimates for the circulation in the vortex head, obtained in chapter 6, given its distance from the wall, it seems that the effect of the mirror image of the vortex head can be ignored.

The vortex head rises in the flow. This rise is most rapid when the head is just created and decreases when the hairpin vortex is advected downstream. The measurements indicate that for the hemisphere on a smooth surface, the head rises more rapidly than in the case of the droplet. On the other hand, for the droplet, the neck might be expected to push the head upwards more than in the case of the hemisphere, since it is aligned more in the direction of the flow. Probably, although the neck pushes the head upwards, the quasi-spanwise vortex has a larger effect on the motion of the vortex head than the neck. In the case of the hemisphere, the quasi-spanwise vortex is located somewhat downstream of the head and therefore it pushes the head slightly upwards. In the case of the droplet, the quasi-spanwise vortex is located upstream of the head and therefore it draws the head towards the wall.

The mutually induced velocity of the legs did not seem to be a prominent effect. This may be expected from the low value of their circulation. The simulations indicated that, with a circulation of $|\Gamma| = 0.03$, the rise of the legs would be at most $\Delta y/D \approx 0.15$ over the measurement section. However, the observation of the motion of the legs is obscured by the effect of the subsequent vortex, as well as by the shear-effect. Therefore, no very strong claims can be made for their mutually induced velocity.

The effect of the hairpin vortex on the near-wall fluid The hairpin vortices strongly increase the average near-wall velocity, as indicated by both the hot-wire measurements and the visualizations. It seems that the effect of the hairpin vortex on the near-wall fluid is mainly determined by the effect of the legs and the necks. The necks and legs create patches of high-speed fluid adjacent to the vortex. This results in a series of alternating high- and low-speed areas that is supposed to be related to the creation of the quasi-spanwise

vortex, as indicated in chapter 3. The standing vortex also increases the average near-wall velocity. Therefore, for the hemisphere, the velocity difference between the alternating high- and low-speed areas decreases and the creation of a quasi-spanwise vortex is delayed.

The increase of the near-wall velocity is caused by the necks and the legs of the hairpin vortex. However, it is not easy to reconstruct the details of the mechanism by which this happens. The effect of the legs was simulated with a parabolic 3D stationary code. With this code, the only situation that could be simulated was the one in which the legs were initially parallel with the wall. It is concluded that in this case the legs hardly increase the near-wall velocity. It is suggested that the angle of the legs with the wall is essential for the experimentally observed increase of the near-wall velocity.

The effect of the riblets It was indicated that the riblets tend to weaken the standing vortex. The hot-wire measurements show that, when riblets are present, the velocity profile downstream of the hemisphere resembles the case of the droplet. In particular, the upward motion of the head decreases and a rise in the legs occurs that leads to the creation of a secondary vortex, just as in the case of the droplet. These observations emphasize the importance of the effect of the standing vortex.

The generalization of the results It is not obvious that the present results can be extended to a boundary layer velocity profile that is not artificially disturbed. For all measurements presented in this thesis, the background velocity field was strongly influenced by the wake of the obstruction (for the droplet) or by the standing vortex (for the hemisphere). This means that the cases presented here can not be assumed to be fully applicable to the evolution of hairpin vortices in a turbulent boundary layer. However, the reported mechanisms can be expected to play a similar role in real turbulence. In particular, it is demonstrated that the velocity profile plays an important role in the evolution of the hairpin vortex and its generation of secondary vortices. This conclusion will still hold in a real turbulent boundary layer flow.

8.1.2 The results of the simulations

The motion of a spanwise vortex The simulations show that the motion of a spanwise vortex in a shear flow is affected by $\partial\omega/\partial y$. In particular, a negative vortex is drawn towards the wall while a positive vortex is pushed away from it. This effect is found to strongly influence the motion of the spanwise vortex. This analysis indicates that an isolated hairpin vortex head should move towards the wall. However, the visualizations indicate a rise of the hairpin vortex head away from the wall. It seems that the effect of the vorticity in the background flow is smaller than the other effects that influence the motion of a hairpin

vortex head (such as the effect of the legs of the vortex or the effect of the quasi-spanwise vortex).

Although, in our experiments, the effect of the boundary layer vorticity is not sufficiently strong to draw the hairpin head towards the wall, the effect might be more important in a real turbulent flow. In that case, this mechanism might provide a clue to the generation of new vortices at the wall in a real flow. In the conceptual picture given by Hinze (1975) the creation of a new hairpin vortex at the wall is initiated by some outer layer structure that causes a near-wall disturbance. The effect of the boundary layer vorticity, as explained above, provides a mechanism that pushes a large vortex from the outer part of the boundary layer towards the wall again. This effect might account for the generation of some of the new turbulent eddies at the wall.

The effect of streamwise vortices on the u -velocity The legs of a hairpin vortex are able to create a strong inflectional u -profile as long as they are embedded in the lower part of the laminar boundary layer. This observation corresponds to the fact that in a turbulent boundary layer, secondary vortices are created in the inner part of the boundary layer where the velocity gradient is largest.

This mechanism can be related to some experimental observations shown in chapter 5. The hot-wire measurements in this chapter indicate that the direct effect of the legs on the u -velocity field is larger for the droplet than for the hemisphere. For the droplet, the legs create a strong velocity gradient above the location where they rise in the flow (due to the secondary deformation) and both the hot-wire measurements and the visualizations indicate that a new vortex is created at this location. These effects do not occur for the hemisphere. This is explained by the fact that for the droplet, the legs are embedded within a region with a substantial velocity gradient. For the hemisphere, the near-wall velocity gradient is concentrated closer to the wall and the legs largely seem to move over it (see chapter 3). It seems that the case of the hemisphere can be compared to the simulation of the vortex legs above a thin boundary layer, while the case of the droplet can be compared to the case of the vortex legs embedded within a thick boundary layer. However, the observed correspondance is only tentative, since our simulations are restricted to stationary vortex legs whose vorticity is strictly parallel to the wall.

8.2 Suggestions for further research

- The present experimental results have been obtained by a combination of flow visualization and single-wire hot-wire measurements. Both techniques have their limitations. To improve on the present measurements, it would be worthwhile to measure the v -velocity in combination with the u -velocity (e.g. with cross-wires or two-component LDA). This would allow for a

more accurate determination of the effect of the legs and would lead to a better estimate of the circulation in the legs. In the explanation of the present measurements, the v -velocity often had to be inferred from the change in the u -velocity (for instance when it is claimed that high speed fluid is 'dragged towards the wall'). It is better to measure these effects directly.

- It is shown that the standing vortex strongly affects the wake and the hairpin vortex shedding downstream of the hemisphere. It is interesting to see whether the standing vortex can be removed by other means, such as suction, and what the effects of its absence are on the shedding frequency, the length of the wake and the evolution of the hairpin vortices. Similarly, it might be interesting to investigate these phenomena when injecting high-speed fluid into the wake of the droplet.
- In the present measurements, a comparison has been made between three configurations: a hemisphere on a grooved and a smooth wall and a droplet on a smooth wall. In the case of the hemisphere, the most dominant effect of the riblets was the weakening of the standing vortex. In order to gain insight into the drag reducing properties of riblets, it would be more interesting to see what the effect of these riblets is when no standing vortex is present. Therefore, more insight will be gained by examining the fourth case too: the evolution of hairpin vortices downstream of a droplet on a wall with riblets. In this case, ordinary triangular riblets should be used and not the more complicated riblet shape that was used in the present experiments.
- The presented simulations have been performed using a parabolic 3D code. It appeared that this code was not able to reproduce the experimentally observed increase in the near-wall velocity in the region below the hairpin vortex with the estimated values of the parameters. It is suggested that this is due to the fact that in the experiments, the hairpin vortex legs are advected under an angle to the wall: a case that cannot be simulated with our code. In order to find out whether this attribution is correct, it should be examined if this increase in the near-wall velocity can be reproduced with a full 3D instationary code. Instead of trying to simulate with this code a complex structure like a hairpin vortex, it could be sufficient to simulate the effect of a simple vortex pair on the near-wall velocity, when this pair is advected under an angle with the wall while embedded in a laminar boundary layer profile.

Appendix A

The numerical code

A.1 Annotation

Throughout this appendix, Δ will indicate a discretization step, j will indicate the x -coordinate, k the y -coordinate and l the z -coordinate, while n will indicate the time coordinate. The spatial coordinates will be indicated in subscript while the time coordinate will be indicated in superscript. For example, ω_{jk}^n is the vorticity at location $x = j\Delta x$, $y = k\Delta y$ at time $n\Delta t$.

In addition, a shorthand notation will be used for the first- and second-order differences. In the x -direction, for example, these will be indicated by L_x and L_{xx} , respectively.

A.2 Description of the numerical program

A.2.1 The equations

Two-dimensional equations The method used for the calculations is a finite difference scheme using central (second-order accurate) differences. The equations are solved by an *Alternating Direction Implicit*-method (Fletcher 1988, Hirsch 1988) solving a Poisson equation.

The equations for the calculations in the xy -plane are the transport equation for the vorticity and the Poisson equation relating ω and ψ (in which a quasi-temporal term is added):

$$\frac{\partial \omega}{\partial t} + \frac{\partial}{\partial x} \left(\omega \frac{\partial \psi}{\partial y} \right) + \frac{\partial}{\partial y} \left(-\omega \frac{\partial \psi}{\partial x} \right) - \frac{1}{Re} \left(\frac{\partial^2 \omega}{\partial x^2} + \frac{\partial^2 \omega}{\partial y^2} \right) = 0 \quad (\text{A.1})$$

$$\frac{\partial \psi}{\partial \tau} - \left(\frac{\partial^2 \psi}{\partial x^2} + \frac{\partial^2 \psi}{\partial y^2} + \omega \right) = 0 \quad (\text{A.2})$$

In these equations, the sign of the vorticity is defined by:

$$\omega \equiv \frac{\partial v}{\partial x} - \frac{\partial u}{\partial y} \quad (\text{A.3})$$

Starting the calculation, one has a velocity field and the initial distribution of the vorticity, $\omega^{t=0}$. For calculating the evolution of this initial situation, first the vorticity equation is solved after the time step Δt . For this first step, in equation (A.1) $\partial\psi/\partial y$ is replaced by the initial value for u and similarly $-\partial\psi/\partial x$ is replaced by the initial value for v . The vorticity equation gives the vorticity distribution at one time step later, $\omega^{t=1}$. Next, $\omega^{t=1}$ is introduced into the modified Poisson equation. From this, the corresponding value for the stream function, $\psi^{t=1}$, is determined from equation (A.2) using an iterative procedure¹. Then the next value for the vorticity, $\omega^{t=2}$, can be calculated. This procedure is repeated up to a specified number of time steps.

The accuracy of the new value for ψ is determined by a threshold value ϵ for the largest value of $\Delta\psi^{n+1}$ in the computational domain; as long as any value of ψ_{jk} is changed too much in two successive iterations, the iteration is continued. The value for ϵ is chosen by the user².

Equations (A.1) and (A.2) can now be rewritten into a three-level scheme³. Using

$$u = \partial\psi/\partial y$$

$$v = -\partial\psi/\partial x$$

¹The modification of the Poisson equation is required by the use of the iterative procedure. Essentially, the modification turns the analytical Poisson equation into a time dependent differential equation of a type that corresponds to an exponentially converging solution, where the convergence speed is proportional to $\Delta\tau$. In this way, for a given value of ω_{jk} , after a number of fictitious time steps $\Delta\tau$ a sufficiently accurate value for the corresponding ψ_{jk} is found. These time steps are fictitious because, in contrast to the evolution of ω , the evolution of ψ towards an accurate solution of the Poisson equation has nothing to do with the time evolution of the flow simulated here; in the real flow the stream function takes on the appropriate form corresponding to the vorticity distribution instantaneously. Therefore, $\Delta\tau$ and Δt are not in any way related to each other. The fictitious time steps $\Delta\tau$ just resemble successive steps in an iterative procedure.

²Each subsequent step introduces a small inaccuracy. Therefore, when the time step Δt is made smaller and the number of steps is thus increased, ϵ should be decreased to retain the same overall accuracy (although this effect is usually very small). In addition, to retain the same accuracy, ϵ should also be decreased when $\Delta\tau$ is made smaller, because $\Delta\psi^{n+1}$ is not the difference in ψ as compared to the final solution (which is unknown), but as compared to the solution found in the previous step of the iteration, which becomes small automatically when $\Delta\tau$ becomes small. However, $\Delta\tau$ should not become too large either, because then $\Delta\psi^{n+1}$ would become too large, which results in an overshoot with respect to the proper value for ψ . The differential equation (A.2) might then result in an oscillatory exponential amplification of $\Delta\psi^{n+1}$ which results in a breakdown of the computation.

³In a three-level scheme by definition a quantity q^{n+1} is calculated from q^n and q^{n-1} . In this case we have a three-level scheme because $\Delta\omega^n$ implicitly contains ω^{n-1} .

and defining that $\Delta\omega^n \equiv (\omega^n - \omega^{n-1})$, the vorticity equation becomes

$$\begin{aligned} & \frac{(1 + \gamma)\Delta\omega_{jk}^{n+1} - \gamma\Delta\omega_{jk}^n}{\Delta t} = \\ & -(1 - \beta)(L_x u + L_y v)\omega_{jk}^n - \beta(L_x u + L_y v)\omega_{jk}^{n+1} + \\ & \frac{1 - \beta}{Re}(L_{xx} + L_{yy})\omega_{jk}^n + \frac{\beta}{Re}(L_{xx} + L_{yy})\Delta\omega_{jk}^{n+1} \end{aligned} \quad (\text{A.4})$$

while the modified Poisson equation becomes

$$\begin{aligned} \frac{((1 + \gamma)\Delta\psi_{jk}^{n+1} - \gamma\Delta\psi_{jk}^n)}{\Delta\tau} &= (1 - \beta)(L_{xx} + L_{yy})\psi_{jk}^n + \\ & \beta(L_{xx} + L_{yy})\psi_{jk}^{n+1} + \omega_{jk} \end{aligned} \quad (\text{A.5})$$

In these equations β and γ are introduced. Clearly, β and γ both determine the extent to which the discretization is implicit: for $\beta = 0$ and $\gamma = 0$ the equation is fully explicit.

The right-hand terms in equation (A.5) can now be rewritten, using

$$(1 - \beta)\psi^n + \beta\psi^{n+1} = \psi^n + \beta\Delta\psi^{n+1}$$

A similar procedure is applied for ω in the right-hand side of equation (A.4), and then all terms containing $\Delta\omega^{n+1}$ and $\Delta\psi^{n+1}$ are shifted to the left hand side. This results in the three-level scheme that has been used.

The ADI-method implies that in order to calculate one new time step, both equations are solved in two successive half time steps. In the first half time step the equation is solved with respect to the x -derivatives while in the second time step the equation is solved with respect to the y -derivatives. Both separate steps can be written in the form of a tridiagonal matrix equation that is solved efficiently by the Thomas-algorithm. For this procedure the above equations have to be split in an x - and a y -part. For $\Delta\psi^{n+1}$ this can be done by the approximation:

$$\left(1 - \frac{\beta\Delta\tau}{(1 + \gamma)}(L_{xx} + L_{yy})\right)\Delta\psi_{jk}^{n+1} \approx \left(1 - \frac{\beta\Delta\tau}{(1 + \gamma)}L_{xx}\right) \times \left(1 - \frac{\beta\Delta\tau}{(1 + \gamma)}L_{yy}\right)\Delta\psi_{jk}^{n+1}$$

and in a similar way for $\Delta\omega^{n+1}$. For the first half time step the modified Poisson equation therefore becomes

$$\begin{aligned} \left(1 - \frac{\beta\Delta\tau}{(1 + \gamma)}L_{xx}\right)\Delta\psi_{jk}^{n+\frac{1}{2}} &= \frac{\Delta\tau}{(1 + \gamma)}(L_{xx} + L_{yy})\psi_{jk}^n + \frac{\gamma}{1 + \gamma}\Delta\psi_{jk}^n + \\ & \frac{\Delta\tau}{(1 + \gamma)}\omega_{jk}^n \end{aligned} \quad (\text{A.6})$$

and for the second it is

$$\left(1 - \frac{\beta\Delta\tau}{(1+\gamma)}L_{yy}\right)\Delta\psi_{jk}^{n+1} = \Delta\psi_{jk}^{n+\frac{1}{2}} \quad (\text{A.7})$$

In the same way, the vorticity transport equation is split in two separate equations. In the first half time step the equation to be solved is:

$$\begin{aligned} \left(1 - \frac{\beta\Delta t}{Re(1+\gamma)}L_{xx} + \frac{\beta\Delta t}{1+\gamma}L_x u_{jk}^n\right)\Delta\omega_{jk}^{n+\frac{1}{2}} = \\ \frac{\Delta t}{Re(1+\gamma)}(L_{xx} + L_{yy})\omega_{jk}^n + \frac{\gamma}{1+\gamma}\Delta\omega_{jk}^n \\ - \frac{\Delta t}{1+\gamma}(L_x u_{jk}^n \omega_{jk}^n + L_y v_{jk}^n \omega_{jk}^n) \end{aligned} \quad (\text{A.8})$$

and in the second step this is:

$$\left(1 - \frac{\beta\Delta t}{Re(1+\gamma)}L_{yy} + \frac{\beta\Delta t}{1+\gamma}L_y v_{jk}^n\right)\Delta\omega_{jk}^{n+1} = \Delta\omega_{jk}^{n+\frac{1}{2}} \quad (\text{A.9})$$

Finally, values should be chosen for γ and β . Several simulations were made to establish proper values for these parameters. It was found that γ hardly had any effect on the results of the calculation and therefore was set to zero. It was also found that β should not be taken too small in order for the ψ calculation to converge. This was to be expected because a fully explicit scheme is less stable than an implicit scheme. As long as the value chosen for β was sufficiently large, it had no significant effect on the results of the calculation. As long as $\beta \geq 0.5$ the program continued to converge. The value $\beta = 1.0$, which was used for the computations, corresponds to the fully implicit scheme. The time step Δt was chosen according to the CFL criterion to be a constant fraction of Δx .

Parabolic three-dimensional equations For the computation of the downstream evolution of the vorticity⁴, from the current vorticity and velocity fields the next value is determined for ω_{kl} and u_{kl} . Then ψ_{kl} is determined by iteration. Then, again, ω_{kl} and u_{kl} are determined at the next x -location. Essentially, the procedure simulates a steady initial vorticity distribution at $x = 0$ whose downstream effects are to be determined (see figure A.1). In accordance with equation A.3, the sign of the vorticity is defined by

$$\omega_x \equiv \frac{\partial w}{\partial y} - \frac{\partial v}{\partial z} \quad (\text{A.10})$$

The full steady equations for ω_x , ψ_x and u are

$$\frac{\partial(u\omega_x)}{\partial x} + \frac{\partial}{\partial y} \left(-\omega_x \frac{\partial\psi_x}{\partial z} \right) + \frac{\partial}{\partial z} \left(\omega_x \frac{\partial\psi_x}{\partial y} \right) - \omega_x \frac{\partial u}{\partial x}$$

⁴Note that the indices kl are now used, corresponding to the YZ -plane in which the streamwise vorticity ω_x is determined.

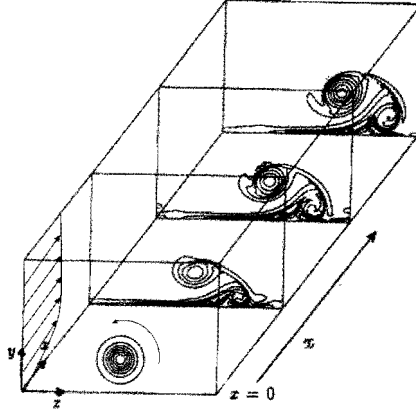


Figure A.1: The parabolic three-dimensional code computes the stationary downstream evolution of a streamwise vortex.

$$-\omega_y \frac{\partial u}{\partial y} - \omega_z \frac{\partial u}{\partial z} - \frac{1}{Re} \left(\frac{\partial^2 \omega_x}{\partial x^2} + \frac{\partial^2 \omega_x}{\partial y^2} + \frac{\partial^2 \omega_x}{\partial z^2} \right) = 0 \quad (\text{A.11})$$

$$\frac{\partial \psi_x}{\partial \tau} - \left(\frac{\partial^2 \psi_x}{\partial x^2} + \frac{\partial^2 \psi_x}{\partial y^2} + \frac{\partial^2 \psi_x}{\partial z^2} + \omega_x \right) = 0 \quad (\text{A.12})$$

$$2u \frac{\partial u}{\partial x} + \frac{\partial(vu)}{\partial y} + \frac{\partial(wu)}{\partial z} + \frac{\partial p}{\partial x} - \frac{1}{Re} \left(\frac{\partial^2 u}{\partial x^2} + \frac{\partial^2 u}{\partial y^2} + \frac{\partial^2 u}{\partial z^2} \right) = 0 \quad (\text{A.13})$$

In these equations, several terms have to be discarded to make them manageable. In particular, all second derivatives with respect to x are neglected. For ω and u this implies that the diffusion of vorticity and impulse in the x -direction are negligible in comparison with the convective terms, which seems to be a reasonable assumption. The application of the Poisson equation in two dimensions implies that in any yz -plane two-dimensional continuity is supposed to hold: effects of a nonzero in- or outflow in any yz -plane are supposed to be negligible⁵. In addition, the pressure term in the equation for u is discarded.

Now the terms in the vorticity-equation containing ω_y and ω_z can be rewritten:

$$-\omega_y \frac{\partial u}{\partial y} - \omega_z \frac{\partial u}{\partial z} = \left(\frac{\partial w}{\partial x} - \frac{\partial u}{\partial z} \right) \frac{\partial u}{\partial y} + \left(\frac{\partial u}{\partial y} - \frac{\partial v}{\partial x} \right) \frac{\partial u}{\partial z} = \frac{\partial w}{\partial x} \frac{\partial u}{\partial y} - \frac{\partial v}{\partial x} \frac{\partial u}{\partial z}$$

In order to be able to compute vortex-stretching and -tilting effects, these streamwise gradients are retained. Therefore, during a run of the program,

⁵Although this procedure is somewhat questionable, it is based on the assumption that the effect of this approximation is small since the $\partial u/\partial x$ -terms are relatively small. This is especially true when ω_x is small, as is the case in the simulations of chapter 7.

the old values for v_{kl} and w_{kl} are stored in order to be able to compute $\partial v/\partial x$ and $\partial w/\partial x$ with first-order accuracy. With respect to everything else, the same applies as for the two-dimensional equations. The final three-level splitted equations for ω and u now become the following. For ω_x the first half x -step becomes (the subscript x is dropped):

$$\begin{aligned} \left(1 - \frac{\beta\Delta x}{\text{Re}(1+\gamma)u_{kl}^n}L_{zz} + \frac{\beta\Delta x}{(1+\gamma)u_{kl}^n}L_z w_{kl}^n\right) \Delta\omega_{kl}^{n+\frac{1}{2}} &= \frac{\gamma}{1+\gamma}\Delta_{kl}^n + \\ \frac{\Delta x}{\text{Re}(1+\gamma)u_{kl}^n}(L_{yy} + L_{zz})\omega_{kl}^n - \frac{\Delta x}{(1+\gamma)u_{kl}^n}(L_y v_{kl}^n + L_z w_{kl}^n)\omega_{kl}^n + \\ \frac{\Delta x}{(1+\gamma)u_{kl}^n} \left(-\frac{\Delta w_{kl}^n}{\Delta x}L_y u_{kl}^n + \frac{\Delta v_{kl}^n}{\Delta x}L_z u_{kl}^n\right) \end{aligned} \quad (\text{A.14})$$

and the second half x -step is

$$\left(1 - \frac{\beta\Delta x}{\text{Re}(1+\gamma)u_{kl}^n}L_{yy} + \frac{\beta\Delta x}{(1+\gamma)u_{kl}^n}L_y v_{kl}^n\right) \Delta\omega_{kl}^{n+1} = \Delta\omega_{kl}^{n+\frac{1}{2}} \quad (\text{A.15})$$

while for u the first half x -step becomes

$$\begin{aligned} \left(1 - \frac{\beta\Delta x}{2\text{Re}(1+\gamma)u_{kl}^n}L_{zz} + \frac{\beta\Delta x}{2(1+\gamma)u_{kl}^n}L_z w_{kl}^n\right) \Delta u_{kl}^{n+\frac{1}{2}} &= \\ \frac{\gamma}{1+\gamma}\Delta u_{kl}^n + \frac{\Delta x}{2\text{Re}(1+\gamma)u_{kl}^n}(L_{yy} + L_{zz})u_{kl}^n \\ - \frac{\Delta x}{2(1+\gamma)u_{kl}^n}(L_y v_{kl}^n + L_z w_{kl}^n)u_{kl}^n \end{aligned} \quad (\text{A.16})$$

and the second half x -step is

$$\left(1 - \frac{\beta\Delta x}{2\text{Re}(1+\gamma)u_{kl}^n}L_{yy} + \frac{\beta\Delta x}{2(1+\gamma)u_{kl}^n}L_y v_{kl}^n\right) \Delta u_{kl}^{n+1} = \Delta u_{kl}^{n+\frac{1}{2}} \quad (\text{A.17})$$

A.2.2 The discretization

The discretization determines which grid points are involved in the evaluation of the derivatives L_x , L_y , L_{xx} and L_{yy} . For both the first and second-order spatial differences, three-point central differences have been used. The expressions are:

$$L_x(u\omega)|_{j,k} = \frac{1}{\Delta x}(u_{j+\frac{1}{2},k}\omega_{j+\frac{1}{2},k} - u_{j-\frac{1}{2},k}\omega_{j-\frac{1}{2},k}) \quad (\text{A.18})$$

$$L_{xx}\omega|_{j,k} = \frac{1}{\Delta x^2}(\omega_{j+1,k} - 2\omega_{j,k} + \omega_{j-1,k}) \quad (\text{A.19})$$

The expression $u_{j+\frac{1}{2},k}$, that is used in equation (A.18), is a shorthand notation for $(u_{j+1,k} + u_{j,k})/2$, and likewise for the other expressions.

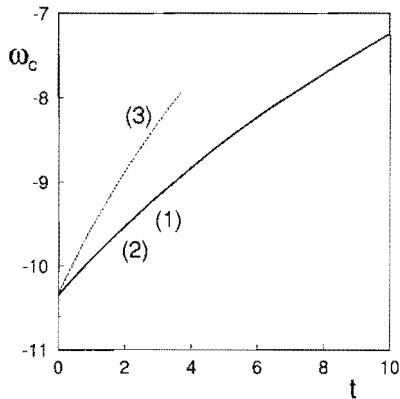


Figure A.2: The vorticity in the centre of a Gaussian vortex with $\Gamma = -2$ in a uniform velocity field at $Re = 1500$ for a grid size of $\Delta x \times \Delta y = 0.025 \times 0.013$. (1) analytical (2) central differences ($U = 0.0$) (3) central differences ($U = 1.0$)

In order to test the discretization, the development of a Gaussian vorticity distribution was computed in a uniform flow and the decay of the central vorticity was compared to the theoretically expected results. The results are shown in figure A.2. The figure shows that for a stationary vortex, the diffusion of the vorticity in the vortex core closely follows the theory. On the other hand, when the vortex is advected by a uniform flow with $U = 1$, the diffusion of the vorticity increases substantially. The resulting diffusion of the vorticity corresponds to an effective Reynolds number of 775, instead of 1500! It is beyond doubt that this has affected the results of the computations. However, it should be realized that the 'rebound' occurred due to the diffusion of vorticity at the wall, where the streamwise velocity is small and correspondingly, the artificial additional diffusion is small. In addition, although the absolute values are affected by the artificial diffusion, the trends indicated in chapter 7 are not.

For the 2D calculations on the spanwise vortex, the number of grid points was typically 600×300 for a domain of $x \times y$ equal to 15×4 . For $\Gamma = -2$ this produces a grid Reynolds number of up to $Re_c \approx 75$. This cell Reynolds number is rather large, but no oscillations appeared. Some calculations have been performed using a first-order upwind scheme, but this increased the artificial diffusion of the vorticity dramatically. Therefore, the central difference scheme was used for the computations in chapter 7. To prevent the occurrence of oscillations, we were limited to moderate values for the circulation of the vortex.

In addition, it was verified that a different value of the grid size did not result in notable differences with respect to the results of the calculation, as shown in figure A.3a. The smallest grid size in the figure is of the order of the grid size that was used for the computations (in chapter 7, $\Delta x \times \Delta y$ is typically 0.025×0.013). The small differences that occur are probably due to the increased diffusion that

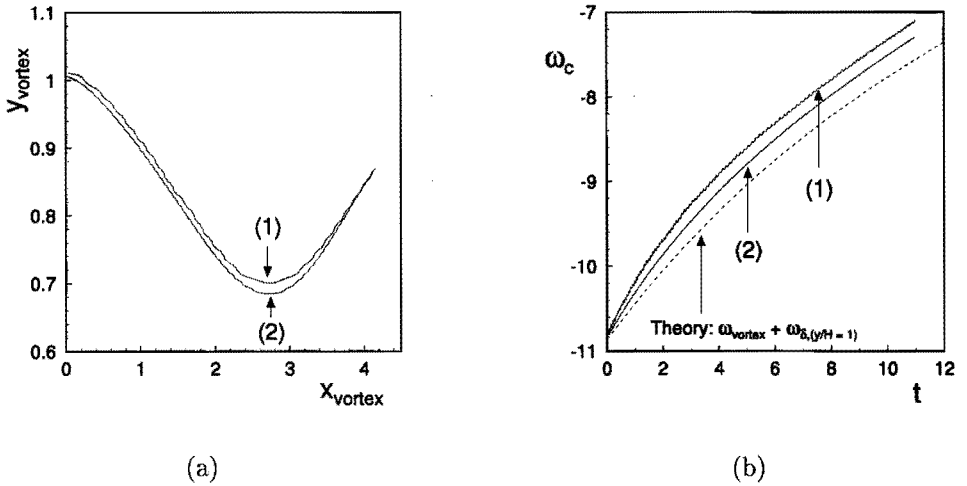


Figure A.3: The effect of the grid size for a vortex with $\Gamma = -2$, for $Re = 1500$, $U = 1$ and $\delta/H = 1.75$ (a) The vortex trajectory (b) The vorticity in the vortex centre (1) $\Delta x = 0.04$, $\Delta y = 0.02$ (250×200 grid points) (2) $\Delta x = 0.02$, $\Delta y = 0.01$ (500×400 grid points)

was indicated in figure A.2. This suggestion is also supported by figure A.3b. This figure shows that the decay of the vorticity at the location of the vortex centre increases for a larger grid size, which means that the artificial viscosity increases when a larger grid size is used. The broken line in the figure corresponds to the theoretically expected value for the vorticity in the centre of the vortex⁶, plus the additional vorticity that is due to the vorticity of the boundary layer⁷. The difference with the theoretically expected value is less than in figure A.2. This is due to the fact that the vortex is embedded entirely in the laminar boundary layer and is therefore advected with a velocity that is smaller than U : the artificial viscosity shown by figure A.2 really represents the worst case. Δt was typically set to $0.1\Delta x$. This makes the Courant number slightly smaller than 1 in this direction (the exact value depends on the circulation of the imposed spanwise vortex).

⁶This is given by

$$\omega_c = \frac{\Gamma}{\pi(4t/Re + R^2)}$$

⁷In the figure, a constant vorticity is added that corresponds to the vorticity at the initial location of the vortex. In reality, this additional vorticity is not constant but increases somewhat as the vortex moves towards the wall: the real difference with the theoretically expected value is therefore somewhat worse.

For the parabolic 3D calculations on the streamwise vortices, the number of grid points was typically set to 300×200 for a domain of $x \times y$ equal to 3×2 . This implies a grid Reynolds number of $Re_c \approx 1$. The step in the streamwise direction Δx is chosen to be 0.04. Since the time step t_{ij} is derived from $\Delta x/u_{ij}$, the Courant criterion is automatically satisfied.

A.3 The boundary conditions

At the plane of inflow, a Blasius velocity profile is inserted for $u_{0,k}$. The appropriate $\psi_{0,k}$ and $\omega_{0,k}$ distributions are calculated from this velocity profile.

For the 2D-calculations, the second-order derivatives were set to zero at the plane of outflow, as well as at the upper boundary. For instance:

$$\psi_{Nx+1,k} = 2\psi_{Nx,k} - \psi_{Nx-1,k}$$

and the same procedure is applied to u , v and ω ⁸. It was found that at the plane of outflow, these boundary conditions tend to push an approaching vortex with negative circulation down towards the wall. For a vortex of $\Gamma = -5.0$ this effect can already become significant as far as 2.5 unity lengthscales upstream of the outflow boundary. In order to verify that this effect did not have an effect on the results, a simulation was repeated with a different set of boundary conditions at the plane of outflow⁹. This did not have any effect on the vortex trajectories that are shown in chapter 7.

At the wall, u and ψ are set to zero and ω is calculated by the third-order expression

$$\omega_{j,0} = \frac{1}{2\Delta y^2}(\psi_{j,2} - 8\psi_{j,1} + 7\psi_{j,0}) \quad (\text{A.20})$$

as indicated by Fletcher (1988). The derivation of equation (A.20) is presented below.

For the parabolic 3D calculations, periodic boundary conditions were used at the sides of the domain. At the upper boundary of the domain as well as at the wall, the same conditions were applied as for the 2D computations. At the plane $x = 0$ the laminar boundary layer profile was used, and throughout the simulation, the u -velocity at the wall was kept at $u = 0.01$. It was not possible to use $u = 0$ because the equations (A.14) - (A.17) contain a factor $1/u$.

The vorticity boundary condition at the wall The boundary condition at a no-slip wall is $u_{j,0} = 0$. In second-order accuracy this implies that

$$\left. \frac{\partial \psi}{\partial y} \right|_{j,0} = \frac{1}{2\Delta y}(\psi_{j,1} - \psi_{j,-1}) = 0 \quad (\text{A.21})$$

⁸This set of conditions may seem somewhat unusual: if $\partial^2\psi/\partial x^2 = 0$, it is more consequent to set $\partial v/\partial x = 0$ than $\partial^2 v/\partial x^2 = 0$. However, it was found that this did not lead to any noticeable change in the result.

⁹ $\partial\psi/\partial x$ was set to zero, which was found to have a tendency to push the vortex upward.

while in third-order accuracy this becomes

$$\left. \frac{\partial \psi}{\partial y} \right|_{j,0} = \frac{1}{6\Delta y} (2\psi_{j,-1} + 3\psi_{j,0} - 6\psi_{j,1} + \psi_{j,2}) = 0 \quad (\text{A.22})$$

For the method of the derivation, see e.g. Hirsch (1988)¹⁰. The vorticity is given by

$$\frac{\partial^2 \psi}{\partial y^2} = -\omega$$

which is in three-point central differences at the wall:

$$\omega_{j,0} = -\frac{1}{\Delta y^2} (\psi_{j,-1} - 2\psi_{j,0} + \psi_{j,1}) \quad (\text{A.25})$$

An expression for $\psi_{j,-1}$ should be inserted in equation (A.25) that satisfies $\partial\psi/\partial y = 0$ at the wall. This expression can be obtained from equation (A.22), which produces equation (A.20). Note that if no special wall boundary condition is applied for the vorticity and $\psi_{j,-1}$ is just set to zero, for a linear near-wall velocity profile the resulting wall vorticity as calculated from equation (A.25) is exactly half the value it should be.

¹⁰The third-order accurate expression for $\left. \frac{\partial \psi}{\partial y} \right|_{j,0}$ can be found from the general claim that

$$\left. \frac{\partial \psi}{\partial y} \right|_{j,0} = \frac{1}{\Delta y} (a\psi_{j,-1} + b\psi_{j,0} + c\psi_{j,1} + d\psi_{j,2})$$

and by the subsequent Taylor expansion of the ψ -function at these locations:

$$\begin{aligned} \psi_{j,-1} &= \psi_{j,0} - \Delta y \left. \frac{\partial \psi}{\partial y} \right|_{j,0} + \frac{\Delta y^2}{2} \left. \frac{\partial^2 \psi}{\partial y^2} \right|_{j,0} - \frac{\Delta y^3}{6} \left. \frac{\partial^3 \psi}{\partial y^3} \right|_{j,0} + \dots \\ \psi_{j,1} &= \psi_{j,0} + \Delta y \left. \frac{\partial \psi}{\partial y} \right|_{j,0} + \frac{\Delta y^2}{2} \left. \frac{\partial^2 \psi}{\partial y^2} \right|_{j,0} + \frac{\Delta y^3}{6} \left. \frac{\partial^3 \psi}{\partial y^3} \right|_{j,0} + \dots \\ \psi_{j,2} &= \psi_{j,0} + 2\Delta y \left. \frac{\partial \psi}{\partial y} \right|_{j,0} + 4 \frac{\Delta y^2}{2} \left. \frac{\partial^2 \psi}{\partial y^2} \right|_{j,0} + 8 \frac{\Delta y^3}{6} \left. \frac{\partial^3 \psi}{\partial y^3} \right|_{j,0} + \dots \end{aligned} \quad (\text{A.23})$$

In this way, the values of the coefficients can be determined:

$$\begin{aligned} (a + b + c + d)\psi &= 0 \\ (-a + c + 2d)\partial\psi/\partial y &= \partial\psi/\partial y \\ (a + c + 4d)\partial^2\psi/\partial y^2 &= 0 \\ (-a + c + 8d)\partial^3\psi/\partial y^3 &= 0 \end{aligned} \quad (\text{A.24})$$

This can be solved to give the values: $a = \frac{1}{3}$, $b = \frac{1}{2}$, $c = -1$ and $d = \frac{1}{6}$.

A.4 Testing the program

A.4.1 Moving Lamb dipole

It was tested whether the program could accurately and without undue distortion predict the movement of an isolated Lamb dipole. Two runs were made for $Re_d = 10^3$ and $Re_d = 10^6$ where the Reynolds number is based on the distance between the centres of the vortices. The simulations were performed on a grid of 201×251 , with a grid size of 0.04×0.04 . This corresponds to the grid Reynolds numbers $Re_c \approx 33$ and $Re_c \approx 33000$, respectively. It was found that the dipole moves as expected even for the highest Reynolds number. However, for $Re = 10^6$ small oscillations were found, which did not appear for $Re = 10^3$ (Dankers, 1993). The stability of the scheme for these large values of Re_c can be explained by the choice of the boundary conditions. These impose almost no restrictions on the flow.

A.4.2 Lamb vortex impact on the wall

The collision of a Lamb dipole with a wall was calculated (Dankers, 1993). The results of this simulation were compared with the results of a simulation of Orlandi (1990).

For our simulation the number of grid points was 201×161 for a Reynolds number of 800. In the resulting contour plots for the vorticity distribution (figure A.4) it can be seen that both poles of the dipole generate a region with opposite vorticity at the wall, which subsequently interacts with the primary patch of vorticity to form a new dipole. In this way, the original single dipole is split into two new dipoles. Since the old poles have a larger circulation than the newly generated poles, the new dipoles move along curved trajectories towards each other. The development is illustrated by figure A.4. In this figure, Orlandi's results are given at the right and our own results at the left. A good correspondence exists between Orlandi's results and our own simulations.

A.5 Viscous growth

In the simulations, initial values were used for the vortex radius R and the boundary layer thickness δ . These two parameters do not retain a constant value during the simulation: they grow by viscous effects. For the 2D calculations on the spanwise vortex, the laminar boundary layer growth over the length of the domain is represented by

$$\delta(x) = 5\sqrt{\frac{\nu(x_0 + x)}{U_\infty}} = \delta_0\sqrt{1 + 25\frac{\nu x}{U_\infty\delta_0^2}} = \delta_0\sqrt{1 + \frac{25}{Re_u}\frac{x}{\delta_0^2}} \quad (\text{A.26})$$

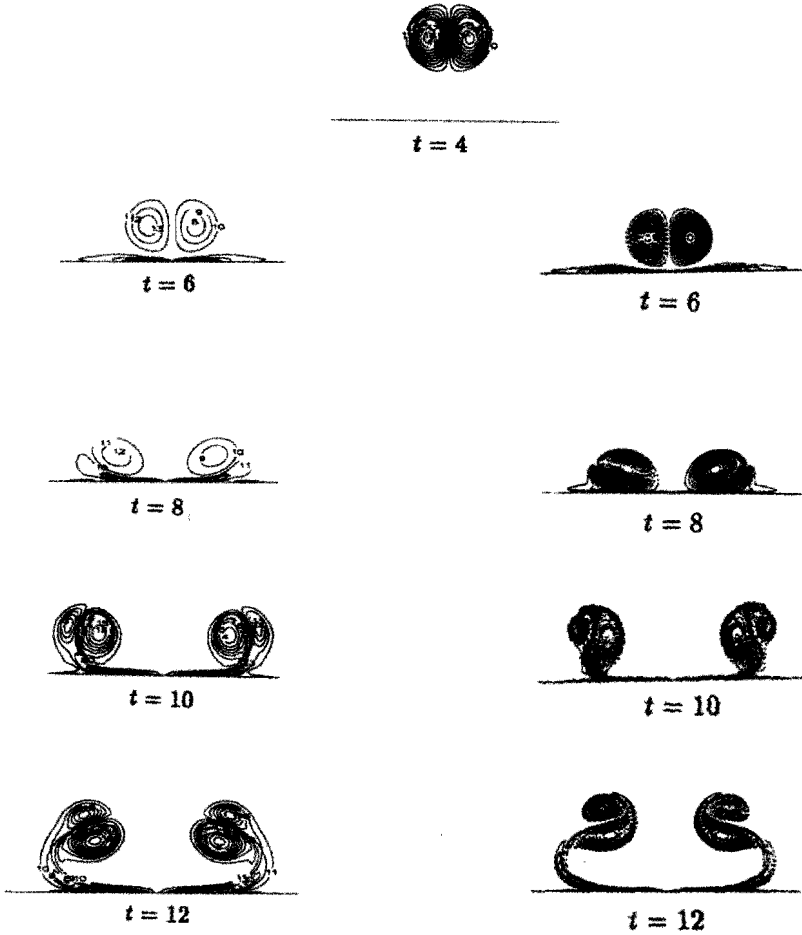


Figure A.4: The vorticity contour plots for the collision of a Lamb dipole with the wall at different times for $Re = 800$. **left:** the present calculations, **right:** the calculations of Orlandi (1990).

in which δ_0 is the initial boundary layer thickness and Re_u represents the Reynolds number based on the unity length ($Re_u \equiv U/\nu$). Assuming that the length of the domain is 10, the boundary layer increases over the computational domain as a function of viscosity and initial boundary layer thickness as follows:

δ_0	Re	$\Delta\delta/\delta_0$
3.5	1500	1 %
1.75	1500	3 %
0.50	1500	29 %
0.25	1500	91 %

It seems that for $\delta_0 < 1$, a substantial growth of the boundary layer occurs. For $\delta_0 = 0.25$ the growth of the boundary layer is of the same magnitude as the cross-stream motion of the vortex. In addition, the artificial viscosity that is present in the simulations makes this growth even larger than indicated above. However, the v -velocity induced by the growing boundary layer does not seem to affect the trajectory of the vortex, that continues to move along a straight path.

The initial vorticity distribution in the vortex core is Gaussian with a radius R . The increase in the core radius can then be estimated from

$$\Delta R/R = \sqrt{1 + 4t/ReR^2} - 1 \tag{A.27}$$

which leads to an increase of the core radius given by

R	Re	t	$\Delta R/R$
0.25	1500	10	19 %
0.25	500	10	51 %

The increase in the vortex radius for low Reynolds numbers is substantial, but it is small when compared to the cross-stream movement of the spanwise vortex.

A.6 Tracking a vortex

In chapter 7 the path of a spanwise vortex is calculated. Several methods can be used for tracking a vortex:

- track the location of the local maximum in the vorticity that is created by the presence of the vortex
- track the blob of fluid initially present in the vortex core (at the location of the vortex centre the local velocity is obtained by interpolation of the velocity at the grid points and this is multiplied by dt to find the new location of the vortex)

- track the location of minimum pressure

In our case, a combination of the first two methods was applied. First, the approximate location of the vortex core was found by tracking a blob of fluid. Then, in a small area around this location, the grid point was determined at which the vorticity had its maximum, and then the location of the vortex was determined from a linear interpolation between the grid points. This linear interpolation is based on the assumption that the vortex is located somewhere between the grid point Q_0 with the highest vorticity and the neighbouring grid point Q_+ with the highest-but-one vorticity. It assumes that the gradient in the vorticity is equal at both sides of the vortex core and can be approximated by $(\omega(Q_-) - \omega(Q_0))/(Q_- - Q_0)$, where Q_- is the neighbour of Q_0 that is opposite to Q_+ . The location of the vortex follows then from:

$$Q_{vortex} = Q_+ + \frac{1}{2}(Q_0 - Q_+) \frac{2\omega(Q_0) - \omega(Q_-) - \omega(Q_+)}{\omega(Q_0) - \omega(Q_-)} \quad (\text{A.28})$$

This interpolation is applied in both the x - and the y -direction.

For very weak vortices in a boundary layer, the local vorticity gradient in the boundary layer was larger than the vorticity gradient in the vortex core itself and it was not possible anymore to determine a local maximum. However, such a weak vortex causes only a very weak deformation of the boundary layer profile. Therefore it is possible to subtract from the calculated vorticity distribution the vorticity distribution that corresponds to an undisturbed laminar boundary layer. Although this method induces a lot of scatter, the vortex location is clearly defined.

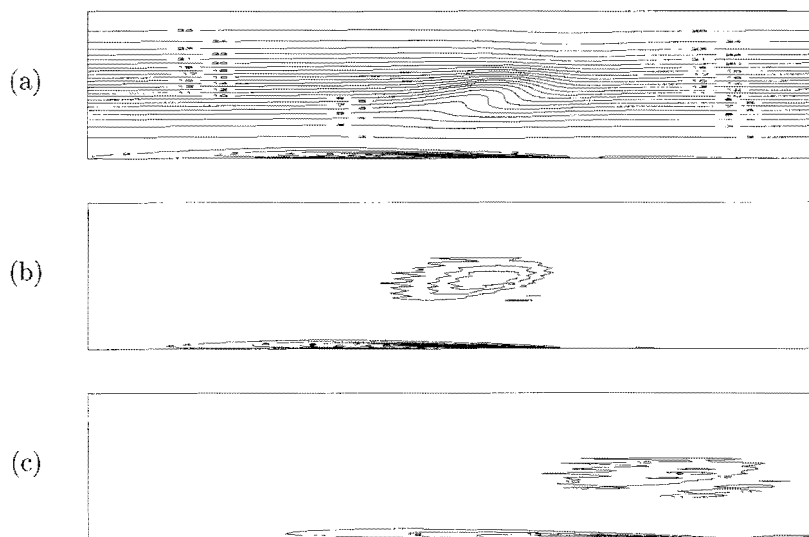


Figure A.5: A weak vortex immersed in a laminar boundary layer ($\Gamma = -0.1$, $Re = 2200$; between adjacent vorticity contour lines $\Delta\omega^* = 0.04$). (a) the vorticity field at $t^* = 4$. (b) and (c) show the vorticity field after subtraction of the boundary-layer vorticity at $t^* = 4$ and $t^* = 8$.

Appendix B

The pressure gradient

It has been argued throughout this thesis that a pressure gradient is induced in the flow by the obstacle. The pressure has been measured through small holes in the wall, that were located in the plane of symmetry downstream of the obstacle. For the measurements, a capacitance pressure sensor was used (type 590, Datametrics). The measured pressure is shown in figure B.1 as a function of the downstream distance from the obstruction.

The figure shows that the pressure drops to a negative minimum value immediately downstream of the obstruction. With increasing distance, the pressure increases steadily and reaches a positive maximum between $x/D = 1.5$ and $x/D = 2$. Then it slowly drops to zero. The extent of the region upstream of the positive maximum corresponds to the length of the recirculation area that was visualized in chapter 3. The figure indicates that a hemisphere induces somewhat stronger pressure fluctuations than a droplet. This corresponds to the observation in chapter 3 that the wake of a hemisphere is perturbed stronger

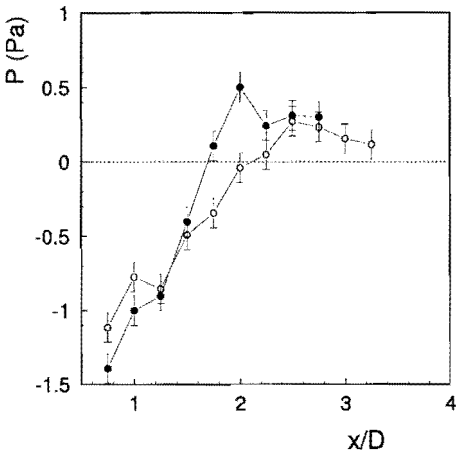


Figure B.1: Measurements of the pressure at the wall in the plane of symmetry downstream of an obstacle on a smooth wall for $Re_D = 1730$. (o) droplet (●) hemisphere

than the wake of a droplet. The pressure fluctuation induced by the obstruction is large when compared to the pressure drop that is induced by the boundary-layer growth. In the area where the vortex street was generated, the pressure gradient is approximately $dp/dx = -1.64$ Pa/m, which implies a pressure drop of $\Delta p = -0.08$ Pa over the range $0 < x/D < 3$.

Bibliography

- [1] Acarlar, M.S. & C.R. Smith **1987a**, A study of hairpin vortices in a laminar boundary layer. Part 1. Hairpin vortices generated by a hemisphere protuberance, *J. Fluid Mech.* **175**, 1 - 41.
- [2] Acarlar, M.S. & C.R. Smith **1987b**, A study of hairpin vortices in a laminar boundary layer. Part 2. Hairpin vortices generated by fluid injection, *J. Fluid Mech.* **175**, 43 - 83.
- [3] Backwelder, R.F. & H. Eckelman **1979**, Streamwise vortices associated with the bursting phenomenon, *J. Fluid Mech.* **94**, 577 - 594.
- [4] Blackwelder, R.F. **1983**, Analogies between transitional and turbulent boundary layers, *Phys. Fluids* **26**, 2807 - 2815.
- [5] Blokland, R. & K.K. Prasad **1986**, Some visualization studies on turbulent boundary layers using multiwire hydrogen bubble generation, *Proceedings Agard Conference*, 28/1 - 28/12.
- [6] Blom, J. **1970**, An experimental determination of the turbulent Prandtl number in a developing temperature boundary layer, *thesis Eindhoven University of Technology*.
- [7] Bosch, E. van den **1997**, *report Eindhoven University of Technology*, to be published.
- [8] Bradshaw, P. **1971**, An introduction to turbulence and its measurement, *Oxford: Pergamon*.
- [9] Cantwell, B.J. **1981**, Organized motion in turbulent flow, *Ann. Rev. Fluid Mech.* **13**, 457 - 515.
- [10] Choi, K.S. **1989**, Near wall structure of a turbulent boundary layer with riblets, *J. Fluid Mech.* **208**, 417 - 458.
- [11] Choi, K.S. **1989**, Drag reduction mechanisms and near-wall turbulence structure with riblets, *Proceedings of the IUTAM Symposium Zurich/Switzerland*, 553 - 560.

- [12] Choi, H., P. Moin & J. Kim **1993**, Direct numerical simulation of turbulent flow over riblets, *J. Fluid Mech.* **255**, 503 - 539.
- [13] Coustols, E. **1995**, Lecture notes, *Summer School 'Control of flow instabilities and Unsteady Flows': Udine.*
- [14] Doligalski, T.L. & J.D.A. Walker **1984**, The boundary layer induced by a two-dimensional vortex, *J. Fluid Mech.* **139**, 1 - 28.
- [15] Dankers, R.J. **1993**, Het berekenen van tweedimensionale stromingsproblemen volgens de ADI methode, *report R-1201-S, Eindhoven University of Technology.*
- [16] Doligalski, T.L., C.R. Smith & J.D.A. Walker **1994**, vortex interactions with walls, *Annu. Rev. Fluid Mech.* **26**, 573 - 616.
- [17] Ersoy, S. & J.D.A. Walker **1985**, Viscous flow induced by counter-rotating vortices, *Phys. of Fluids, vol. 28(9)*, 2687 - 2698.
- [18] Fletcher, C.A.J. **1988**, Computational Techniques for Fluid Dynamics, vol I & II, *Berlin: Springer Verlag.*
- [19] Galen, R.A.M.L. van **1994**, Design of a modular multichannel hot-wire anemometer system, *report R-1312-D, Eindhoven University of Technology.*
- [20] Goldstein, R.J. **1983**, Fluid Mechanics Measurements, *Washington: Hemisphere Publishing Corporation.*
- [21] Haji-Haidari, A. **1990**, Generation and growth of single hairpin vortices, *thesis Lehigh University.*
- [22] Head, M.R. & P. Bandhyopadhyay **1981**, New aspects of turbulent boundary-layer structure, *J. Fluid Mech.* **107**, 297 - 338.
- [23] Herweijer, J.A. **1995**, The small-scale structure of turbulence, *thesis Eindhoven University of Technology.*
- [24] Hinze, J.O. **1975**, Turbulence - second edition, *New York: McGraw-Hill.*
- [25] Hirata, M. & N. Kasagi **1979**, Studies of large-eddy structures in turbulent shear flows with the aid of flow visualization techniques, *Studies in Heat transfer, eds: J.P. Hartnett et al., Washington: Hemisphere Publishing Corporation.*
- [26] Hirsch, C. **1988**, Numerical Computation of Internal and External Flows, vol I & II, *Chichester: Wiley.*
- [27] Hon, T.L. & J.D.A. Walker **1987**, An analysis of the motion and effects of hairpin vortices, *Lehigh University: report FM-11.*

- [28] Kim, H.T., S.J. Kline & W.C. Reynolds **1971**, The production of turbulence near a smooth wall in a turbulent boundary layer, *J. Fluid Mech.* **50**, 133 - 160.
- [29] Klebanoff, P.S. **1954**, Characteristics of turbulence in a boundary layer with zero pressure gradient, *NACA Tech. Note No. 3178*.
- [30] Kline, S.J. & P.W. Runstadler **1959**, Some preliminary results of visual studies of the flow model of the wall layers of the turbulent boundary layer, *Trans. ASME Ser. E* **2**, 166-170.
- [31] Kline, S.J., W.C. Reynolds, F.A. Schroub & P.W. Runstadler **1967**, The structure of turbulent boundary layers, *J. Fluid Mech.* **30**, 741 - 774.
- [32] Kline, S.J. **1992**, Boundary layer structure - A summary ('Ringi').
- [33] Kunen, J.M.G. **1984**, On the detection of coherent structures in turbulent flows, *thesis Delft University of Technology*.
- [34] Lesieur, M. **1993**, Turbulence in Fluids, *Dordrecht: Kluwer*.
- [35] Lian, Q.X. **1990**, A visual study of the coherent structure of the turbulent boundary layer in flow with adverse pressure gradient, *J. Fluid Mech.* **215**, 101 - 124.
- [36] Luton, A., S. Ragab & D. Tellionis **1995**, Interaction of spanwise vortices with a boundary layer, *Phys. Fluids* **7**, 2757 - 2765.
- [37] Nitschke, P. **1984**, Experimental investigation of the turbulent flow in smooth and longitudinal grooved tubes, *thesis Max Planck Institute für Strömungsforschung, Göttingen*.
- [38] Nychas, S.G., H.C. Hershey & R.S. Brodkey **1973**, A visual study of turbulent shear flow, *J. Fluid Mech.* **61**, 513 - 540.
- [39] Orlandi, P. **1990**, Vortex dipole rebound from a wall, *Phys. Fluids* **A2**, 1429 - 1436.
- [40] Perry, A.E. & M.S. Chong **1982**, On the mechanism of wall turbulence, *J. Fluid Mech.* **119**, 173 - 217.
- [41] Rao, K.N., R. Narashimha & M.A. Badri Narayanan **1971**, The 'bursting' phenomenon in a turbulent boundary layer, *J. Fluid Mech.* **48**, 339 - 352.
- [42] Robinson, S.K. **1991**, The Kinematics of Turbulent Boundary Layer Structure, *NASA Technical Memorandum 103859*.
- [43] Sankaran, R., M. Sokolov & R.A. Antonia **1988**, Substructures in a turbulent spot, *J. Fluid Mech.* **197**, 389 - 414.

- [44] Savaş, Ö & D. Coles **1985**, Coherence measurements in synthetic turbulent boundary layers, *J. Fluid Mech.* **160**, 421 - 446.
- [45] Schlichting, H. **1955**, Boundary-layer theory, *New York: McGraw-Hill*.
- [46] Schwartz - Van Manen, A.D. **1992**, Coherent structures over grooved surfaces, *thesis Eindhoven University of Technology*.
- [47] Smith, C.R. & S.P. Schwartz **1983**, Observation of streamwise rotation in the near-wall region of a turbulent boundary layer, *Phys. Fluids* **26**, 641 - 652.
- [48] Smith, C.R. & S.P. Metzler **1983**, The characteristics of low-speed streaks in the near-wall region of a turbulent boundary layer, *J. Fluid Mech.* **129**, 27 - 54.
- [49] Smith, C.R., J.D.A. Walker, A.H. Haidari & U. Sobrun **1991**, On the dynamics of near-wall turbulence, *Phil. Trans. R. Soc. Lond. A*, 131 - 175.
- [50] Stoffels, F.A. **1994**, Numerieke analyse van longitudinale wervels in een laminaire grenslaag, *report R-1270-A, Eindhoven University of Technology*.
- [51] Taylor, B.K. **1990**, Pressure gradient effects on the development of hairpin vortices in an initially laminar boundary layer, *thesis Lehigh University*.
- [52] Theodorsen, T. **1952**, Mechanism of turbulence, *Proc. Second Midwestern Conference of Fluid Mechanics*, Ohio State University.
- [53] Vissers, J.L.A. **1996**, Development of a pseudo-spectral code for 2D flow simulations, *report Eindhoven University of Technology*.
- [54] Walker, J.D.A. **1990**, Models based on dynamical features of the wall layer, *Appl. Mech. Rev.* **43**, 232 - 239.
- [55] Walsh, M.J. & A.M. Lindemann **1984**, Optimization and application of riblets for turbulent drag reduction, *AIAA paper No. 84-0347*.

Summary

This thesis is the result of an investigation of the evolution of hairpin vortices in a laminar flow. The work is motivated by the fact that hairpin vortices seem to play an important role in the maintenance of turbulence for turbulent flows over a solid wall. The final aim of the research on the dynamics of hairpin vortices is to obtain a better understanding of turbulent flows.

The main part of this thesis shows the results of experimental work. Hairpin vortices are generated downstream of a hemisphere or a droplet-shaped obstacle that is placed on a wall. Two types of walls have been used: a smooth wall and a wall with longitudinal riblets. The vortices that are shed downstream of the obstacle assume the shape of a hairpin vortex under the influence of the background shear-flow. The dynamics of these vortices have been investigated using bubble-wire visualization and hot-wire anemometry.

It is found that regular vortex shedding can be observed only over a very limited range of Reynolds numbers. The range depends somewhat on the shape of the obstacle, but in general it seems that only for Reynolds numbers between 1500 and 2000 the vortex shedding is really periodic.

Upstream of the hemisphere, a standing vortex is generated. This vortex strongly influences the shedding of the hairpin vortices. If the standing vortex is not present, a long wake area is observed downstream of the obstacle. In this case, the wake shortens and the Strouhal number increases if the Reynolds number is increased. If the standing vortex is present, the wake area is shorter and the shedding frequency is higher. In this case, if the Reynolds number is increased, the length of the wake does not decrease any further and the Strouhal number remains constant.

By the interaction of the hairpin vortices and the stationary 'background'-velocity profile, a new vortex is generated. This vortex is called the 'quasi-spanwise vortex'. The evolution of this vortex is influenced by the presence of the standing vortex. In addition, the standing vortex strongly influences the velocity profile downstream of the hemisphere and therefore it also influences the secondary deformation of the hairpin vortex and its ability to generate secondary vortices. The most important effect of the riblets is the weakening of the standing vortex.

The experimental results are complemented with numerical results that have been obtained with a two-dimensional code based on finite-differences. These calculations have been made to gain more insight into the interaction between the vortices and the flow near the wall. The effect of both a spanwise and a streamwise vortex on a boundary-layer flow with a laminar velocity profile is investigated. The spanwise vortex corresponds to the head of the hairpin vortex, while the streamwise vortex corresponds to a vortex leg. For the circulation and the diameter of the vortex experimental values are used and for a number

of cases the results of the simulations are compared to the experiments. For the spanwise vortex, the simulations indicate that, given the experimental conditions, the near-wall flow is hardly influenced by the vortex head. For the streamwise vortices, the simulations indicate that a point of inflection is created in the streamwise velocity profile between the legs, but only if the legs are immersed sufficiently far into the boundary layer. In the simulations, attention is also paid to the general case of the dynamics of a spanwise vortex in a laminar boundary layer for various values of the Reynolds number and the circulation of the vortex. Due to the vorticity gradient in the laminar boundary layer, the spanwise vortex is pushed in the direction perpendicular to the main flow. More specific: a vortex with positive vorticity moves into the direction in which the background vorticity increases, while a vortex with negative vorticity moves in the opposite direction. If the vortex approaches the wall, the no-slip condition at the wall leads to the generation of a secondary vortex with a vorticity that is opposite to the circulation of the primary vortex. This vortex pushes the primary vortex away from the wall again (a 'rebound'). The rebound occurs in an earlier stage when the circulation is higher, the Reynolds number is lower or the boundary layer is thicker. If the simulation is continued, one observes that eventually the primary vortex starts moving towards the wall again. However, in the case of a hairpin vortex this motion is obscured by the much larger effects of the necks, the legs and the velocity gradient in the wake of the obstacle.

Samenvatting

Dit proefschrift is het resultaat van een onderzoek naar de ontwikkeling van haarspeldwervels in een laminaire stroming. De motivatie voor dit werk ligt in het feit dat, voor een turbulente stroming over een vaste wand, haarspeldwervels een belangrijke rol lijken te spelen in het in stand houden van de turbulentie. Het uiteindelijke doel van het onderzoek naar de dynamica van haarspeldwervels is een beter begrip van turbulente stromingen.

Het grootste gedeelte van het proefschrift betreft de resultaten van experimenteel werk. Voor de generatie van de wervels is in een laminaire stroming een half bolletje of een traanvormige obstructie op een wand geplaatst. Er zijn hierbij twee soorten wanden gebruikt: een vlakke wand en een wand met longitudinale ribbels. De wervels, die stroomafwaarts van de obstructie worden afgeschud, nemen onder invloed van het snelheidsprofiel van de stroming de vorm van een haarspeldwervel aan. De dynamica van deze wervels is onderzocht met behulp van bellendraadvisualizatie en hittedraadanemometrie.

Het blijkt dat slechts in een vrij klein gebied van Reynoldsgetallen een regelmatige wervelafschudding kan worden waargenomen. Dit Reynolds-gebied is enigszins afhankelijk van de vorm van de obstructie, maar in het algemeen kan men zeggen dat slechts in het geval dat het Reynoldsgetal tussen de 1500 en de 2000 ligt, de haarspeldwervels echt periodiek worden afgeschud.

Stroomopwaarts van het halve bolletje wordt een staande wervel gegenereerd. Deze wervel heeft een sterke invloed op de afschudding van de haarspeldwervels. Wanneer de staande wervel niet aanwezig is kan een lang zoggebied waargenomen worden achter de obstructie. In dit geval wordt bij toenemend Reynoldsgetal het zoggebied korter en neemt het Strouhalgetal toe. Wanneer de staande wervel wel aanwezig is, is het zoggebied veel korter en de afschudfrequentie is hoger. Hier neemt bij toenemend Reynoldsgetal de afmeting van het zoggebied niet verder af en ook blijft het Strouhalgetal in dit geval constant.

Door de interactie van de haarspeldwervels en het stationaire 'achtergrond'-snelheidsprofiel wordt een nieuwe wervel gegenereerd. Deze wervel wordt de 'quasi-spanwise vortex' genoemd. De ontwikkeling van deze wervel wordt door de aanwezigheid van de staande wervel beïnvloedt. Ook blijkt dat de staande wervel een belangrijke invloed heeft op het snelheidsprofiel stroomafwaarts van de halve bol en daarmee ook op de secundaire deformatie van de haarspeldwervel en diens vermogen om secundaire wervels te genereren. Het belangrijkste effect van de longitudinale ribbels is het verzwakken van de staande wervel.

Het experimentele gedeelte is aangevuld met enige numerieke resultaten verkregen met een 2-dimensionale eindige differentie code. Dit is gedaan om een beter inzicht te krijgen in de interactie tussen de wervels en de stroming in de buurt van de wand. Hiermee is de invloed onderzocht van zowel een transversale wervel als een longitudinale wervel op een grenslaagstroming met een laminair

snelheidsprofiel. De transversale wervel zou men hierbij kunnen beschouwen als de doorsnede van de kop van de haarspeldwervel en de longitudinale wervel als een wervelbeen. Voor de circulatie en de diameter van de wervel zijn waarden genomen die overeenkomen met de experimenteel gegenereerde haarspeldwervels en waar mogelijk zijn de numerieke resultaten vergeleken met de experimenten. Op grond van deze simulaties blijkt dat de kop van een haarspeldwervel, onder de omstandigheden van deze experimenten, niet veel invloed uitoefent op de snelheid in het gebied dicht bij de wand. Bij de simulatie van de longitudinale wervels blijkt er tussen de wervels een buigpunt in het u -profiel ontstaat, mits de wervels zich voldoende diep in de grenslaag bevinden.

Bij de numerieke simulaties is ook aandacht besteed aan het algemene geval van de dynamica van een transversale vortex in een laminaire grenslaag voor uiteenlopende waarden van het Reynolds getal en de circulatie in de wervel. Onder invloed van de vorticitetsgradiënt in de laminaire grenslaag heeft de beweging van een dergelijke wervel ook een component in de richting loodrecht op de hoofdstroom. In het bijzonder beweegt een wervel met positieve vorticitet in de richting waarin de achtergrondvorticitet toeneemt, en een wervel met negatieve vorticitet in de tegenovergestelde richting. Wanneer een wervel de wand nadert, wordt ten gevolge van de no-slip conditie aan de wand een secundaire wervel gegenereerd met een vorticitet van tegengesteld teken. Deze wervel duwt de primaire wervel weer van de wand af (een 'rebound'). Deze rebound vindt eerder plaats wanneer de circulatie van de primaire wervel sterker is, het Reynoldsgetal kleiner is of de dikte van de grenslaag groter is. Na verloop van tijd begeeft de wervel zich dan opnieuw naar de wand. In het geval van een haarspeldwervel worden deze effecten echter overschaduwd door andere verschijnselen, zoals de snelheidsgradiënt in het zog van de obstructie en de invloed van de nekken en de benen van de haarspeldwervel.

Nawoord

Het is nu maandagavond 10 februari 1997 en morgenochtend ga ik dit proefschrift bij de drukker inleveren. Ruim vier jaar werk zit erop en het enige dat mij nog rest, is om iedereen te bedanken die me tijdens mijn promotie met raad, daad en enthousiasme heeft geholpen. In het bijzonder wil ik hier Jan Voskamp bedanken, die zich als mijn dagelijkse begeleider gedurende de laatste maanden met ongebroken enthousiasme door mijn continue tekstproductie heeft weten heen te ploegen. Verder wil ik mijn promotoren Gert-Jan van Heijst en Anton van Steenhoven bedanken voor hun enthousiasme en het grondig lezen van de tekst en Rini van Dongen en Fons de Waele voor hun kritische opmerkingen. Bovendien ook dank aan mijn moeder, Lies Zondag, voor een laatste correctie van het Engels.

In de loop van dit project hebben velen op diverse gebieden een bijdrage geleverd. Veel dank aan Johan Stouthart en Roger van Galen, die beide een grote bijdrage aan de beginfase van dit project hebben geleverd en aan Gerard Trines en mijn collega en kamergenoot Arnold Moene, die gedurende het laatste deel van dit werk vaak mijn vraagbaak waren. Bovendien dank aan alle studenten die in de loop der jaren hebben bijgedragen aan dit project. Met name wil ik hier Fred Stoffels, Ruud Heijmans en Elwin van den Bosch noemen, die als afstudeerders een rol hebben gespeeld in het ontwikkelen en testen van de software.

Over promovendi kort voor hun promotie bestaan vele stereotypen. Het schijnt dat dit een periode is waarbij ze voor nauwelijks iemand meer aanspreekbaar zijn, dat ze bij nacht en ontij nog op hun werk kunnen worden aangetroffen waar ze gestrest nog bezig zijn een laatste meting te verrichten, een tekst op tijd af te krijgen of LATEX zover proberen te krijgen dat het plaatje wel op de goede pagina wordt gezet. Wanneer ze dan eindelijk thuiskomen zijn ze niet te genieten en zitten ze met hun gedachten voortdurend bij hun werk. Ik vrees dat de meeste van deze stereotypen ook op mij betrokken zouden kunnen worden. Met name wil ik hier dan ook mijn vriendin Wendy Schrama bedanken, die me door al het gestress van afgelopen periode heen heeft weten te loodsen.

En tenslotte rest het mij nog iedereen te bedanken die een rol heeft gespeeld in de afgelopen 4 jaar, maar die ik hierboven niet met name heb genoemd.

Herbert

Curriculum Vitae

Herbert Zondag werd geboren op 5 maart 1969 te Rotterdam. Kort daarop verhuisden zijn ouders naar Houten, vanwaaruit hij in de periode 1981 - 1987 het Christelijk Gymnasium te Utrecht bezocht. Vervolgens doorliep hij in de periode 1987 - 1992 de studie Experimentele Natuurkunde aan de Rijksuniversiteit Utrecht, waarbij hij afstudeerde binnen de groep Gecondenseerde Materie. In november 1992 begon hij aan een promotieonderzoek aan de Technische Universiteit Eindhoven waarvan dit proefschrift het resultaat is.

Stellingen

behorende bij het proefschrift

‘The Dynamics of Hairpin Vortices in a Laminar Boundary Layer’

H.A. Zondag, 9 april 1997

1. Haarspeldwervels kunnen worden gegenereerd door een obstructie op een vaste wand in een stroming te plaatsen. Bij het gebruik van deze methode dient men zich echter te realiseren dat de vorm van deze obstructie de verdere ontwikkeling van de wervel beïnvloedt.

Dit proefschrift

2. Voor een niet-gestroomlijnde obstructie op een wand met longitudinale ribbels leidt de aanwezigheid van de ribbels tot een sterke verzwakking van de staande wervel die zich stroomopwaarts van een dergelijke obstructie bevindt.

Dit proefschrift

3. Een transversaal georiënteerde twee-dimensionale wervel in een niet-uniforme, parallelle achtergrondstroming beweegt loodrecht op de stromingsrichting als gevolg van de vorticeitsgradiënt in die achtergrondstroming.

Dit proefschrift

4. Het meest dominante effect van een haarspeldwervel op de achtergrondstroming is de verhoging van de snelheid in de buurt van de wand, met name in het gebied terzijde van de benen van de wervel.

Dit proefschrift

5. Het ontslag van professor Diekstra op grond van het plegen van plagiaat, ondanks zijn kwaliteit als docent en zijn successen als pleitbezorger voor de psychologie, geeft aan hoezeer de universiteit meer op onderzoek dan op onderwijs gericht is.

6. De maatschappelijke discussie over het broeikaseffect lijkt iedere keer even te verstommen op het moment dat er weer een elfstedentocht gereden wordt.

7. In de discussie over bezuinigingen op onderwijs moet niet uit het oog verloren worden dat onderwijs, los van zijn maatschappelijke functie, bijdraagt aan het individuele welzijn van mensen en derhalve ook als een goed op zich gewaardeerd moet worden.

8. Een universiteit is vaak zeer herkenbaar: een verzameling bijzonder lelijke betonnen blokkendozen, veelal in een buitenwijk van de stad. De conclusie dringt zich op dat dit wel eens een afspiegeling zou kunnen zijn van haar maatschappelijke positie.

9. In Nederland wordt regelmatig kritiek geleverd op de ondergeschikte positie van de vrouw binnen het Islamitische recht. Men moet hierbij echter niet vergeten dat binnen het Nederlandse recht de gehuwde vrouw tot 1957 in juridisch opzicht handelingsonbekwaam was, en dat tot 1970 de man wettelijk het hoofd van het gezin was. Pas in 1985 zijn in Nederland de laatste ongelijkheden in de positie van de man en de vrouw binnen het huwelijk opgeheven.
10. Een paar geografische overzichtskaartjes van een regio waarop grondsoorten, klimaat, delfstoffen en lokaal voorkomende plagen als tseetsee staan aangegeven, aangevuld met wat technische gegevens over landbouwproductiviteit en transportmogelijkheden, geven vaak meer inzicht in de ontwikkelingsgeschiedenis van die regio dan dikke boeken over de verrichtingen van de diverse koningen, keizers of farao's die in de loop der tijden in het gebied hebben geheerst.
11. In de kerkelijke geschiedschrijving wordt het ontstaan van een burgeroorlog nog al eens verklaard door te wijzen op de strijdige theologische ideeën van beide partijen, terwijl er volledig voorbij wordt gegaan aan de maatschappelijke achtergrond van het conflict. Deze benadering dient als een vorm van geschiedvervalsing beschouwd te worden.
12. Tegenwoordig wordt er al geklaagd over het weer wanneer de neerslag slechts enige millimeters per uur bedraagt. Het is goed op zo'n moment te bedenken dat er tenminste één geval bekend is waarbij in 40 dagen wel 9 kilometer regen is gevallen; dat is ruim 9 meter per uur.
naar Ambrose Bierce (1842 - 1914?), The Devil's Dictionary
13. Het schrijven van stellingen heeft veel gemeen met het schrijven van Sinterklaasgedichten.